THÈSE POUR OBTENIR LE GRADE DE DOCTEUR DE L'UNIVERSITÉ DE MONTPELLIER

En biophysique

École doctorale Information Structures Systèmes (I2S)

Unité de recherche UMR 5221 – Laboratoire Charles Coulomb (L2C) à Montpellier

Étude multimodale en optique non linéaire de l'assemblage du collagène aux cicatrices fibrotiques de la moelle épinière dans un modèle murin

Présentée par Joshua de Lizaraga
Le 27 novembre 2025

Sous la direction de Csilla Gergely

Devant le jury composé de

Pierre-François Brevet	Professeur	Inst. Lumière Matière - Lyon	Président
Serge Monneret	Directeur de recherche	Inst. Fresnel - Marseille	Rapporteur
Sylvie Callas	Maître de Conférences – HDR	L2C - UM	Examinateur
Zsuzsanna Heiner	Professeur	SALSA - Humboldt University	Examinateur
Csilla Gergely	Professeur	L2C - UM	Directrice de thèse
Thierry Cloitre	Maître de Conférences	L2C - UM	Co-encadrant
Florence Perrin	Professeur	MMDN - UM	Co-encadrante

UNIVERSITÉ DE MONTPELLIER

Multimodal non-linear optical approach to assess fibrillogenesis in collagen constructs and spinal cord injury in mice model

**

Étude multimodale en optique non linéaire de l'assemblage du collagène aux cicatrices fibrotiques de la moelle épinière dans un modèle murin

Every great and deep difficulty bears in itself its own solution.
It forces us to change our thinking in order to find it

Niels Bohr

(1885-1962)

Physicist

Table of contents

Acknowledgements 8
Publications and Scientific communications 11
Abbreviations 12
List of Figures 14
List of tables 16
Abstract 17
Résumé 19
General introduction 25
I. State of the art and objectives 30
I.1. Spinal Cord Injuries 30
I.1.1 Context: Incidence, causes and outcomes 30
I.1.2 Spinal Cord 33
I.1.2.1 Healthy spinal cord anatomy in human 33
I.1.2.2 Spinal Cord injury 34
I.1.2.3 The primary and secondary injuries 35
I.1.2.4 The Glial and fibrotic scar 36
I.1.2.5 The chronic phase 37
I.1.2.6 SCI animal models 39
I.2 Collagen 41
I.2.1 Collagen biology 41
I.2.1.1 The Triple-Helix Structure 41
I.2.1.2 Classification of collagen types 43
I.2.1.3 Telocollagen and Atelocollagen 45
I.3 Nonlinear optics (NLO) 47
I.3.1 SHG in non-centrosymmetric structures 49
I.3.2 Imaging collagen with SHG microscopy 52
I.3.3 Collagen imaging in Spinal Cord Injury (SCI) 54
I.3.4 Second harmonic Scattering (SHS) for probing collagen architecture 55
I.3.5 Vibrational Sum Frequency Generation (VSFG) 59
I.4 Atomic Force Microscopy (AFM) 64
I.5 Objective of the work 65
II. Materials and Methods 70
II.1 Biological samples 70

II.1.1 Ethics 70
II.1.2 Murine model 70
II.1.3 Spinal cord injury and post-operative cares 70
II.1.4 Tissues preparation for ex vivo analysis 71
II.2 Collagen samples 72
II.2.1 Cold Start method 72
II.2.2 pH controlled method 73
II.2.3 Ionic forces to form bundles of fibers 73
II.2.4 Peptides model 73
II.3 Imaging and spectroscopic techniques 74
II.3.1 Multiphoton microscopy (MPM) 74
II.3.1.1 Setup 74
II.3.1.2 Resolution and z-stack 76
II.3.1.3 Mosaic acquisitions 77
II.3.1.4 Image analysis 78
II.3.1.5 Preprocessing with ImageJ 78
II.3.1.6 Fingerprint method 79
II.3.1.7 3D Variance 81
II.3.2 Second harmonic scattering (SHS) 88
II.3.2.1 Setup 88
II.3.2.2 Hyperpolarizability 90
II.3.2.3 Polarization-Resolved (P-SHS): Depolarization ratio 94
II.3.3 Vibrational Sum Frequency Generation 96
II.3.3.1 Setup 96
II.3.3.2 Spectra treatment and analysis 97
II.3.3.3 Determination of angle θ 100
II.3.4 Atomic Force Microscopy (AFM) 105
III. Results and discussion 107
III.1 Bright field images 107
III.2 SHG Imaging 108
III.2.1 Fingerprint algorithm results 112
III.2.2 Discussion on the evolution of the fibrotic scar by 2D analysis 121
III.2.3 3D Variance results 124
III.2.4 Discussion on the evolution of the scar in 2D and 3D Analysis 128

III.3 In-vitro collagen constructs 132
III.3.1 Collagen growth method 132
III.3.1.1 Cold Start method 132
III.3.1.2 pH Controlled collagen growth 133
III.3.1.3 Ionic forces to form bundles of collagen fibers 134
III.3.2 Second harmonic scattering (SHS) experiments 135
III.3.2.1 Hyperpolarizability 135
III.3.2.2 Depolarization ratio 137
III.3.3 Vibrational Sum Frequency Generation (VSFG) experiments 142
III.3.3.1 VSFG spectra of the PPG peptide, Tcol and Acol 143
III.3.3.2 Determination of tilt angle θ 148
III.3.3.3 AFM images of collagen constructs 154
IV. General conclusion and perspectives 159
V. References 165
VI. Appendix 182
Appendix I 182
Appendix II 183
Appendix III 184
Appendix IV 185
Appendix V 186

Acknowledgements

First of all, I would like to thank Dr. Pierre Lefebvre for allowing me to carry out this thesis at the Charles Coulomb laboratory. It was a chance to be part of this project at the frontier of biology and physics. It gave me the opportunity to discover and understand experiments in a whole new light.

I would like to express my sincere gratitude to my supervisor Pr. Csilla Gergely for her invaluable guidance, advice and continuous support throughout my PhD. I am deeply thankful for her straightforwardness, which, though sometimes challenging, was always constructive and ultimately beneficial. Her confidence in me, as well as her constant encouragement, helped me to overcome both scientific and personal apprehensions. I am also grateful for her kindness and humanity, which allowed me to move forward despite often difficult challenges. I am truly indebted to her for giving me the opportunity to be her PhD student and to work on this project.

I would like to thank Dr. Serge Monneret and Pr. Pierre-François Brevet for agreeing to review my manuscript and more generally, all the members of the jury including Pr. Zsuzsanna Heiner, Dr. Sylvie Callas and Dr. Christian Jonin.

I am very grateful to Dr. Christian Jonin for all his help and expertise regarding the SHS experiment and VSFG methodologies that I discovered during this thesis. These projects would not have come to this result in the same way without his presence and invaluable support.

Thank you to Thierry Cloitre for his advice and constant expertise on so many subjects. His insightful guidance has been invaluable, and I will strive to make the best use of it in the future. Huge thanks to Dr. Yannick Gerber and Pr. Florence Perrin for all your advice, availability and kindness throughout these three years. I am especially grateful for the high-quality samples you provided. One thing is certain: I now know how important it is to be careful and not to overinterpret images specifically in biology.

I would like to express my gratitude to Dr. Marta Martin. Marta, thank you for everything you have done for me over these past years. My thesis certainly would not have been completed, at least not in the same way, without your presence, your joy and your willingness to always show up with a smile. You are truly a wonderful person, and I am deeply thankful for having you by my side throughout this journey.

I would also like to thank Dr. Estelle Salmon for her advice and for the moments we shared in the laboratory, or at the canteen. Thank you for helping me realize that I had every right to pursue this PhD and that I owed it only to myself. With your open-mindedness, good spirit and energy you have been a constant source of support. I will always remember the rigor, attention to detail and genuine satisfaction in doing science by your side.

A big thank you also to Pr. Zsuzsanna Heiner for introducing me to VSFG and have accepted the collagen project. Thank you for your availability and for the time you dedicated during my visit to your lab in Berlin, as well as for all the explanations you so generously provided both then and afterward.

The support and friendship of my colleagues and fellow PhD students greatly make my time delightful in the lab. I would firstly like to thank Valentin Develay, a fellow PhD student, without whom this thesis would not have been possible under these conditions. We shared countless laughs and found moments to breathe during the most challenging times. I promise next time I'll be the one to offer you a candy. Thank you for everything, Valentin, I wish you all the best for the future and truly hope our paths will cross again soon. Many thanks to Laura Vazquez, who joined us in this final year in the team and in our desk, for the moments of laughter and confusion we shared. I wish you all the very best for the future. I have been very fortunate to work with many colleagues during this time. In particular, I would like to thank Imane Belkasmi for her time and for the exchanges we share, both scientific and around our different passions. Thank you for involving me in your project, which allowed me to discover new techniques and explore different scientific questions. I hope you do the best in your new project and studies. I am also grateful to Dr. Richard Younes, whose good humor and kindness always provided a welcome break. Thanks for all the scientific discussions we had on a wide range of topics. I hope you do the best in your new journey and hope to see you soon. I would also like to express my acknowledgement to Ibtissam El Jadydy Hamidou, who did considerable work on the MPM data analysis during her internship. Your help was invaluable in keeping me on schedule. Thanks to all of you for your generosity and your humor, allowing me to feel the best in the lab.

Thank you to Juliette Plo, Benjamin Benhamou-Bui and Thomas Alfonso, close friends and fellow PhD candidates for your time, patience and kindness. Your optimism brought light to my days when they sometimes felt overwhelmed. I am truly grateful for the moments we shared,

both inside and outside the lab, which made this journey far more enjoyable. I wish you all the success you deserve in your careers and your life and hope our paths will continue to cross in the future.

This last part is dedicated to acknowledge all the people outside the laboratory and beyond the scientific context, who allowed me to maintain a balanced social life throughout this challenging journey. Many thanks to my close friends Dr. Domitille Baux and Dr. Loucif Remini, who had already defended their thesis, for their understanding, their help and their empathy, as well as for the advice that helped me better navigate this stage on my life. A special thank you to Emilien, Josselin and Iris. We went through major challenges at the same time and your unconditional love and support was of great help. Emilien, thank you for your precious help and attentive ear, for introducing me to new musical worlds and for supporting the various projects I had in mind. Iris, your laughter was the best medicine during these three years. You are a wonderful person, always ready to help others and I have always enjoyed our conversations. Josselin, thank you for all the moments we shared, the laughs, the karaoke sessions and the time for relaxation that were truly necessary for me. I hope you all the best in your next journey. Finally, I would like to thank my family for their unwavering support and patience throughout this journey. To my parents, who taught me perseverance and gave me the freedom to follow my own path. We have faced many challenges in recent years, including one of the most difficult right now. You taught me to fight for what I want, today I give this same advice back to you. This insidious illness may be hard to bear, but as long as you keep fighting, together, like a rock, nothing will overcome you. These words are difficult for me to write, but I want you to know how deeply I love you. Thanks for your understanding, your patience and above all the unconditional support, no matter the project, even when you did not always fully understand it. It is because of you that I have come this far, and thanks to your help and your listening ear that I am able to keep moving forward.

This work was supported by the Region Occitanie (DRTES – SAEDS N°22009669).

Publications and Scientific communications

Publications

2025

De Lizaraga Joshua, Martin Marta, Salmon Estelle, Cloitre Thierry, Gergely Csilla, Jonin Christian, (2025). Probing the Role of Telopeptides in Collagen Fibrillogenesis by Second Harmonic Scattering. J. Phys. Chem. B 129, 9020–9029. https://doi.org/10.1021/acs.jpcb.5c02016

2023

Manesco, C., Saavedra-Villanueva, O., Martin, M., De Lizaraga, J., Varga, B., Cloitre, T., Gerber, Y.N., Perrin, F.E., Gergely, C., 2023. Organization of collagen fibers and tissue hardening: Markers of fibrotic scarring after spinal cord injury in mice revealed by multiphoton-atomic force microscopy imaging. Nanomedicine: Nanotechnology, Biology and Medicine 53, 102699. https://doi.org/10.1016/j.nano.2023.102699

Scientific communications

2025

- *2nd International Conference on BioMedical Photonics*, Apr 2025, Palavas Les Flots, France. **Poster presentation**

Joshua de Lizaraga, Marta Martin Fernandez, Estelle Salmon, Thierry Cloitre, Csilla Gergely, Christian Jonin. (2025 April). Second Harmonic Scattering as a Tool for Investigating Collagen Assembly Dynamics.

- *2nd International Conference on BioMedical Photonics*, Apr 2025, Palavas Les Flots, France. **Poster presentation**

Joshua de Lizaraga, Marta Martin Fernandez, Estelle Salmon, Thierry Cloitre, Christian Jonin, Csilla Gergely, Zsuzsanna Heiner. (2025 April). Unveiling the Structural and Chiral Differences Between Telocollagen and Atelocollagen by Using VSFG Spectroscopy.

- *2nd International Conference on BioMedical Photonics*, Apr 2025, Palavas Les Flots, France. **Communication in congress**

Joshua de Lizaraga, Thierry Cloitre, Marta Martin Fernandez, Christian Jonin, Yannick Gerber, Florence Perrin, Csilla Gergely (April 2025). A 3D imaging approach to assess collagen remodeling in spinal cord injury.

- Invited Seminary, *Laboratoire Interdisciplinaire des Environnements Continentaux*, Mar, 2025, Nancy, France.

Joshua de Lizaraga (March 2025). From Light to Insight: Laser Photonics for Biological Exploratio

Abbreviations

Abbreviations

Acol: atelocollagen

AIS: ASIA (American spinal injury association) impairment scale

AFM: atomic force microscopy

CaF_2: calcium fluoride

CNS: central nervous system

CSPGs: chondroitin sulfate proteoglycans

DR: Depolarization ratio

ECM: Extracellular matrix

eGFP: enhanced green fluorescent protein

FP: Fingerprint algorithm

HS: hemisection

HWP: half-wave plate

MPM: multiphoton microscopy

NA: numerical aperture

LUT: Look-up table

OPC(s): Oligodendrocyte Precursor Cell(s)

PC: Polarizing cube

PF: pass filter

PM/ PMT(s): photomultiplier

PPG_{10}: $(Pro\text{-}Pro\text{-}Gly)_{10}$ peptide

R / C: Rostral / Caudal

ROI: region of interest

SCI: spinal cord injury

SHG: second harmonic generation

SHS: second harmonic scattering

SD: standard deviation

Tcol: telocollagen

TGF-β: transforming growth factor β

VSFG / SFG: vibrational sum frequency generation

Wpi: week post injury

2PEF: two-photon excited fluorescence

3D-DV: 3D directional variance

List of Figures

Figure 1: Spinal cord injury from traumatic causes by WHO region 1959-2011 31
Figure 2: Spinal cord functions and extent of paralysis by injury level and AIS severity 33
Figure 3: Anatomy and vertebral organization of the human spinal cord 35
Figure 4: Pathophysiology of traumatic spinal cord injury 38
Figure 5: Collagen occurrence and hierarchical structure 42
Figure 6: Difference between telocollagen and atelocollagen 46
Figure 7: Jablonsky energy diagrams of two-photon excited fluorescence (TPEF) and SHG 50
Figure 8: Dipole orientation and phase-matching in SHG 51
Figure 9: SHG signal generation in collagen fibers 53
Figure 10: Collagen extension around lesion site over time (SHG imaging) 55
Figure 11: Principles of second harmonic scattering (SHS) 57
Figure 12: VSFG input geometries and energy diagram 60
Figure 13: AFM experimental setup 65
Figure 14: Schema of collection of longitudinal spinal cord section 72
Figure 15: Multiphoton microscopy (MPM) setup 75
Figure 16: Collagen fiber length and end-to-end distance to determine tortuosity 80
Figure 17: Definition of orientation angles and weighted vectors for 3D directional variance 85
Figure 18: Simulated fiber stacks for 3D variance algorithm validation 88
Figure 19: Hyper-Rayleigh Scattering (HRS) experimental setup 89
Figure 20: Laboratory and molecular frames (polarization analysis) 90
Figure 21: Orientation of collagen molecule in laboratory coordinates with Euler angles 91
Figure 22: SHS intensity of atelocollagen solution at pH=2 93
Figure 23: SHS intensity in function of the incident power in collagen solutions at pH=2 94
Figure 24: Vibration Sum Frequency Generation (VSFG) setup 96
Figure 25: Euler transformation from laboratory to molecular frame 103
Figure 26: Schematic representation of the VSFG experiment and molecular orientation of side chain of collagen molecule 104
Figure 27: Bright-field images of 50 µm thick longitudinal spinal cord sections at 2, 4 and 6 wpi. 108
Figure 28: MPM acquisition on 50µm thick longitudinal sections of injured spinal cord at 1wpi 109
Figure 29: Evolution of collagen formation around the lesion site over time following spinal cord injury, revealed by MPM imaging on 50 µm thick longitudinal sections 110
Figure 30: Region of interest determination on a 6 wpi section 112
Figure 31: Tortuosity of collagen fibers across spinal cord regions at different post-injury timepoints. 113
Figure 32: Temporal evolution of collagen fiber tortuosity within rostral, lesion and caudal regions. 114
Figure 33: Evolution of total fiber length across timepoints for each region 117
Figure 34: Evolution of 2D Variance across timepoints for each region.. 119
Figure 35: Evolution of entropy across timepoints for each region 120
Figure 36: 3D collagen orientation in the lesion core over time and their respective orientation histogram 125
Figure 37: Variance of collagen fiber orientation in 3D SHG datasets across post-injury timepoints 126
Figure 38: AFM images of in-vitro type I collagen fibrils obtained with Cold Start method 133
Figure 39: AFM imaging of in-vitro type I collagen fibrils prepared by pH control method. 134
Figure 40: AFM characterization of modified type I collagen matrices (Oh et al., 2020) 134
Figure 41: Hyperpolarizability as a function of pH for A) Atelocollagen and B) Telocollagen 136
Figure 42: Polarization Curves for Atelocollagen A) at pH 2 C) at pH 3 and Telocollagen B) at pH 2 D) at pH 3 . 137
Figure 43: Depolarization ratio evolution as a function of pH for A) Atelocollagen and B) Telocollagen. 138

Figure 44: AFM topographic images and amplitude images of the atelocollagen sample at pH=2 and pH=3 .. 141
Figure 45: AFM topographic images and amplitude images of the telocollagen sample at pH =2 and pH=3 142
Figure 46: Normalized VSFG spectra recorded in the 1150-1700cm-1 spectral range under ppp, ssp and psp polarization combinations for the PPP_{10} peptide, Tcol at pH=3 and Acol at pH=3 143
Figure 47: VSFG experimental geometry in reflection mode and Omit map (Fo-Fc) of a representative triplet of Pro-Pro-Gly 144
Figure 48: Example of Gaussian fitting procedure applied to the ppp-polarized VSFG spectrum of collagen..... 147
Figure 49: Experimental VSFG spectra of the PPG10 peptide model compared with theoretical fits. 149
Figure 50: Polarization-resolved VSFG spectra of telocollagen and atelocollagen at pH=3 152
Figure 51: 3D reconstructions of topographic AFM height images of atelocollagen and telocollagen on CaF2 at pH=3 with Tables displaying the corresponding RMS values.. 155
Figure 52: AFM height and amplitude images of atelocollagen and telocollagen on CaF2 at pH=3, and at three different scan sizes 156
Figure 53: AFM phase images of atelocollagen at pH=3 and telocollagen on CaF2 at pH=3, and at three different scan sizes. 157
Figure 54: Broadband coherent anti-Stokes Raman scattering (BCARS) spectra and chemical imaging of mouse spinal cord tissue at 6 weeks post-injury 164
Figure 55: AFM topographic images and amplitude images at different scales of the atelocollagen sample at pH=2 182
Figure 56: AFM topographic images and amplitude images at different scales of the telocollagen sample at pH=2 183
Figure 57: AFM topographic images and amplitude images at different scales of the atelocollagen sample at pH=3 184
Figure 58: AFM topographic images and amplitude images at different scales of the atelocollagen sample at pH=3 185
Figure 59: Gaussian fits for the ppp-polarized VSFG spectrum of PPG_{10} amide I band 186
Figure 60: Gaussian fits for the ppp-polarized VSFG spectrum of PPG_{10} amide II and III bands..... 187
Figure 61: Gaussian fits for the ppp-polarized VSFG spectrum of Tcol amide II and III bands..... 188
Figure 62: Gaussian fits for the ppp-polarized VSFG spectrum of Acol amide I band 189
Figure 63: Gaussian fits for the ppp-polarized VSFG spectrum of Acol amide II and III bands. 190

List of tables

Table 1: Summary of 2D metrics determined for collagen fibers in rostral, lesion and caudal regions at 2, 4 and 6 wpi..... 121
Table 2: Comparison of 3D variance and 2D entropy of collagen fiber for each region at 2, 4 and 6 wpi 128
Table 3: Depolarization ratio (DR) values measured for Acol and Tcol at different pH levels..... 140
Table 4: Selected vibrational peaks of the measured VSFG spectra (1135-1700 cm-1)..... 148
Table 5: Extracted hyperpolarizability tensor elements for telocollagen and atelocollagen 149
Table 6: Representative vibrational bands used for orientational analysis of the PPG10 peptide, with the corresponding tilt angles θ (in degrees)..... 150
Table 7: Representative vibrational bands used for orientational analysis in telocollagen and atelocollagen at pH=3, with corresponding tilt angles θ (in degrees)..... 153

Abstract

Spinal cord injury (SCI) represents one of the most devastating conditions affecting the central nervous system, leading to severe motor, sensory, and autonomic impairments. Following trauma, a dense fibrotic scar rapidly develops at the lesion site. This scar is characterized by extensive formation of extracellular matrix proteins, including type I collagen. Although collagen is widely recognized as a major component of fibrosis, many aspects of its organization remain poorly understood. In particular, the relationship between its fibrillar alignment, and higher-order supramolecular assemblies during fibrillogenesis remains poorly understood. Fibrillar collagen exhibits a highly ordered, non-centrosymmetric structure that makes it detectable by nonlinear optical (NLO) imaging as second harmonic generation (SHG) imaging.

This thesis presents a comprehensive investigation into the multiscale structure and organization of collagen through a multimodal strategy combining NLO imaging and spectroscopy. The work was structured around two complementary approaches: an *ex vivo* study focusing on a murine spinal cord injury SCI model, and an *in vitro* study addressing the fundamental mechanisms of collagen fibrillogenesis. This dual approach enabled us to analyze collagen formation within fibrotic tissue in a complex biological environment, while also allowing to monitor the evolution of polar order and band-specific orientation in simplified model systems.

The *ex vivo* part of this work follows collagen reorganization along the rostrocaudal axis at different timepoints post-injury. SHG imaging and a custom made, subsequent 2D fingerprint data analysis quantified fiber tortuosity, orientation, and heterogeneity, while 3D variance analysis captured volumetric disorder. The 2D analysis revealed three phases of scar evolution: an initial phase of collagen formation, a disorganized phase with increased fiber density and heterogeneity, and a later phase suggesting fibers' reorganization. Interestingly, 2D and 3D analyses diverged in the rostral and caudal regions but converged at the lesion core, suggesting a homogenous remodeling across the depth of the spinal cord tissue. In 2D, heterogeneity rose between 2 and 4 weeks before decreasing at 6 weeks, suggesting transient disorganization followed by partial reorganization. In contrast, 3D variance decreased at 4 weeks and rose again at 6 weeks, pointing to the opposite temporal trend. This discrepancy indicates that planar metrics and volumetric descriptors capture distinct facets of scar remodeling: 2D emphasizes

surface-level alignment and density of collagen fibers, whereas 3D analysis exhibits depth-dependent fluctuations and organization of fibers in microdomains.

Next we adopted a bottom-up approach, to dissect the molecular and supramolecular mechanisms of collagen fibrillogenesis *in vitro*. Simplified models of collagen peptides and fibrillar assemblies were studied under controlled conditions. A multimodal strategy combining second harmonic scattering (SHS) to probe molecular symmetry and supramolecular arrangement, and vibrational sum frequency generation (VSFG) measurements to analyze molecular orientation and structure, as well as atomic force microscopy (AFM) to visualize fibrillar morphology at the nanoscale was employed. This multimodal approach identified structural signatures of collagen at different stages of fibrillogenesis and demonstrated the crucial role of telopeptides in modulating polar order and supramolecular organization. Our results demonstrate that collagen assembly in fibers is determined not only by the intrinsic properties of the triple helix but also by the presence of the telopeptides, specific molecular domains at the end of the helices with the pH further modulating the supramolecular arrangement.

Altogether, this thesis demonstrates the potential of multimodal nonlinear optical methods to characterize collagen organization across different scales, in *in vitro* models and in *ex-vivo* fibrotic spinal cord tissue.

Résumé

Les lésions de la moelle épinière (LME) constituent l'une des affections les plus sévères du système nerveux central. Elles sont responsables de déficits moteurs, sensoriels et autonomes souvent irréversibles, qui altèrent profondément la qualité de vie des patients. À l'échelle mondiale, leur incidence est estimée entre 250 000 et 500 000 nouveaux cas par an, avec une prévalence croissante liée notamment aux accidents de la voie publique et aux chutes. Les conséquences sociales et économiques sont majeures : la prise en charge des patients implique des hospitalisations longues, des soins de rééducation coûteux et une dépendance fonctionnelle durable. Malgré des décennies de recherche, aucune thérapie régénérative efficace n'a encore permis de restaurer une fonction neurologique complète après une telle lésion.

À la suite du traumatisme initial, une cascade de réponses tissulaires se déclenche aboutissant à la formation d'une cicatrice fibreuse. Celle-ci se caractérise par une accumulation progressive de matrice extracellulaire (MEC), dominée par le collagène. Le collagène de type I, en particulier, joue un rôle majeur : il confère rigidité mécanique au site lésionnel, délimite physiquement la zone endommagée et établit une barrière qui freine la régénération axonale. Cette production soutenue de collagène conduit à une fibrose persistante, qui limite la plasticité tissulaire et favorise la chronicité de la lésion. Bien que le collagène soit largement reconnu comme un constituant central de la fibrose, de nombreux aspects de son organisation restent mal compris. En particulier, les relations entre l'alignement des fibrilles de collagène et leurs assemblages au cours de la fibrillogenèse demeurent encore peu élucidées. Le collagène fibrillaire présente une structure hautement ordonnée et non centrosymétrique, qui le rend détectable par imagerie optique non linéaire (ONL), en particulier par le signal de génération de seconde harmonique (SHG).

Notre travail propose une étude de la structure et de l'organisation du collagène au moyen d'une stratégie multimodale combinant l'imagerie et spectroscopie d'ONL. Cette thèse s'articule ainsi autour de deux approches, une étude *ex vivo*, sur des tissues de moelle épinier d'un modèle murin de LME afin de suivre l'évolution de la lésion fibreuse au cours du temps et dans différentes régions de la moelle, et une étude *in vitro* visant à explorer les mécanismes de l'assemblage du collagène partant des simple peptides, au fibrilles et fibres, obtenues par diverses méthodes de croissance de ces structures.

La partie *ex vivo* de ce travail, se concentre sur le suivi de la croissance du collagène et de son organisation le long de l'axe rostro-caudal de la moelle épinière à différents temps post-lésion. Compte tenu des propriétés intrinsèques du collagène (structure fibrillaire non centrosymétrique), nous avons eu recours à l'imagerie SHG, couplée à une analyse 2D dite Fingerprint method, développée au sein du laboratoire. Cette approche permet de quantifier la tortuosité des fibres, leur degré d'organisation ou encore la longueur totale des fibres présentes. En complément, une analyse de variance 3D développée par Liu *et al.* (2017), a été utilisée afin de caractériser le désordre à l'échelle volumique. Ces approches combinées nous ont permis de suivre, de manière temporelle et spatiale, l'évolution du réseau collagénique au sein de la lésion.

Dès 2 semaines post-lésion (2 wpi) (Figure R 1.A), le signal SHG révèle une accumulation marquée de collagène au site lésionnel, avec une extension déjà visible vers les zones périphériques. À 4 wpi la présence de collagène reste nette, et l'imagerie complémentaire en 2PEF (non présentée ici) suggère des altérations structurelles plus profondes du tissu. À 6 wpi le collagène demeure abondant et s'étend davantage en périphérie, tandis que le signal 2PEF révèle une désorganisation tissulaire accentuée.

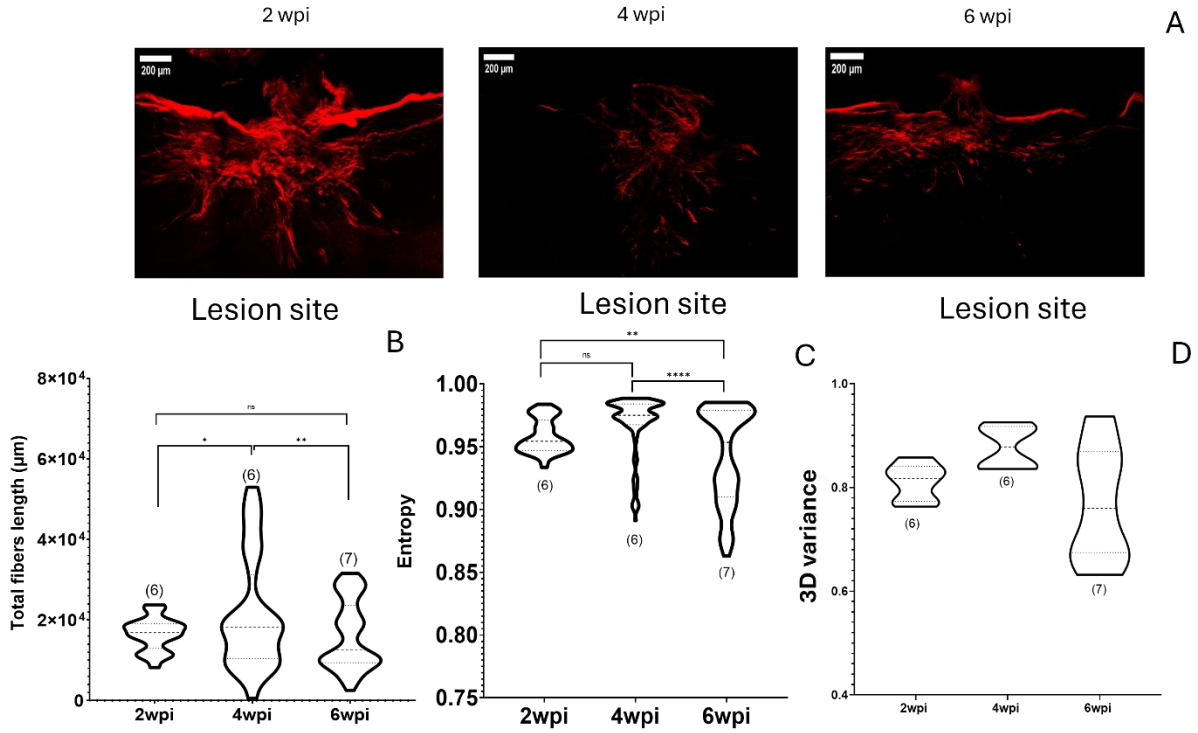

Fig R 1: A) Images SHG (fausse couleur) de la moelle épinière à 2, 4 et 6 semaines post-lésion (barre d'échelle = 200 µm). B, C) Résultats de l'analyse 2D (N = 3 souris, deux coupes/souris, ≥ 15 plans par coupe) : B) longueur totale des fibres, C) entropie 2D du réseau fibrillaire. D) Analyse 3D de la variance mesurant l'organisation volumétrique des fibres.

L'analyse quantitative en 2D confirme ces observations. La longueur totale des fibres (Figure B) augmente entre 2 et 4 semaines, traduisant une phase de production accrue de collagène, avant de diminuer à 6 semaines, ce qui suggère une phase de réorganisation. L'entropie 2D (Figure C), reflétant le désordre fibrillaire, reste globalement élevée, indiquant une absence d'organisation marquée. On observe néanmoins une hausse à 4 wpi suivie d'une légère baisse à 6 wpi, suggérant que certaines sous-populations de fibres commencent à adopter un arrangement plus structuré. L'analyse 3D de la variance (Figure D), qui prend en compte l'ensemble des fibres d'un volume, met également en évidence un désordre accrue à 4 wpi suivi d'une diminution à 6 wpi. Cependant, les valeurs restent élevées dans tous les cas, confirmant l'absence d'orientation préférentielle à l'échelle du volume. Les résultats obtenus révèlent que le remodelage du collagène après LME commence par une phase initiale de dépôt primaire (2 wpi), suivie d'une expansion chaotique à 4 wpi, puis d'un assemblage, compaction des fibres tardive à 6 wpi. Néanmoins, l'évolution n'est pas strictement similaire en 2D et en 3D. À 4 wpi en particulier, les indicateurs 2D traduisent un état de désorganisation maximale, alors que les mesures 3D montrent déjà l'émergence de sous-populations de fibres partiellement orientées, notamment dans les régions rostrales et caudales. Ce décalage souligne que l'approche 2D, en projetant des structures volumétriques, tend à amplifier le désordre apparent, un phénomène également observé dans d'autres tissus fibreux. Ainsi, les descripteurs 3D apportent une lecture complémentaire, en révélant des dynamiques d'alignement qui échappent à l'analyse planaire 2D seule.

Dans un second temps, nous avons abordé l'étude *in vitro* afin de suivre les mécanismes d'assemblage, la fibrillogenèse du collagène. Deux formes de collagène ont été considérées : le télocollagène (Tcol), qui conserve les terminaisons telopeptides aux extrémités de la triple hélice, et l'atélocollagène (Acol), dont ces régions ont été retirées via un clivage enzymatique. Les telopeptides sont connus pour accélérer la fibrillogenèse et favoriser l'assemblage spatial du collagène en faisceaux de fibres.

Pour caractériser ces processus, nous avons mis en place une méthode dite « bottom-up » consistant à étudier la molécule de collagène en remontant jusqu'à l'assemblage en fibres. Nous avons eu recours à la Second Harmonic Scattering (SHS), une technique complémentaire à l'imagerie SHG qui permet de sonder l'évolution de la fibrillogenèse en fonction du pH à travers deux paramètres : la première hyperpolarisabilité moléculaire (β) et le rapport de

dépolarisation (DR). La première hyperpolarisabilité (β) est une grandeur physique qui traduit l'efficacité avec laquelle une molécule ou un assemblage convertit la lumière incidente en un signal harmonique. Dans le cas du collagène, β rend compte du degré d'organisation non centrosymétrique des triples hélices. En parallèle, le ratio de dépolarisation (DR) renseigne sur la symétrie effective de cette organisation : un DR faible traduit une réponse dominée par une symétrie dipolaire simple, tandis qu'une augmentation du DR indique l'apparition de contributions plus complexes.

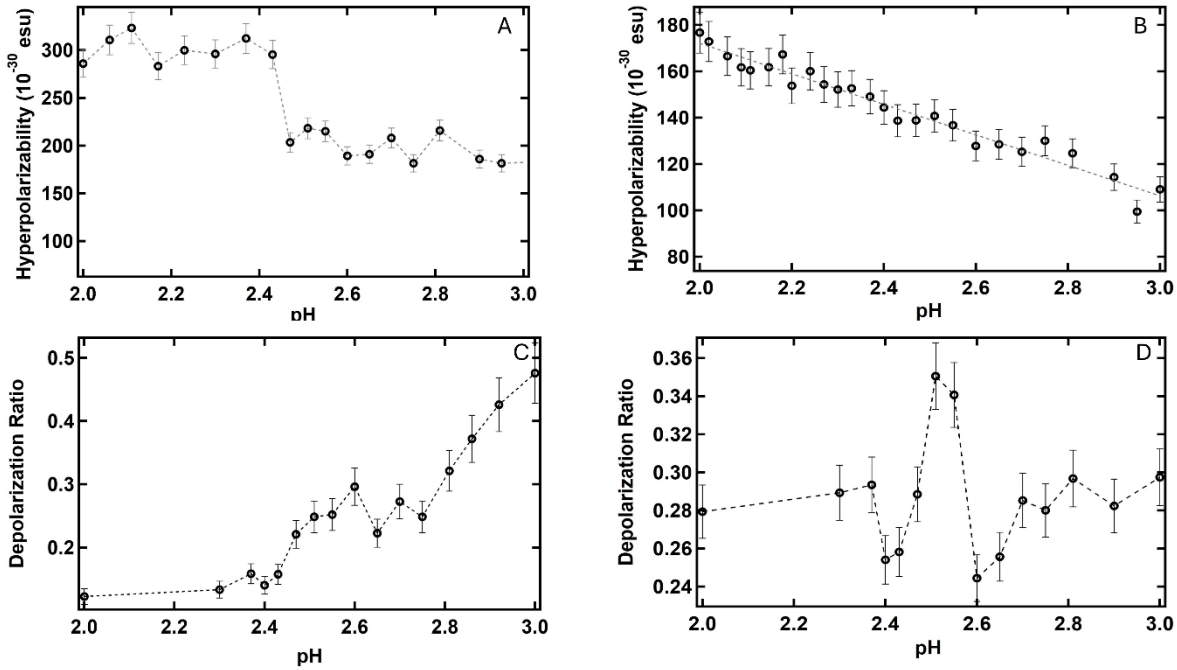

Fig R 2: A, B) Evolution de l'hyperpolarisabilité β respectivement du Acol et Tcol en fonction du pH. C, D) Evolution du rapport de dépolarisation (DR) du Acol et Tcol respectivement du Acol et Tcol.

Les résultats montrent que l'atelocollagène (Acol) (Figure R 2.A) présente des valeurs de β nettement plus élevées que le télocollagène (Tcol) (Figure R 2.B), indiquant une organisation plus constructive des triples hélices en absence de télopeptides. Cependant, l'évolution diffère selon le pH : Acol présente une chute abrupte de β autour de pH 2.4, marquant un déclenchement soudain de la fibrillogenèse, tandis que Tcol évolue de façon progressive et linéaire, traduisant une transition plus contrôlée. Le suivi du DR confirme cette divergence : Acol (Figure R 2.C) montre une augmentation continue du DR entre pH 2 et 3, indiquant une évolution vers une symétrie plus complexe lors de la fibrillogenèse. À l'inverse, Tcol (Figure R 2.D) conserve un DR stable, ne révélant qu'une réorganisation transitoire avant de retrouver son état initial. Ces différences sont corroborées par l'AFM : Acol forme des fibrilles isolées et

désordonnées, alors que Tcol développe un réseau fibrillaire dense et parallèle. Ensemble, ces observations indiquent que l'absence de télopeptides favorise une fibrillogenèse soudaine et instable, tandis que leur présence stabilise le processus et permet la formation progressive d'un réseau cohésif.

Afin de sonder plus finement l'organisation moléculaire, nous avons eu recours à la spectroscopie vibrationnelle SFG (VSFG). Cette approche est sensible à l'orientation des liaisons chimiques au sein de structures non centrosymétriques, et permet ici d'accéder aux angles d'inclinaison (θ) des modes vibrationnels par rapport à l'axe de la triple hélice. Les peptides modèles PPG_{10} ont été utilisés comme référence afin de caractériser la triple hélice.

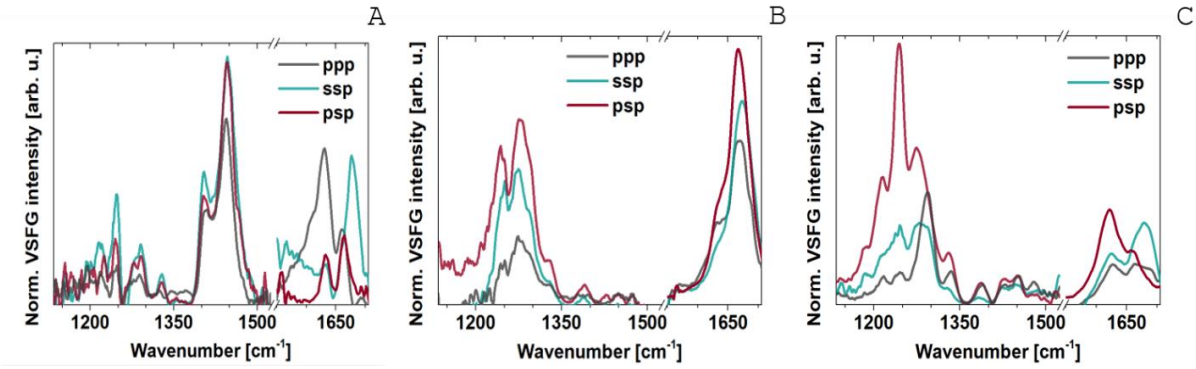

Fig R 3: Spectres VSFG normalisés enregistrés dans la gamme spectrale 1150-1700 cm^{-1} sous les combinaisons de polarisation ppp (noir), ssp (cyan) et psp (rouge). (A) Peptide PPG_{10}, (B) télocollagène (Tcol) à pH 3, (C) atélocollagène (Acol) à pH 3.

Avant d'accéder aux informations d'orientation, il convient de noter que les spectres complets (Figure R 3) présentent une grande complexité, avec de nombreux recouvrements de bandes. Nous avons donc sélectionné un sous-ensemble de pics bien définis, retrouvés de manière reproductible dans Acol et Tcol, et, lorsque possible, dans le peptide modèle PPG_{10}. Pour chacun de ces pics, l'intensité mesurée dans différentes polarisations a été analysée à l'aide d'un modèle reliant les susceptibilités microscopiques (β) aux susceptibilités effectives mesurées $\chi_{eff}^{(2)}$. Le fit de ce modèle permet d'extraire les angles d'inclinaison (θ, tilt angle) associés à chaque mode vibrationnel.

Les angles d'inclinaison mesurés pour Acol et Tcol sont très similaires dans les vibrations liées au squelette moléculaire (bandes amide I et amide III), ce qui indique que le retrait des telopeptides ne perturbe pas de manière significative l'orientation locale de la triple hélice. Les principales différences apparaissent dans les modes vibrationnels des chaînes latérales (CH_2 et CH_3), où Acol présente des orientations distinctes par rapport à Tcol. Cela suggère un rôle

spécifique des telopeptides dans la régulation de l'assemblage supramoléculaire, probablement en contraignant les interactions latérales et en stabilisant les liaisons inter-fibrillaires. En leur absence, les chaînes latérales peuvent adopter des arrangements spatiaux légèrement différents, reflétant une perte de contraintes d'assemblage plutôt qu'une perturbation du squelette hélicoïdal.

Dans l'ensemble, cette thèse met en évidence le potentiel des approches optiques non linéaires multimodales pour caractériser l'organisation du collagène à différentes échelles, aussi bien dans des modèles *in vitro* que dans des tissus *ex vivo* de moelle épinière lésée.

General introduction

Since its invention in the 17th century, microscopy has profoundly transformed the way biology is studied and understood. By making the invisible visible, it has provided scientists with the means to explore the architecture of cells, tissues and organs at unprecedented levels of detail. Successive technological advances from bright field to fluorescence, confocal and multiphoton microscopy have progressively expanded our ability to interrogate biological material across scales. Microscopy has become not only a tool for observation but also a driver of discovery, closely tied to labeling strategies for generating optical contrast. The introduction of histological dyes, fluorescent probes and genetically encoded markers such as GFP (green fluorescent protein), profoundly expanded our capacity to visualize specific biomolecules. By providing targeted contrast, labeling techniques have made it possible to address questions that would otherwise have remained inaccessible. Importantly, these methods remain widely used in clinical practice, where histological stains and immunohistochemistry are essential for diagnostics and pathology. Yet, labeling has some limitations, since they often require invasive preparation and cannot always capture the native dynamic context of living tissues. These limitations have encouraged the emergence of new strategies known as label-free imaging. Rather than relying on external reporters, label-free techniques exploit the intrinsic optical, vibrational or structural properties of biological tissues to generate contrast. Among the earliest and most widely used are infrared (IR) and Raman spectroscopies, which probe the vibrational fingerprints of molecular bonds. IR spectroscopy, developed in the early 1900s by William Coblentz provides a molecular signature. Raman spectroscopy, discovered by C.V. Raman in 1928 offered complementary vibrational information with the advantage of minimal water interference. Over the past decades, both IR and Raman have been used in the biomedical field, to classify tissues, analyze biofluids. These two spectroscopies' techniques have laid the foundation for more advanced nonlinear methods in biophotonics as second-harmonic generation (SHG). SHG is a nonlinear optical process that arises only in non-centrosymmetric structures making it ideally suited for imaging fibrillar collagen. Because collagen is one of the strongest SHG emitters, SHG microscopy has become a reference technique for monitoring extracellular matrix organization in both physiological and pathological contexts, during tumor progression (Provenzano et al., 2006) or fibrotic scars developments in injured spinal cord (Manesco et al., 2023). Another label-free technique that can provide high resolution

topography and nanoscale mechanical information is atomic force microscopy (AFM). Unlike optical methods, AFM relies on the direct interaction between a nanometric probe and the sample surface. Taken individually, label-free techniques provide a unique but partial perspective on biological systems: vibrational spectroscopies reveal chemical fingerprints or SHG reports on the supramolecular order of collagen fibers. Therefore, our multimodal approach (including NLO imaging and spectroscopy) is expected to bring in a more complete view on the collagen fibers' organization on multiple scales: on *in vitro* grown collagen structures and in biological tissue in the context of fibrotic scar in a spinal cord injury (SCI).

After SCI, a fibrotic scar rapidly forms, characterized by the apparition of extracellular matrix proteins such as type I collagen. This structure is mainly produced by invading perivascular fibroblasts and progressively expands into the surrounding tissue (Soderblom et al., 2013). While collagen I is a well-established hallmark of fibrosis, its organization and dynamics have been less investigated in the context of the SCI. Recent work by Manesco et al., (2023) has characterized growth of fibrillar collagen I at the lesion site, highlighting its structural contribution to scar formation.

The aim of our work was therefore to gain a deeper understanding of collagen remodeling within the injured spinal cord. Manesco et al., (2023) focused their study on planar observations, providing valuable but limited insights into the structure of the fibrotic scar. Collagen fibers form complex three-dimensional networks and their organization is known to influence both the mechanical properties of the extracellular matrix (ECM) (Shoulder & Raines, 2009). For this reason, we implemented a 3D analysis capable of capturing not only the orientation of collagen fibers within the imaging plane but also their distribution across depth. In addition, our work investigated large spinal cord regions, including the lesion site and the adjacent regions following the rostrocaudal axis, named here rostral and caudal. These regions are critical interfaces where the scar expands and interacts with the surrounding spinal cord. By comparing collagen organizations across these regions, we aimed to determine whether scar maturation follows a uniform trajectory along the rostrocaudal axis or whether distinct structural patterns emerge. To capture the dynamic evolution of fibrosis, we monitored collagen organization at multiple post-injury timepoints (1, 2, 4 and 6 weeks), providing a spatiotemporal perspective on how fibrillar architecture evolves during scar formation. This temporal and regional analysis provides new insights into the spatial heterogeneity of scar formation. To

complement this *in vivo* scar maturation investigation, we developed a bottom-up approach designed to better understand the intrinsic properties of collagen assembly. While spinal cord imaging provides insight into the collective organization of fibers within the scar, it does not resolve the molecular and supramolecular mechanisms that govern collagen fibrillogenesis. To address this, we used telocollagen (Tcol), which retains the telopeptides required for physiological fibrillogenesis and atelocollagen (Acol), in which these domains are enzymatically removed. By comparing these two forms, we can determine the specific role of telopeptides in driving fiber alignment and supramolecular assembly. We employ two label-free spectroscopic techniques, the second harmonic scattering (SHS) and vibrational sum frequency generation (VSFG), to probe *in vitro* collagen models at multiple levels or organization, from molecular vibrational signatures to fibrillar packing.

The structure of this manuscript is as follows:

- **Chapter I. State of the art and objectives.** It introduces the scientific context, with a focus on spinal cord injury and fibrotic scar formation, to provide the necessary background for understanding the biological processes under study. As the fibrotic scar was assessed in this work via monitoring of collagen fibers, the second part of this chapter is dedicated to the different types of collagens, their structure and the difference between Atelo-collagen (Acol) and Telo-collagen (Tcol). The third part of this chapter presents the state of the art of the nonlinear optical methods used to follow the dynamic of the fibrotic scar, the evolution and conformation of collagen during its fibrillogenesis. Atomic force microscopy (AFM), used only in tapping mode for high resolution imaging of collagen samples, is introduced. The chapter ends with the objective of our study and the multimodal approaches we propose to use to bring complementary innovative information on collagen fibers' assembly.
- **Chapter II. Materials and Methods.** It details the experimental approaches employed to study the fibrotic scarring process and fibrillogenesis. The first part is dedicated to the biological tissue samples followed by the *in vitro* protocols to grow collagen fibers. The third part presents the NLO imaging and spectroscopic techniques, as well as the data analysis. This part introduces the multiphoton microscopy (MPM), the custom-made fingerprint algorithm and 3D variance analysis used to investigate the fibrotic

scar, followed by the SHS and VSFG techniques with their associated analysis framework, to probe collagen organization and assembly.

- **Chapter III Results and discussion.** It presents the experimental results we've obtained on murine injured spinal cord tissues. First, bright field images of spinal cord are used to localize and define the area of the lesion. This is followed by SHG imaging and analyses, where the fingerprint algorithm and 3D variance are applied to investigate collagen organization at the supramolecular level. The third part presents the AFM images of various *in vitro* collagen structures, mainly obtained by pH-controlled methods. Finally, the SHS and VSFG measurements are presented, pointing out the complementarity of the two techniques to investigate the role of telopeptides in fibrillogenesis.

- **Conclusion and perspective.** The final section reminds the context of this work, namely the need to better understand collagen remodeling during fibrotic scar formation after spinal cord injury and supramolecular organization during fibrillogenesis. We conclude on the adequacy of the NLO techniques to highlight the impact of telopeptides on fibrillogenesis and to characterize structural signature of the fibrotic scar across rostral, caudal and lesion site regions of the spinal cord. Finally, perspectives are discussed, including the integration of broadband coherent anti-Stokes Raman Spectroscopy (BCARS) for chemical mapping of scar tissues, as well as ongoing VSFG analysis to further refine our understanding of collagen organization.

Chapter I

--

State of the art and objectives

I. State of the art and objectives

I.1. Spinal Cord Injuries

I.1.1 Context: Incidence, causes and outcomes

Spinal cord injury (SCI) is a devastating medical condition characterized by disruption of sensory, motor and autonomic functions. The spinal cord, a vital component of the central nervous system, serves as the main pathway for nerves conduction, enabling communication between the brain and the rest of the body. Any lesion of the spinal cord may result in partial or complete loss of function below the site of injury depending on its severity. SCI not only leads to physical disability but also has a huge impact on the emotional and social life of patients, which also generates an important cost for the healthcare system.

The World Health Organization (WHO) estimated in a report from 2013 that between 250,000 and 500,000 people suffer a spinal cord injury annually. Cripps et al. (2011) provide a more specific estimate of 10.4 to 83 cases per million people, depending on the country, 39 per million in the United States and 15 per million in Australia. They also report that in high-income countries, the aging population contributes to a significant number of SCI cases with low-height falls, whereas in low and middle-income countries, road traffic accidents and occupational injuries are more prevalent. Note that in this report, the lifetime costs of SCI range from $1.1 to $4.7 million USD per individual, making it one of the most expensive chronic conditions. WHO in collaboration with The International Spinal Cord Society (ISCoS) published in 2013 the International Perspectives on Spinal Cord Injury (IPSCI) report, where they present a global synthesis of data on SCI incidence, causes, rehabilitation services and societal reintegration challenges. More recent reviews confirm a substantial variability in incidence, ranging from 13 to 53 cases per million (cpm) across WHO regions, up to 54 cpm in the USA and as broad as 3.3 to 195 cpm across 49 countries depending on methodology and population exposure. The average age at injury has also increased in high-income countries, with the USA reporting a rise from 29 years in the 1970s to 43 years since 2015 (Perrin et al., 2025). They highlighted road traffic injuries, falls and violence as the top contributors of SCI, where young males and elderly adults are considered as high-risk population. Non-traumatic SCIs account for a growing

portion of the burden, particularly among older adults. As shown in figure 1, road traffic accidents are overrepresented in the world, accounting for approximately 40 to 50% of traumatic SCI. Falls represent about 32%, a percentage that increases with the aging of the population. Violence and sports-related injuries together account for a smaller part, approximately 20%. Etiology varies significantly with geography, economic development and societal context. Moreover, the male-female ratio for SCI is 2:1, with specific risk peaks during adolescence for females, and during youth and elderly ages for males. This demographic insight is essential for tailoring prevention campaigns and healthcare responses. Understanding the full scope of SCI causes and outcomes helps structure not only in structuring rehabilitation programs, research but also in informing research and policies targeting both traumatic and non-traumatic SCI.

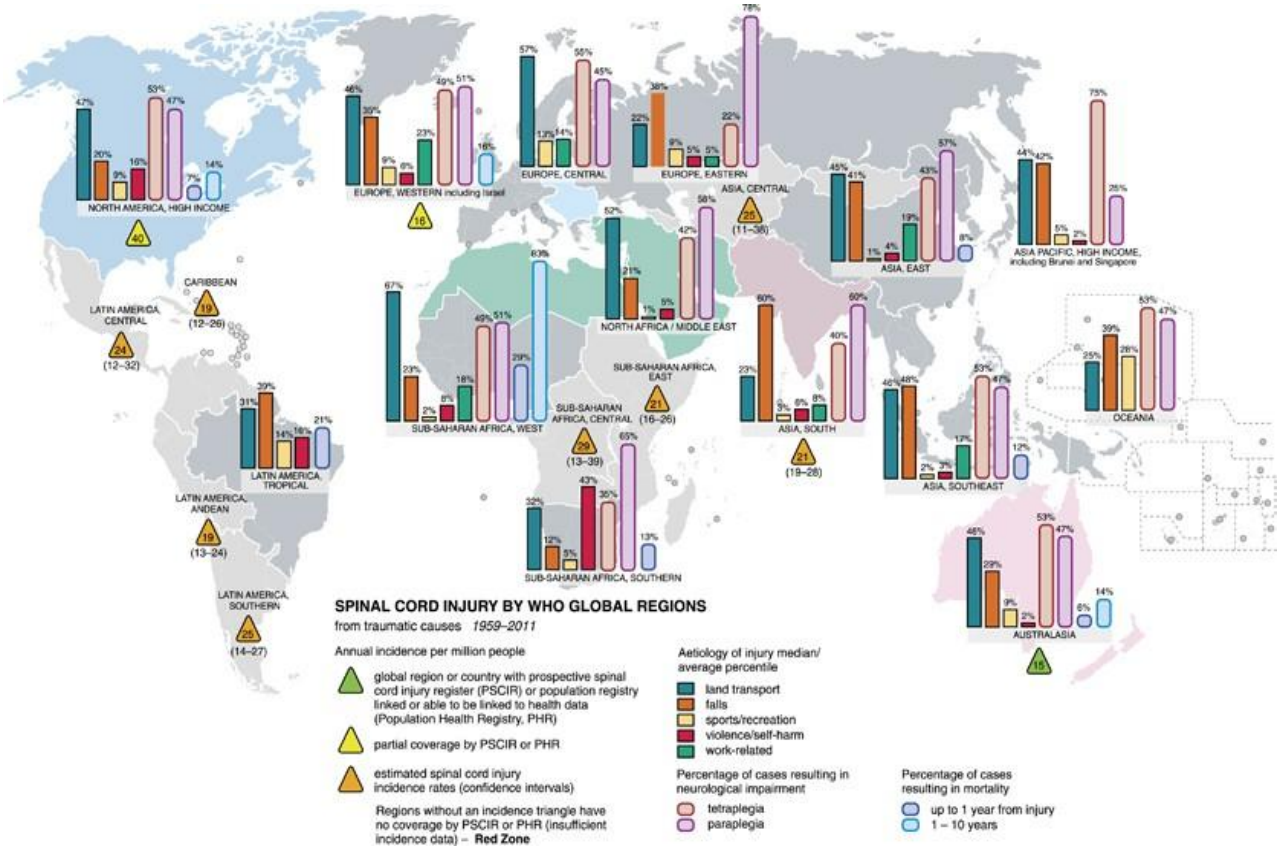

Figure 1: Spinal cord injury from traumatic causes by WHO region 1959-2011, From (B B Lee et al., 2014)

The clinical presentation of SCI depends on both the severity (complete or incomplete) and anatomical level of the injury (cervical, thoracic, or lumbar). Cervical lesions often result in tetraplegia, involving paralysis of all four limbs, while thoracic or lumbar injuries usually lead to paraplegia. According to data cited in Merritt et al. (2019), since 2010, partial tetraplegia is

the most common outcome (46% of cases in the U.S.), followed by complete paraplegia (21%), partial paraplegia (20%), and complete tetraplegia (13%). Notably, cervical level C5 is the most frequently injured spinal segment, accounting for nearly 50% of cervical SCIs, likely because of its anatomical role at the transition between the highly mobile upper cervical spine and the more rigid lower thoracic regions, making it biomechanically vulnerable to trauma such as motor vehicle collisions and falls (Alizadeh et al., 2019; Swartz et al., 2005; Foroutan et al., 2024). The initial phase of SCI, called the primary injury, is characterized by mechanical damage resulting from trauma including contusion, compression, or transection of spinal tissue. This is rapidly followed by a secondary injury cascade, involving a combination of vascular damage, excitotoxicity, oxidative stress, inflammation, and apoptosis. These processes exacerbate the initial lesion and contribute to progressive tissue loss. As the lesion evolves, these mechanisms also trigger extensive remodeling of the ECM which results in scar formation. In particular, the fibrotic scar produces a dense collagen-rich matrix that stabilizes the injured area but simultaneously acts as a major barrier to axonal regeneration. The formation of the glial scar and fibrotic matrix plays a central role in limiting axonal regeneration. C. Manesco et al, (2023; 2025) emphasized the biomechanical and structural transformations of the spinal extracellular matrix following trauma. Using multiphoton microscopy and atomic force microscopy (AFM), she observed that the orientation and density of collagen fibers growing at the injury site correlate with increased tissue stiffness, which may hinder axonal growth in the spinal cord.

The long-term clinical consequences of SCI are multifaceted and debilitating, encompassing motor, sensory and autonomic disorders (see figure 2). Motor disorders primarily manifest as paralysis (tetraplegia or paraplegia), muscle weakness and progressive atrophy. Sensory disorders include chronic neuropathic pain, loss or alteration of senses below the level of injury. Autonomic disorders involve impairments of vital functions, such as bladder control or respiratory regulation.

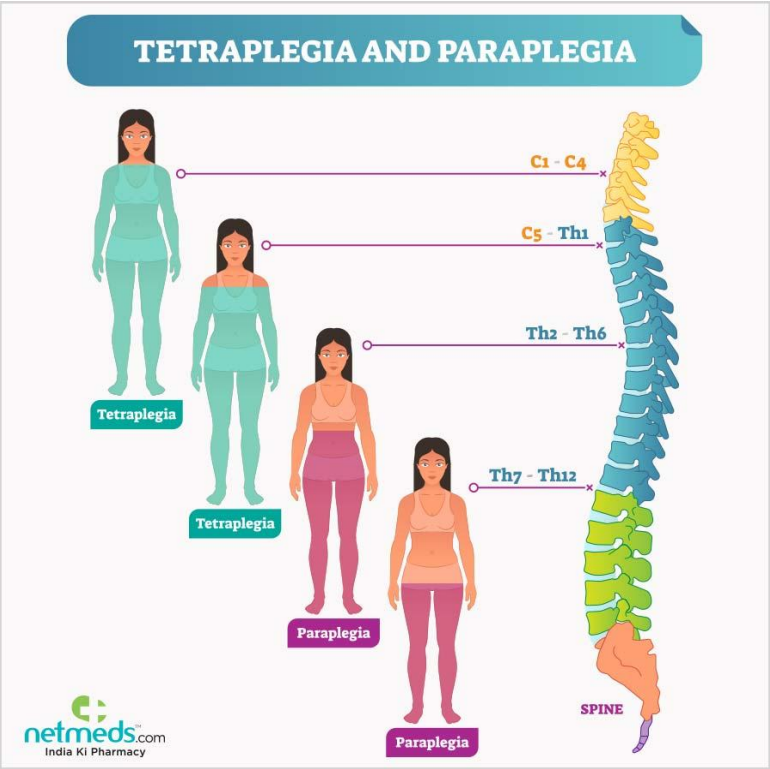

Figure 2: Spinal cord level-dependent functions and the extend of paralysis after SCI, shown in relation with injury severity using AIS classification (AIS impairment scale, a clinical scale that classifies the completeness of the injury from A to E)

Merritt et al. (2019) reported that pressure sores affect up to 20% of long-term SCI patients, while urinary complications can affect more than 45%. These secondary conditions further compromise quality of life and often result in long-term institutional care. Life expectancy is significantly reduced in individuals with complete high-level cervical lesions. However, advances in acute care, surgical decompression, ventilatory support, and early rehabilitation have significantly improved survival and quality of life outcomes (Hu et al., 2023). Beyond standard care, numerous experimental strategies are under investigation. These include pharmacological approaches, stem cell therapy, neuromodulation and biomaterial scaffolds but most of these are in preclinical or early clinical trials (Flack et al., 2022). Despite this broad spectrum of approaches, no curative treatment is currently available.

I.1.2 Spinal Cord

I.1.2.1 Healthy spinal cord anatomy in human

The spinal cord is a highly structured tissue, part of the central nervous system (CNS) extending from brain down through the spine and protected by the vertebral column. The spinal cord is enclosed in three meningeal layers: dura mater, arachnoid and pia mater, each layer having a

special role, pia mater is the innermost layer, attached to the cord's surface, envelops blood vessels and maintains the ionic and metabolic environment (Patel & Kirmi, 2009). The arachnoid middle layer has a trabecular structure, forming the subarachnoid space where cerebrospinal fluid circulates. This fluid provides both mechanical cushioning and biochemical exchange, for example by delivering glucose and ions to neural tissue and clearing metabolic waste products from the extracellular space (Jessen et al., 2015). The dura mater is composed of dense connective tissue and anchors the spinal cord within the spinal canal, forming a robust barrier against trauma or infection (Ünal & Sezgin, 2021). A scheme of the spinal cord including all these layers is presented in figure 3. The spinal cord is divided into grey matter (central, neurons body-rich region) and white matter (peripheral, mainly composed of ascending and descending myelinated axons). The segmental architecture varies along the rostro caudal axis, as shown in figure 3: cervical and lumbar enlargements display a greater amount of grey matter due to dense motor innervation of the limbs. Central nervous system tissue contains a vast diversity of neuronal subtypes and non-neuronal cells (glial cells) as astrocytes, oligodendrocytes or microglia.

I.1.2.2 Spinal Cord injury

When an injury occurs, it induces a complex cascade of events that modifies structures and functions of the spinal cord. While the initial trauma inflicts physical disruption on the spinal cord structure, it is the progressive biological response that defines tissue degeneration and limits recovery. Glial reactivity after spinal cord injury, including astrocytic and microglial activation, has been recognized as a central component of the traumatic response of the spinal cord (Silver & Miller, 2004). The extracellular matrix (ECM) provides a dynamic scaffold that regulates cellular adhesion, signaling and tissue mechanics. Manesco et al. (2023) showed that post-traumatic collagen realignment and fibrotic thickening coincide with increased tissue stiffness, as measured by atomic force microscopy (AFM) and nonlinear optical imaging. In humans, this response is commonly divided into successive phases, starting by the acute phase (first 48h), a subacute phase (up to 2 weeks), an intermediate phase (until 6 months) to finish by the chronic phase (beyond), although these temporal boundaries are not strictly defined and remained model-dependent (Ahuja et al., 2017). In our case, mouse model, similar phases can be distinguished, but they evolve on a different timescale (usually shorter) with inflammatory and scarring responses occurring within days to weeks rather than months. Given this

accelerated progression, experimental rodent models are particularly valuable to investigate the dynamics of the post-injury response.

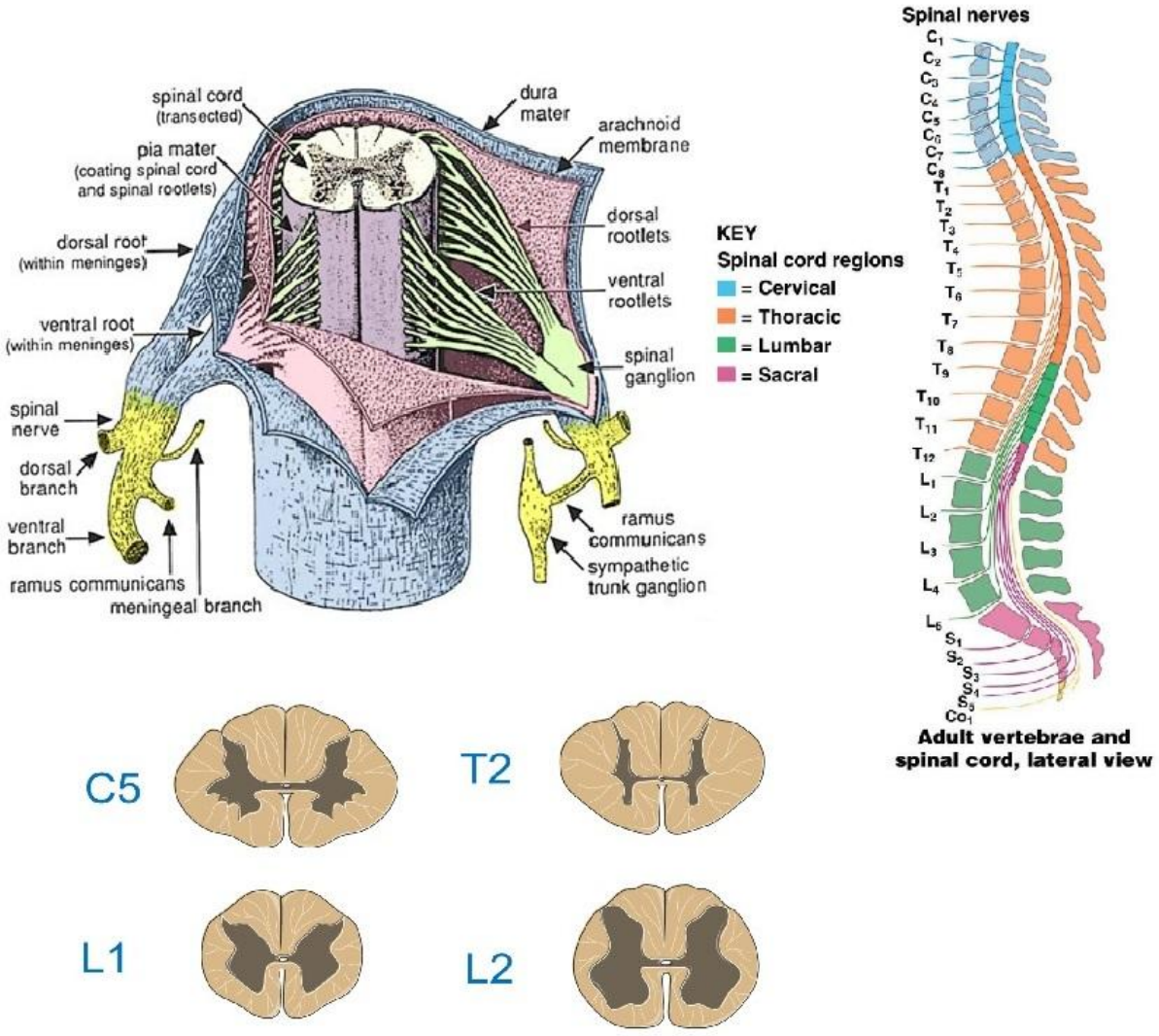

Figure 3: Top left: anatomy of an healthy human spinal cord, top right: spinal cord division into 8 cervical, 12 thoracic, 5 lumbar and 5 sacral vertebrae with axial views at different levels (C5, T2, L1, L2) Modified from https://vanat.ahc.umn.edu/neurLab2/pages/MeningesDrawing.html, Lecture Presentation by Lori Garrett on The Spinal Cord, Spinal Nerves, and Spinal Reflexes and https://anatomytool.org/content/servier-drawing-spinal-cord-cross-sections-labels

I.1.2.3 The primary and secondary injuries

After a CNS trauma, a dynamic and multifactorial cascade of pathological events takes place, beginning from a primary mechanical insult and evolving to complex secondary processes over time. The primary injury corresponds to the immediate physical trauma, like contusion, compression, transection, section or stretch, which causes irreversible damage to neurons,

axons and vascular structures at the lesion site (Ahuja et al., 2017). This mechanical disruption induces hemorrhage, axonal shearing, and cell death, forming the initial epicenter of tissue damage. Following this initial trauma, a secondary injury cascade is rapidly triggered contributing in fact to extend tissue damage well beyond the initial mechanical insult. This phase includes oedema, neuroinflammation, oxidative stress, excitotoxicity, ionic imbalance, mitochondrial dysfunction and vascular permeability, all of which compromising tissue homeostasis and cell survival (Ahuja et al., 2017; Cheng et al., 2023). The onset of the secondary injury begins within minutes to hours post-trauma, but its effects persist for days to weeks, defining the subacute phase of SCI. During this time, additional cell death, demyelination and glial activation intensify the lesion extension (Xiao et al., 2022). Research indicates that the timing and magnitude of these secondary responses are highly dependent on injury severity and species (Alizadeh et al., 2019). In murine models, glial and fibrotic scarring can begin within a week post-injury, highlighting the importance of early biological processes linked to fibrosis. Studies by Manesco et al., (2023) show that fibrillar collagen formation and ECM remodeling occur after injury at 1 wpi, contributing to the modified biomechanical properties of the spinal cord. Furthermore, astrocyte and microglia mediated release of cytokines and peripheral immune cell infiltration are predominant in the first week, amplifying neuroinflammation and thus secondary degeneration (Cheng et al., 2023; Sterner & Sterner., 2023). It has been suggested in rodent models that fibroblast migration and collagen formation occur very early after injury (Li et al., 2022; Ayazi et al., 2022)

Another considerable event following injury is the formation of a glial scar, initiated within few days post-lesion. In parallel, a fibrotic scar develops in the lesion core, composed of fibroblasts producing ECM, notably fibrillar collagens (Li et al., 2021; Soderblom et al., 2013; Ayazi et al., 2022). These two scars are established within one to two weeks after the injury. While both scars contribute to stabilizing the injured tissue, this work focuses on the fibrotic scar.

I.1.2.4 The Glial and fibrotic scar

The formation of glial and fibrotic scars is considered as a central hallmark of the spinal tissue response after spinal cord injury, as it greatly influences the pathological landscape and recovery potential of the CNS. Both scars begin to develop almost immediately after injury. Reactive astrocytes and microglia are among the first responders, becoming activated within 24-48 hours post-injury. Their rapid migration toward the lesion site and subsequent proliferation are crucial steps in the initiation of scar formation (Bellver-Landete et al., 2019).

The glial scar is characterized by a dense network of reactive astrocytes that surround the lesion, serving both protective and inhibitory roles in axonal regeneration (Bellver-Landete et al., 2019; Wu et al., 2021). In parallel, the fibrotic scar contributes to the healing process primarily through ECM remodeling. This involves multiple cell types, including pericytes, macrophages and fibroblasts, which drive fibroblast proliferation and ECM remodeling, thereby creating a more rigid environment at the injury site (Yao et al., 2022; Li et al., 2022). The distinction between glial and fibrotic scars is important, as glial cars predominantly consist of astrocytic and microglia cells, while fibrotic scars are characterized by their ECM composition (Dias et al., 2021). The mature glial scar forms a dense, fibrin- and ECM-rich barrier around the lesion. While protective in containing further damage, it poses a major obstacle to axonal regeneration through the upregulation of inhibitory molecules such as chondroitin sulfate proteoglycans (CSPGs) and tenascin (Fawcett & Asher, 1999). In parallel, the fibrotic scar continues to mature driven by different signaling pathways, notably involving transforming growth factor TGF-β, which regulates ECM deposition and inflammatory cell recruitment (Jin et al., 2022; Moretti et al., 2022). Following the acute and subacute phases, the lesion progresses into a chronic stage, during which scar consolidation occurs.

I.1.2.5 The chronic phase

The intermediate phase of SCI, often defined in humans as lasting up to six months post-injury, is characterized by a complex interplay of biological processes (Ahuja et al., 2017). In rodent models, these processes evolve on a much shorter timescale, with extracellular matrix remodeling and scar maturation occurring within weeks rather than months. During this transitional stage, inflammatory responses may begin to decline, yet ECM remodeling continues and scar tissue progressively matures. As the lesion progresses into the chronic phase, two pathological features dominate: persistent demyelination and scar formation. Incomplete or dysfunctional remyelination in the chronic phase by oligodendrocyte precursors cell (OPCs) is common at this stage (Silver & Miller, 2004). Although restoration of myelin has long been considered essential for recovery, evidence suggests that remyelination alone may not suffice. For example, Duncan et al. (2018) demonstrated in a contusive mouse model that locomotor recovery could occur independently of oligodendrocyte-derived myelin, pointing to compensatory neuroplasticity and synaptic adaptation.

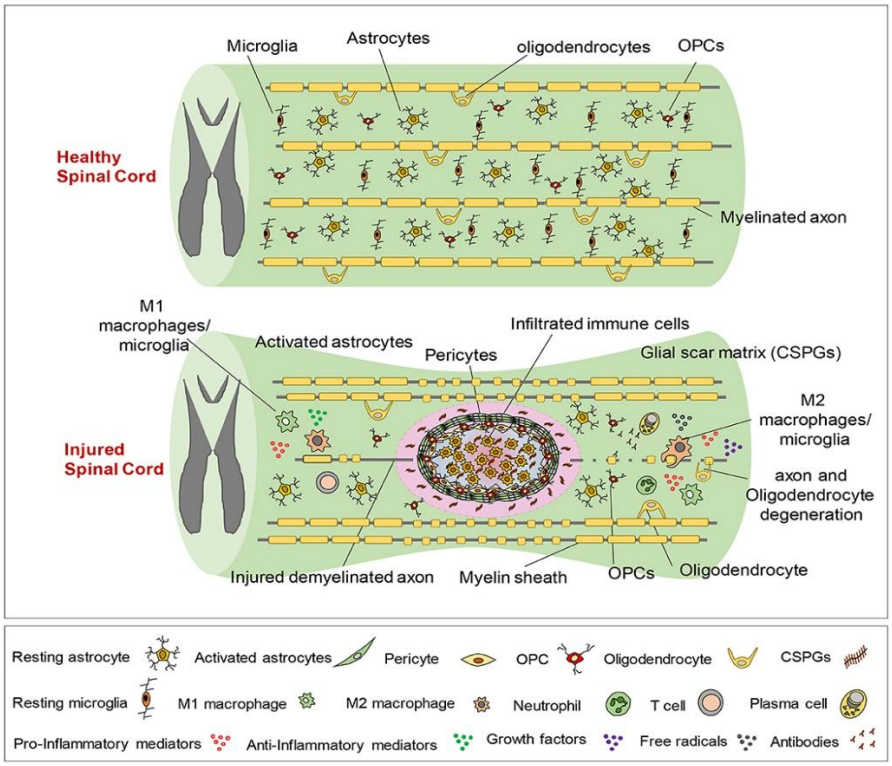

Figure 4: Pathophysiology of traumatic spinal cord injury. Schematic composition of normal and injured spinal cord. From Alizadeh et al., 2019

Glial and fibrotic scars consolidate during the chronic phase. At the lesion core, the fibrotic scar is characterized by a dense deposition of ECM (Norenberg et al., 2004). The resultant scar exhibits a rigid, collagen-rich structure that mechanically stiffens the injured spinal cord (Manesco et al., 2023). Finally, cystic cavitation is frequently observed, resulting from the collapse of necrotic parenchyma. These cavities can enlarge into syrinxes filled with cerebrospinal fluid, which contribute to progressive neurological decline (Ahuja et al., 2017). Importantly, cavitation is species-dependent: common in large animals, variable in rats and often absent in mice.

While such structural barriers seem to reinforce the inhibitory landscape of the chronic lesion, they also underscore why recovery cannot rely only on structural repair. For instance, studies indicate that in human SCI, astrocytic proliferation and ECM deposition may be limited and complete glial encapsulation of the lesion is reported to be rare (Gashtrodkhani et al., 2024). As research has progressed, attention has shifted towards the concepts of neuroplasticity and axonal sprouting in the chronic phase of SCI. These processes can counterbalance the traditional view of the scar as purely inhibitory. This has fueled interest in combinatorial strategies, such as the transplantation of induced pluripotent stem cell (iPSC)-derived neural cells, which not

only remyelinate but may also secrete neurotrophic factors that reshape the lesion environment (Suzuki et al., 2021).

I.1.2.6 SCI animal models

The study of spinal cord injury relies heavily on the use of animal models to investigate the biological molecular and cellular processes induced by trauma and to evaluate the potential of therapeutic interventions. One of the core requirements in developing these models is achieving reproducibility, not only in the mechanical induction of the lesion but also in the pathophysiological response that follows (Verstappen et al., 2022; Cheriyan et al., 2014). An experimental SCI model must faithfully emulate the spatial, temporal and mechanical features of human injuries, thereby ensuring that *in vivo* findings are robust, reproducible, and translatable to the clinical settings. Strikingly, this balance remains a considerable challenge. The type of injury, the anatomical location of the lesion and the species selected for the study must all be chosen with care to avoid producing data that fail to reflect the clinical reality of human spinal trauma (Manesco, 2023). The transection and hemisection models have historically been employed due to their anatomical precision and reproducibility. These models involve the complete or partial severing of the spinal cord, typically at thoracic levels, under direct visualization. They provide a controlled framework for studying axonal regeneration and the integration of transplanted cells. However, such models rarely mirror the pathophysiological complexity of human SCI, as they do not reproduce important clinical features such as multifactorial scar formation or the diffuse and often asymmetric nature of human lesions (Mistry et al., 2022; Gliksten & Yip, 2023). Moreover, in mice model, cystic cavitation is absent regardless of the lesion model, further limiting their translational relevance. Their utility is therefore primarily confined to the exploration of intrinsic regenerative mechanisms at molecular and cellular levels rather than modeling the full scope of post-traumatic spinal cord pathology.

Contusion models, on the other hand, have become the most widely used approach to mimicking traumatic SCI. In these models, a calibrated mechanical force is delivered to the exposed spinal cord using devices such as the Infinite Horizon. The resulting injuries recreate many hallmarks of human SCI, including intramedullary hemorrhage, neuronal necrosis, progressive demyelination and the emergence of astroglial and fibrotic scarring. Notably the

cellular and molecular architecture of the resulting lesions share close histological resemblance to human chronic SCI (Marinelli et al., 2019, Bellver-Lanete et al., 2019). For these reasons, contusion models are especially valuable for evaluating interventions aimed at remyelination, neuroprotection and extracellular matrix remodeling.

Compression models offer another valuable approach, especially when attempting to replicate conditions associated with chronic mechanical stress, such as spinal canal stenosis or vertebral displacement. These injuries are typically induced using calibrated clips or forceps. They result in tissue deformation, sustained ischemia and extensive gliosis, providing an excellent framework for studying long-term cellular responses, glial reactivity and extracellular matrix changes. These models are particularly appropriate for examining the deposition of fibrotic elements such as type I collagen that can be monitored using SHG imaging (Campagnola, 2011; Manesco et al., 2023).

Ischemic models, while less frequently used, provide insight into SCI mechanisms where vascular compromise is the initiating factor. These models involve transient occlusion of vessels such as the descending aorta or anterior spinal artery, resulting in localized ischemia and selective gray matter damage. They are especially informative for investigating the blood-spinal cord barrier, oxidative stress responses, and the interactions between neurovascular units under hypoxic conditions (Xing et al., 2025). However, they tend to yield predictable lesion morphologies and require more complex surgical procedures.

The species chosen for SCI modeling in animals is also important. Rodents are by far the most used due to their genetic manipulability, cost efficiency, and ease of handling. Nonetheless, their relatively small spinal cord dimensions, rapid healing processes and differences in glial cell reactivity limit the extent to which findings can be extrapolated to human physiology (Filipp et al., 2019, Perez et al 2021). Larger species such as pigs and non-human primates offer anatomical and histological features that more closely resemble those of humans, including gray and white matter distribution, cavitation phenomena and glial scarring patterns. These models are thus better suited for translational studies but are constrained by ethical, financial and logistical considerations (Wu et al., 2021; Poulen & Perrin, 2024). Ultimately, no single model can comprehensively replicate all the complexities of human SCI. Each model offers specific advantages aligned with certain research objectives. Models that can generate reproducible spinal cord injuries with defined glial and fibrotic structures provide a robust

platform for studying SCI. When these models also allow longitudinal assessment of functional outcomes and are compatible with high resolution imaging techniques such as second harmonic generation (SHG), they offer particularly rich opportunities to integrate biological insights. The careful alignment between model selection, injury parameters and readout methodologies remain a foundational step for enhancing the relevance and impact of preclinical SCI research.

I.2 Collagen

I.2.1 Collagen biology

I.2.1.1 The Triple-Helix Structure

Collagen architecture is central to its biological function and mechanical robustness. The molecular foundation of this architecture lies in the α-polypeptide chains whose specific sequence and stereochemistry enable the formation of a supramolecular helix, which has been the focus of intense structural and biochemical investigations since the mid-20th century (Ramachandran & Kartha, 1955; Rich & Crick, 1961).

Each collagen molecule consists of three α-chains, which can be identical (homotrimers) or different (heterotrimers), depending on the collagen type. In the case of collagen type I it is typically composed of two α1(I) chains and one α2(I) chain (Brown & Timpl, 1995). These α-chains range in size from 662 to over 3,000 amino acids (Ricard-Blum, 2011) and feature a repeating tripeptide motif Gly-X-Y, where X and Y are frequently proline and hydroxyproline, respectively (Myllyharju, 2004). The presence of glycine at every third position is essential: due to its small side chain, glycine permits the tight packing of the three chains into a narrow left-handed superhelix (Ramachandran & Kartha, 1955). The α-chains themselves are not right-handed helices as in standard α-helical proteins but rather adopt a unique polyproline type II-like conformation (Shoulder & Raines, 2009). When three of these chains are coiled together, they form a right-handed superhelix, a structure distinct from either α-helices or β-sheets in conventional proteins (Cowan et al, 1955; Rich & Crick, 1961). This arrangement, with its characteristic 3.3 residues per turn and 2.86 Å axial translation, was elucidated through X-ray diffraction of collagen-rich tissues like rat tail tendon (Cowan et al., 1955; Rich & Crick, 1961). Figure 6 presents the collagen' structure at different levels, from the amino acids chains to the collagen fibers.

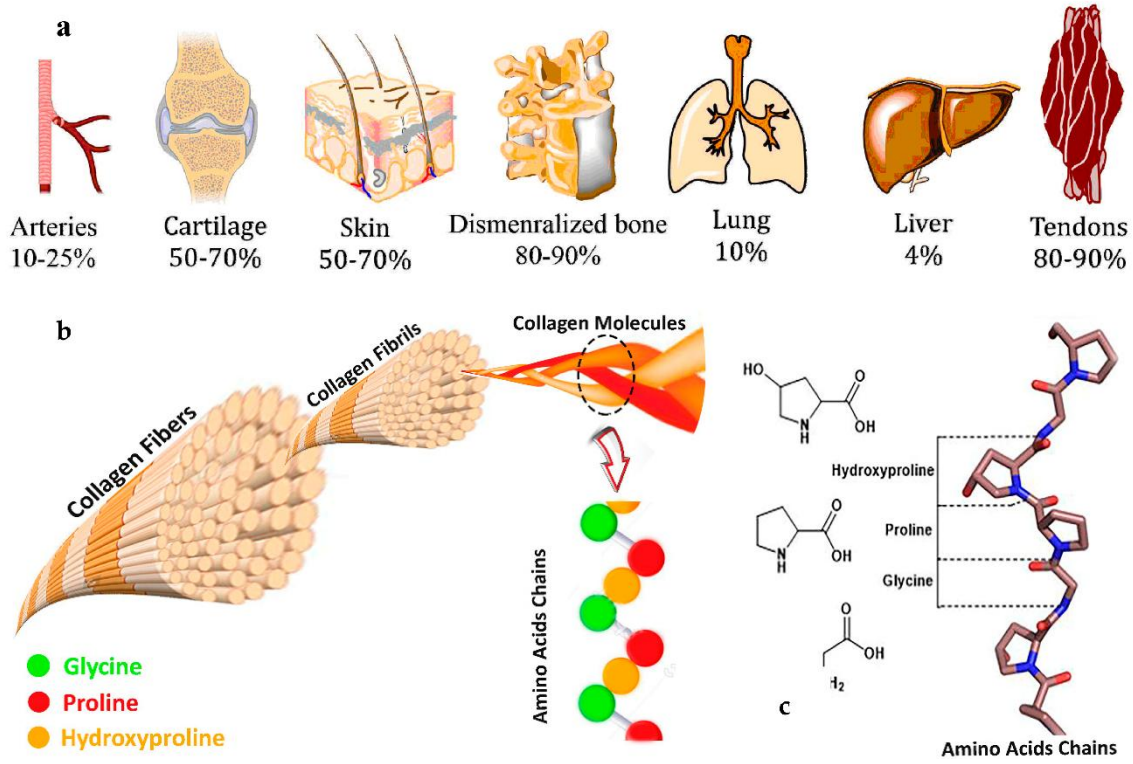

Figure 5: Occurrence of collagen in different mammals' organs. b) different levels of collagen's structure. The amino acids chains composed of glycine, proline and hydroxyproline, are coiled together in a triple helix structure forming the collagen molecules. Collagen molecules assemble into fibrils, and a bundle of fibrils create collagen fibers. From (Jafari et al., 2020).

The stabilization of the triple helix depends on several structural features. Hydroxyproline, a post-translational modification of proline, plays a particularly important role in thermal stability. Gustavson (1954) demonstrated a direct correlation between hydroxyproline content and collagen's melting temperature. Nishihara and Doty (1958) demonstrated that collagen's denaturation temperature increases with hydroxyproline content, establishing a clear correlation between hydroxyproline and thermal stability. This finding was later supported by molecular modeling and Fourier transform analysis, which revealed how proline and hydroxyproline, due to their rigid pyrrolidine rings, influence the electron density maps and X-ray scattering patterns of collagen (Rich & Crick, 1961; Barth & Zscherp, 2002). The hydroxyl group can participate in inter-chain hydrogen bonding with carbonyl oxygens of neighboring peptide chains, enhancing helix stability. Variation in the third layer line intensity observed in X-ray diffraction studies of collagen has been linked to differences in pyrrolidine ring content, highlighting the structural importance of proline and hydroxyproline residues (Bansal, 1977).

The symmetry and periodicity of the triple helix have been extensively studied using synthetic peptides. One of the most well-characterized models is the collagen-mimetic peptide (Pro-Pro-

$Gly)_{10}$, also known as PPG_{10}. This 30-residue peptide assembles spontaneously into a stable triple helix and exhibits the same structural parameters as natural collagen, namely a 2.8Å helix radius and a 28.6 Å repeat along the fiber axis (Okuyama et al., 1981; Beck & Brodsky, 1998). These peptides, and their variants, are invaluable for studying the contributions of individual residues to helix formation and stability.

From a functional perspective, the robustness of the triple helix allows collagen to act as a semi-rigid rod, ideal for transmitting mechanical forces within connective tissues. However, this rigidity is not absolute. Interruptions in the Gly-X-Y motif or regions with imperfect sequences can introduce kinks or flexibility into the helix. Such irregularities are essential in certain types of collagens, particularly those involved in basement membranes or with anchoring functions like collagen type IV or VII (Ricard-Blum, 2011). Type I collagen stands out among the fibrillar collagens due to its prevalence and mechanical properties. It forms thick fibrils with a characteristic D-periodicity of 67 nm and is found in tissues subject to high tensile stress, such as tendons, skin, and bones (Kadler et al., 2007). The heterotrimeric nature of type I collagen ($\alpha1(I)_2\alpha2(I)$) introduces subtle asymmetries in the triple helix, which may influence fibrillogenesis and interaction with other ECM proteins. These structural subtleties are likely relevant to pathological conditions where collagen turnover is disrupted, such as fibrosis or scarring after spinal cord injury (Manesco et al., 2023). During the biosynthesis of type I collagen, the triple helix formation begins in the endoplasmic reticulum. This process is chaperoned by proteins such as HSP47 and involves critical enzymatic modifications like lysine hydroxylation and glycosylation, which further influence the stability and eventual extracellular cross-linking of the fibrils (Myllyharju, 2004). The assembly of the three α-chains into the procollagen triple helix is a tightly regulated process, with mutations or misfolding often leading to connective tissue disorders such as osteogenesis imperfecta or Ehlers-Danlos syndrome (Prockop & Kivirikko, 1995).

I.2.1.2 Classification of collagen types

Collagens represent a highly diverse family of proteins, comprising at least 28 distinct types encoded by 42 different genes in vertebrates (Myllyharju, 2004). These types are classified into five categories based on their supramolecular organization within the ECM: fibrillar, network-forming, FACIT (Fibril-Associated Collagens with Interrupted Triple Helices), beaded filament-forming and anchoring fibril-forming collagens. Despite their diversity, all collagens share a common hallmark: the presence of triple-helical domains based on a repeating (Gly-X-

Y) amino acid motif, which contributes to molecular stability. In some types, such as collagen IV, interruptions in this motif introduce flexibility (Shoulders & Raines, 2009).

Fibrillar collagens are the best-characterized subgroups and include types I, II, III, V, XI, XXIX and XXVII. They are characterized by long, uninterrupted triple-helical domains that self-assemble into cross-striated fibrils with a regular D-banding periodicity (~ 67nm), stabilized by lysyl oxidase-mediated cross-linking (Ricard-Blum, 2011). Type I collagen, the most abundant, representing more than 90% of total collagen in some tissues (Karsdal et al., 2016), forms heterotypic fibrils with types III, V and XII in tissues such as skin, tendon, and cornea (Ricard-Blum, 2011). Type I collagen forms heterotypic fibrils in association with types III and V, with the type V playing a regulatory role in fibril nucleation and diameter (Wenstrup et al., 2004). Its robust fibrillar organization makes it essential in both physiological and pathological ECM remodeling. Similarly, type II collagen forms fibrils with types IX and XI in cartilage (Diab et al., 1996). These combinations enable collagen networks to adjust their mechanical properties for tissue-specific requirements. Type III collagen is often co-expressed with type I and is found in extensible tissue such as skin, lung and vascular walls, contributing to elasticity and compliance.

Type V is crucial for initiating fibrillogenesis and defining fibril diameter in tissues such as the cornea and placenta (Fichard et al., 1994). Types XXIV and XXVII, more recently discovered, are expressed during development and bone formation, though their functions are still under investigation (Plumb et al., 2007).

Type IV collagen is the prototypical member of the network-forming collagens group, localized mainly in basement membranes. Unlike fibrillar collagens, it possesses multiple interruptions in its triple helix, allowing flexibility and lateral branching, essential for forming two-dimensional meshworks stabilized by NC1 and 7S domain interactions (Vanacore et al., 2005). Different heterotrimeric isoforms confer tissue-specific properties, especially in the kidney glomerular basement membrane and central nervous system (Kalluri, 2003). Network-forming collagens provide filtration, compartmentalization and scaffolding functions in epithelial and endothelial tissues and are crucial for organ development and tissue polarity.

Due to its abundance and structural prominence, type I collagen turnover plays a critical role in maintaining ECM homeostasis. In healthy tissues, a balance between collagen I synthesis, assembly and degradation ensure mechanical stability while allowing for adaptive remodeling.

This balance becomes particularly relevant in conditions of injury, such as SCI, where collagen I is not only upregulated but also structurally reorganized within fibrotic regions (Manesco, 2023). The degradation of type I collagen is mediated primarily by matrix metalloproteinases (MMPs), particularly MMP-A, MMP-8 and MMP-13. These collagenases cleave the triple-helical domain at a specific site, producing one-quarter and three-quarter fragments, which are subsequently degraded by cysteine cathepsins (Arseni et al., 2018). This stepwise degradation allows the matrix to be reshaped in response to inflammation, regeneration or mechanical stress. Additionally, sheddases (a group of membrane-bound enzymes) target membrane-associated collagens and release their ectodomains into the ECM, modulating not only structural dynamics but also cell signaling pathways (Ricard-Blum, 2011). The activity of these proteases is finely regulated by tissue inhibitors of metalloproteinase (TIMPs). In physiological conditions, the MMP/TIMP ratio governs the pace of ECM remodeling. However, in pathological contexts such as SCI, this balance is often disrupted, leading to persistent accumulation of type I collagen and formation of dense, fibrotic barriers that impair neuronal regeneration (Galli et al., 2018; Wu et al., 2022).

I.2.1.3 Telocollagen and Atelocollagen

Type I collagen is biosynthesized in a precursor form known as procollagen, which contains non-helical propeptides at both the N- and C-terminal ends. Upon secretion, specific enzymatic cleavage of these terminal regions yields the mature collagen molecule, which retains short non-triple-helical extensions known as telopeptides. Depending on whether these telopeptides are preserved or enzymatically removed, two forms of type I collagen are distinguished: telocollagen (Tcol) and atelocollagen (Acol) (Maher et al., 2022). Tcol maintains its telopeptides at both ends of the triple helix. These regions, although non-helical, are essential for initiating intermolecular cross-linking and promoting fibrillogenesis. Their presence enhances lateral interactions between collagen molecules, resulting in the formation of dense, well-organized fibrillar networks that support tissue architecture (Shayegan et al., 2016; Tihăuan et al., 2022). Studies have shown that telopeptides improve gelation kinetics, mechanical stiffness, and fibril density in collagen-based hydrogels (Slyker et al., 2022).

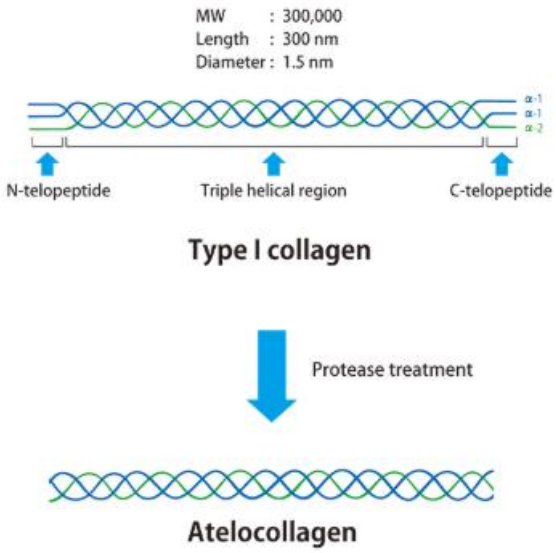

Figure 6: Difference between Tcol and Acol. Tcol contains the triple helical region, also named procollagen, (composed of three α-chains). After a protease treatment both N- and C- terminal are cleaved. Acol is the procollagen (only the triple helical domain remains). From https://atelocollagen.com/en/information/info210928

In contrast, Acol is produced by enzymatic removal of the telopeptide domains, commonly for clinical or experimental use where reduced immunogenicity or altered assembly behavior is desired. However, the absence of telopeptides significantly modifies the polymerization process, often leading to slower gel formation, lower stiffness, and altered supramolecular organization of fibrils (Maher et al., 2022; Antoine et al., 2014). Functionally, the removal of telopeptides affects collagen's interactions with cell receptors and matrix proteins. For instance, telopeptides carry type-specific antigenic determinants, which facilitate selective recognition and signaling, especially in types I and III (Velling et al., 2002). These domains also influence the formation of mineralized tissues, and their removal may impair the structural integration of collagen within the ECM (Shin et al., 2023). From a pathological perspective, telopeptides play a crucial role in fibrotic progression. The presence of telopeptide-rich type I collagen enhances fibril entanglement and matrix compaction, contributing to the formation of fibrotic scars in conditions such as SCI (Manesco et al., 2023). In contrast, Acol has shown anti-fibrotic properties in vitro, inhibiting TGF-β1 induced fibrotic responses in Tenon's capsule fibroblasts (Shin et al., 2023). Altogether, while telocollagen represents the native, physiologically relevant form of collagen I, suited for robust matrix formation and load-bearing functions, atelocollagen offers a bioengineered alternative with distinct physical and immunological properties. The

differences between these two forms are not only structural but deep functional, and they underpin divergent behaviors in tissue engineering, regenerative medicine, and modulation of fibrosis. The telopeptides not only promote lateral alignment of tropocollagen molecules but also serve as essential reactive sites for enzymatic cross-linking, notably via lysyl oxidase, enabling the formation of covalent bonds that stabilize the supramolecular fibrillar architecture (Eyre & Wu, 2005). Their absence in atelocollagen thus hampers fibril nucleation, slows gelation, and alters the mechanical resilience of the resulting matrix. Atelocollagen and telocollagen are both collagen type I (fibrillar), this mean that they can be observed using non-linear optics (NLO) microscopy. The next section will describe approaches in non-linear optics to study type I collagen.

I.3 Nonlinear optics (NLO)

The field of nonlinear optics (NLO) emerged as a pivotal extension of classical optics following the advent of high-intensity laser sources in the 1960s, allowing access to light-matter interactions beyond the linear regime. In linear optics, the response of a dielectric medium to an incident electric field E(t) is proportional to the field strength and its describes by a induced polarization: $P(t) = \epsilon_0 \chi^{(1)} E(t)$, where $\chi^{(1)}$is the linear susceptibility tensor and ϵ_0 is the permittivity of a free space. However, when the amplitude of the applied fields becomes comparable to the atomic-scale binding forces within the medium, the response becomes nonlinear. In this regime, the induced polarization P(t), which represents the material's response to the optical field, can no longer be described solely by a first-order term. Instead, it is expressed as a power series expansion in E(t):

$$\begin{aligned} P(t) &= \epsilon_0 \left[\chi^{(1)} E(t) + \ \chi^{(2)} E^2(t) + \chi^{(3)} E^3(t) + \cdots\right] \\ &\equiv P(t) = P^{(1)} + P^{(2)} + P^{(3)} + \cdots \\ &\equiv P(t) = P^{(1)} + P^{(NL)} \end{aligned} \quad (1)$$

Where $\chi^{(n)}$ are the n-th order nonlinear susceptibilities of the medium. The second-order term is responsible for key nonlinear optical effects such as second harmonic generation (SHG) or sum-frequency generation (SFG), whereas the third-order terms accounts for third harmonic generation (THG), Kerr effects, and four-wave mixing. These phenomena are intimately linked to the microscopic nonlinearity in the material's potential and can be derived from classical models of anharmonic oscillators and quantum mechanical perturbation theory (Boyd, 2008).

A fundamental aspect of $\chi^{(2)}$ is its dependence on symmetry: it vanishes identically in centrosymmetric media under the electric dipole approximation. This arises because a material with inversion symmetry satisfies:

$$P(-E) = -P(E) \tag{2}$$

Implying the absence of even-order terms in the polarization expansion (Boyd, 2008). Therefore, only in non-centrosymmetric media does $\chi^2 \neq 0$, enabling SHG and related phenomena. An example of non-centrosymmetric material is the beta barium borate (BBO), a uniaxial birefringent crystal widely used in SHG experiments. In biological systems, this condition is fulfilled in highly ordered protein assemblies like type I collagen or sarcomeres (Campagnola & Loew, 2003; Chen et al., 2012). The formal birth of nonlinear optics is often traced to a landmark experiment in 1961 by Franken, Hill, Peters and Weinreich at the University of Michigan, when they demonstrated for the first time the generation of light at twice the frequency of the fundamental beam (SHG) (Franken et al., 1961). This discovery was made possible by the recent invention of the laser (Maiman, 1960), which provided the coherent and high-intensity light necessary to push the electromagnetic field strength beyond the linear response regime of materials. In the years that followed, theoretical frameworks for these observations were rapidly developed, particularly through the formulation of nonlinear polarization expansions by Bloembergen & Pershan (1962) and Shen (1984). These early contributions laid the foundation for understanding how the second-order nonlinear susceptibility tensor governs frequency mixing, SHG and sum-frequency generation. All of this macroscopic description of nonlinear effects are grounded in Maxwell's equations, which govern the propagation of electromagnetic fields. In a nonlinear dielectric medium without free charges or currents, the wave equation for the electric field becomes:

$$\nabla^2 E(r,t) - \frac{1}{c^2}\frac{\partial^2 E(r,t)}{\partial t^2} = \frac{1}{\epsilon_0 c^2}\frac{\partial^2 P(r,t)}{\partial t^2} \tag{3}$$

Here P(r,t) includes both linear and nonlinear polarization terms. In the specific case of second harmonic generation, we focus on the second-order nonlinear polarization $P^{(2)}(2\omega)$, which acts as a source term oscillating at twice the frequency of the incident field. This source drives the generation the second harmonic wave $E(2\omega)$. The advent of nonlinear optics has not only enriched the theoretical framework of light-matter interaction but has also given rise to a suite of powerful imaging modalities. Among these, second harmonic generation (SHG) has emerged

as a particularly valuable technique for biological applications. In the context of spinal cord injury, the presence of collagen, a non-centrosymmetric structure, can be followed by this technique.

I.3.1 SHG in non-centrosymmetric structures

For SHG to occur effectively, a fundamental requirement is that the material lacks inversion symmetry. This condition ensures that the second-order nonlinear susceptibility tensor $\chi^{(2)}$is non-zero, thereby allowing a coherent nonlinear optical response. In centrosymmetric materials, the electric dipole approximation leads to an even-order cancellation in the polarization expansion, as the induced polarization satisfies P(-E) = -P(E), nullifying all even-order nonlinearities including SHG (Boyd et al., 2008; Shen, 1984). Therefore, only non-centrosymmetric media exhibit significant SHG signals. Examples include certain birefringent nonlinear crystals such as BBO, as well as biological assemblies like type I collagen or myosin fibers, which display intrinsic molecular asymmetry (Campagnola & Loew., 2003; Chen et al., 2012; Adur et al., 2012). At the microscopic level, SHG results from the interaction of two photons of identical frequency ω with a nonlinear medium, producing a single photon at frequency 2ω. This process is governed by the second-order nonlinear polarization:

$$P^{(2)}(2\omega) = \epsilon_0 \chi^{(2)} E^2(\omega) \tag{4}$$

This nonlinear source term feeds into the inhomogeneous wave equation derived from Maxwell's equation (3) and drives the emitted second harmonic field. Figure 7 represents a Jablonski energy diagram, where we can see that unlike in fluorescence, no real intermediate state is populated in SHG. Because $\chi^{(2)}$ is a second-rank tensor with up to 27 components, symmetry considerations are essential for simplifying its structure. For instance, under Kleinman symmetry (absence of strong dispersion), many tensor components are either equal or vanish, reducing complexity. In cylindrically symmetric biological samples like aligned collagen fibrils, only a subset of components such as χ_{zzz}, χ_{zxx} or χ_{xxz} dominate (Rivard et al., 2010; Nadiarnykh et al., 2010).

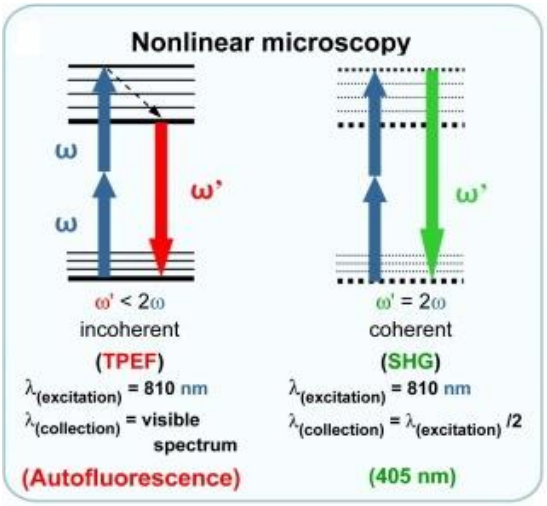

Figure 7: Jablonsky energy diagrams of two-photon excited fluorescence (TPEF) and SHG

These components influence the SHG intensity depending on the polarization of both the excitation and the detected signal, forming the basis for polarization-resolved SHG imaging.

The efficiency of SHG also depends strongly on phase-matching conditions. Constructive interference of the generated 2ω wave requires that the wavevector mismatch Δk be minimized:

$$\Delta k = k_{2\omega} - 2k_{\omega} \tag{5}$$

When $\Delta k = 0$, the SHG signal builds up coherently along the propagation direction. In practice, perfect phase matching is rarely achieved in biological tissues due to scattering, dispersion and microscopic disorder. However, partial or quasi-phase matching may occur when the local arrangement of nonlinear sources (e.g. collagen fibers) satisfies the coherence requirements over short distances, see figure 8B (Kumar et al., 2018).

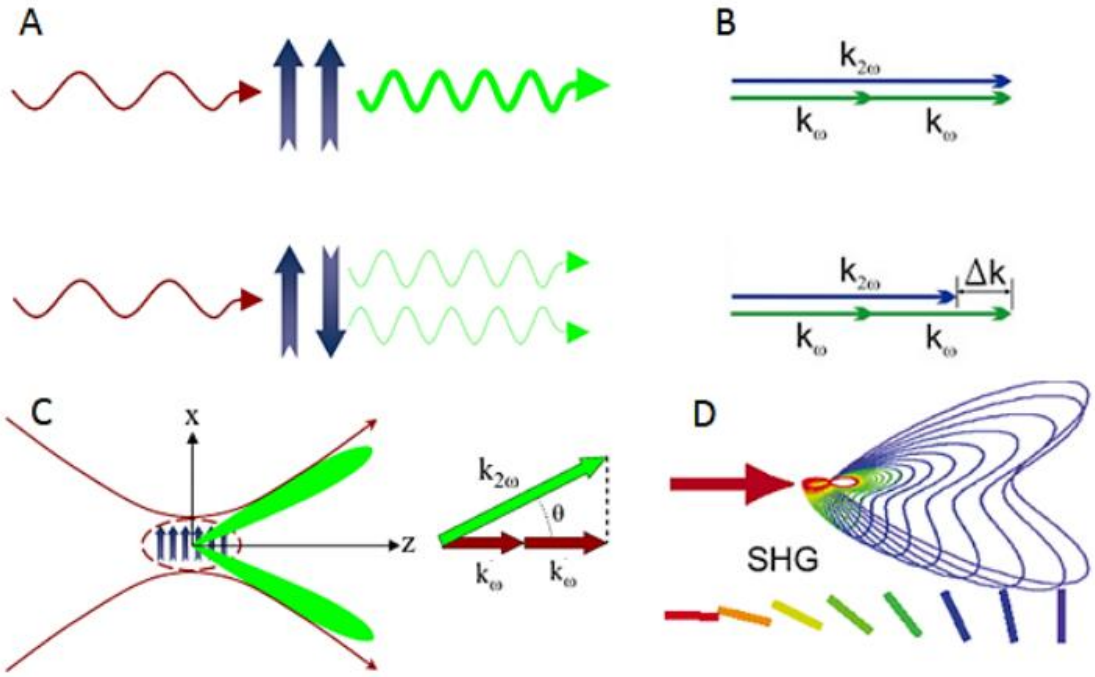

Figure 8: Dipoles directionality in SHG generation in (A), dipoles orientation in the same direction (up) induces SHG signal, while antiparallel orientations (down) result in destructive interferences and null SHG signal. In (B) phase matching conditions in a perfect matching case (up) where $k_{2\omega}$ the wave vector with double frequency is equal to k_ω the wave vectors of the incident beam, and (down) a common case in tissues with a phase mismatch factor Δk. In (C), the radiation directionality in the case of a focused beam where the emission wave is orientated with an angle Θ against the optic axis. In (D), the radiation pattern depending on the dipole's orientation against the optic axis. (Source: Manesco., 2023)

Another convenient property of SHG is its coherent nature; the emitted signal is highly sensitive to the relative orientation and phase of the contributing dipoles see figure 8.C (Pena, 2006). Consequently, SHG microscopy is not only label-free and non-destructive but also offers intrinsic contrast based on molecular order and symmetry. The interplay between beam geometry, tissue anisotropy, and molecular orientation leads to characteristic angular distributions of SHG emission. These directional patterns, dependent on both the local orientation of the dipoles and the angle of incidence, define the spatial emission profile of the second harmonic field (Figure 8C-D). In tightly focused beams, forward and backward SHG components can exhibit different intensities and spatial symmetries, offering additional structural insights into the organization of fibrillar proteins like collagen. This sensitivity allows the extraction of quantitative information about fiber orientation and packing density in biological tissue (Williams et al., 2005). SHG intensity scales quadratically with the excitation power and the effective component of $\chi^{(2)}$,making it a robust probe of submicron-scale structural heterogeneity.

I.3.2 Imaging collagen with SHG microscopy

Second Harmonic Generation (SHG) microscopy has emerged over the past two decades as a premier label-free imaging technique to visualize fibrillar collagen in biological tissues. Among all endogenous sources of SHG in the ECM, type I collagen is by far the most efficient and consistent generator of second-harmonic signals, owing to its dense fibrillar packing, structural polarity, and non-centrosymmetric organization (Strupler et al., 2007; Campagnola et al., 2002; Zipfel et al., 2003). Unlike fluorescence-based methods that require external staining or tagging, SHG exploits the intrinsic nonlinear optical properties of the collagen triple helix, especially its highly ordered fibrillar arrangement. The SHG signal arises from the coherent addition of frequency-doubled photons generated by the interaction of the incident light with non-centrosymmetric molecular structures. Type I collagen, with its chiral and asymmetric triple-helix and its polar alignment within fibrils, provides the optimal conditions for constructive SHG emission (Freund et al., 1986; Pena et al., 2005). Collagen I fibrils exhibit strong SHG signals in the forward and backward directions (Figure 9), depending on their size, orientation, and scattering environment. Fibrils with diameters between 50 and 500 nm, commonly found in skin, tendon, and fibrotic tissue, are within the optimal range for SHG detection (Stoller et al., 2002; Strupler et al., 2008). The label-free nature of SHG microscopy makes it particularly well-suited for longitudinal or *in vivo* studies, where repeated staining or sample degradation is a concern.

In the context of spinal cord injury (SCI), type I collagen is not normally present in the healthy parenchyma but becomes abundantly expressed within fibrotic regions following trauma. Manesco (2023) demonstrated that SHG microscopy can selectively reveal the organization of the collagen-rich fibrotic scar, distinct from glial and immune cell components. Particularly, SHG enabled high-resolution visualization of aligned, dense collagen I fibrils that form a barrier to axonal regrowth, a phenomenon not detectable with conventional histology or immunostaining (Manesco, 2023; Strupler et al., 2007). Beyond its specificity, SHG also provides quantitative and morphological data. Because the SHG signal depends on the second-order nonlinear susceptibility tensor $\chi^{(2)}$, it is highly sensitive to the molecular organization, density, and orientation of collagen fibrils within the focal volume (Pena et al., 2005). Techniques such as polarization-resolved SHG (P-SHG) and backward-to-forward SHG ratio

(B/F ratio) analysis have been used to infer fibril tilt, symmetry, and spatial coherence-parameters that correlate with tissue remodeling and pathological progression (Tuer et al., 2011; Stoller et al., 2002).

Compared to histological techniques like immunohistochemistry for collagen I, SHG microscopy offers three major advantages:

- Non-invasiveness: no fixation, staining or tissue clearing required.
- 3D resolution: SHG is compatible with deep tissue imaging via multiphoton excitation.
- Molecular specificity: SHG selectively highlights highly ordered collagen, avoiding signal contamination from disorganized ECM or other proteins (Brown et al., 2003).

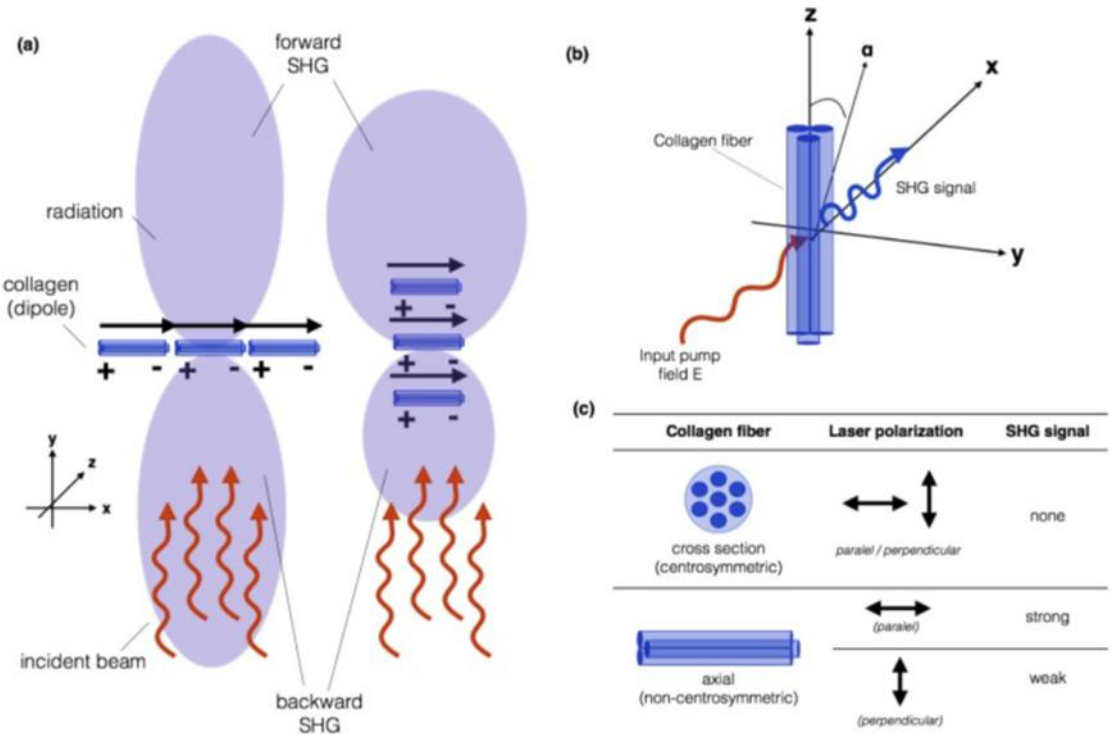

Figure 9: SHG signal generation in collagen fibers, with a) SHG signal radiation pattern with different number of dipole, parallel and perpendicular to the laser propagation (representing here collagen fibers), in forward and backward direction, b) geometrical arrangement in collagen fibers and SHG signal propagation, c) SHG signal intensity depending on the polarization of incident beam. From Mostaço-Guidolin et al., 2017

Duboisset (2009) emphasized that this high specificity arises because only non-centrosymmetric assemblies with consistent molecular polarity contribute to the SHG signal. Disordered or denatured collagen (e.g., gelatin) leads to a weaker SHG signal, making the technique particularly useful for tracking collagen integrity and fibrillar organization (Duboisset, 2009; Pena et al., 2006).

Moreover, the quantitative nature of SHG has made it a valuable tool in fibrosis assessment. By counting the number of SHG-positive voxels in a given volume, researchers can estimate the degree of collagen deposition, although the interpretations must be cautious. As Duboisset notes, SHG is a coherent process, meaning its intensity scales with the square of the local collagen density and is strongly modulated by fibrillar orientation and packing. Thus, signal strength does not directly equate to collagen quantity (Duboisset, 2009; Stoller et al., 2002). Nonetheless, SHG has proven particularly powerful in identifying spatial patterns of fibrosis, enabling high-resolution mapping of pathological collagen networks in a variety of organs, including kidney, lung, liver, and CNS (Strupler et al., 2008; Pena et al., 2006)

I.3.3 Collagen imaging in Spinal Cord Injury (SCI)

Spinal cord injury (SCI) triggers a complex cascade of cellular and molecular events, leading to the formation of a dense and persistent glial and fibrotic scar. While most studies have focused on glial components such as astrocytes and microglia, recent evidence highlights the importance of extracellular matrix remodeling, particularly the deposition of fibrillar collagen, mainly type I, in the formation of the fibrotic scar (Manesco, 2023). Unlike collagen type IV, which is found in basal lamina and does not emit SHG signals, fibrillar collagens such as type I possess a non-centrosymmetric triple-helical structure that strongly emits SHG, making them ideal targets for non-invasive optical imaging. Type I collagen is virtually absent in healthy spinal cord parenchyma but becomes over-expressed after injury, particularly at chronic stages (Galli et al., 2018). SHG microscopy has revealed that collagen type I expression begins as early as 1-week post-injury (1wpi), with increased deposition up to 6 weeks in CX3CR1$^{+/eGFP}$ mouse model. This expression remains spatially restricted to the ipsilateral side of the lesion, in hemisection models (Manesco et al., 2023) and aligns with the progression of fibrotic scar formation. Multiphoton microscopy monitoring the SHG signal allows the label-free, three-dimensional imaging of collagen in SCI tissues. Manesco's approach integrated SHG imaging with polarization-resolved modalities (P-SHG) to extract symmetry-related metrics and used both open-source software (CT-FIRE/CurveAlign) and a custom MATLAB pipeline (Fingerprint) for detailed fiber analysis. SHG signal intensity, fiber density, tortuosity, and orientation entropy were calculated across longitudinal spinal cord sections, enabling a detailed mapping of the fibrotic scar's progression along the rostro-caudal axis. SHG imaging was

paired with atomic force microscopy (AFM) to assess tissue stiffness. The injured site exhibited progressive stiffening from 1wpi, directly correlating with collagen accumulation.

Collagen imaging (Figure 10) also proved useful in evaluating treatment responses. In Manesco's work, a transient inhibition of microglia proliferation via GW2580 (a CSF1R inhibitor) reduced collagen type I deposition and decreased SHG signal intensity at 6wpi. This supports the hypothesis that microglia contribute to ECM remodeling and highlights collagen as a potential biomarker to monitor treatment efficacy in preclinical studies.

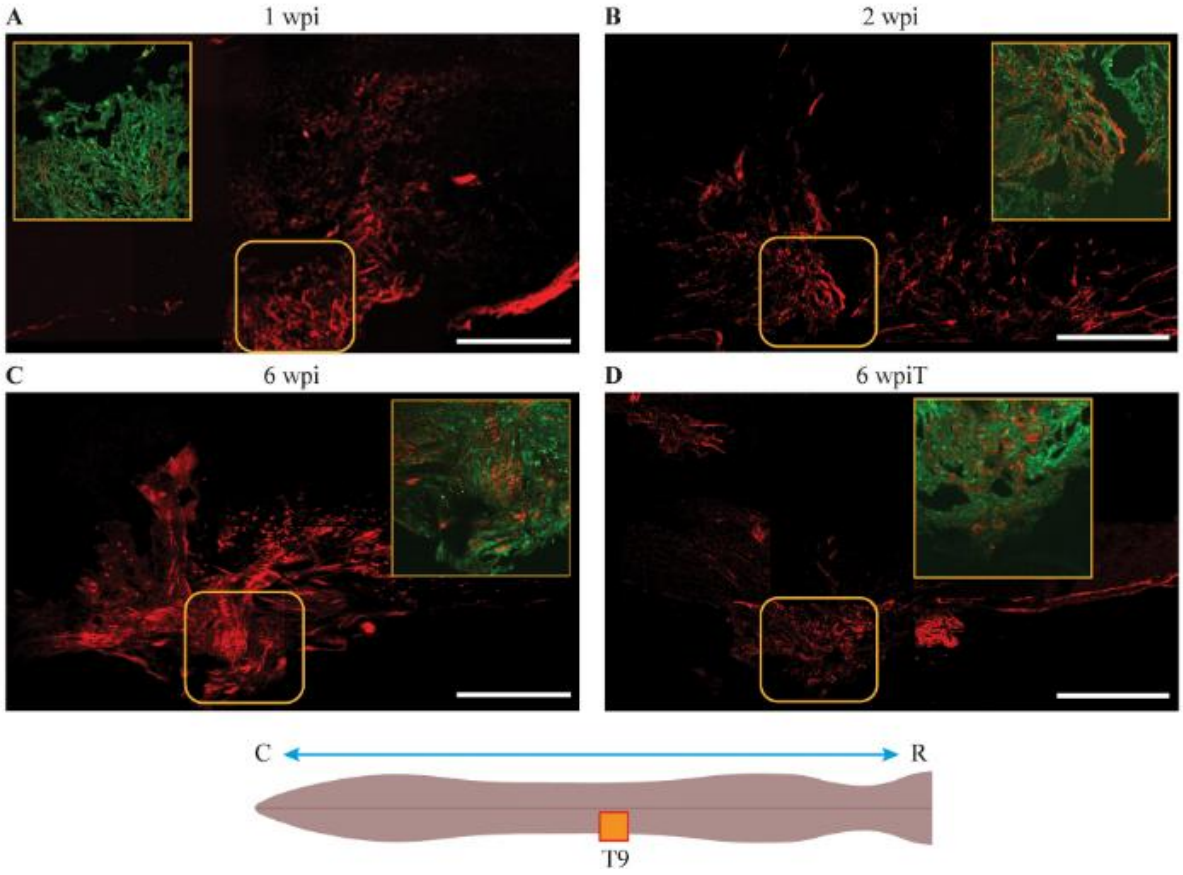

Figure 10: Extension of fibrillar collagen around the lesion site. Mosaic reconstruction of SHG images, showing the fibrotic extension at: A. 1wpi, B. 2wpi, C. 6wpi and D. 6wpiT. Insets are merged 2PEF (green) - SHG (red) zoomed images, centered at the lesion site as indicated by the yellow rounded squares (432 × 432 µm). The mean rostro-caudal extension of the injury was found to be 870 ± 300, 1200 ± 400, 1800 ± 200 and 950 ± 250 µm for at 1wpi, 2wpi, 6wpi and 6wpiT, respectively. Scale bar is 400 µm.

I.3.4 Second harmonic Scattering (SHS) for probing collagen architecture

Building upon the principles of second harmonic generation (SHG), second harmonic scattering (SHS) expands nonlinear optical analysis to disordered or non-aligned molecular systems, where the coherent SHG signal typically vanishes. In SHS, the emphasis shifts from phase-

matched coherent generation to the incoherent summation of scattered second-harmonic light, which is particularly useful in probing the orientational and structural properties of nanoscale assemblies like collagen fibrils in solution (Revillod et al., 2021). The SHS process lies the second-order nonlinear susceptibility tensor $\chi^{(2)}$, which describes how a medium polarizes in response to an incident electromagnetic field at frequency ω to emit radiation at frequency 2ω. However, unlike SHG microscopy, where coherent interference requires phase matching, SHS relies on the statistical averaging over a large number of randomly oriented nonlinear emitters. Consequently, the total intensity is an incoherent sum of the SHG signals from individual scatterers, described via orientational distributions of the molecular hyperpolarizability tensors β and their relation to $\chi^{(2)}$. This second-rank tensor describes how the induced dipole moment $p^{(2\omega)}$ of a single molecule or scattering unit responds to the incident field:

$$p_i^{2\omega} = \sum_{jk} \beta_{ijk} E_j(\omega) E_k(\omega) \tag{6}$$

The hyperpolarizability tensor β captures the nonlinear response at the molecular scale. Each of its components depend on the spatial symmetry and electronic distribution of the molecule, particularly its lack of inversion symmetry. In centrosymmetric molecules, β vanishes under the electric dipole approximation. In contrast, in non-centrosymmetric molecules such as collagen, β is superior to 0 enabling efficient nonlinear scattering. The work by Deniset-Besseau et al., (2009) experimentally measured the second order hyperpolarizability of type I collagen and established its predominant tensorial components based on polarization-resolved SHS. Their study revealed that the dominant contribution to β in collagen originates from the longitudinal axis of the triple helix, consistent with its anisotropic structural organization. They quantitatively modeled the collagen molecule as a cylindrical scatterer and extracted values for the main hyperpolarizability components β_{zzz} and β_{zxx} showing that this non-centrosymmetric configuration leads to a measurable SHS signal even in randomly oriented samples. Similar studies have investigated β in other molecular systems to correlate structure with nonlinear optical responses.

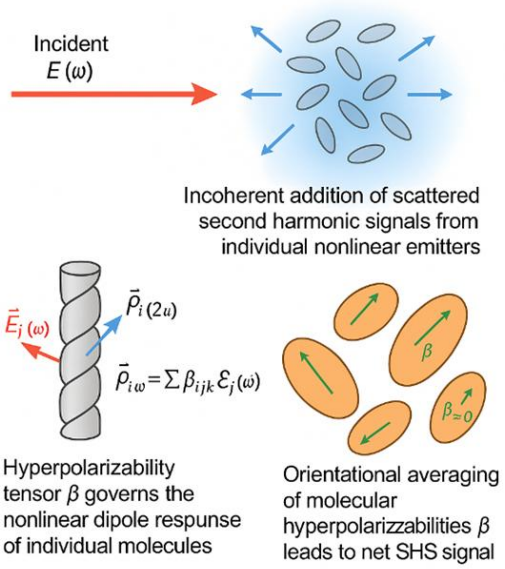

Figure 11: Schematic illustration of SHS in disordered molecular system (top). An incident electromagnetic field at frequency ω interacts with a suspension of randomly oriented nonlinear emitters, generating second harmonic radiation at 2ω through incoherent summation (bottom left). At the molecular level, the induced nonlinear dipole $\overrightarrow{p^{2\omega}}$ depends on the hyperpolarizability tensor β and the incident fields $E_j(\omega), E_k(\omega)$ (Bottom right). Orientational averaging of the molecular hyperpolarizability tensors β leads to a net measurable SHS signal.

Similar studies have investigated the first hyperpolarizability β in other molecular systems, for example with para-nitroaniline (PNA), a prototypical push-pull molecule with strong donor-acceptor interactions, exhibiting a dominant β_{zzz} component aligned along its molecular axis due to efficient intramolecular charge transfer. This has made it a benchmark compound in molecular nonlinear optics (Oudar & Chemla, 1977). Duboisset et al. (2013) showed that the first hyperpolarizability of peptides and collagen can be modeled as the coherent sum of elementary units, suggesting that the nonlinear optical response primarily originates from peptide bonds rather than side chains. This highlights the sensitivity of β to the supramolecular organization of the macromolecule. These comparisons underscore that the dominant components of β often align with the molecular axis and are strongly influenced by the molecular conformation and electronic delocalization. In the case of collagen, the triple helix's chirality and its repetitive hydrogen-bonded motif reinforce the alignment of nonlinear dipolar contributions along the fibril axis, enhancing the axial components of the tensor. With this understanding, the total SHS intensity I_{SHS} observed in the experiments can be expressed as:

$$I_{SHS} \propto G < \beta : e_\omega e_\omega >^2 \quad (7)$$

With G a geometric factor incorporating the experimental configuration, e_ω are the polarization vectors of the incident field. The orientational averaging (<…> part in equation 7) reflects the

fact that molecules are randomly distributed in solution, and this averaging affects the overall polarization dependence and SHS angular pattern. The squared modulus in the equation highlights the incoherent nature of the SHS signal. This formalism allows us to directly relate the experimentally observed SHS intensity to the intrinsic nonlinear optical properties of the molecule responses. It also sets the stage for introducing observables such as the depolarization ratio, which probes anisotropy in these orientational averages.

A key observable derived from polarization resolved second harmonic scattering (P-SHS) is the depolarization ratio, defined as the ratio of SHS intensity recorded in the perpendicular ($I_{\perp}$) and parallel ($I_{\parallel}$) polarization configurations with respect to the incident beam:

$$DR = \frac{I_{\perp}}{I_{\parallel}} \tag{8}$$

Physically, ($I_{\perp}$) and ($I_{\parallel}$) represent the components of the emitted second harmonic intensity along orthogonal polarization channels, and arise from the interaction between the incident electric field and the molecular hyperpolarizability tensor β. Specifically, these intensities are functions of the projections of the β tensor on the laboratory axes, modulated by the orientation of the molecules relative to the incident field and detection geometry. DR provides a sensitive probe of the anisotropic arrangement of nonlinear optical scatterers within a sample. In highly isotropic solutions, β-dependent contributions are averaged symmetrically in all directions, leading to comparable values for ($I_{\perp}$) and ($I_{\parallel}$), and consequently $DR \approx 1$. In contrast, anisotropic arrangements, such as collagen, tend to yield lower values of DR, as the second harmonic emission becomes directionally biased along the preferred molecular axis (Tuer et al., 2011).

This makes the DR a particularly informative parameter in biological systems. In type I collagen, ordered and aligned fibrillary structures are known to result in low DR values (Deniset-Besseau et al., 2009; Chen et al., 2012). More generally, Revillod et al. (2021) emphasized the robustness of DR as a structural probe, since it is a relative measure and therefore insensitive to absolute intensity fluctuations. This makes it highly practical for comparative studies, including the monitoring of fibrillogenesis, the quantification of collagen organization, and the detection of pathological remodeling processes. While SHS has proven to be a powerful tool for probing structural anisotropy and supramolecular organization, it lacks the chemical specificity required to distinguish between different molecular environments. The

SHS signal, being purely electronic in origin, integrates over all molecular contributions without resolving distinct chemical functionalities. To overcome this limitation and to gain deeper insight into the chemical nature and interfacial structure of biological assemblies, we now turn to vibrational sum frequency generation (VSFG). This technique extends second-order nonlinear optics by combining the structural sensitivity of SHG/SHS with vibrational spectroscopy, enabling label-free, interface-specific detection of molecular vibrations. In the next section, we explore how VSFG complements SHS in the context of collagen studies, offering new insight into fibrillogenesis, hydration state, and biochemical heterogeneity of atelocollagen and telocollagen.

I.3.5 Vibrational Sum Frequency Generation (VSFG)

Building on the interface sensitivity of second harmonic techniques, vibrational sum frequency generation (VSFG) expands the capabilities of nonlinear optical imaging by adding a vibrational spectroscopic dimension. While SHG and SHS are highly effective in detecting non-centrosymmetric molecular order, they lack intrinsic chemical specificity, as they rely exclusively on the electronic part of the second-order susceptibility tensor $\chi^{(2)}$. In contrast, VSFG enables access to molecular vibrational modes by linearly driving molecular vibrations with a tunable infrared field, when this excitation coincides with a vibrational resonance, the resulting polarization is mixed with a narrowband visible beam to generate a coherent sum-frequency signal at $\omega_{SFG} = \omega_{vis} + \omega_{IR}$ (Figure 12.A). This resonant enhancement enables VSFG to distinguish chemical species directly at interfaces such as solid-liquid and air-liquid boundaries, where conventional infrared or Raman spectroscopies are dominated by bulk contributions and lack inherent interfacial specificity (Shen & Ostroverkhov, 2006). The underlying concept of optical frequency mixing was formulated in the early 1960s in the general framework of nonlinear optics (Armstrong et al., 1962), but the first demonstrations of vibrational SFG as a surface-specific probe were reported only in 1987 by Shen and his wo-worker (Guyot-Sionnest, Hunt & Shen, 1987; Zhu et al., 1987), followed by Shen's influential 1989 review that established VSFG as a robust interfacial vibration technique. Its development was driven by the need for interfacial-sensitive spectroscopies capable of resolving molecular structure and dynamics at buried interfaces such as solid/liquid or air/ liquid boundaries, which elude traditional IR spectroscopy, which cannot selectively probe interfaces due to bulk

absorption and poor directional discrimination. Raman scattering can provide orientational information but unlike VSFG it does not offer intrinsic surface specificity.

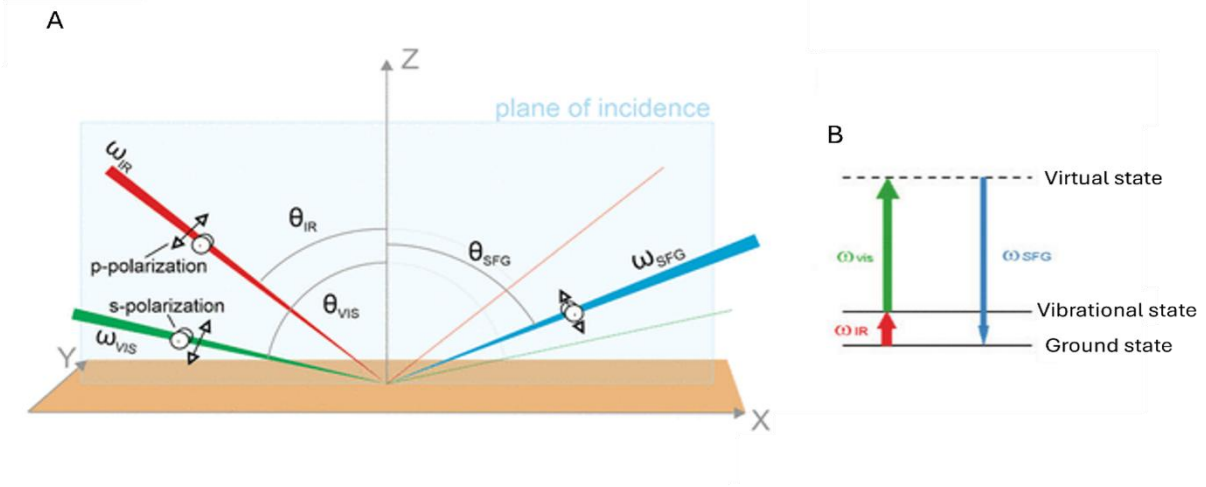

Figure 12: A) Non-collinear input geometries for SFG at interface. B) Energy diagram of vibrationally resonant SFG. From Pramhass & Rupprechter, 2021

VSFG is a coherent nonlinear optical process induced by the interaction of a visible field $E(\omega_{vis})$ and a tunable infrared field $E(\omega_{IR})$, generating an emitted field at the sum frequency $\omega_{SFG} = \omega_{IR} + \omega_{vis}$ (Figure 12.B). The second-order material polarization ($P_i^{(2)}$) is expressed as:

$$P_i^{(2)}(\omega_{SFG}) = \epsilon_0 \sum_{jk} \chi_{ijk}^{(2)} E_j(\omega_{vis}) E_k(\omega_{IR}) \tag{9}$$

where $\chi_{ijk}^{(2)}$ is the second-order susceptibility tensor, ϵ_0 is the permittivity of free space, $E_j(\omega_{vis}), E_k(\omega_{IR})$ are the j- and k- components of the electric fields of the visible and infrared beams. This polarization feeds into the nonlinear wave equation, which governs the generation and propagation of the emitted field:

$$(\nabla^2 + k^2)E(\omega_{SFG}) = -\mu_0 \omega_{SFG}^2 P^{(2)}(\omega_{SFG}) \tag{10}$$

with $P^{(2)}(\omega_{SFG})$is the second-order nonlinear polarization, $E(\omega_{SFG})$ is the electric field vector at frequency ω_{SFG}, ∇^2 is the Laplacian operator (describing wave propagation), μ_0 is the vacuum permeability, $k = \frac{n(\omega_{SFG})\omega_{SFG}}{c}$ is the wavevector magnitude of the sum-frequency field

in a medium of refractive index n (c is speed of the ligth and n(ω_{SFG}) is the refractive index evaluated at the frequency (ω_{SFG})). The solution to this equation shows that the emitted VSFG field is radiated coherently and directionally and is proportional to the magnitude of $P^{(2)}$, hence to $\chi^{(2)}$.

In VSFG, chemical specificity is achieved when the IR frequency resonates with a molecular vibrational mode, leading to an enhanced nonlinear response. Susceptibility is thus decomposed into vibrationally resonant and non-resonant parts:

$$\chi^{(2)} = \chi_{NR}^{(2)} + \sum_{q} \frac{A_q}{\omega_{IR} - \omega_q + i\Gamma_q} = \chi_{NR}^{(2)} + \chi_{Res}^{(2)} \tag{11}$$

Here $\chi_{NR}^{(2)}$ represents the non-resonant background response, while the second term captures the resonant contributions from each vibrational mode q. $\omega_q$is the frequency of the q-th vibrational mode, Γ_q is the damping constant or linewidth (reflecting vibrational lifetime and broadening) and A_q is a complex amplitude proportional to the product of the mode's IR transition dipole moment and its Raman polarizability derivative. This dual dependence explains why VSFG selectively probes modes that are simultaneously IR- and Raman-active. The complex nature of A_q gives rises to characteristic spectral lineshapes due to interference between resonant and non-resonant terms. The non-resonant term possesses both an amplitude and a phase. This phase can be particularly important when the non-resonant response overlaps with one of the input frequencies, as observed at aqueous interfaces or on metal surfaces (Shen & Ostroverkhov, 2006; Sun et al., 2019). In contrast, the resonant term directly reflects the IR-active vibrational modes weighted by their Raman activity and provides information on molecular information at the interface (Richmond, 2002; Shen & Ostroverkhov, 2006). This formalism connects molecular-scale vibrations (transition dipole moments and polarizability derivatives) with the macroscopic VSFG signal. This dual sensitivity to amplitude and phase provides a framework to extract both structural and dynamical information at interfacial system.

In VSFG, the polarization of the input and output electromagnetic waves critically determines which components of the second-order susceptibility tensor $\chi_{ijk}^{(2)}$ contribute to the measured signal. These tensor elements encode information about molecular symmetry, orientation and vibrational anisotropy. The VSFG signal intensity is thus strongly polarization-dependent and by carefully selecting polarization combinations, commonly abbreviated as ssp, sps, ppp, one

can isolate different elements of $\chi^{(2)}$. The letters s and p indicate the polarization of the detected SFG signal, the visible beam, and the infrared beam, respectively. "s" refers to polarization perpendicular to the plane of incidence, and "p" to polarization parallel to the plane. For example, ssp selects $\chi^{(2)}_{yyz}$, sps selects $\chi^{(2)}_{yzy}$ while ppp involves a linear combination of multiple tensor components, including: $\chi^{(2)}_{zzz}, \chi^{(2)}_{xxz}, \chi^{(2)}_{zxx}$. The polarization-resolved approach provides a means to probe the anisotropy and symmetry of interfacial molecular ensembles. Importantly, the symmetry of the molecular system restricts which components of $\chi^{(2)}$are non-zero. For molecules with a $C_{\infty v}$ symmetry, such as linear chains or cylindrical structures aligned along a principal axis (e.g. collagen fibers), only a few independent elements remain: $\chi^{(2)}_{zzz}, \chi^{(2)}_{xxz} = \chi^{(2)}_{yyz}, \chi^{(2)}_{zxx} = \chi^{(2)}_{zyy}, \chi^{(2)}_{xzx} = \chi^{(2)}_{yzy}$ (Hirose et al., 1992). These symmetrical relations, combined with polarization selection, make it possible to determine the average tilt angle θ between the molecular axis and the surface normal by comparing the relative strength of the contributing tensor components (Zhuang et al., 1999).

To connect molecular-level susceptibility $\chi^{(2)}_{ijk}$ with the detected macroscopic signal, one must consider the boundary conditions at the interface. The electric fields experienced by the interfacial molecules are not equal to the incident fields, they are modified by Fresnel transmission coefficients $L_i(\omega)$, which depend on the angle of incidence, frequency and polarization of each beam, as well as on the complex refractive indices of medium 1, medium 2 and the interfacial layer (often approximated by an effective index). Usually in VSFG experiments, reflection geometry is employed and the $L_i(\omega)$ are therefore often referred to as Fresnel reflection coefficients. These coefficients arise from solutions to Maxwell's equations at dielectric boundaries (Richmond, 2002). They describe how the incident Cartesian field components (i= x, y, z) are transformed into the local fields at the interface and act as weighting factors that modulate the contribution of each susceptibility element to the effective response. This leads to the definition of an effective susceptibility:

$$\chi^{(2)}_{eff} = \sum_{ijk} L_i(\omega_{SFG}) L_j(\omega_{vis}) L_k(\omega_{IR}) \chi^{(2)}_{ijk} \tag{12}$$

The VSFG intensity measured in a given polarization is then proportional to:

$$I_{SFG} \propto \left|\chi^{(2)}_{eff}\right|^2 I_{vis} I_{IR} \tag{13}$$

For molecular systems with axial symmetry, the dominant hyperpolarizability component is often β_{zzz}, aligned along the molecular axis. The macroscopic susceptibility elements are then obtained by orientational averaging over the tilt angle θ between the molecular axis and the surface normal, yields to:

$$\chi_{zzz}^{(2)} \propto < \cos^3\theta > \beta_{zzz},\ \chi_{xzz}^{(2)} \propto < cos\theta sin^2\theta > \beta_{zzz} \qquad (14)$$

Assuming azimuthal isotropy, we integrate over the Euler angles ϕ and ψ, while retaining θ as a free variable. By inserting these into the Fresnel-weighted $\chi_{eff}^{(2)}(\theta)$ and fitting to the experimentally measured intensity I_{VSFG}, we can extract the average molecular tilt angle at the interface, even using a single polarization configuration such as ppp (Zhuang et al., 1999). This technique has been applied to extract orientation information from Langmuir monolayers, lipid bilayers, surface-bound peptides and collagen fibers (Johansson & Koelsch., 2014; Teulon et al., 2016).

While VSFG spectroscopy is primarily sensitive to achiral molecular order at interfaces, it can also probe chiral structures through the emergence of distinct chiral contributions to $\chi^{(2)}$. This extends the chemical and structural sensitivity of the technique, enabling the investigation of molecular chirality at interfaces, particularly in biological systems such as peptides, proteins or DNA (Yan et al., 2014). Chirality in VSFG arises when the interfacial molecular arrangement lacks mirror symmetry. This absence of symmetry allows for non-zero contributions from the pseudoscalar or chiral components of the second-order nonlinear susceptibility tensor, $\chi^{(2)}$. While achiral VSFG is generally interface-specific due to the cancellation of electric-dipole $\chi^{(2)}$can remain non-zero even in the bulk. For example, Johnson et al. (2007) demonstrated bulk chiral VSFG signals in poly-L/D-lactic acid, where the helical arrangement of the polymer chains breaks mirror symmetry and leads to a finite bulk. Furthermore, under conditions of electronic resonance, chiral VSFG can acquire additional bulk sensitivity, providing access to molecular ordering beyond the interface. Note that chiral VSFG signals are typically much weaker than achiral contributions and are often observed under specific polarization configurations such as psp, which suppress the dominant achiral $\chi^{(2)}$ components while retaining sensitivity to chiral elements (Belkin et al., 2001). The second-order susceptibility $\chi^{(2)}$ for a chiral system can be decomposed into achiral (symmetric) and chiral (antisymmetric) components. The achiral part transforms normally under mirror operations, whereas the chiral

part changes sign under inversion, reflecting its pseudoscalar nature. In the case of $C_{\infty v}$ symmetry, the allowed components of $\chi^{(2)}$are strictly constrained by symmetry. The presence of an infinite-fold rotational axis and a vertical mirror plane forbid all antisymmetric tensor elements, including those responsible for chiral optical responses. Thus, individual molecules with $C_{\infty v}$ symmetry cannot generate chiral VSFG signals under the electric-dipole approximation (Hirose et al., 1992; Wang et al., 2005). However, when molecules organize into chiral supramolecular structures (e.g. twisted collagen fibrils or oriented helical peptide assemblies) the global interfacial symmetry can be reduced, enabling an emergent chiral optical response even though the constituent units remain individually achiral (Belkin & Shen, 2001; Gogoi et al., 2021; Rocha-Mendoza et al., 2007).

I.4 Atomic Force Microscopy (AFM)

AFM is a powerful imaging technique capable of resolving surface morphology at nanometer resolution, widely used in the study of collagen fibrils. Since its introduction by Binnig et al. in 1986, AFM has enabled high-resolution morphological imaging at the nanometer scale without the need for staining, fluorescence labeling, or vacuum operation. These advantages have rendered AFM particularly attractive for examining the intricate architecture of biological systems in a near-physiological state or in air-dried preparations (Gutsmann et al., 2003).

The basic principle of AFM relies on the interaction between a sharp tip and the surface of a sample. The tip, attached to a flexible cantilever, experiences deflections as it moves across the surface contours, which are measured via laser reflection onto a photodiode. The resulting signal allows for the construction of a high-resolution map of the sample's topography (Binnig et al., 1986). Among the different operational modes of AFM, contact mode is the most straightforward and works well for rigid samples. In this mode, the tip remains in continuous physical contact with the surface and a feedback loop maintains a constant repulsive force by adjusting the vertical position of the scanner. For soft or fragile materials, such as collagen, it can introduce significant lateral forces and tip-induced deformation. In such cases, amplitude-modulation mode (also called tapping) is preferred: In this mode, the cantilever oscillates near its resonance frequency and makes brief, intermittent contacts with the surface while feedback maintains a constant oscillation amplitude (setpoint), enabling height, amplitude and phase images. The height image is reconstructed from the z motion required to hold the setpoint, the

amplitude reports variations in local tip-sample interaction strength and the phase channel represents the phase lag between drive and response. The phase is highly sensitive to dissipative, viscoelastic and adhesive contrasts. Tapping can be performed in air or liquids and allows imaging of native collagen fibrils and other soft biomaterials (Putman et al., 1994; Magonov et al., 1997; Garcia & Pérez, 2002). An illustrative schematic (Figure 13) shows the cantilever's interaction with the sample surface during force-distance spectroscopy, highlighting the feedback loop's regulation during approach and retract phases.

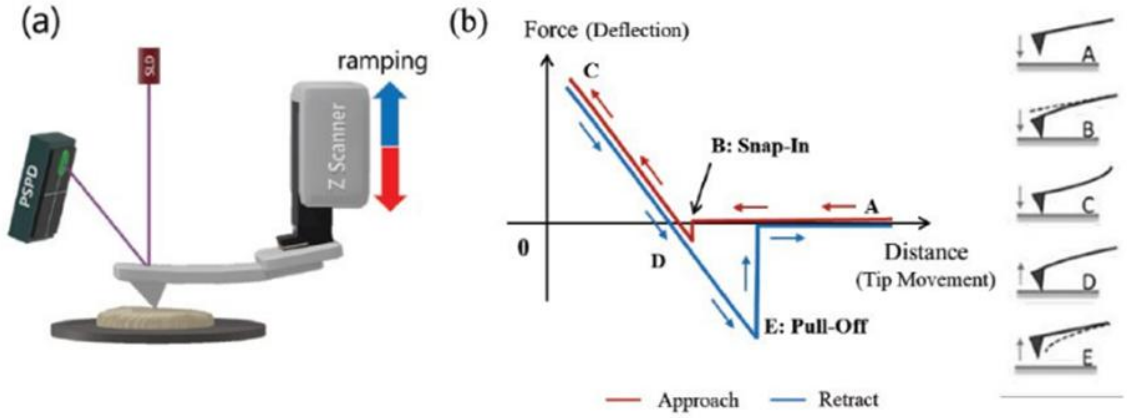

Figure 13: (a) Schematic experimental setup for FD spectroscopy, including the Z scanner movements during approach and retract in red and blue, respectively. (b) Exemplary approach and retract curves, in red and blue, respectively. The different interaction regions between the tip and the sample are labeled by the letters A to E and the according cantilever deflection for each region is shown on the right. From Park systems

These different types of images are essential for characterizing the hierarchical structure of collagen. In this context, AFM has proven highly effective in visualizing the characteristic 67nm periodic D-band pattern (Gisbert et al., 2021). Studies have shown that collagen's fibrillogenesis is influenced by factors such as ionic strength, pH, temperature, and the presence or absence of telopeptides (Drzewiecki et al., 2016; Harris & Reiber, 2013). AFM imaging provides direct morphological evidence of these effects, allowing the comparison of different collagen preparations under controlled conditions.

I.5 Objective of the work

This thesis is a continuation of the research initiated in the frame of the doctoral thesis of Clara Manesco, whose work focused on understanding the structural and mechanical properties of collagen in the injured mouse spinal cord. Her study combined AFM force measurements of

the Young's modulus at the lesion core coupled with a novel image analysis approach applied to SHG microscopy data. She employed a fingerprint-based algorithm developed during her thesis, which enabled the determination of the skeleton map of collagen fibers within images. From these maps, physical parameters such as fiber tortuosity, total fiber length, entropy and variance were extracted, providing a comprehensive structural description of the collagen network depositions at the injury site. Clara Manesco's work was restricted to the lesion core characterization, using 30µm thick longitudinal tissue sections acquired with a 16x objective and a 3µm z-resolution. While this approach offered high-quality 2D analysis, it did not allow the investigation of the 3D structuration of collagen and its evolution on the rostro-caudal axis. Her approach remained spatially restricted, both in terms of resolution and anatomical coverage, focusing exclusively on the lesion core. The present work is motivated by the need to broaden both the spatial and temporal analysis of fibrotic scarring following SCI. It aims to address unresolved questions about collagen dynamics within the lesion site, in adjacent zone or remote tissue regions, and at multiple post-injury timepoints. Complementarily, we undertake a bottom-up approach to resolve how collagen's molecular conformation and orientational order emerge during fibrillogenesis.

The first objective of this work is to improve our understanding of collagen remodeling along the rostrocaudal axis following spinal cord injury. Furthermore, we hypothesize that the density of collagen in perilesional regions could serve as a quantitative marker of fibrotic scar evolution. We expect that collagen content increases with time post-injury and that the presence of collagen in adjacent zones reflects the propagation and resolution of inflammatory and fibrotic responses. To test these hypotheses, we implement a higher-resolution 3D SHG imaging approach, using 50µm thick section and a new objective allowing imaging at 1.5µm z-resolution. This technical improvement enables better visualization of collagen and allows reconstruction of 3D images. We also aim to evaluate whether the temporal dynamics of collagen distribution correlate with spatial variation across the lesion, rostral and caudal regions.

The second objective of this work is to apply a bottom-up approach to study in-vitro growth and organization of type I collagen under controlled conditions. We aim to better understand the molecular mechanisms that might underline the *ex vivo* observations. Our work will specifically address the differential assembly of atelocollagen and telocollagen. We hypothesize

that the presence of telopeptides in telocollagen facilitates and directs fibrillogenesis, resulting in more organized and aligned collagen structures. In contrast, atelocollagen, which lacks telopeptides, is expected to form disordered and less-twister fibrils.

To test these hypotheses, we employ vibrational sum frequency generation (VSFG) spectroscopy to detect differences in molecular conformation between atelocollagen and telocollagen after drying. We hypothesize that, despite identical amino acid composition, the two forms will exhibit distinct VSFG spectral signatures, reflecting different triple helix organization and supramolecular packing and spatial arrangement. In parallel we use second harmonic scattering (SHS) in liquid conditions to monitor the evolution of collagen during fibrillogenesis. By analyzing the macroscopic hyperpolarizability (β) tensor and the depolarization ratio and assuming a specific molecular symmetry, we presume that the telocollagen will have a higher β than atelocollagen, because of its more structured network. We also suppose that telocollagen will have a more constant depolarization ratio link to a more stable structure. Although the current *in vitro* setup does not yet constitute a model of fibrosis per se, we consider it a foundational step toward reproducing fibrotic organization in a controlled environment. We hypothesize that insights from the *in vitro* behavior of telocollagen and atelocollagen may help interpret the structural variability observed in the fibrotic scar and the surrounding tissue following spinal cord injury. In particular, the ordered growth of telocollagen in vitro may parallel the more organized collagen structures seen in mature lesion zones.

Chapter II

--

Materials and Methods

II. Materials and Methods

II.1 Biological samples

To characterize the structural organization of post-lesional scar tissue in the spinal cord, a T9 lateral hemisection (HS) was surgically induced in a transgenic mouse model expressing eGFP in astrocytes). Following lesion induction, tissues were harvested at different time point, fixed in paraformaldehyde and prepared for high-resolution imaging using multiphoton microscopy (MPM).

II.1.1 Ethics

All experimental procedures were conducted in accordance with European legislative, administrative and statutory measures for animal experimentation (86/609/EEC). The study received approval from the local ethics committee (n°36), the Veterinary Services Department of Hérault, and the French Ministry of National Education, Higher Education and Research (n°34118).

II.1.2 Murine model

Transgenic mice expressing enhanced green fluorescent protein (eGFP) under the control of the Aldh1l1 promoter (Aldh1l1 – EGFP) OFC789Gsat/Mmucd) were used in this study to selectively label astrocytic populations. Mice were obtained from the Mutant Mouse Regional Resource Centre (MMRRC) and maintained on a Swiss Webster background. Animals were housed under controlled environmental conditions, including stable temperature and humidity, a 12-hour light/dark cycle, and ab libitum access to food and water. Only heterozygote females Aldh1l1 were used for this work.

II.1.3 Spinal cord injury and post-operative cares

Adult female transgenic Aldh1l1-EGFP mice (3 months old) were anesthetized with 3-4% isoflurane (Vetflurane, Virbac, France) for induction, and anesthesia was maintained with 1-2% isoflurane delivered in 1L/min oxygen throughout the surgical procedure. To prevent corneal desiccation, ophthalmic gel was applied to the eyes. A lateral hemisection of the spinal cord was performed at thoracic level T9, using a micro knife (ref. 10315-12, Fine Science Tools, FST). The lesion was made from the midline of the spinal cord to the lateral edge, selectively cutting the left side. This injury model results in complete paralysis of the left hind limb, while respiratory functions remain unaffected. Mice were monitored individually for 1 hour following

surgery Postoperative care included manual bladder expression twice daily, maintained until the recovery of bladder sphincter control. Body weight was recorded daily to assess general health status until the animals were sacrificed for tissue collection. Tissues were collected at different time-points: 1 week, 2 weeks, 4 weeks and 6 weeks post-injury (wpi). (For more detailed on previous studies, see Noristani et al. 2016)

II.1.4 Tissues preparation for ex vivo analysis

To preserve tissue integrity for downstream analyses, the spinal cord was fixed via intracardiac perfusion. Mice received an intraperitoneal injection of a lethal dose of tribromoethanol (500 mg/kg, Sigma-Aldrich, Darmstadt, Germany). After opening the thoracic cavity and sectioning the diaphragm, a needle connected to a peristaltic pump was inserted into the left ventricle. The right atrium was incised to allow drainage and prevent backflow. Perfusion was performed first with 40 ml of cold PBS to flush out blood and prevent clot formation, followed by 4% paraformaldehyde (PFA, Sigma-Aldrich) as fixative. The spinal cord was then carefully removed from the vertebral column. Surrounding tissues were dissected away and each vertebra was detached and further post-fixed in 4% PFA for 2 hours at room temperature. Tissues were then cryoprotected in a 30% sucrose solution, embedded in Tissue-Tek O.C.T compound and frozen. Blocks were stored at -80°C then transferred to -20°C for cryosectioning. Sections were cut on the longitudinal axis (50µm thick) using a Microm HM550 cryostat (ThermoFisher Scientific, Waltham, MA, USA) and collected at -20°C on Superfrost Plus microscope slides. An illustration of spinal cord sections is shown in figure 14.

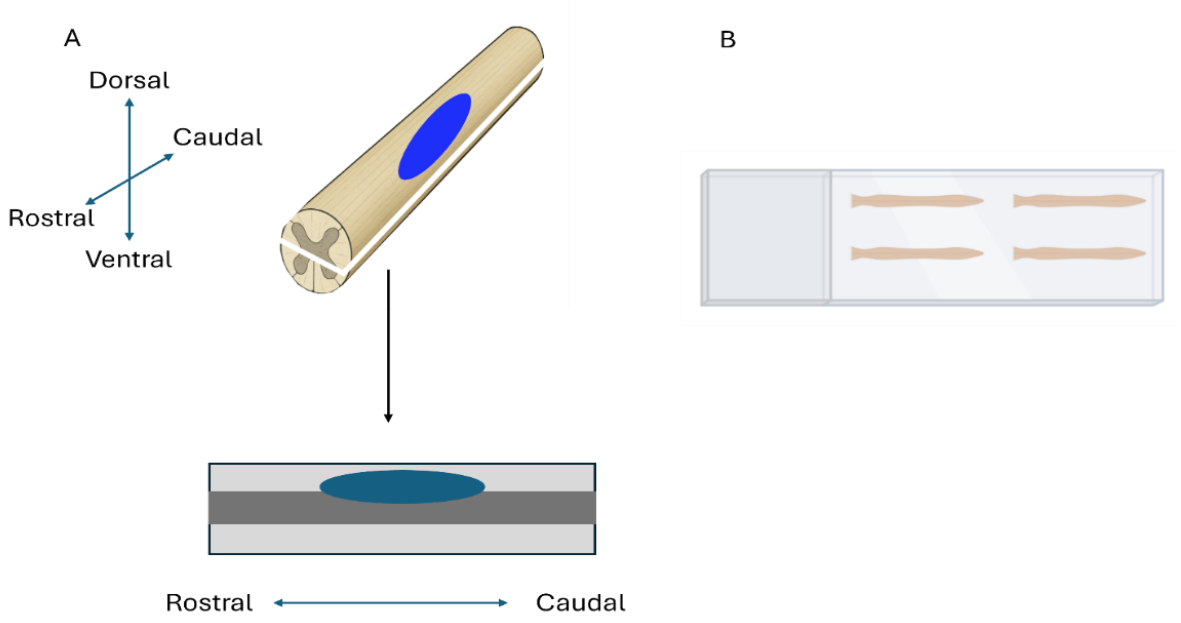

Figure 14: Schematic of the spinal cord sections collection. (A) Longitudinal view of the injured spinal cord. (B) 50 µm-thick longitudinal sections were collected along the dorso-ventral axis. Thus, the lesion is visible on all sections (200 µm intervals between each section along the dorso-ventral axis).

II.2 Collagen samples

In the frame of the work concerning the bottom-up approach of constructing collagen structures, it was necessary to establish experimental protocols to produce and observe fibrils at various stages of maturation. Several methods described in the literature were explored and evaluated. We describe here three specific approaches that were implemented and contributed directly to our experimental findings.

II.2.1 Cold Start method

The method, originally developed by Gale et al. (1995), utilizes type I collagen monomers dissolved in an acidic solution (pH=2) to prevent fibril formation. Two variants of bovine collagen I were employed: Telocollagen (Tcol) (ref. 5225) and Atelocollagen (Acol) (ref. 5005) both purchased from Advance Biomatrix. Each stock solution was initially diluted at 0.4 mg/ml in 0.01M HCl. Then mix 1:1 with phosphate buffer (PBS) to reach a final concentration of 0.2 mg/ml, pH=6.8 and ionic strength of 0.2. The diluted solutions are then incubated at 34°C for various durations to allow fibrillogenesis. Polymerization was stopped by a 1:10 dilution in distilled water. A drop (60µl) of the resulting solution was deposited on freshly cleaved mica for 30min, rinsed gently and left to air dry overnight.

II.2.2 pH controlled method

The bovine type I collagen (monomers in acidic solution), Acol (ref. 5005), Tcol (ref. 5225) were purchased from Advance Biomatrix and solutions were prepared in a quartz cell used for SHS. Both samples were diluted at a concentration of 2.1 mg/mL in 0.01M HCl. The pH was regulated (from 2 to 7) by gradually adding small quantities, 10 µL of 0.1M NaOH Deposition on mica or CaF2 substrate was done in the same way as in the previous protocol. Briefly, 60µL of the solution was deposited on the surface (freshly cleaved for the mica) for 30 min, gently rinsed 10 times with 60µL of distilled water and left to air dry.

II.2.3 Ionic forces to form bundles of fibers

Type I bovine collagen (in 0.01M HCL, Biomatrix, ref. 5005 and ref. 5225) was used to prepare collagen matrices, following the protocol described by Oh et al., 2020. For native matrices, the collagen solution was mixed with 10x PBS (Sigma-Aldrich, USA), 1N NaOH and 20µM HEPES to adjust the pH to the physiological value of 7. The final volume was completed with deionized water to obtain a collagen concentration of 1 mg/ml. The solution was mixed on ice and allowed to self-assemble for 30 minutes at 37°C. For modified fibril bundling conditions, a certain volume of deionized water was replaced by a neutralized solution (N-solution) prepared by mixing 1N sulfuric acid with 1N sodium hydroxide. The final collagen concentration and pH remained at 1 mg/ml and pH 7. N-solution was added at 5%, 20% or 50% of the total collagen solution volume. Collagen matrices were formed on fresh cleaved mica.

II.2.4 Peptides model

To complement our bottom-up approach, we incorporated a simplified model of collagen-like molecules. As described in Chapter I (I.2.1.1), natural collagen consists of repeating Gly-X-Y triplets, in which X and Y are frequently proline and hydroxyproline, critical for triple helix formation and stability. To reproduce this structural motif in a controlled system, we employed synthetic $(Pro\text{-}Pro\text{-}Gly)_{10}$ peptides, which are known to self-assemble into collagen-mimetic triple helices (Deniset-Besseau et al., 2009). These peptides were purchased from Peptides International (product OPG-4006, purity > 95%).

The peptide was first solubilized in 0.05mM acetic acid to prepare a solution at 3.3 mg/ml. Depending on the imaging technique, the peptide solution was deposited either on freshly cleaved mica or on CaF2 substrates (for VSFG measurements). Following deposition, the

samples were gently rinsed by carefully applying 30µl of Milli-Q water (10 times at least) using a micropipette, to remove unbound material while preserving the assembled structures. The substrates were then air-dried at room temperature overnight prior to imaging.

II.3 Imaging and spectroscopic techniques

II.3.1 Multiphoton microscopy (MPM)

II.3.1.1 Setup

Combined two-photon excited fluorescence (2PEF) and second harmonic generation (SHG) imaging was performed using a custom-built multiphoton microscope based on an upright scanning system (SliceScope, Scientifica LTD/, UK) equipped with a galvanometric scan head (MP-2000, Scientifica). An Olympus x25 long working distance water immersion objective (XLPLN25XWMP2, 1.05NA, Olympus, Japan) was used for excitation and 2PEF signal collection. The schematic setup of the MPM system is shown in Figure 15. Samples were excited at 870nm using a femtosecond Ti:Sapphire laser (Tsunami, Spectra-Physics, USA) operating in pulsed mode (760-900nm range) at a repetition rate of 80MHz. Beam polarization was adjusted using a combination of achromatic wave plates. The 2PEF signal was epi-collected through the objective and detected via a photomultiplier tube (PMT). The SHG signal was collected in transmission through a high numerical aperture condenser (U-AAC, 1.4 NA, Olympus, Japan) filtered and detected using a second PMT.

Our experimental setup enabled the simultaneous detection of multiple optical signals derived from the sample. These included:

i) A broad-spectrum tissue autofluorescence, used to visualize general tissue morphology,
ii) The endogenous fluorescence of astrocytes cells expressing eGFP (emission peak at 510nm)
iii) The second harmonic generation (SHG) signal, centered at 435nm (half the excitation wavelength of 870nm), originating from non-centrosymmetric structures such as collagen fibers.

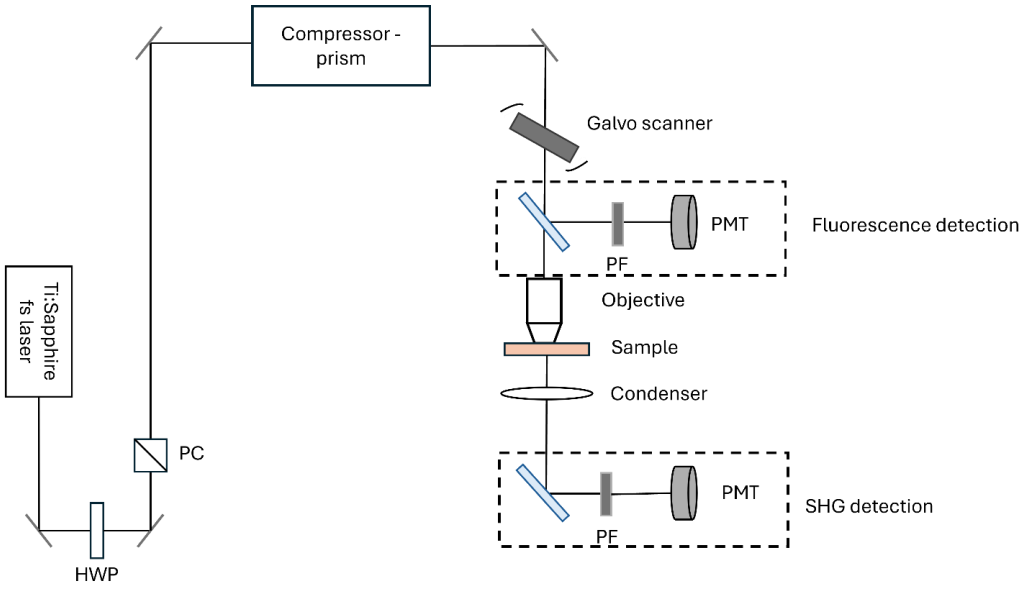

Figure 15: Schematic of the multiphoton microscopy (MPM) setup. A Ti:Sapphire femtosecond laser provides the excitation beam. The output power is tuned by a half-wave plate (HWP) combined with a polarizing cube (PC), which also allows adjustment of polarization. A prism compressor compensates for group velocity dispersion before the beam enters the scanning unit. A pair of galvanometric mirrors (Galvo scanner) directs the beam across the sample, which is focused through a high-numerical-aperture objective onto the specimen mounted on a coverslip. The generated signals are collected in two detection geometries: second-harmonic generation (SHG) is detected in the forward direction, while multiphoton-excited fluorescence (TPEF) is collected in the backward direction. Both signals are spectrally separated by dichroic mirrors and filtered with band-pass filters (PF) before detection by photomultiplier tubes (PMTs)

To isolate these signals, a series of dichroic mirrors and optical filters were used. The 2PEF signals were filtered sequentially through a 735nm long-pass dichroic mirror (FF735-Di02, Semrock, USA), a 750nm short-pass filter (FESH0750, Thorlabs Inc., USA), and a 450nm long-pass filter (62-942, Edmund Optics Ltd., UK). The SHG signal, collected in the forward direction, was filtered through a 482nm long-pass dichroic mirror (86-331, Edmund Optics Ltd., UK), a 550nm short-pass filter (84-708, Edmund Optics Ltd., UK), and a 447nm high-performance band-pass filter (NT 48-074, Edmund Optics Ltd., UK), allowing for precise spectral isolation of the harmonic signal.

The detection system consisted of two separate photomultiplier tubes (PMTs), one for each signal channel. The 2PEF signal was detected using a standard R928P PMT (Hamamatsu, Japan), while the SHG signal was collected using a high-sensitivity GaAsP photomultiplier (H7422P, Hamamatsu, Japan). Although both PMTs are compatible with photon-counting acquisition modes, in this study they were operated in analog mode, as described by Xu et al., 2013. To ensure consistency across imaging sessions, PMTs gain were initially set at the beginning of each session and maintained as constant as possible throughout the acquisition. However, in certain instances, gain adjustments were necessary during imaging to compensate

for unexpected signal fluctuations. In such cases, corrections were applied during image preprocessing to normalize intensity variations and ensure comparability across datasets.

As previously discussed in Chapter I (I.3.1), the coherent nature of the second harmonic generation (SHG) signal implies that its intensity is influenced by multiple parameters. These include the intensity (or power) and polarization state of the excitation beam, as well as the relative orientation, density and spatial organization of molecular dipoles within the focal volume (Pena, 2006). In the case of collagen, these dipoles originate from the triple-helical structure of individual collagen molecules, which assemble into fibrils, then fibril bundles, ultimately forming mature collagen fibers.

In our experimental setup, the excitation power delivered to the sample was stabilized using an achromatic λ/2 waveplate followed by a Glan-type polarizer. The half-wave plate rotated the plane of linear polarization, thereby modulating the fraction of light transmitted through the polarizer and maintaining a constant injected power into the microscope. To minimize photobleaching and photodamage, a mechanical shutter was placed directly after the laser source and was opened only during active image acquisition. Additional shutters were also installed in front of the PMTs to further reduce unnecessary exposure and ensure PMT stability.

II.3.1.2 Resolution and z-stack

High-resolution imaging of biological tissues requires an optimal compromise between field of view, spatial resolution and working distance (Oheim et al., 2001). To meet these constraints, we used a x25 water immersion objective (XLPLN25XWMP2, 1.05NA, Olympus, Japan) with a numerical aperture (NA) of 1.05, a working distance of 2mm and a field of view of approximatively 1mm, providing high image quality when combined with multiphoton excitation and confocal detection. The theoretical resolution of the system is defined by the following classical expressions (Jonkman et al., 2003):

$$Lateral\ resolution\ (\delta_{xy}) = \frac{0.61\ \cdot\ \lambda}{NA} \tag{15}$$

$$Axial\ resolution\ (\delta_z) = \frac{2 \cdot \lambda \cdot n}{NA^2} \tag{16}$$

Where λ is the emission wavelength, n the refractive index of the immersion medium and NA the numerical aperture of the objective. For our system, assuming λ=435nm and NA = 1.05, the calculated lateral resolution was approximately 0.3 µm, and the axial resolution was approximately 1µm.

Z-stacks were acquired within 550x550 µm fields, with an image size of 1024 x 1024 pixels and a 1.5µm steps size along the Z-axis, matching the axial resolution of the system. The objective head was translated using a motorized drive with a precision of 50-100nm. Imaging was systematically centered at the injury epicenter, with acquisition fields spanning the rostral-caudal axis over a total distance of 2mm centered on the lesion site. Image acquisition was initiated on the ipsilateral border zone (where SHG intensity from collagen fibers was highest), followed by two additional fields progressively extending toward the contralateral side, resulting in a total of three adjacent fields in this direction. To enhance the signal-to-noise ratio (SNR), each imaging plane was averaged over six consecutive acquisitions, which also helped to reduce acquisition time without compromising image quality.

II.3.1.3 Mosaic acquisitions

To assess both the spatial extension of collagen and the temporal evolution of fiber organization following spinal cord injury, we performed large-field acquisitions through mosaic imaging. Each mosaic was composed of 12 adjacent tiles, covering a total area of approximately $3mm^2$ with 2mm along the rostro-caudal axis and 1.5mm in ipsilateral-contralateral axis. This acquisition strategy enabled comprehensive visualization of both the lesion core and the peri-lesional zones.

For each region, a z-stack acquisition was performed across the full thickness of the cryosection (50µm), using a step size of 1.5µm. Typically, 35 planes were recorded per stack, starting from the first detectable SHG signal and continuing until it faded. Each individual z-plane consisted of six average acquisitions, which were later combined to reconstruct high-quality slices with improved signal-to-noise ratio (SNR). We average 6 fast scans of the same field instead of using a very long dwell time per pixel. This gives us the same gain in signal-to-noise ratio, but it is safer for the sample and more robust experimentally. With shorter pixel dwell times we limit local heating and photodamage, which is important for collagen and surrounding tissue. By spreading the total dose over several passes, the sample has time to dissipate heat in between, and we can also detect or discard occasional instabilities (e.g. laser fluctuations, motion)

between frames. The final image is the average of the 6 frames, with improved SNR and without overstressing the sample

Image preprocessing was carried out using Fiji (ImageJ). Averaging of the six raw images per plane and normalization of the intensity values across mosaic tiles were performed prior to stitching. BigStitcher plugin was used for accurate 3D reconstruction of the full mosaic volume. For 3D visualization, reconstructed stacks were imported into Napari, an open-source viewer optimized for large multidimensional datasets. Quantitative analyses were then performed using two custom pipelines:

- A 2D morpho-textural analysis with the "Fingerprint" method developed previously by Oscar Saavedra and Clara Manesco (Manesco et al., 2023)
- A 3D collagen organization analysis following the method described by Liu et al., 2021.

This workflow allowed precise quantification of collagen architecture and spatial heterogeneity across different time points post-lesion.

II.3.1.4 Image analysis

Raw images acquired via multiphoton microscopy (MPM) often contain significant background noise and intensity inhomogeneities, which can alter both qualitative observation and quantitative analysis. Therefore, a preprocessing step is essential prior to any image reconstruction. This involves normalization and alignment across image tiles and z-plan. These corrections allow the generation of clean, high-contrast composite images, suitable for both 2D morphometric assessment and 3D spatial reconstruction and analysis. Complete mosaics covering large tissue volumes were reconstructed to preserve anatomical context and enable a consistent analysis of collagen distribution and organization around the lesion.

II.3.1.5 Preprocessing with ImageJ

Before proceeding with mosaic reconstruction and quantitative analysis, raw image stacks were subjected to a series of preprocessing steps to ensure consistency and optimize data quality. The first step was intensity normalization, designed to compensate for intensity differences between mosaic tiles due to acquisition variability. For each image tile I_i, the normalization was performed using the following linear rescaling formula:

$$I_i^{norm}(x,y) = \frac{I_i(x,y) - \min(I_i)}{\max(I_{all}) - \min(I_{all})} \quad (17)$$

Where $I_i(x, y)$ is the original intensity at pixel (x, y) in image I_i, and $\min(I_{all})$, $\max(I_{all})$ are the global minimum and maximum intensity values across all images in the mosaic. This ensures that the dynamic range of all tiles is matched to a common reference, avoiding artificial contrast discontinuities between adjacent images.

Following normalization, a manual selection was carried out to exclude Z-planes that were overly noisy or degraded. Usually, the first and last plane were deleted from the total image, bearing almost no signal.

Once the dataset was cleaned and rescaled, a full-field reconstruction was performed using BigStitcher (ImageJ), optimized for stitching large multidimensional datasets (Hörl et al., 2019). Each mosaic consisted of 12 tiles arranged in a 4 x 3 grid. After stitching, a Gaussian filter was applied to the reconstructed mosaic to smooth residual high-frequency noise and improve overall image readability, while preserving structural features relevant for subsequent 2D and 3D analyses.

II.3.1.6 Fingerprint method

To assess the organization of the collagen network revealed by SHG imaging, we employed the Fingerprint Enhancement (FP-E) method, a quantitative image analysis tool specifically developed for fibrous biological structures (Manesco et al., 2023; Manesco et al., 2025). This algorithm enables the extraction of structural metrics of collagen fibers from skeletonized images. The algorithm processes SHG images through the following steps:

- Image enhancement to improve signal contrast and continuity
- Orientation mapping to estimate local fiber direction
- Binarization to segment collagen fibers from background
- Skeletonization to reduce fibers to their medial axes
- Untangling to separate overlapping or crossing fibers

The resulting skeleton map serves as a basis for computing quantitative descriptors, each of which reflects a specific aspect of the collagen network's morphology and arrangement. Importantly, although the SHG data were acquired as three-dimensional stacks, the Fingerprint method operates on a 2D basis. That is, the analysis is performed independently for each optical section (z-plane). This approach allows for precise localization of collagen architecture within specific depths of the tissue and facilitates the quantification of local matrix heterogeneity. Each

z-plane was treated as an independent observation, and metrics were compared individually. Though this method allows us to extract structural descriptors of collagen network that will be presented in the next sections.

II.3.1.6.1 Total Fiber Length (F_l)

Total fiber length is calculated as the sum of the lengths of all identified collagen segments in the skeleton map, expressed in micrometers.

$$F_l = \sum_{i=1}^{N} L_i \tag{18}$$

Where L_i is the length of the i-th fiber and N is the total number of detected fibers in the 2D plane.

It represents the total amount of detectable fibrillar collagen in the imaged region. An increase in fiber length typically reflects collagen accumulation during scar formation. A reduction may suggest matrix degradation, delayed deposition or reorganization of the matrix.

II.3.1.6.2 Tortuosity

A unitless measure of the curvature of individual fibers, calculated as the ratio between their actual path length and the direct distance between their endpoints.

$$\tau_i = \frac{L_{curve,i}}{L_{straigth,i}} \geq 1 \tag{19}$$

With τ=1 meaning the fiber is perfectly straight and τ≥1 when the fiber is curved, meandering or looped, meaning lower is the tortuosity straighter is the fiber (Figure 16). Increased tortuosity indicated disorganized ECM or immature collagen fibers; low tortuosity is typical of aligned, tension-bearing collagen found in structured or healthy tissues.

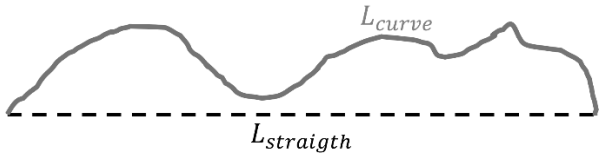

Figure 16: Schematic of collagen fiber length (L_{curve}) or end-to-end distance ($L_{straigth}$), adapted from Clara Manesco PhD thesis

II.3.1.6.3 Orientation Entropy (S)

It quantifies the degree of directional disorder in the angular distribution of collagen fibers.

$$S = -\frac{1}{\ln(N_B)} \sum_{\beta=-90^\circ}^{90^\circ} p(\beta) \ln\big(p(\beta)\big) \quad (20)$$

Where $p(\beta)$ is the probability of fiber being oriented at angle β and $N_B$is the total number of angular bins used (e.g., 180). Entropy ranges from 0 to 1 with 0 meaning highly aligned network (ordered) and 1 random fiber orientation (disordered). Note that high entropy is observed in disorganized scar tissue, where collagen fibers lack preferential orientation.

II.3.1.6.4 Local Angular Variance (Var(θ))

It evaluates the coherence of fiber orientation within local neighborhoods, based on circular statistics. Unlike linear measurements, angular data (e.g., 0° and 180°) are periodic, so standard linear variance measures would yield misleading results. Instead, circular variance is used: it first computes the mean orientation $\bar{\theta}$ using the average direction of unit vectors on the unit circle. Then, it measures how much each local orientation θ_j deviates from this mean, accounting for angular periodicity. We start with the mean orientation calculation.

$$\bar{\theta} = \frac{1}{2}\arg\left(\sum_{j=1}^{N} e^{i2\theta_j}\right) \quad (21)$$

Then with the angular variance:

$$Var(\theta) = \frac{1}{N}\sum_{j=1}^{N}(1 - \cos(2\theta_j - 2\bar{\theta})) \quad (22)$$

This metric measures how consistently the orientations of neighboring pixels or fiber segments align with the local average direction. Low variance indicates well-aligned local structures. A high local variance indicates random or chaotic angular distribution suggesting disorganized or fragmented fibers, often present in early post-injury stages, regions with active remodeling, or mechanically disrupted zones.

II.3.1.7 3D Variance

To complement the 2D orientation analysis (Fingerprint method), a 3D structural analysis was conducted to evaluate the spatial organization of collagen fibers across the volume of the spinal cord. This approach was essential to capture fiber alignment and remodeling in a biologically

relevant volume, especially for tracking scar development over time. The method was implemented following the 3D weighted orientation vector summation algorithm originally proposed by Liu et al., 2015 and expanded upon in Liu et al., 2017. The algorithm is specifically designed for SHG image stacks and enables voxel-wise extraction of fiber orientation with high spatial accuracy.

Prior to orientation analysis, SHG image stacks were acquired at a voxel resolution of approximately 0.5 x 0.5 x 1.5 μm^3. To allow isotropic analysis and prevent bias introduced by anisotropic sampling, the data were resampled using cubic interpolation to a voxel resolution of 0.5 x 0.5 x0.5 μm^3. This isotropic rescaling ensured that gradient computations in x, y and z dimensions contributed equally to orientation estimations.

To prepare the image stacks for analysis, a series of preprocessing steps were applied, the same as for the FingerPrint method, including intensity normalization to standardize signal amplitude across the volume, Gaussian filtering to reduce high-frequency noise and manual filtering to exclude overly degraded planes. Once this preparatory phase was completed, the processed images were used as input for the orientation algorithm.

Each voxel within the 3D image volume was analyzed in the context of its 3 x 3 x 3 neighborhood. For a given central voxel at coordinates (x_0, y_0, z_0), a cubic region of interest with 27 voxels (including the center) was defined. The algorithm then excluded the center, yielding a total of 26 neighboring voxels used for gradient computation. For each of these neighbors, the local image intensity gradient ∇I was estimated using finite difference approximations, which are numerical methods for approximating the derivatives of a function based on discrete sampling points. In our case, the simplest forward or central difference scheme was used: for instance: $\frac{\partial I}{\partial x} \approx \frac{I(x+1,y,z)-I(x-1,y,z)}{2\Delta x}$, where Δx represents the voxel spacing. Similar expressions were applied along the y and z axes.

These partial derivatives $\frac{\partial I}{\partial x}$, $\frac{\partial I}{\partial y}$ and $\frac{\partial I}{\partial z}$form a 3D gradient vector $\overrightarrow{g_i}$ for each voxel i. The gradient vector points in the direction of the steepest intensity change in the SHG signal, which is assumed to be perpendicular to the local orientation of the fiber. However, by analyzing the gradient directions across the neighborhood and weighing their contribution, we infer the most probable direction of fiber alignment at the central voxel. This directional information is critical

because SHG imaging captures the coherent response of aligned collagen fibrils, meaning that intensity patterns directly relate to structural orientation.

The principal orientation at the central voxel was then estimated through a weighted summation of these surrounding gradient vectors. The orientation vector $\overrightarrow{V_0}$ was defined as the sum:

$$\overrightarrow{V_0} = \sum_{i=1}^{N} w_i \cdot \overrightarrow{g_i} \tag{23}$$

Where $\overrightarrow{g_i}$ is the normalized gradient vector at the ith neighboring voxel, and wi the corresponding weight with N here equals to 124. To determine a fiber inside a kernel, two different weights are determined.

The total weight w_i was calculated as the product of the two components (weight):

$$w_i = w_{dist}(i) \cdot w_{intensity}(i) \tag{24}$$

The first component accounts for the spatial proximity of the neighbor voxel $\vec{r_i}$ to the central voxel $\overrightarrow{r_0}$. It ensures that closer neighbors contribute more significantly to the final orientation estimation, thereby minimizing the influence of outlier vectors located farther away. This is crucial to reduce the bias caused by spatially distant voxels that might lie across local structural discontinuities. The weight is defined using a Gaussian decay function:

$$w_{dist}(i) = \exp\left(-\frac{\left|\left|\vec{r_i} - \overrightarrow{r_0}\right|\right|^2}{2\sigma_d^2}\right) \tag{25}$$

Where $\left|\left|\vec{r_i} - \overrightarrow{r_0}\right|\right|^2$ is the Euclidean distance between voxel I and the center, and σ_d is a spatial decay parameter, typically set to match the voxel spacing. The effect of this formulation is to give uniformly scaled influence on all vectors by controlling their relative distance, preventing longer-distance gradients from disproportionately affecting the summation.

The second component, intensity-based weight, was designed to emphasize the contribution of voxels with high local signal contrast. Unlike a direct use of the gradient norm, here the weight was calculated using a local contrast dispersion formula:

$$w_{intensity}(i) = \sqrt{\frac{1}{3}} - \sqrt{\frac{1}{2}\sum_{j=1}^{3}\left(a_j - \bar{a}\right)^2} \quad (26)$$

With a_j the normalized intensity component along each of the three gradient axes (x, y, z) and $\bar{a}$ their average. This calculation quantifies how evenly the signal gradient is distributed across the three axes. When the dispersion is low, meaning the gradient components are similar and balanced, the weight is high. This condition is associated with structurally coherent regions where collagen fibers exhibit stable, predictable orientation. Conversely, if one component dominates or if the distribution is erratic (high variance), the voxel is considered less reliable for directional estimation and its contribution is downweighted. In this way, the weighting favors regions with consistent gradient behavior, helping to mitigate the influence of noisy or isotropic regions where fiber orientation cannot be clearly inferred.

These two components (spatial proximity and intensity coherence) were combined multiplicatively, ensuring that only gradients from voxels both close in space and reliable in signal contributed significantly. This combined weight was then used to perform the weighted summation of the orientation vectors, yielding a robust estimation of fiber directionality at each voxel.

Once the weighted vector $\overrightarrow{V_0}$ was computed, it was normalized and used to derive angular descriptors characterizing the fiber orientation in 3D. As illustrated in figure 17, the orientation represented as a red vector was expressed in terms of four angles: θ, β, φ and γ and range from 0° to 180°. The angle θ represents the azimuthal orientation within the XY plane. Angles $\beta$and γ were defined as the angles of the fiber projections in the XZ and YZ planes, measured from the X and Y axes respectively. These two angles will serve to determine the angle φ which defines the angle between the projection of the fiber and the z plane.

Knowing β and γ we can determine φ, which is the angle between z axis and the fiber represented in red in figure 17:

$$tan^2\varphi = \frac{1}{tan^2\beta} + \frac{1}{tan^2\,\gamma} \quad (27)$$

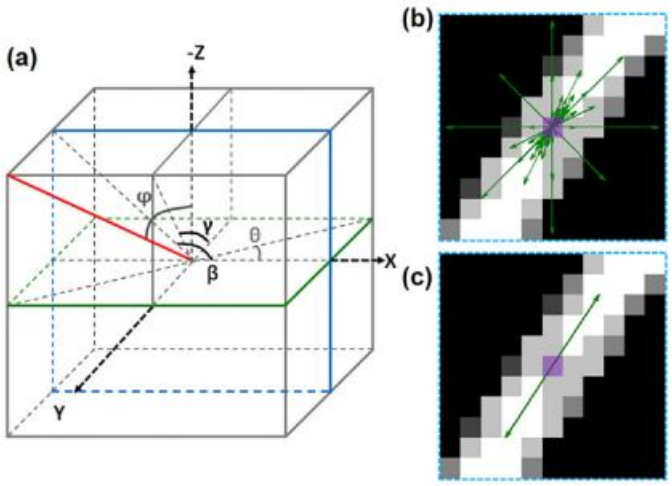

Figure 17: a) an azimutal angle θ in the transverse plane and a polar angle φ are used to define an orientation (red solid line) in 3D space. Angles β and γ, acquired by projecting the fiber to zx and yz plane, respectively, are defined and used in the determination of 3D directional variance. To find the θ, β and γ angles a n x n x n voxel window is projected onto the xy, zx and yz planes respectively. The weighted vector summation algorithm is then used to acquires the values of the corresponding angles as illustrated in b) and c). b) Weighted vectors through the center pixel of the n x n projection are acquired by considering both the vector length and intensity fluctuations along the direction of all possible vectors crossing the pixel. c) The orientation of the center pixel (marked in purple) is calculated by summation of all weighted vectors. From Liu et al., 2017

Before computing any statistical descriptors, the distributions of the angles θ and φ were examined across the entire volume. These histograms provided initial insight into the preferred orientations of collagen fibers. In particular, the distribution of θ, corresponding to the azimuthal angle in the transverse (XY) plane, offered information on whether fibers tended to align mediolaterally or rostrocaudally. Conversely, the distribution of φ, which reflects the inclination of fibers relative to the XY plane, revealed whether fibers predominantly extended within the imaging plane of exhibited vertical (dorsoventral) components.

To assess the global alignment of fibers while accounting for their axial symmetry, a 3D directional variance V_{3D} was computed using the transformed angular values. Because collagen fibers imaged via SHG are axially symmetric (i.e., indistinguishable at 0° and 180°), traditional directional statistics must be adapted to handle bidirectional orientation. This is typically addressed by doubling the angular values before calculating mean vectors or variances, converting the data to circular form. While this is straightforward for the azimuthal angle θ, the polar angle φ poses difficulties due to its sensitivity to out-of-plane deviations. To manage this, the method leverages the projection angles β and γ to define a combined weighting factor b_j for each voxel:

$$b_j = \left(\frac{1}{tan^2(2\beta_j)} + \frac{1}{tan^2(2\gamma_j)} \right) \tag{28}$$

The mean directional components across all N voxels are computed as:

$$\bar{C}_{3D}^{a} = \left(\frac{1}{N}\right)\sum_{j=1}^{N}\left(\frac{b_j}{\sqrt{1+b_j^2}}\cos(2\theta_j)\right) \quad (29.a)$$

$$\bar{S}_{3D}^{a} = \left(\frac{1}{N}\right)\sum_{j=1}^{N}\left(\frac{b_j}{\sqrt{1+b_j^2}}\sin(2\theta_j)\right) \quad (29.b)$$

$$\bar{Z}_{3D}^{a} = \left(\frac{1}{N}\right)\sum_{j=1}^{N}\left(\frac{SI}{\sqrt{1+b_j^2}}\right) \quad (29.c)$$

With $SI = (-1)\cdot(\varphi - 90)/|\varphi - 90|$ when φ≠90° and SI = 1 when φ=90°. Each component plays a distinct role: $\bar{C}_{3D}^{a}$evaluates the degree of alignment along the X-axis, $\bar{S}_{3D}^{a}$along the Y-axis and $\bar{Z}_{3D}^{a}$captures the vertical inclination of fibers relative to the XY plane. A mean directional vector from the combination of these components is determined by:

$$\bar{R}_{3D}^{a} = \sqrt{(\bar{C}_{3D}^{a})^2 + (\bar{S}_{3D}^{a})^2 + (\bar{Z}_{3D}^{a})^2} \quad (30)$$

A high value of $\bar{R}_{3D}^{a}$indicates strong directional coherence (well-aligned fibers), while lower values suggest disordered or isotropic arrangements. The final measure of global directional variability is then computed as:

$$V_{3D} = 1 - \bar{R}_{3D}^{a} \quad (31)$$

For completeness, the circular representation of orientation can also be computed using:

$$\bar{C}_{3D}^{c} = \frac{1}{N}\sum_{j=1}^{N} sin\varphi_j cos\theta_j \quad (32.a)$$

$$\bar{S}_{3D}^{c} = \frac{1}{N}\sum_{j=1}^{N} sin\varphi_j sin\theta_j \quad (32.b)$$

$$\bar{Z}_{3D}^{c} = \frac{1}{N}\sum_{j=1}^{N} cos\varphi_j \qquad (32.c)$$

These formulations allow direct comparisons with standard circular statistics, though the axial formulation provides more robust metrics for fiber-like SHG signals. Note that a lower value of V_{3D} thus corresponds to a higher degree of fiber alignment within the 3D volume, with 0 meaning a perfect alignment. This makes V_{3D} a reliable scalar descriptor for quantifying the overall structural coherence of collagen fibers.

To validate the functionality of the orientation extraction algorithm and the calculation of V_{3D}, a series of control simulations were analyzed by Liu et al., 2017. These simulations results are shown in figure 18, where both orientation maps are presented, θ (top) and φ (bottom). The stacks generated start from high level of alignment (left) to low (right). Computed Values of V_{3D}directly reflected the structural organization: low variance in highly aligned stacks is close to 0 (0.085), and progressively increasing values as disorder increased (0.919 for the less aligned simulated stack). These results confirm that the algorithm is capable of reliably distinguishing between degrees of orientation coherence, validating its use in complex biological samples such as the spinal cord injury.

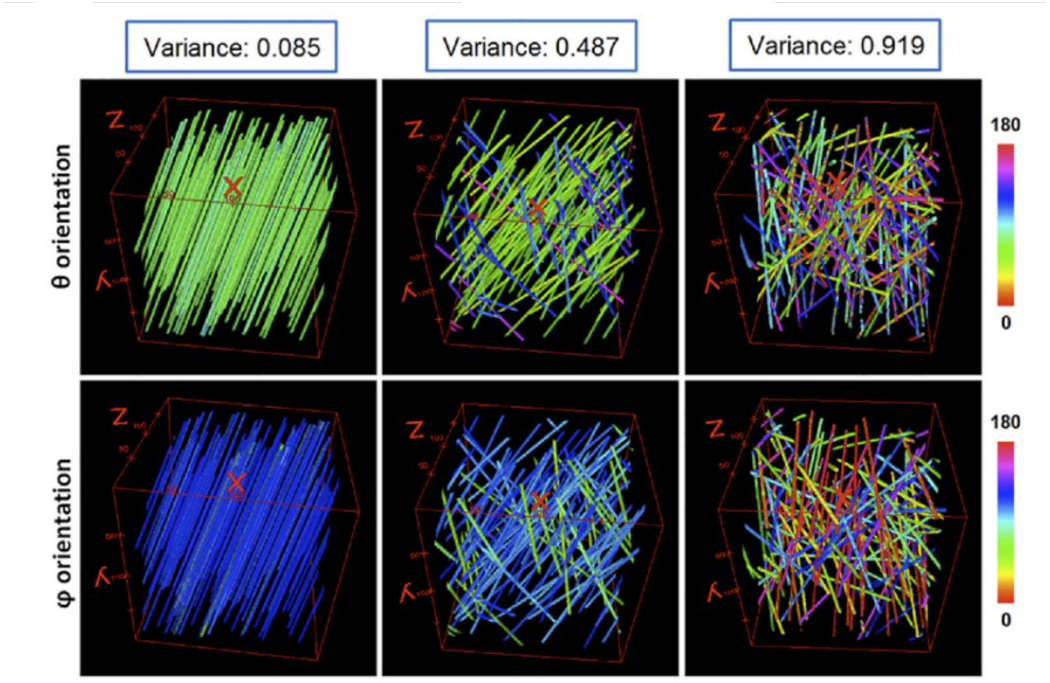

Figure 18: Simulated fiber stacks used to test the 3D directional variance algorithm. The θ (top) and φ (bottom) orientation maps of these stacks are represented by different colors (see color bars). Stack with high (left), intermediate (middle) and low (right) levels of fiber alignment are shown along with the corresponding directional variance values on top of orientation maps.

II.3.2 Second harmonic scattering (SHS)

II.3.2.1 Setup

SHS is a powerful nonlinear optical technique that provides direct access to the first hyperpolarizability of molecules. This quantity reflects the intrinsic capacity of a molecular system to exhibit a nonlinear response when exposed to an external oscillating electric field. In practice, SHS is highly sensitive to molecular symmetry and orientation, making it an especially valuable tool for probing the organization of biomolecules such as collagen in solutions. Beyond the extraction of hyperpolarizability itself, polarization-resolved SHS experiments can be conducted in order to obtain information on the symmetry of the nonlinear response, which is captured by the so-called depolarization ratio (Deniset-Besseau et al., 2009; Duboisset, 2009).

The experimental SHS setup is presented in figure 19.

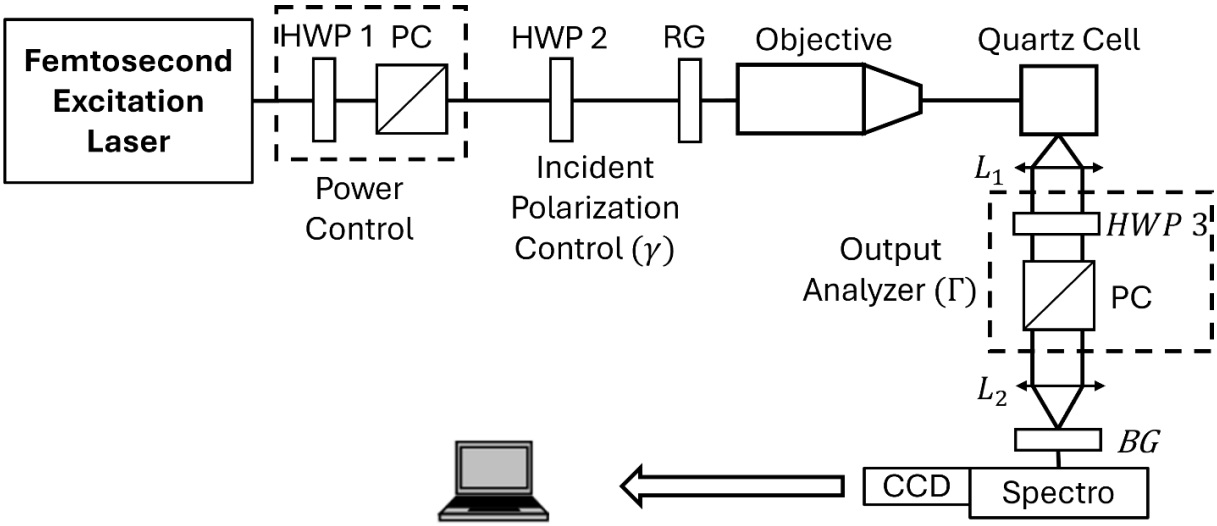

Figure 19: Hyper-Rayleigh Scattering (HRS) experimental setup. HWP : half-wave plate; RG is red and BG is blue filters; L1 and L2 : 25mm focal lenses

Experimental setup includes the use of a Ti:Sapphire femtosecond laser emitting pulses tuned at 790 nm with a duration of 140 fs at a repetition rate of 80 MHz. The laser power was set to 500mW for all the experiments. A half-wave plate coupled with a polarizing cube was used to control the incident power. Another half-waveplate was used to control the incident light polarization. The laser beam is focused onto a quartz cell containing our sample, by using x10 NIR Mitutoyo microscope objective, NA=0.25 meaning that the theorical spot size on the quartz cell is 3.5µm diameter. The SHS intensity is collected at a right angle to avoid unwanted incident signal by a Princeton SP150 spectrometer (300 lines/mm) coupled with a cooled Princeton Pixis 100 BR CCD camera. To select the output polarization (Γ angle, see Figure 20) of the SHS intensity, a half-wave plate at 400 nm combined with a polarizing cube are introduced before the spectrometer. The polarization measurements entail recording the vertically polarized harmonic intensity emitted ($\Gamma = 0°$ (Vertical)) at a right angle while rotating the linear polarization of the incident beam from $\gamma = 0°$ to $\gamma = 180°$ (see Figure 20). The incident light was linearly polarized, whereas no output polarization was selected to record the entire emitted SHS signal.

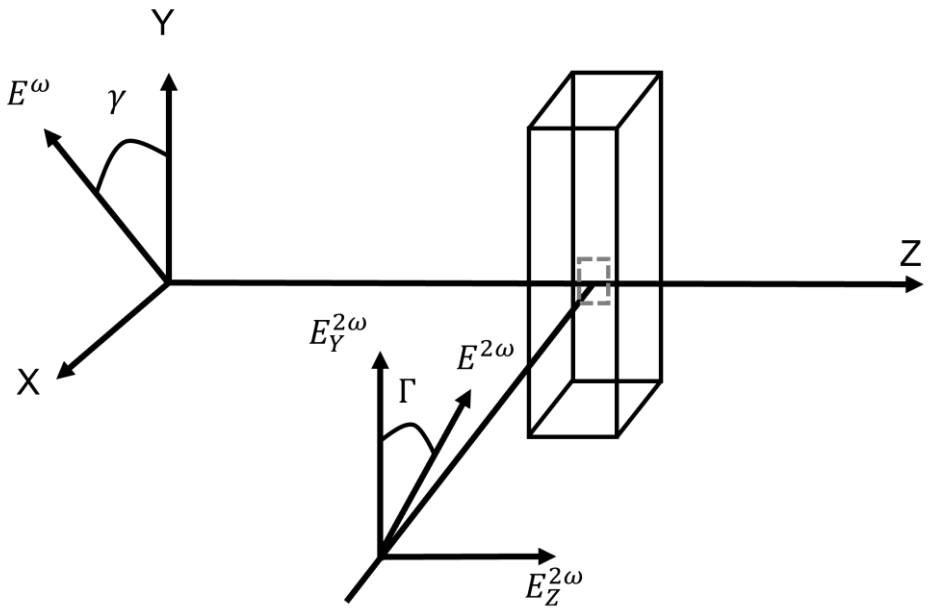

Figure 20: Laboratory and molecular frames. Polarization angle γ of the excitation electric field E^{ω} and analysis of the polarization of the radiated electric field $E^{2\omega}$ at an analyser angle Γ.

II.3.2.2 Hyperpolarizability

The second-order hyperpolarizability tensor, denoted as $\beta(2\omega, \omega, \omega)$, quantifies the nonlinear optical response of a molecule when subjected to an external electric field. This tensor is of central importance for describing how molecules such as collagen interact with electromagnetic radiation, particularly in the context of second harmonic generation (SHG) and second harmonic scattering (SHS) experiments. Because hyperpolarizability is a tensor, the number of independent components and relative magnitude are strongly dictated by molecular symmetry. Collagen, with its triple helical architecture composed of three nearly identical α-chains, can be viewed as a rigid molecule with C_3 symmetry. However, in practice, this symmetry is often reduced further to $C_{\infty V}$, corresponding to an idealized rod-like geometry with cylindrical symmetry. This approximation greatly simplifies the analysis by reducing the number of non-vanishing hyperpolarizability components while still capturing the essential optical behavior observed in P-SHS. In our experiments, measurements are taken in the laboratory frame (X, Y, Z), whereas the hyperpolarizability tensor is initially described in the molecular frame (x, y, z) (Figure 21).

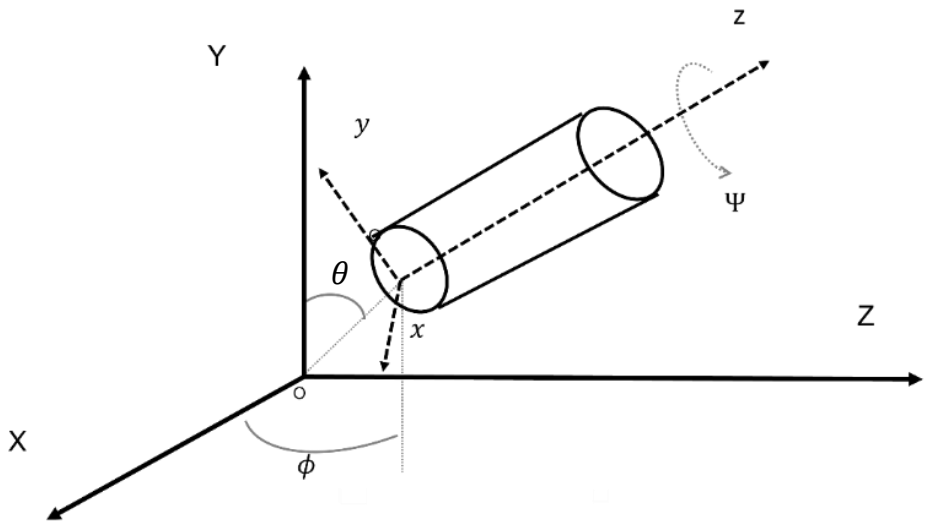

Figure 21: Molecular frame (x, y, z) and orientation of the collagen molecule viewed as a cylinder in the laboratory frame (X, Y, Z). The cylinder is following the z axis.

In the $C_{\infty V}$ symmetry, the number of independent components of the hyperpolarizability tensor is significantly reduced. Under this symmetry, the only non-zero tensor elements are: β_{zzz} and $\beta_{zxx} = \beta_{zyy} = \beta_{xxz} = \beta_{yyz} = \beta_{xzx} = \beta_{yzy}$ in the molecular frame (x, y, z) where the z axis is the symmetry axis of the triple helix, here considered as a cylinder (Figure 21). All other components are symmetry-forbidden and therefore vanish. In an even more reduced approximation, applied to isolated triple helices (Deniset-Besseau et al., 2009), β_{zzz} is taken as the only dominant component, reflecting the strong nonlinear optical response along the helical axis. To relate the components of the hyperpolarizability tensor in these two frames, we employed the Euler's angles (Ψ, Φ, θ) presented in figure 21, to define the orientation of the molecule relative to the laboratory axes.

Using the Euler angles, the components of the hyperpolarizability tensor in the laboratory frame β_{IJK}can be expressed in terms of the molecular frame components β_{ijk}as follows:

$$\beta_{IJK} = \sum_{i,j,k} T_{Ii} T_{Jj} T_{Kk} \beta_{ijk} \tag{33}$$

Here, T represents the transfer matrix, which is a function of the Euler angles. This matrix describes the rotation needed to align the molecular frame with the laboratory frame.

The reduction to $C_{\infty V}$ symmetry implies that all other tensor components, such as those involving mixed indices (e.g., β_{xyz}, β_{xxy} etc.), become zero due to the symmetry constraints. This reduction allows experimental techniques such as SHS to focus on the dominant tensor elements, enhancing the sensitivity and specificity of measurements. This, in turn, leads to more accurate interpretations of collagen's nonlinear optical properties.

In a binary system consisting of a solute (collagen) in a solvent such as water, the SHS intensity arises from the sum of contributions of all molecules within the scattering volume (Deniset-Besseau et al., 2009; Revillod et al., 2021). The scattered intensity can be written as:

$$I(2\omega) = G[N_{solvent}\beta^2_{solvent} + N_{solute}\beta^2_{solute}]I^2(\omega) \quad (34)$$

where G is a constant containing the instrumental scattering geometry and the local-field correction factor. $N_{solvent}$ and N_{solute} stand for the number of molecules in the excitation volume for the solvent and the solute, respectively. The hyperpolarizability terms β represents the orientationally averaged squared second-order polarizabilities, reflecting the molecular response to the applied electric field, and I(ω) is the fundamental input intensity.

For collagen solutions, the laboratory-frame tensor elements β_{YZZ} and β_{ZZZ} make the dominant contributions and the SHS intensity can therefore be expressed as:

$$I(2\omega) = GN < |\beta_{YZZ}|^2 + |\beta_{ZZZ}|^2 > I(\omega)^2 \quad (35)$$

An effective hyperpolarizability is then defined as $\beta^{SHS} =< |\beta_{YZZ}|^2 + |\beta_{ZZZ}|^2 >^{1/2}$, which serves as a compact descriptor of the molecular response to the applied electric field.

An example of SHS spectrum recorded for atelocollagen solution at pH=2 at a fixed fundamental wavelength of 790 nm and an acquisition time of 30s is displayed in figure 22. A broad background was consistently observed, which is likely attributable to fluorescence from trace impurities or weak non-phase-matched contributions along the beam path. This baseline did not interfere with our analysis as the maximum of the SHS signal intensity is around 395nm is then obtained by fitting the spectra with a Gaussian profile. To determine the hyperpolarizability of collagen β_{solute}, we employed the internal reference method. This approach compares the SHS signal of the collagen solution to that of pure water, whose

hyperpolarizability is well established ($\beta_{H_2O} = 0.087 \times 10^{-30}$ esu (Deniset-Besseau et al., 2009). By plotting the SHS intensity as a function of the squared input intensity ($I(\omega)^2$), we obtained linear relationships for both the solvent (slope α) and the collagen solution (slope α') (Figure 23). The solute hyperpolarizability is then isolated:

$$\beta^2_{solute} = \frac{\left(\frac{\alpha'}{\alpha} - 1\right) N_{solvent} \beta^2_{solvent}}{N_{solute}} \tag{36}$$

where $N_{solvent}$ and N_{solute} are the molecular concentrations. This method allows for accurate determination of β_{solute} while minimizing the influence of instrumental fluctuations.

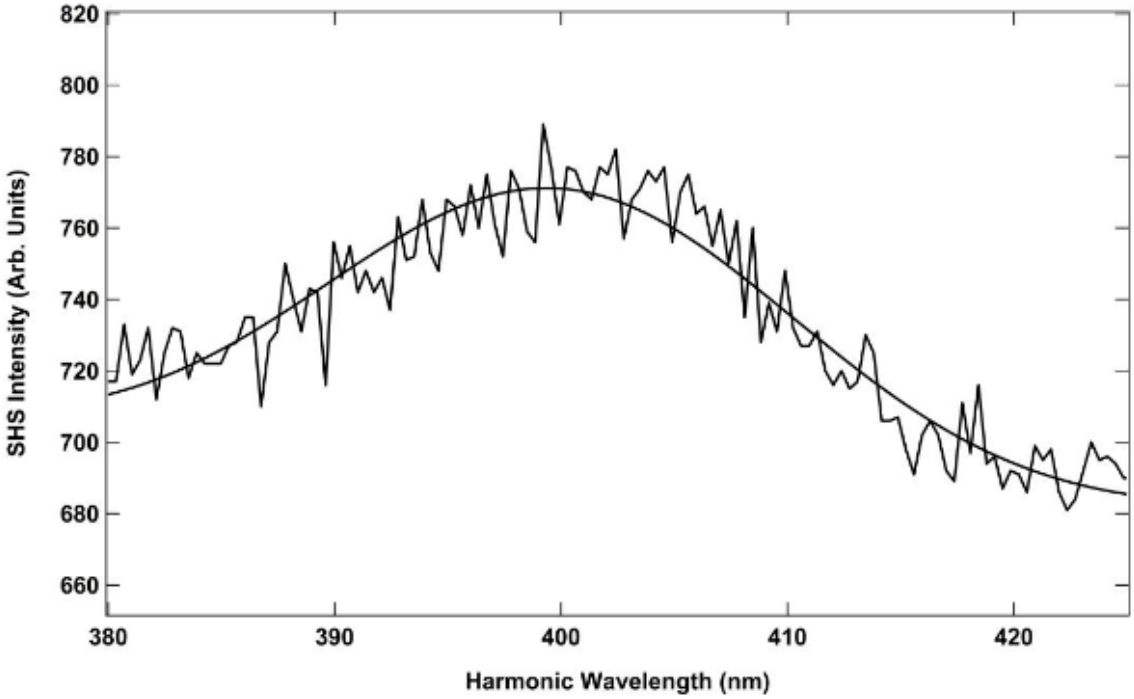

Figure 22: SHS intensity recorded as a function of the wavelength for a fixed fundamental of 790nm and an acquisition time of 30s for Acol solution at pH=2

Once β_{solute} was determined under reference conditions, its evolution under variation of pH was monitored. By comparing SHS intensities from two states, "solution 0" is the initial solution and "solution 1" for the solution across a range of pH we can determine the hyperpolarizability tensor as:

$$\beta_{solution_1} = \beta_{solution_0} \cdot \sqrt{\frac{I_{solution_1}}{I_{solution_0}}} \quad (37)$$

which enables direct tracking of changes in molecular hyperpolarizability as collagen transitions from monomeric to fibrils states.

II.3.2.3 Polarization-Resolved (P-SHS): Depolarization ratio

Beyond the absolute magnitude of hyperpolarizability, polarization-resolved SHS provides additional structural information on the symmetry of the molecules. In this approach, the SHS intensity was measured for two scattered beam polarizations (output): vertical ($\Gamma = 0°$) and horizontal ($\Gamma = 90°$), while rotating the incident polarization angle γ from 0° to 180° (Figure 20). The resulting polarization curves can be described by:

$$I^{\Gamma}(2\omega) = a^{\Gamma}\cos^4\gamma + b^{\Gamma}cos^2\gamma sin^2\gamma + c^{\Gamma}\sin^4\gamma \quad (38)$$

where the coefficients a, b and c are the coefficients used to fit the recorded polarization curve for a given output polarization.

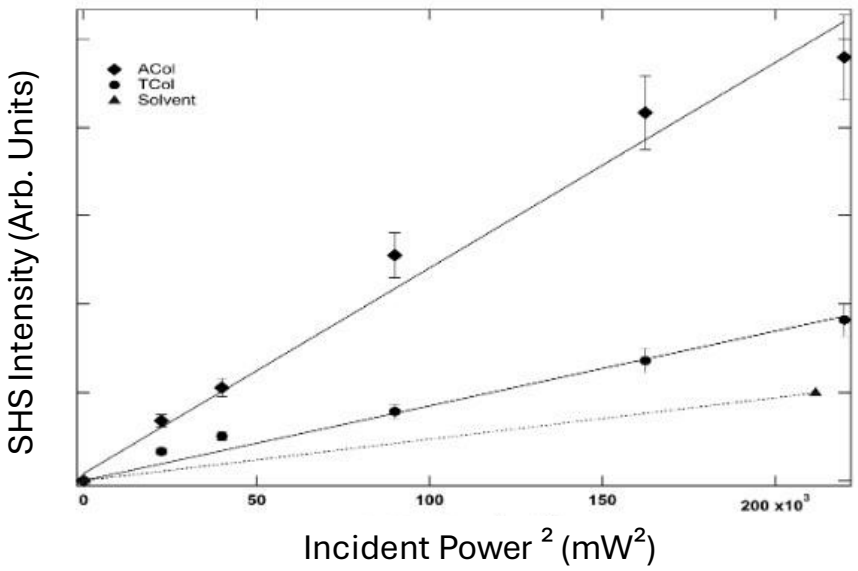

Figure 23: SHS Intensity in function of the square of incident power for the solvent (here H2O) and Tcol and Acol at 2.1 mg/ml and pH 2

From these fits, the depolarization ratio DR known as $DR = c^{\Gamma}/a^{\Gamma}$ can be expressed by using the relationship between a and c and the hyperpolarizability tensor elements in the laboratory frame as:

$$DR = \frac{< |\beta_{ZXX}|^2 >}{< |\beta_{ZZZ}|^2 >} \tag{39}$$

linking the SHS anisotropy directly to the ratio of laboratory frame hyperpolarizability components. These laboratory frame elements themselves are orientationally averaged combinations of molecular frame components (Deniset-Besseau et al., 2009; Bersohn et al., 1966), expressed as:

$$\beta_{ZZZ}^2 = \frac{1}{7}\beta_{zzz}^2 + \frac{6}{35}\,\beta_{zzz}\beta_{zxx} + \frac{9}{35}\beta_{zxx}^2 \tag{40.a}$$

$$\beta_{ZXX}^2 = \frac{1}{35}\beta_{zzz}^2 - \frac{2}{105}\beta_{zzz}\beta_{zxx} + \frac{11}{105}\beta_{zxx}^2 \tag{40.b}$$

Assuming $u = \frac{\beta_{zxx}}{\beta_{zzz}}$, DR can be written as a function of u:

$$DR = \frac{< |\beta_{ZXX}|^2 >}{< |\beta_{ZZZ}|^2 >} = \frac{3 - 4u + 20u^2}{15 + 36u + 72u^2} \tag{41}$$

This parameter provides a sensitive probe of molecular symmetry: a DR value of around 0.11 is indicative of predominantly dipolar behavior, while a DR approaching 0.67 suggests octopolar characteristics (Asselberghs et al., 2006).

Polarization measurements were recorded for collagen solutions at pH=2 and pH=3. Increasing pH promotes oligomerization and the formation of higher-order aggregates. By monitoring the depolarization ratio, we were able to follow this structural evolution: changes in DR values reflect shifts in the relative contributions of β_{zzz} and β_{zxx}, thereby reporting on the emergence of more symmetric, fibrillary assemblies from initially dipolar monomers. To reduce acquisition times, only two key analyzer orientations (corresponding to the maximum and minimum of the vertical polarization curve) were repeatedly measured, which enabled reliable DR estimation without recording a full polar diagram.

II.3.3 Vibrational Sum Frequency Generation

II.3.3.1 Setup

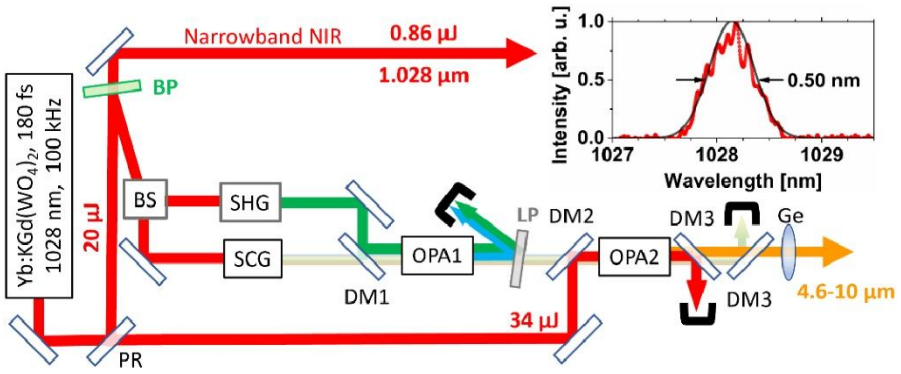

Figure 24: Schematic layout of the light source driving the VSFG spectrometer. PR: partial reflector, BS: beam splitter, SCG: supercontinuum generation unit, SHG: second-harmonic generation unit, OPA1 and OPA2: optical parametric amplifiers, DM1: dichroic mirror, high reflection at 515 nm and high transmission at > 1.1 µm, DM2: dichroic mirror, high reflection at 1028 nm and high transmission at > 1.1 µm, DM3: dichroic mirror, high reflection at 1-1.25 µm and high transmission above 4.5 µm, BP: ultra-narrow bandpass filter, LP: longpass thin-film interference filter, Ge: germanium collimating lens. Half-wave plates are not shown. Inset: The spectrum of the ps-NIR pulses measured using an FTIR spectrometer. The FWHM is 0.50 nm. From Heiner et al., 2024

The VSFG experiments were conducted at the SALSA Laboratory (Humboldt University zu Berlin), under the supervision of Prof. Dr. Zsuzsanna Heiner, where the system was designed, built, and optimized specifically for vibrational spectroscopy on biological interfaces. The system has been continuously developed with several major milestones. An early version was reported by Heiner et al. (2017), followed by a LiGaS7-based mid-IR source described in Heiner et al. (2019). In the present configuration presented in figure 24 by Heiner et al. (2024), the upconversion beam path has been modified providing a more energetic mid-IR output. The system was driven by a solid-state Yb:$KGd(WO_4)_2$ laser (Pharos SP, Light Conversion Ltd.) oscillator-amplifier operating at a central wavelength of 1028 nm, with an energy of 60 µJ and a repetition rate of 100 kHz. In this work, the "visible" upconversion arm is implemented as a narrowband ps-NIR beam at 1.028 µm (Heiner et al. 2024). The output beam was split into two paths:

1. One path, where about 2 W of the laser power is passed through an ultra-narrow bandpass filter centered at 1028nm to produce the narrowband (FWHM: ~0.5 nm) upconversion beam.

   This configuration yields picosecond NIR pulses that serve as the visible upconversion beam in the VSFG process.
2. The reflected part from the filter (20 µj part on the scheme) is split into two parts (cf. BS in Figure 24). One portion is frequency-doubled in a 2 mm BBO crystal (type I phase

matching) to generate 514 nm pump pulses for the optical parametric pre-amplifier (OPA1). The other portion is used to produce a broadband supercontinuum in a YAG crystal, providing the seed for OPA1.

Both beams are then recombined and focused on OPA1, where the 1100-1300 nm spectral region is amplified. The signal from OPA1 then seeds the second OPA stage (OPA2), which is pumped by the remaining (4 W) of the 1028 nm fundamental. OPA2, based on LiGaS7 crystal, generates tunable MIR pulses in the range of 1000-2200 cm^{-1}.

The ps-NIR and MIR beams are spatially and temporally overlapped on the sample surface using:

- A motorized delay stage for precise temporal alignment
- A mirror-based beam recombination system for spatial superposition

To suppress atmospheric interferences (especially from $H_2O$and CO_2 in the MIR), the beam path includes a custom-built dry-air purged enclosure surrounding all critical components of the MIR line. The visible and MIR pulses were focused onto the sample and overlapped temporally and spatially. The angles of incidence were 68° and 57°, respectively. The VSFG signal was collected in reflection geometry by a 320 mm imaging spectrometer equipped with a Peltier-cooled CCD. The generated VSFG signal is collected in two spectral windows, 1000-1400 cm^{-1} and 1500-1700 cm^{-1}, in ppp, ssp and psp polarization combinations (the order of polarizations corresponds to SFG, narrowband NIR and MIR beams, respectively), with an acquisition time of 50 s per spectrum. All measurements were performed at different sample positions to account for structural heterogeneity in the probed materials. All spectra were:

- Calibrated in frequency using polystyrene film references
- Background-subtracted by acquiring a spectrum with the MIR beam blocked
- Normalized to the spectrally flat non-resonant VSFG response of a gold (111) surface, which provides a reproducible reference response for correcting the instrument function and ensuring comparability of spectra across the measured window.

II.3.3.2 Spectra treatment and analysis

The output of the VSFG experiment consists of a set of intensity spectra corresponding to the sum frequency signal generated, recorded as a function of the wavenumber. These raw spectra contain both the vibrational signature of the probed interfacial molecules and additional

background contributions that must be addressed prior to quantitative interpretation. VSFG does not rely on spontaneous emission from excited states as presented in chapter I.3.5, and results as:

$$I_{SFG}(\omega) \propto \left|\chi^{(2)}_{eff}(\omega)\right|^2 I_{vis} I_{IR} \tag{42}$$

Where $\chi^{(2)}_{eff}$ combines resonant and non-resonant contributions. The non-resonant background (NRB) originates from the instantaneous electronic response of the medium. It is coherent with the resonant vibrational contributions, leading to constructive or destructive interference that can distort spectral line shapes. This NRB cannot be eliminated by simple subtraction, it is intrinsic to the VSFG process and must be explicity included during spectral modeling as a complex term as it will be described. In addition to the intrinsic NRB, the signal also contains additive instrumental counts (dark current, readout). These were corrected by subtracting a background with the MIR beam blocked. This ensures that only the genuine VSFG response remains.

$$I_{diff}(\omega) = I_{raw}^{VIS+IR}(\omega) - I_{raw}^{VIS\ ONLY}(\omega) \tag{43}$$

Then, to ensure signal comparability, the intensity of each difference spectrum was divided by the corresponding acquisition time. This normalization converted all datasets into counts per second, compensating for variations in integration time that might arise between spectral regions or sample points:

$$I_{norm_{time}}(\omega) = \frac{I_{diff}(\omega)}{t_{acq}} \tag{44}$$

with t_{acq}corresponding to the acquisition time. This step is essential when averaging spectrum or comparing regions acquired with different acquisition durations. To correct the instrumental response, each sample spectrum was normalized to a reference spectrum measured on a bare gold (111) surface. Prior to normalization, the gold spectrum was corrected for the measured frequency-dependent MIR power at the sample:

$$I_{ref-corr}(\omega) = \frac{I_{ref}(\omega)}{P_{IR}(\omega)} \tag{45}$$

The final normalized spectrum for each area of the sample was obtained by dividing the time-corrected difference spectrum by this corrected reference:

$$I_{final}(\omega) = \frac{I_{norm-time}(\omega)}{I_{ref-corr}(\omega)} \tag{46}$$

This normalization step ensures that the resulting spectra reflects the sample's intrinsic VSFG response and is independent of the instrumental transfer function or MIR spectral profile. For each spectral region, several spectra were recorded at different sample locations and averaged:

$$I_{avg}(\omega) = \frac{1}{N}\sum_{i=1}^{N} I_{final,i}(\omega) \tag{47}$$

For spectral analysis, the effective nonlinear susceptibility was expressed as a coherent sum of a complex non-resonant background and Lorentzian-shaped resonances:

$$\chi^{(2)}_{eff}(\omega) = \chi^{(2)}_{NR} e^{i\Phi} + \sum_j \frac{A_j}{\omega - \omega_j + i\Gamma_j} \tag{48}$$

where $\chi^{(2)}_{NR} e^{i\Phi}$ represents the complex non-resonant contribution, A_j is the amplitude of the j-th vibrational mode, ω_j its central frequency and Γ_j its linewidth (half-width at half maximum).

In practice, the experimental spectra were analyzed by fitting the model of Eq. (47) to the normalized data. During this fitting process, the amplitude $\chi^{(2)}_{NR}$ and phase ϕ of the non-resonant contribution were treated as global free parameters. For each vibrational mode j, the amplitude A_j, central frequency ω_j, and linewidth Γ_j were adjusted. This procedure allows the non-resonant background to be explicitly modeled and separated from the resonant response, ensuring that the extracted peak parameters correspond only to the vibrational modes of the sample. After fitting, the non-resonant background term can be mathematically separated. This allows reconstruction of the purely resonant contribution as:

$$I_{SFG}(\omega) \propto \left| \sum_j \frac{A_j}{\omega - \omega_j + i\Gamma_j} \right| \tag{49}$$

After normalization and global fitting with the model described in Eq 48 and 49, selected spectral regions of interest were further analyses using Gaussian peak fitting. The fitting procedure was performed using OriginPro (OriginLab, USA), which employs a non-linear least-squares algorithm based on the Levenberg-Marquardt method to optimize the fit parameters. In this context, the amplitude and linewidth were either freely adjusted or constrained within reasonable bounds depending on prior spectral knowledge, while the peak center was always determined by the fitting process and served as the main indicator for vibrational assignment. In practice, the number of Gaussian components used for the fitting depended on the spectral region. For the spectral region from 1200 to 1450 cm^{-1}, which encompasses the amide III band together with several vibrational modes from amino-acid side chain, 10 Gaussian components were fitted. For each fitted peak, the algorithm yielded the amplitude, central frequency and linewidth. This dense spectral zone required detailed decomposition to resolve subtle conformational signatures of the collagen matrix. Conversely, the amide I region (≈ 1600-1700 cm^{-1}), dominated by the C=O stretching mode and commonly used to probe secondary structure, was modeled with only 2-3 peaks, as it exhibited fewer resolvable features and peaks under our experimental conditions. Despite its lower spectral complexity, this region remained crucial for identifying helix-related conformational changes in collagen.

II.3.3.3 Determination of angle θ

As described before, the measured VSFG intensity for a given polarization combination can be expressed as:

$$I_{VSFG}(\omega) \propto \left|\chi^{(2)}_{eff}(\omega)\right|^2 I_{vis} I_{IR} \tag{48}$$

Where I_{vis} and I_{IR} are the intensities of the input visible and IR beams, and $X_{eff}^{(2)}$ is the effective second-order susceptibility, given by:

$$X^{(2)}_{eff} = \sum_{ijk} L_i(\omega_{VSFG}) L_j(\omega_{vis}) L_k(\omega_{IR}) \chi^{(2)}_{ijk} \tag{49}$$

Here $L_i(\omega)$ are the Fresnel factors, accounting for field transmission and refraction at the interface, where i represent VSFG, VIS and MIR, and $\chi^{(2)}_{ijk}$ are the macroscopic tensor components of susceptibility (Lambert e al., 2005). However, in VSFG the measured signal depends not only on the intrinsic molecular susceptibility tensor but also on the choice of

polarization. Effective susceptibility corresponds to a Fresnel-weighted projection of the tensor elements onto the incident and emitted field polarizations. Each polarization combination (ssp, sps, pss and ppp) therefore probes different tensor components, allowing selective access to specific element of $\chi^{(2)}$.

For the polarization that we used, the effective susceptibilities can be written as (Zhuang et al., 1999, Nguyen et al., 2009):

$$\chi^{(2)}_{eff,SSP} = L_{yy}(\omega_{VSFG})L_{yy}(\omega_{vis})L_{zz}(\omega_{IR})sin\alpha_{IR}\chi^{(2)}_{yyz} = F_{yyz}\chi^{(2)}_{yyz} \quad (50.1)$$

$$\chi^{(2)}_{eff,PSP} = L_{zz}(\omega_{VSFG})L_{yy}(\omega_{vis})L_{yy}(\omega_{IR})sin(\alpha_{VSFG})\cos(\alpha_{IR})\,\chi^{(2)}_{zyx} - L_{xx}(\omega_{VSFG})L_{yy}(\omega_{vis})L_{zz}(\omega_{IR})\cos(\alpha_{SFG})\sin(\alpha_{IR})\,\chi^{(2)}_{xyz} \quad (50.2)$$

$$\begin{aligned}\chi_{eff,PPP} = {} & -L_{xx}(\omega_{VSFG})L_{xx}(\omega_{vis})L_{zz}(\omega_{IR})cos\alpha_{VSFG}\cos\alpha_{vis}sin\alpha_{IR}\chi^{(2)}_{xxz} \\ & - L_{xx}(\omega_{VSFG})L_{zz}(\omega_{vis})L_{xx}(\omega_{IR})cos\alpha_{VSFG}\sin\alpha_{\mathrm{vis}}cos\alpha_{IR}\chi^{(2)}_{zxz} \\ & + L_{zz}(\omega_{VSFG})L_{xx}(\omega_{vis})L_{xx}(\omega_{IR})sin\alpha_{VSFG}cos\alpha_{vis}\cos\alpha_{\mathrm{IR}}\chi^{(2)}_{zxx} \\ & + L_{zz}(\omega_{VSFG})L_{zz}(\omega_{vis})L_{zz}(\omega_{IR})sin\alpha_{VSFG}sin\alpha_{vis}sin\alpha_{IR}\chi^{(2)}_{zzz} \\ & = F_{xxz}\chi^{(2)}_{xxz} + F_{xzx}\chi^{(2)}_{xzx} + F_{zxx}\chi^{(2)}_{zxx} + F_{zzz}\chi^{(2)}_{zzz} \qquad (50.3)\end{aligned}$$

Here $\alpha_{VSFG}, \alpha_{vis}, \alpha_{IR}$ are the incident angles of each beam. The factors F_{ijk} represent the combined Fresnel and geometric weights applied to each susceptibility element. With this formulation we can distinguish single-polarization schemes such as ssp, sps or pss isolate individual tensor components, whereas the ppp configuration yields a weighted combination of four distinct elements. Therefore, ppp spectra are generally richer in structural information but also require more elaborate analysis to disentangle contributions. The Fresnel factors account for the discontinuity of the electromagnetic fields across dielectric boundaries and ensure that the effective field acting on the interfacial molecules is properly described. The Fresnel factors $L_{ii}(\omega)$ (with $i = x, y, z$) are defined as:

$$L_{xx}(\omega_i) = \frac{2n_1(\omega_i)\cos(\gamma_i)}{n_1(\omega_i)\cos(\gamma_i) + n_2(\omega_i)\cos(\alpha_i)}, \quad (51.1)$$

$$L_{yy}(\omega_i) = \frac{2n_1(\omega_i)\cos(\alpha_i)}{n_1(\omega_i)\cos(\alpha_i) + n_2(\omega_i)\cos(\gamma_i)}, \quad (51.2)$$

$$L_{zz}(\omega_i) = \frac{2n_1(\omega_i)\cos(\alpha_i)}{n_2(\omega_i)\cos(\alpha_i) + n_{1(\omega_i)\cos}(\gamma_i)} \frac{n_1^2(\omega_i)}{n_1'^2(\omega_i)} \tag{51.3}$$

Here $n_1(\omega_i)$ and $n_2(\omega_i)$ denote the refractive indices of the incident and transmitted bulk media at frequency ω_i while $n_1'(\omega_i)$ is the refractive index of the interfacial layer. The angles α_i and γ_i correspond to the incidence and refraction angles (with respect to the surface normal), determined through Snell's law:

$$n_1(\omega_i)\sin(\alpha_i) = n_2(\omega_i)\sin(\gamma_i) \tag{52}$$

Under the thin-sheet local-field approximation, the effective interfacial index used in the L_{zz}factor can be written as:

$$n_1'(\omega_i) = n_1(\omega_i)n_2(\omega_i)\sqrt{\frac{6 + \mathrm{n}_2(\omega_i)^2 - \mathrm{n}_1(\omega_i)^2}{4\mathrm{n}_2(\omega_i)^2 + 2\mathrm{n}_1(\omega_i)^2}} \tag{53}$$

Experimentally we determine the $\chi_{eff}^{(2)}$that we've defined as:

$$\chi_{eff}^{(2)} = \sum_{ijk} F_{ijk}\chi_{ijk}^{(2)} \tag{54}$$

To retrieve the intrinsic macroscopic elements from the measured effective response, we apply the Fresnel correction (i.e., invert the mapping):

$$\chi_{ijk}^{(2)} = \frac{\chi_{eff,pol}^{(2)}}{F_{ijk}} \tag{55}$$

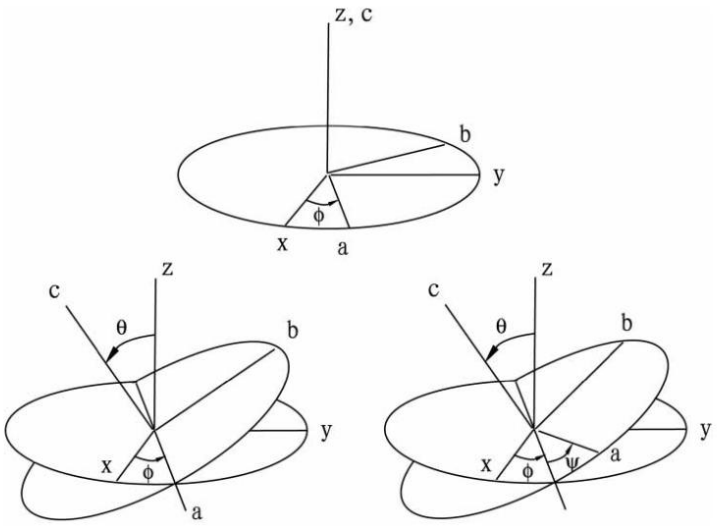

Figure 25: The Euler transformation between the laboratory coordinates x, y, z and the molecular coordinate a, b, c (or x', y' z') through three Euler angles (ϕ, θ, ψ)

The laboratory susceptibility is the orientational average of the molecular hyperpolarizability tensor $\beta_{i'j'k'}$ rotated into the lab frame by Euler transformation (Figure 25):

$$\chi_{ijk}^{(2)} = N_s \sum_{i'j'k'} < R_{ii'} R_{jj'} R_{kk'} > \beta_{i'j'k'}^{(2)} \tag{56}$$

with Ns the surface number density, R_{ii} are direction cosines from the molecular frame (i', j', k') to the lab frame (i, j, k), parameterized by Euler transformation. Similar to the SHS measurements, for collagen we use a molecular axis along the fibril axis under the symmetry $C_{\infty v}$, resulting in only two independent hyperpolarizability components remaining: β_{zzz} and $\beta_{zxx} = \beta_{xxz} = \beta_{xzx}$.

The explicit evaluation of the orientational averages involves integrating over the azimuthal (φ) and twist (ψ) Euler angles. This integration removes cross-terms and yields numerical prefactors in front of the remaining angular functions. These simplified expressions are the ones we use to determine the tilt angle θ:

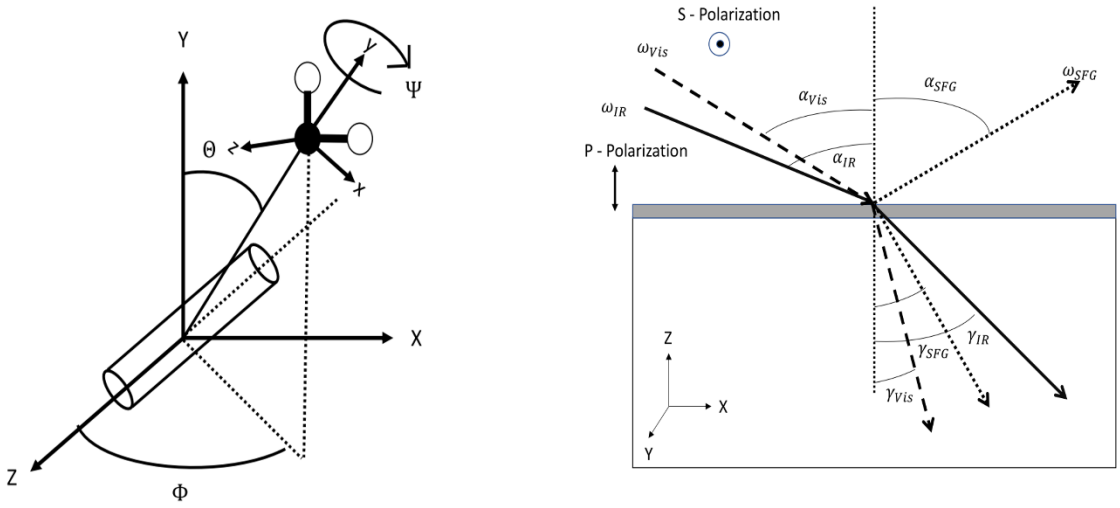

Figure 26: Schematic representation of the VSFG experiment and molecular orientation. (Left) Definition of molecular coordinates and Euler angles (Θ, φ, ψ) describing the orientation of a CH_2 group with respect to the laboratory frame (x, y, z). (Right) Experimental geometry of VSFG: incident mid-IR (ω_{IR})and narrowband visible (ω_{vis}) beams are overlapped at the sample interface, generating a sum-frequency signal (ω_{SFG}).

$$\chi^{(2)}_{XZX} = 1.25\,cos^3(<\theta>)\,sin(<\theta>)\,\beta_{zxx} - 0.5\,cos^3(<\theta>)\,sin(<\theta>)\,\beta_{zzz} - 0.25\,cos(<\theta>)\,sin(<\theta>)\,\beta_{zxx} + 0.5\,cos(<\theta>)\,sin(<\theta>)\,\beta_{zzz} \quad (57.1)$$

$$\chi^{(2)}_{XXZ} = 1.25\,\cos^3(<\theta>)\,\sin(<\theta>)\,\beta_{zxz} - 0.5\,\cos^3(<\theta>)\,\sin(<\theta>)\,\beta_{zzz} - 0.25\,\cos(<\theta>)\,\sin(<\theta>)\,\beta_{zxx} + 0.5\,\cos(<\theta>)\,\sin(<\theta>)\,\beta_{zzz} \quad (57.2)$$

$$\chi^{(2)}_{ZXX} = 1.25\,cos^3(<\theta>)\,sin(<\theta>)\,\beta_{zxx} - 0.5\,cos^3(<\theta>)\,sin(<\theta>)\,\beta_{zzz} - 0.75\,cos(<\theta>)\,sin(<\theta>)\,\beta_{zxx} + 0.5\,cos(<\theta>)\,sin(<\theta>)\,\beta_{zzz} \quad (57.3)$$

$$\chi^{(2)}_{ZZZ} = 2.5\,cos^3(<\theta>)\,sin(<\theta>)\,\beta_{zxx} + cos^3(<\theta>)\,sin(<\theta>)\,\beta_{zzz} + 2.5\,cos(<\theta>)\,sin(<\theta>)\,\beta_{zxx} \quad (57.4)$$

$$\chi^{(2)}_{ZYX} = 0.25\,cos^2(<\theta>)\,sin(<\theta>)\,\beta_{yxz} - 0.5\,cos^2(<\theta>)\,sin(<\theta>)\,\beta_{zyx} - 0.25\,sin(<\theta>)\,\beta_{yxz} \quad (57.5)$$

$$\chi^{(2)}_{ZYX} = 0.75\,cos^2(<\theta>)\,sin(<\theta>)\,\beta_{xyz} - 0.25\,\sin(\theta)\,\beta_{xyz} \quad (57.6)$$

These equations highlight that only two microscopic hyperpolarizabilities contribute. As such, the VSFG analysis effectively reduces to solving for the single orientational parameter θ, which governs the angular dependence of the macroscopic susceptibilities under different polarization combinations. The tilt angle (θ) here corresponds to the angle of the vibrational band with the surface normal as presented in figure 26.

II.3.4 Atomic Force Microscopy (AFM)

AFM images were recorded in air using an Asylum MFP-3D head equipped with a Molecular Force Probe 3D controller (Asylum Research, Santa Barbara, CA, USA). Tapping (AC) mode was selected as imaging mode, and rectangular silicon nitride cantilevers from Olympus (OMCL- AC160TS, Tokyo, Japan) with a nominal force constant 26N/m and tip radius of <10 μm High-resolution topography measurements have been performed and both height, amplitude and phase images were recorded.

Chapter III

--

Results and Discussion

III. Results and discussion

Imaging of spinal cord tissue was performed using MPM, providing structural information across the fibrotic lesion. The eGFP signal, expressed in astrocytes, was visualized using 2-photon excited fluorescence (2PEF) and is displayed in green pseudo-color. Collagen fibers were imaged via SHG, shown in red. All data acquisition was conducted on longitudinal spinal cord sections to enable a rostro-caudal assessment of the lesion architecture and to capture the spatial evolution of the fibrotic scar.

III.1 Bright field images

The first step of the analysis consisted of a qualitative visual examination of the injured spinal cord tissue using bright-field microscopy, which allows the overall morphology of the sample to be evaluated without relying on fluorescence or nonlinear contrast. This approach was used to identify the lesion site and determine its extension. At 1-week post-injury (1 wpi), a pronounced cavity was clearly visible at the lesion epicenter (Figure 27). This empty space corresponded to the zone of initial tissue destruction, where neither gray nor white matter continuity was preserved. The absence of bridging tissue at this stage indicated that no structural reconstruction had yet taken place and the lesion margins appeared sharply demarcated from the surrounding intact tissue.

By 2 wpi, the cavity was no longer open (Figure 27). The lesion area was filled, suggesting that some form of tissue closure had occurred. However, the architecture remains abnormal, with a marked inward folding of the white matter toward the lesion core. The lesion boundaries were still distinct, although less abrupt than at 1 wpi, reflecting the progression of cellular and extracellular matrix remodeling (i.e. glial and fibrotic scarring).

At later time, 4 and 6 wpi, the lesion site remained clearly visible in bright-field images (Figure 27). Compared to 2 wpi, the overall boundaries of the lesion appeared slightly more extended, primarily due to a broader inward folding of the surrounding white matter toward the lesion core. These are qualitative observations and we do not infer morphological stability from bright-field alone. The persistent cavity-like deformation and altered curvature of the surrounding tissue reflected chronic architectural changes, which would later be analyzed in greater detail through multiphoton imaging to assess the organization of collagen fibers within and around the scar.

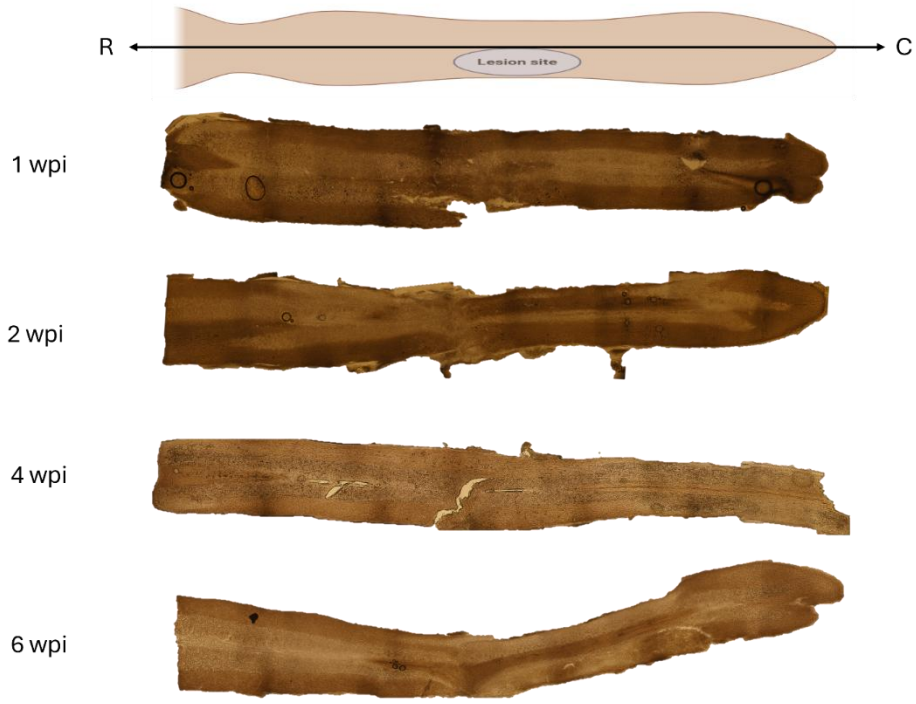

Figure 27: Bright-field images of 50 µm thick longitudinal spinal cord sections showing the macroscopic appearance of the lesion site at different post-lesion times. (Top) Schematic representation of a longitudinal sectioned spinal cord with the lesion site highlighted. The Rostral (R) and caudal (C) orientations are indicated. Representative bright-field images at 1, 2, 4 and 6 wpi, oriented rostral to cauda (left to right).

III.2 SHG Imaging

On longitudinal sections acquired at 1 wpi, MPM allowed reliable localization of the lesion in 2PEF channel (Figure 28). The lesion was located in the lateral portion of the cord and appeared as a well-defined discontinuity in the tissue architecture. In 2PEF channel the signal was primarily associated with the membranes of residual tissue elements and with autofluorescence from the surrounding parenchyma. Astrocytes, identifiable through their intrinsic eGFP expression, were present around the lesion margins (Figure 28.B). The fluorescent signal distribution remained relatively homogeneous in the spared regions, with no localized hyperfluorescence indicative of dense cellular accumulation. SHG imaging failed to reveal any collagen-specific signal within the injured tissue at 1 wpi, indicating an absence (or level below detection) of fibrillar collagen. At this stage, the lesion site is dominated by cellular and membrane-associated elements, with connective tissue reorganization expected to develop in the following weeks. These observations suggest that, at 1 wpi, the fibrotic scar is still in the initial stages of its evolution in Aldh1l1 transgenic mice (Swiss background), before the establishment of a chronic fibrotic scar.

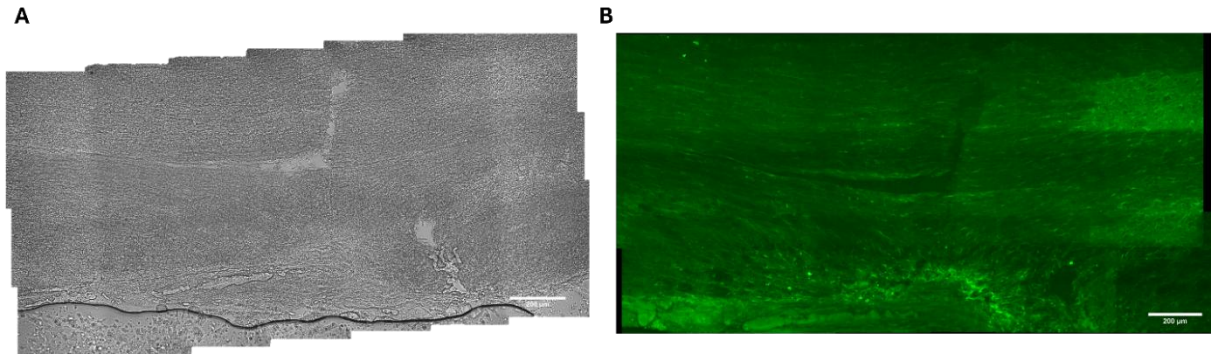

Figure 28: MPM acquisition on longitudinal sections of injured spinal cord at 1wpi. In (A) a bright field image showing the imaged region, with the lesion site located in the lower part of the section. In (B) 2PEF signal (green) highlighting tissue autofluorescence and eGFP expressed in astrocytes and the SHG channel (red) showing no detectable fibrillar collagen at this stage. Scale bar is 200 µm with the field of view centered at the lesion border.

After localizing the lesion in bright field, we proceeded with multiphoton microscopy combining SHG and 2PEF. The aim of this approach was to monitor, *in situ* and without exogeneous labeling, the spatiotemporal dynamics of fibrillar collagen formation within and around the lesion site at different post-injury stages. All acquisitions were performed on mice longitudinal spinal cord sections (50 µm thick), enabling direct visualization of the rostrocaudal axis and facilitating the assessment of tissue continuity across the lesion. This geometry also optimizes detection of rostrocaudal collagen spread and potential asymmetries between rostral and caudal segments. Imaging conditions (laser power, wavelength, objective) were kept the most constant possible across all samples and timepoints to ensure that differences in signal intensity reflected biological variation rather than instrumental drift.

At 1 wpi, no SHG-detectable fibrillar collagen was observed in the lesion core of perilesional zones. Within the sensitivity of our setup, this suggests that the fibrotic scar has not yet consolidated. In figure 29 we present typical MPM images of SCI at 2, 4 and 6 wpi, summarizing the progressive appearance, extension and organization of collagen fibers. At 2 wpi, the 2PEF channel (green) showed that the overall spinal cord architecture remained preserved outside the lesion, with no major structural disruptions in distant tissue regions.

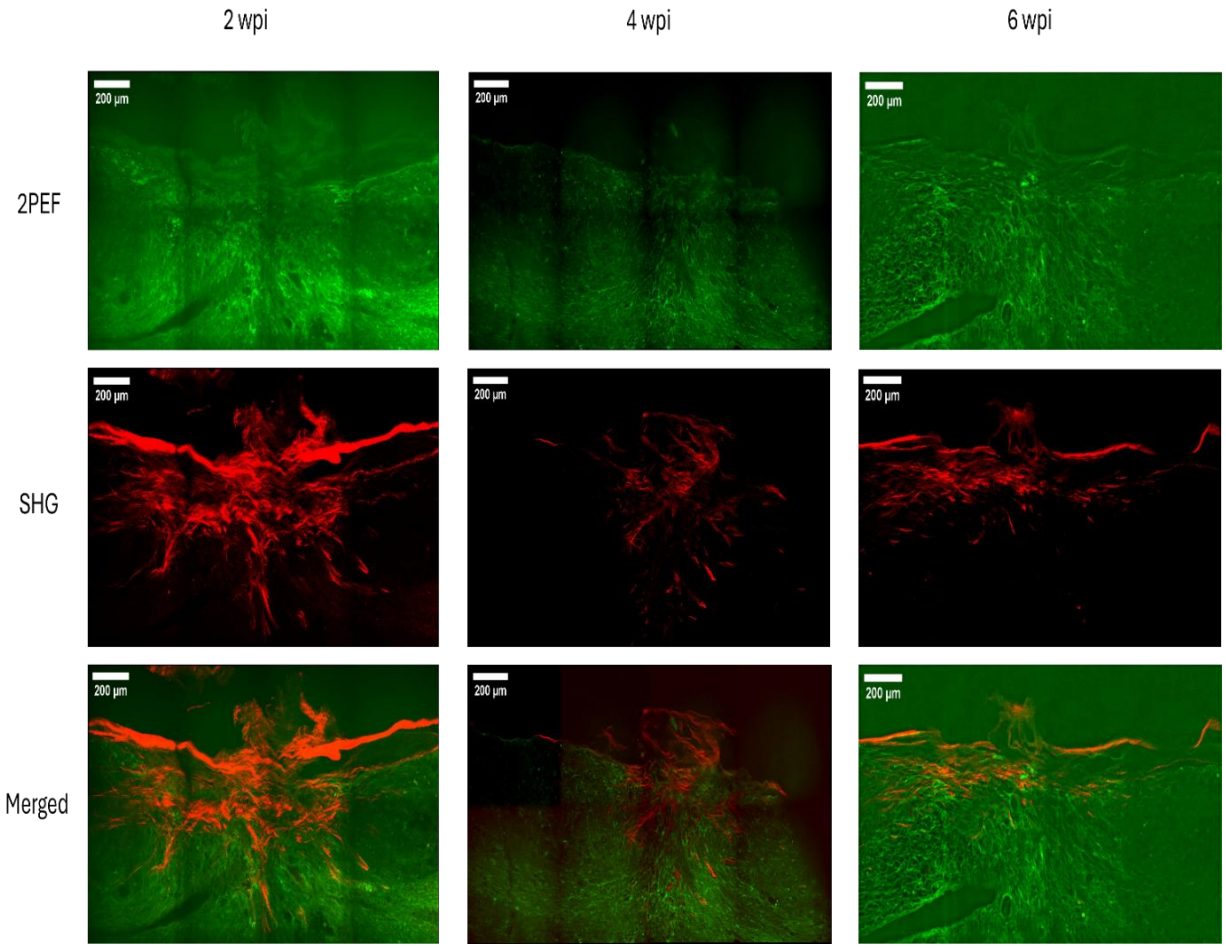

Figure 29: Evolution of collagen formation around the lesion site over time following spinal cord injury, revealed by MPM imaging on 50 µm thick longitudinal sections. For each timepoint, the first row shows the 2PEF channel (green), combining tissue autofluorescence and eGFP expressed in astrocytes; the second row shows the SHG channel (red) revealing fibrillar collagen; the third row presents the merged 2PEF and SHG signals. Left column: 2 wpi, middle: 4wpi, right column: 6wpi. Scale bars: 200 µm.

Lesion zone itself was clearly identifiable, marked by reduced structural organization and a visible invagination of the tissue surface at the lesion site. In the SHG channel (red), collagen was detected for the first time at 2 wpi, appearing as short fibers, irregularly oriented and lacking large-scale organization. Notably, collagen density seems to be greater on the rostral side compared to the caudal side. The lesion core presents a dense but highly disorganized meshwork. Fiber bundles extended in multiple directions (rostrocaudal axis and ipsilateral-contralateral orientation) with no evidence of a dominant alignment pattern visible. This multidirectional arrangement suggests early, unstructured ECM deposition within the injury core, likely reflects the initial invasion of fibroblasts. While collagen density was slightly greater at the rostral border compared to the caudal side, the central lesion area also contained numerous intersecting fibers, creating a heterogeneous texture without clear

compartmentalization. This disorganized stage has been observed in rodent SCI models before the onset of fiber compaction and alignment (Bradbury et al., 2019; Manesco et al., 2023). Importantly, the timing is model- and strain- dependent, in the mouse line used by Manesco et al. (2023), SHG-detectable fibrillar collagen was already present at 1 wpi. The lesion-surrounding meninges exhibited particularly bright SHG signal, consistent with the high density of aligned collagen in the dural membranes.

By 4 wpi, the 2PEF channel continued to show a pronounced invagination at the lesion site. The lesion-adjacent parenchyma displayed numerous 2PEF-dark region apparent “holes” in the fluorescence readout, suggesting focal areas of degradation. These holes were absent at 2 wpi. The surrounding parenchyma, particularly along the rostrocaudal axis, remained largely intact but exhibited subtle morphological irregularities. In the SHG channel, collagen distribution was more extensive than at 2 wpi but showed no dramatic increase in overall density. The strongest signals remained at the lesion borders, with some fibers extending into the lesion zone itself. Fiber organization at the lesion interface was more complex, with tortuous and interwoven bundles. Rostral and caudal SHG intensity appeared somewhat reduced compared to 2 wpi, suggesting possible remodeling or reorganization rather than less collagen in these regions. These structural changes mark a shift from focal apparition of fibers towards partial infiltration and remodeling of the collagen network.

At 6 wpi, the 2PEF channel revealed a lesion site still characterized by invagination, but with far more numerous 2PEF-dark region throughout the tissue, both near and distant from the lesion. This suggests widespread microstructural disruption within the rostro-caudal axis. The tissue appeared more fragmented and irregular overall, with eGFP-positive astrocytes still concentrated at the lesion periphery. The SHG channel displayed a clear evolution compared to earlier stages. Collagen was observed not only at the lesion interface but also extending rostrally and caudally beyond the lesion borders, with comparable signal intensity in both directions. Within the lesion zone itself, collagen is still abundant and is comparable qualitatively to collagen deposition at 4 wpi. The fibers showed more pronounced alignment, often oriented parallel to the rostro-caudal axis. This stage is consistent with a transition to the end of the deposition phase, characterized by both the stabilization and the expansion of the collagen network, potentially reinforcing the physical barrier of the chronic scar.

Our SHG observations described above clearly suggest a temporal progression of collagen fibers following spinal cord injury: no detectable fibrillar collagen at 1 wpi, rapid and widespread appearance by 2 wpi and progressive remodeling and possible extension up to 6 wpi. While such visual inspection provides valuable insight into the spatial and morphological evolution of the fibrotic scar, it remains inherently subjective and limited in its ability to detect subtle changes. In order to quantify these changes and allow robust statistical comparison between timepoints and various regions of the lesioned spinal cord, we next applied computational image analysis methods to extract numerical descriptors of collagen organization from the acquired SHG datasets.

III.2.1 Fingerprint algorithm results

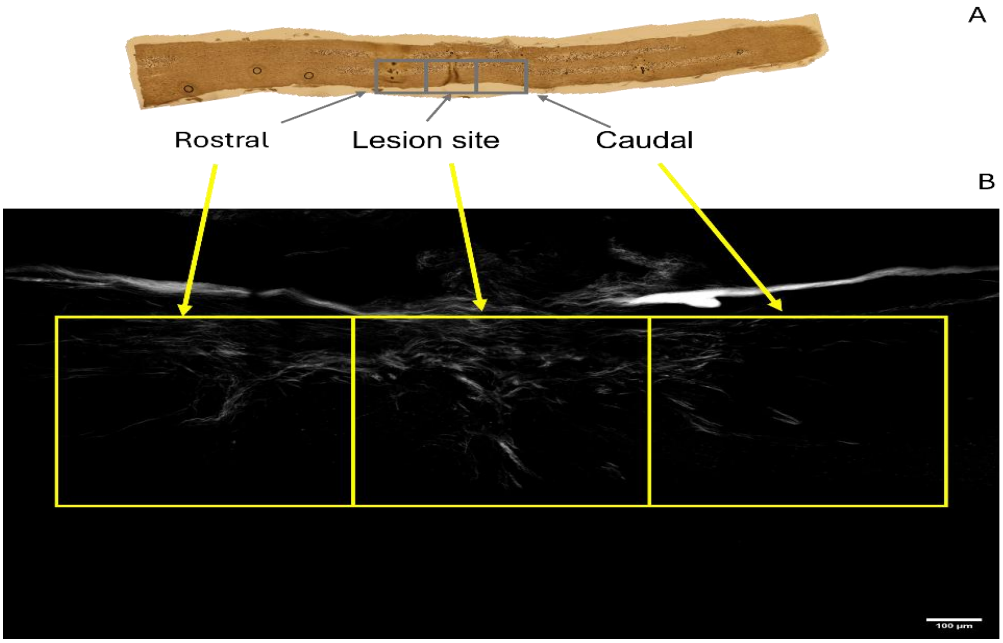

Figure 30: Definition of the ROI for analysis. A) Bright-field image of the spinal cord at 6 wpi, with each ROI determined. The lesion site was identified first, the rostral and caudal regions defined as the areas directly adjacent to the lesion. B) Representative SHG image acquired on a 50 µm thick longitudinal section at 6 wpi. The defined regions are presented as the yellow square (same size for each region) and deliberately excluded the collagen from the meningeal membranes (visible as a very strong SHG intensity), since this highly aligned collagen would create artifacts in the analysis.

We've used the Fingerprint method (Manesco et al., 2023) for the SHG data analysis, an algorithm developed in our laboratory allowing to quantify the fibers' orientation and dispersion in two dimensions. The analysis was performed separately for three distinct anatomically defined regions (Figure 30): the rostral, the lesion site and the caudal regions. This approach allows to assess whether the spatial trends of collagen fibers organization, observed in the SHG images occur uniformly across the lesion environment or follow a rostrocaudal gradient. To

avoid biasing the measurements, meningeal membranes were systematically excluded from the analysis. These structures are composed of densely packed and highly aligned collagen fibers that generate a strong SHG signal but do not reflect the scar remodeling process. Including them would artificially reduce the measured dispersion and overestimate the degree of organization in those regions. Results are presented with a minimum of N=3 animals, for each animal, two tissue sections were acquired and analyzed, giving at least six samples per group. Within each section, planar 2D measurements were performed across at least 15 imaging planes in depth, yielding a minimum of 90 data points per histogram presented for each time point. We first analyzed fiber tortuosity across the three defined regions (rostral, lesion site, caudal). This parameter provides insight into the degree of fiber waviness and therefore indirectly reflects the level of organization within the collagen network.

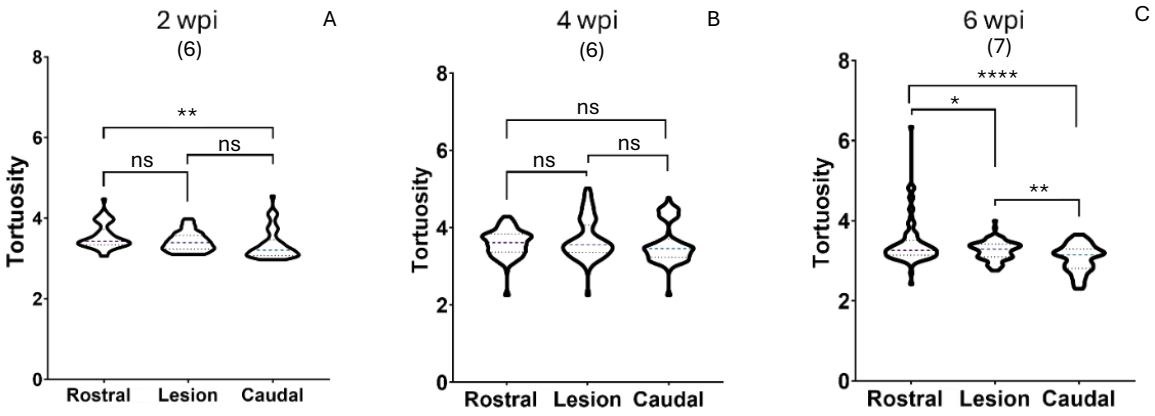

Figure 31: Tortuosity of collagen fibers across spinal cord regions at different post-injury timepoints. Data are presented as violin plots, which represent the distribution of collagen fiber tortuosity values in each zone. The horizontal dashed line indicates the median.

Figure 31 presents the results of tortuosity analysis by timepoint with a violin plot, A violin plot displays the full distribution of the data, where the width of the violin reflects the estimated probability density across values. Here, the central line indicates the mean, and the two thinner lines represent ±1 standard deviation, providing a compact view of both the distribution shape and overall variability. This representation is useful to highlight heterogeneit. At 2 wpi (Figure 31.A), there was no significant difference in tortuosity between the rostral region and the lesion, nor between the lesion and caudal region, indicating that the collagen fibers in these regions are similarly wavy. A significant difference emerged between the rostral and caudal regions, suggesting a different behavior of fibers between these regions. From the violin plots, we infer multiple populations at 2 wpi in rostral and caudal regions, while the lesion site presents only

one main population. At 4 wpi (Figure 31.B), tortuosity values converged across the 3 regions, with no significant inter-zonal differences. Nonetheless, the distributions indicated the emergence of two distinct populations in the caudal region as well as at the lesion site, potentially reflecting heterogeneous remodeling activities within these compartments. This heterogeneity may correspond to a coexistence of more straightened fibers alongside newly deposited tortuous ones. At 6 wpi (Figure 31.C), the analysis revealed more pronounced spatial differences. The highest median tortuosity was observed at the lesion site, exceeding values in both the rostral and caudal regions. This suggests that fibers at the core of the lesion remain more irregular and tortuous even at late stages of scar maturation, possibly due to persistent remodeling or ongoing fibers formation. In contrast, the caudal region showed a shift to lower tortuosity values, consistent with straighter fibers, while the rostral region exhibited intermediate values. Importantly, multiple subpopulations persisted across all regions, showing the heterogeneous nature of the remodeling process. After comparing tortuosity values across regions at a given timepoint, we next analyzed the temporal progression within each zone.

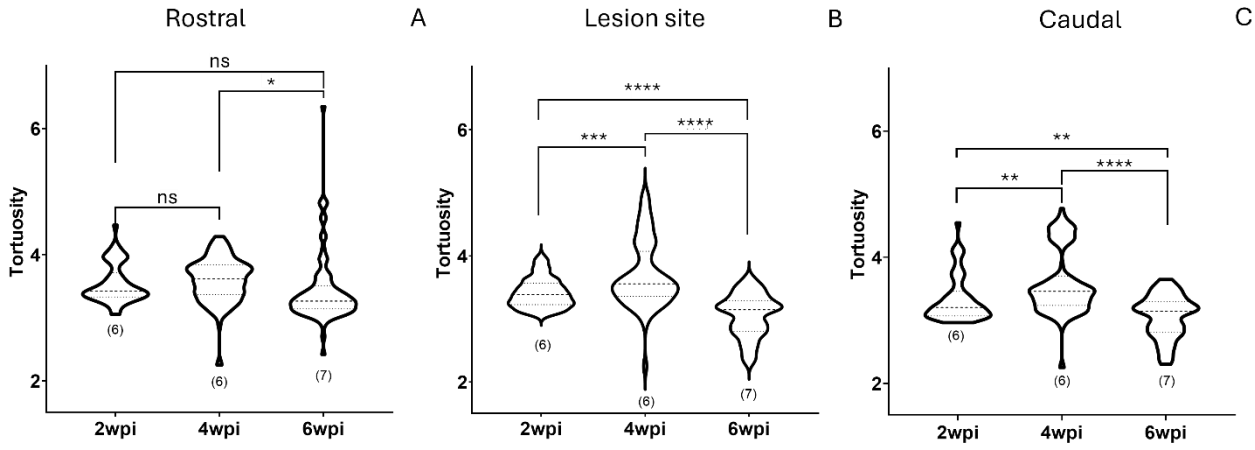

Figure 32: Temporal evolution of collagen fiber tortuosity within rostral, lesion and caudal regions. Violin plots represent the distribution of tortuosity values. The dashed horizontal line represents the median of each group.

When analyzing the temporal dynamics of collagen fiber tortuosity (Figure 32) across the three defined regions, important patterns emerged. In the rostral region (Figure 32.A), collagen tortuosity exhibited a dynamic evolution across the timepoints studied. At 2 wpi, the values were relatively homogenous, with two distinct populations and a moderate median value (3.42), suggesting that early deposition at the rostral end produced a uniform fiber organization. By 4 wpi, the median tortuosity increased compared to 2 wpi to 3.61, while the distribution remained relatively compact, indicative of a dominant fiber population with elevated curvature. This stage

may correspond to an intermediate phase where fibroblast-driven deposition increased collagen density without yet its organization (Soderblom et al., 2013). At 6 wpi, a distinct shift was observed, the median tortuosity decreased significantly to 3.26, while the distribution broadened with the emergence of several distinct subpopulations of fibers characterized by higher tortuosity. This suggests that by this stage, the rostral end no longer behaved as a uniform compartment but instead became a mosaic of differently organized collagen microenvironments. The coexistence of straighter fibers with highly tortuous ones implies an ongoing and perhaps competing balance between alignment forces and remodeling processes that generate local disorganization. The drop in median tortuosity further indicates a partial reorganization of the extracellular matrix, favoring straighter fibers, but the persistence of multiple populations highlights that this reorganization remains incomplete and spatially heterogeneous.

In the lesion site (Figure 32.B), the evolution of tortuosity followed the same dynamic compared to the rostral region. At 2 wpi, the median tortuosity (3.38) was comparable to that observed rostrally (3.42), with only minor differences. The distribution, although relatively broad, remained consistent with the presence of a single main fiber population. This suggests that at this stage, formation of collagen within the lesion site was already occurring in a relatively homogeneous manner, with fibers adopting similar levels of curvature rather than diverging into multiple subgroups. This could reflect the initial deposition of extracellular matrix by infiltrating fibroblasts and meningeal cells, producing collagen fiber that share common growth dynamics (Göritz et al., 2011). By 4 wpi, a significant increase in median tortuosity was observed (3.55), accompanied by the emergence of a distinct subpopulation of fibers displaying much higher tortuosity. This shift indicates the onset of structural diversification within the lesion site, where part of the collagen matrix becomes highly disorganized while another fraction maintains a more moderate curvature. Biologically, this could correspond to a dual process, the continued invasion of fibroblast (Göritz et al., 2011) combined with local remodeling processes in the core (Dias & Göritz, 2018), leading to the coexistence of multiple microarchitectures within the scar. At 6 wpi, the median tortuosity decreased to 3.14, with a new subpopulation characterized by much lower tortuosity values. This pattern implies that, while some collagen fibers remain highly tortuous, others undergo reorganization into straighter, less curved configurations. The coexistence of these divergent fiber populations highlights the dynamic and non-linear nature of fibrotic scar maturation. The emergence of

straighter fibers could represent an attempt at matrix stabilization and mechanical reinforcement. The persistence of highly tortuous fibers may significate that the growth of collagen is still ongoing.

In the caudal zone (Figure 32.C), the tortuosity pattern follows the ones from the lesion or rostral zone. At 2 wpi, the median tortuosity, 3.20, was slightly lower than in the two other regions, although the distribution showed some broadening. The reduced tortuosity compared to the rostral end may reflect asymmetrical dynamics of matrix infiltration, with a collagen formation being more robust or rapid rostrally than caudally, a phenomenon frequently reported in spinal cord injury models where rostrocaudal asymmetry is common (Bighinati et al., 2021). By 4 wpi, a significant increase in the median tortuosity was observed, 3.46, accompanied by the emergence of a clear subpopulation of fibers with much higher curvature. This shift suggests that, unlike the rostral border which maintained more stability at the same timepoint, the caudal side underwent pronounced disorganization. The coexistence of moderately curved fibers with highly tortuous ones highlights heterogeneous remodeling activity. This heterogeneity may arise from uneven fibroblast infiltration or localized variations in mechanical constraints (Pakshir & Hinz, 2018). At 6 wpi, the trend shifted again, the median tortuosity decreased significantly relative to 4 wpi, to 3.14, suggesting that many fibers were undergoing realignment and straightening. At the same time, the distribution revealed that appearance of a new subpopulation of fibers with very low tortuosity, coexisting with those that remained more curved. This duality reflects a partial reorganization of the collagen scaffold, where parts of the caudal matrix are consolidating into straighter, more organized bundles. This may indicate that the caudal zone is less efficient at forming a compact, homogeneous scar.

In addition to tortuosity, we quantified the total fiber length within each region analyzed. This metric represents the cumulative length of all collagen fibers detected. Unlike tortuosity, which captures the geometric organization of fibers, total fiber length reflects the abundance of fibrillar material. A higher total length indicates an increased deposition of collagen and thus a more advanced stage of fibrotic scar formation. Monitoring this parameter over time and across zones therefore allows us to assess both the temporal dynamics of collagen accumulation and potential spatial asymmetries in scar development along the rostrocaudal axis.

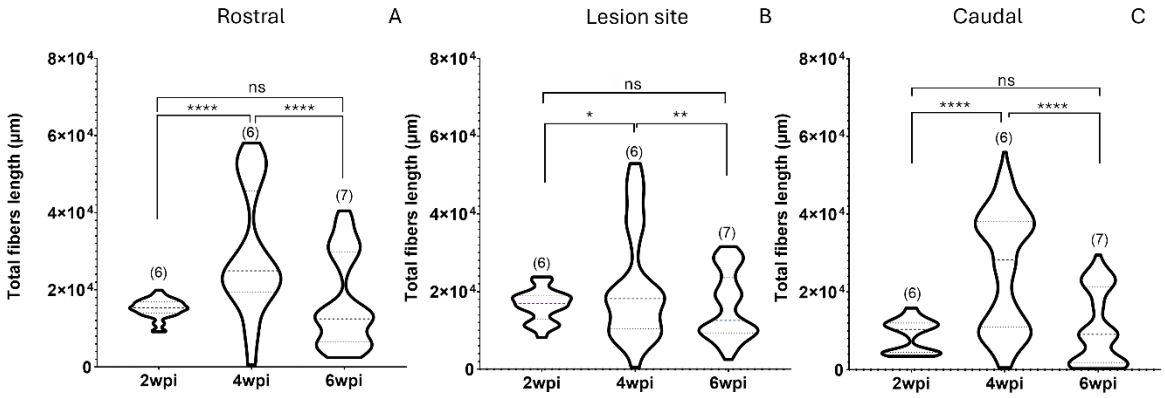

Figure 33: Evolution of total fiber length across timepoints for each region, with N=3 for 2wpi and 4wpi and N=4 for 6wpi. Violin plots represent the distribution of the total fiber length values. The dashed horizontal line represents the median of each group. Each region consist of a square of 660x660nm.

As depicted in figure 33.A in the rostral zone, the total fiber length $1.5x10^4$ µm remained relatively low and stable (one population) at 2 wpi, consistent with the previous results and suggest the beginning of collagen formation. By 4 wpi, a marked increase in total fiber length was observed, from $1.5x10^4$ to $2.4x10^4$µm, both in the median value and in the overall spread of the distribution. Two distinct subpopulations became apparent, one maintaining lower fiber length values and another reaching much higher levels, indicative of collagen apparition. By 6 wpi, the total fiber length decreased sharply compared to 4 wpi, returning closer to early values, with $1.2x10^4$µm. Interestingly, the distribution did not converge back to homogeneity but rather maintained 2 to 3 subpopulations. This implies that while global collagen formation declined, the tissue did not reorganize into a uniform matrix but instead preserved heterogeneous domains. This could reflect the onset of bundle formation, where collagen fibers become more compacted and aligned, reducing the total length detected. At the lesion site (Figure 33.B), the dynamics followed the same trajectory as in the rostral zone. At 2 wpi, the total fiber length was relatively low, $1.7x10^4$ µm, with two main subpopulations, both at the lower end of the range. This suggests that early collagen infiltration into the lesion was modest and structurally limited. By 4 wpi, a significant increase was detectable, due to the distribution, the median values are close, with $1.8x10^4$ µm at 4 wpi. By 6 wpi, a significant reduction occurred, with the median fiber length dropping below the earlier values to $1.2x10^4$ µm. Importantly, the distribution diversified into 3 subpopulations. This fragmentation into multiple states may reflect a reorganization phase, where some regions of the lesion retain dense collagen deposits, while others undergo compaction or even partial resorption. The caudal region displayed the same dynamic (Figure 33.C). At 2 wpi, fiber length values were low ($1x10^4$ µm), but the

distribution already revealed two subpopulations, indicating that at this stage, caudal collagen fibers' formation was not homogeneous. The value at this stage is lower than for the other regions. By 4 wpi, an increase occurred, with median values rising significantly to $2.8x10^4$ µm and 2 well-defined subpopulations emerging. This marked accumulation reflects enhanced fibroblast activity and ECM expansion, processes known to drive fibrotic scar formation (Soderblom et al., 2013). At 6 wpi, a sharp decline was observed, to $9x10^4$ µm, paralleling the trends in rostral and lesion zones. The distribution broadened further, showing 3 subpopulations. As in the other regions, this pattern is consistent with a reorganization process, likely involving the compaction of fibers into bundles.

Another metric of interest is the variance, which represents a measure of the local variability in collagen fiber organization informing on the local organization of ECM. Low variance indicates that fibers in the region share a similar orientation, whereas high variance reflects reduced local orientation.

Figure 34 presents the evolution of the variance across timepoints for each region. In the rostral region (Figure 34.A), variance was relatively low at 2 wpi, with a median value of 0.16, indicating that locally the collagen fibers tend to share the same orientation. By 4 wpi, the variance increased significantly to 0.45, reflecting a more disordered local structuring. This suggests that collagen fibers were undergoing spatially heterogeneous remodeling, potentially influenced by infiltration of fibroblasts (Ayazi et al., 2022). At 6 wpi, variance decreased again, suggesting that the rostral side switched toward a more stabilized and less heterogeneous architecture. This reduction is consistent with the idea that the ECM enters a phase of consolidation, where bundles of aligned fibers reduce local fluctuations in collagen organization.

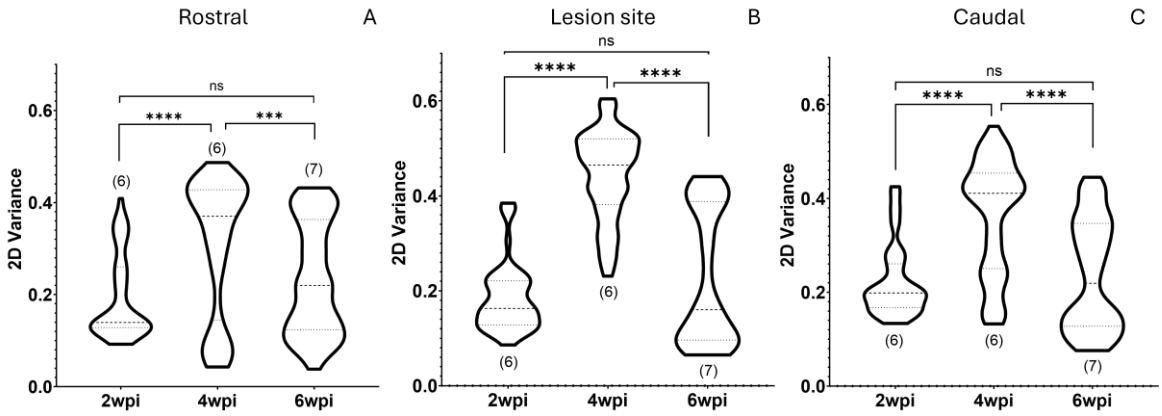

Figure 34: Evolution of 2D Variance across timepoints for each region, with N=3 for 2wpi and 4wpi and N=4 for 6wpi. Violin plots represent the distribution of the 2D variance. The dashed horizontal line represents the median of each group. Each region consists of a square of 660x660nm.

At the lesion site (Figure 34.B), variance was already slightly higher at 2 wpi (0.20) compared to rostral and caudal zones, suggesting that collagen deposition within the lesion was not entirely uniform. By 4 wpi, variance peaked to 0.41, indicating marked heterogeneity in fiber organization. The presence of multiple subpopulations likely reflects the simultaneous presence of aligned bundles and more disordered areas where collagen formation was still ongoing. By 6 wpi, variance decreased to 0.22 but remained higher than in the rostral zone, suggesting that although partial stabilization occurred, the lesion site maintained structural diversity. In the caudal region (Figure 34.C), the variance was low at 2 wpi, as for the other regions. At 4 wpi, variance increased significantly, mirroring the other regions, indicating that remodeling activity extended caudally too. By 6 wpi, variance decreased, as in the other regions, pointing to a progressive stabilization of collagen fibers local organization in the caudal region. Note that similar to the other regions, heterogeneity did not disappear entirely, consistent with a persistent structural complexity at later stages of scar maturation.

Overall, these patterns indicate that variance, as a descriptor of collagen fibers' local orientational heterogeneity, evolves dynamically across zones and timepoints, peaking at 4wpi before partially declining at 6 wpi. To complement this analysis providing a local view, we next examined entropy, which captures the global organization of the collagen network of an entire image of a complete region.

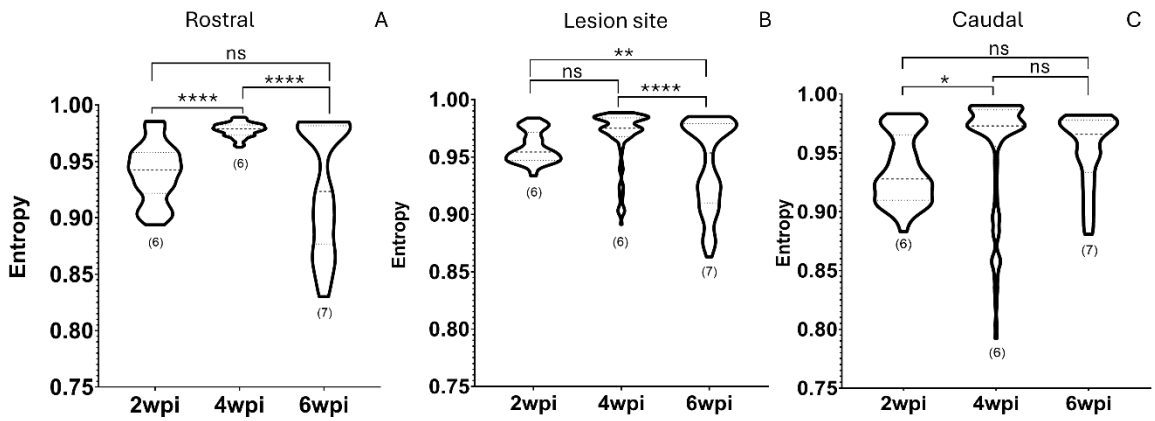

Figure 35: Evolution of entropy across timepoints for each region, consisting of a square of 660 x 660nm. Violin plots represent the distribution of the entropy values. The dashed horizontal line represents the median of each group.

When considering the entire image rather than local zones, orientation entropy values reveal a global increase, reaching levels that remain high (more than 0.9). This indicates that the collagen network presents no preferential orientation emerging at this scale. In the rostral zone (Figure 35.A), entropy was lower at 2 wpi (0.94) than 4 wpi, reflecting a still limited diversity of collagen organization. It then increased significantly at 4 wpi to 0.97, consistent with enhanced collagen deposition by infiltrating fibroblast (Soderblom et al., 2013),and decreased significantly at 6 wpi (0.92). Note that at 6 wpi, the decrease of median value of entropy is due to the apparition of new subpopulations with lower entropy values, suggesting that remodeling activity slows and collagen becomes more bundled with a possible orientation. At the lesion site (Figure 35.B), entropy changes follow the same pattern as in the rostral zone. At 2 wpi, the violin plot evidences the presence of two subpopulations, one with lower entropy values. At 4 wpi, the entropy increases with smaller subpopulations in the lower entropy values. This can reflect the coexistence of highly disorganized collagen fibers in the lesion center and a partial structuration. By 6 wpi, entropy declines significantly with the apparition of a new subpopulation with lower entropy values, suggesting that residual heterogeneity persists even after partial bundle formation. In the caudal zone (Figure 35.C), entropy was lower at 2 wpi, then rose moderately at 4 wpi, indicating some diversification of fiber orientations and density patterns. This increase was less pronounced than in the rostral region, highlighting a more gradual remodeling process in the caudal region. By 6 wpi, entropy decreased again, consistent with consolidation of collagen fibers into more regular bundles, paralleling the behavior of the rostral side.

		Rostral	Lesion site	Caudal
Tortuosity	**2 wpi**	3,42 ± 0,31	3,38 ± 0,23	3,20 ± 0,37
	4 wpi	3,61 ± 0,35	3,55 ± 0,52	3,46 ± 0,51
	6 wpi	3,26 ± 0,53	3,14 ± 0,34	3,14 ± 0,34
Total Fibers Length (µm)	**2 wpi**	(15 ± 2) x 10^3	(17 ± 4) x 10^3	(10 ± 4) x 10^3
	4 wpi	(24 ± 15) x 10^3	(18 ± 14) x 10^3	(28 ± 14) x 10^3
	6 wpi	(12 ± 11) x 10^3	(12 ± 8) x 10^3	(9 ± 7) x 10^3
2D Variance	**2 wpi**	0,16 ± 0,07	0,20 ± 0,07	0,14 ± 0,09
	4 wpi	0,45 ± 0,09	0,41 ± 0,12	0,37 ± 0,15
	6 wpi	0,16 ± 0,14	0,22 ± 0,11	0,22 ± 0,12
2D Entropy	**2 wpi**	0,94 ± 0,02	0,95 ± 0,01	0,92 ± 0,03
	4 wpi	0,97 ± 0,01	0,97 ± 0,02	0,97 ± 0,05
	6 wpi	0,92 ± 0,01	0,95 ± 0,04	0,96 ± 0,03

Table 1: Summary of 2D metrics determined for collagen fibers in rostral, lesion and caudal regions at 2, 4 and 6 wpi. Values are reported as medians ± standard deviation

Table 1 presents the summary of all metrics determined by the Fingerprint method. These results confirm the progressive establishment of the fibrotic scar. By 2 wpi, collagen deposition is already detectable, though still limited and relatively homogeneous. At 4 wpi, collagen growth intensifies and expands in a heterogeneous way. By 6 wpi, signs of maturation emerge as the overall collagen accumulation slows down or become less apparent, likely due to the compaction of fibers into bundles.

III.2.2 Discussion on the evolution of the fibrotic scar by 2D analysis

The quantitative assessment of collagen fibers' remodeling using the Fingerprint method provides important insight into the spatial and temporal evolution of the fibrotic scar after spinal cord injury. Our results highlight the dynamic nature of collagen deposition and reorganization; while also underscoring the coexistence of heterogeneous microenvironments within the scar tissue. These findings resonate with previous reports by Manesco (2023), who demonstrated that fibrillar collagen constitutes a robust structural biomarker of scar maturation when monitored by SHG imaging providing quantitative metrics. In line with this, fibrotic scar formation is marked by the progressive deposition of collagen-rich ECM and the accumulation of fibroblast cells within the lesion core (Soderblom et al., 2013; Dias et al., 2021; Ayazi et al., 2022). Multiple studies in rodents report that collagen formation within 1 or 2 weeks post injury and expands and consolidates by 4 to 6 weeks, forming a capsule-like architecture that compartmentalized the lesion (Wanner et al., 2013; Dias et al., 2018). The cellular sources of

this collagen include meningeal fibroblasts invading from the surface, perivascular fibroblast-like cells and pericytes associated with the vasculature and indirectly astrocytes that shape matrix assembly at the boundary through biochemical signaling (Soderblom et al., 2013; Wanner et al., 2013; Bradbury & Burnside, 2019). Our quantitative, zone-resolved analysis of collagen microarchitecture provides a way to relate what we observe in SHG.

Tortuosity is an intuitive descriptor for the geometric state of fibrillar collagen. Wavy or crimped collagen fibers are characteristic of tissues under low tensile load, reflecting an unstretched configuration that facilitates subsequent reorganization and strain-stiffening and are commonly observed in developing or remodeling connective tissues (Provenzano et al., 2008; Miller et al., 2012). In contrast, straighter collagen fibers are commonly associated with increased matrix tension and alignment, as well as progressive cross-link maturation that supports higher tensile strength (Provenzano et al., 2008; Taufalele et al., 2019; Ellingson et al., 2022). In a dynamic lesion environment, changes in tortuosity may reflect a transition between new collagen deposition and subsequent remodeling: newly synthesized fibrils are inserted in a less stretched, less aligned configuration and only later become more stretched, aligned or compacted as the matrix matures (Taufalele et al., 2019; Lin et al., 2024). In that sense, tortuosity complements the more conventional notion of "alignment". We can observe a network that is globally disordered (no dominant orientation) but locally straightened (low tortuosity in subregions). Note that a globally oriented network may still present high tortuosity if fiber buckle or meander with aligned tracts. This distinction has been emphasized in fibrotic contexts outside the central nervous system (CNS), where tortuosity is a marker of immature or unstable collagen (Provenzano et al., 2008). In SCI, where perivascular and meningeal fibroblasts generate collagen under spatially heterogeneous cues, tortuosity provides a sensitive readout of maturation vs ongoing fiber's formation within each zone (Bradbury & Burnside, 2019). Persistent tortuosity or increase at 4 wpi can be explained as the extension of the lesion with ongoing fiber's apparition, while after 4 wpi the fibrotic scar is in maturation with fibers of lower tortuosity, an evolution that can be explained by reorganization of the collagen network.

Where tortuosity speaks to geometry, total fiber length is a representative of fibrillar abundance. In collagen-rich tissues, higher total length corresponds to higher amount of fibrillar material, while reductions may reflect compaction into bundles or remodeling rather than literal loss of

collagen (Rezakhaniha et al., 2012). Importantly, decreases in total fiber length after an initial peak are well-documented in fibrotic contexts. As fibers coalesce into thicker, straighter bundles, the tracer software represents them with fewer, longer segments, and smaller fibrils may fall below the segmentation granularity. This phenomenon of "losing" collagen signal because of its compaction has been noted in quantitative SHG analyses of fibrosis and tissue remodeling (Bredfelt et al., 2014). Thus, a drop in total length after a mid-point peak is more consistent with bundle formation and architectural consolidation than with degradation. At around 4wpi after SCI, the fibrotic scar is characterized by robust collagen accumulation and fibroblast accumulation (Göritz et al., 2011; Dias et al., 2021). At later stages after SCI, this early accumulation, transitions toward a denser, mechanically reinforced fibrotic scar (Manesco et al., 2023). Our total-length measurements are designed to capture precisely this expansion-compaction sequence, examined zone by zone. In our dataset, the total fiber length increased significantly between 2 and 4 wpi across all regions, consistent with the collagen expansion reported at comparable timepoints in SCI models (Dias et al., 2021). By 6 wpi, however, total fiber length dropped sharply, despite persistent SHG signal. Rather than indicating collagen degradation, this decline likely reflects a transition toward scar maturation, where fibrillogenesis slows and newly deposited fibrils are reorganized into denser network with formation of bundles (Soderblom et al., 2013; Dias et al., 2021; Bradbury & Burnside, 2019).

Variance and entropy complete the 2D picture by quantifying heterogeneity at different spatial scales. Here the variance is inherently local while entropy is more global. Because fibroblasts infiltration and vascular remodeling are inherently uneven after SCI, local variance is expected to peak during active remodeling and decline as the matrix stabilizes into bundles. This type of peak-decline behavior has been described in other models of fibrotic scarring, where scar-forming fibroblasts initially deposit collagen in a spatially heterogeneous manner before consolidating their output into more continuous tracts (Göritz et al., 2011; Dias et al., 2018). For entropy, a higher value implies multiple orientations and intensity modes across the whole field (no dominant direction), whereas a low entropy can occur either when the network becomes uniformly aligned (strong orientation preference) or uniformly disordered (homogenous randomness). In the SCI context, reduced entropy is most consistently interpreted as a result of collagen bundle formation and partial alignment. Such decreases have been reported in connective tissue remodeling where fibrils progressively assemble into bundles (Cox & Erler, 2011; Egeblad et al., 2010). Notably, many CNS scar studies describe capsule-

like collagen that is regionally aligned along the lesion borders but remains globally complex because borders curve and residual disordered domains persist (Wanner et al., 2013). This duality of local order but global complexity fits our observations, where entropy increased from 2 to 4 wpi, reflecting more complexity as collagen "fills in", followed by a partial decline by 6 wpi, consistent with bundle formation and local alignment. Yet the entropy value remained >0.7, confirming that global orientation never dominated, in line with prior reports that CNS fibrotic scars do not resolve into a fully ordered capsule but remain partially heterogeneous (Dias et al., 2018, Dorrier et al., 2021).

From all the metrics determined, we can conclude that collagen remodeling after SCI follows a biphasic trajectory: an early phase of expansion culminating around 4 wpi, followed by a phase of reorganization at 6 wpi. Tortuosity remained broadly comparable for every zone but showed a fluctuation for different timepoints. Total fiber length clearly peaked at 4 wpi before declining, consistent with bundles' formation (Dias et al., 2018). Variance and entropy both increased during the active fibers formation phase and decreased thereafter, reflecting a transition from heterogeneous to a more stabilized but still structurally diverse scaffold (Tran et al., 2021). Importantly, these trends were not restricted to the lesion site but also affected rostral and caudal regions, underscoring that scar maturation is a spatially heterogeneous process (Soderblom et al., 2013). Overall, the 2D analysis provides a coherent picture of collagen dynamics and sets the stage for 3D evaluation (Liu et al., 2015; Manesco et al., 2023).

III.2.3 3D Variance results

In contrast to the 2D analysis, the 3D analysis is restricted to two descriptors: the global variance of the collagen network and the angular distributions θ and φ. The variance in 3D captures the overall heterogeneity of collagen orientation across the entire volume, reflecting whether the network is isotropic or partially aligned. This volumetric measure is conceptually related to entropy in 2D, but it additionally accounts for out-of-plane contributions, which are invisible in single sections (Liu et al., 2015). As in the 2D variance computation, the choice of neighborhood size (i.e., the number of neighbors used to estimate local orientation statistics) also has a significant impact on the 3D analysis. For practical reasons linked to computation time, the 3D neighborhood was limited to 5 neighbors. Increasing the number of neighbors would smooth the estimation and reduce some artifacts, but it would also dramatically increase processing time, making large-volume analyses substantially more demanding. The angular

histograms provide a direct visualization of how fiber orientations are distributed in space, identifying whether collagen bundles preferentially align along one axis or remain randomly organized. Together, these two descriptors allow us to move beyond planar projections and evaluate whether the fibrotic scar acquires depth-dependent orientation patterns that could affect its mechanical properties and its interactions with regenerating axons.

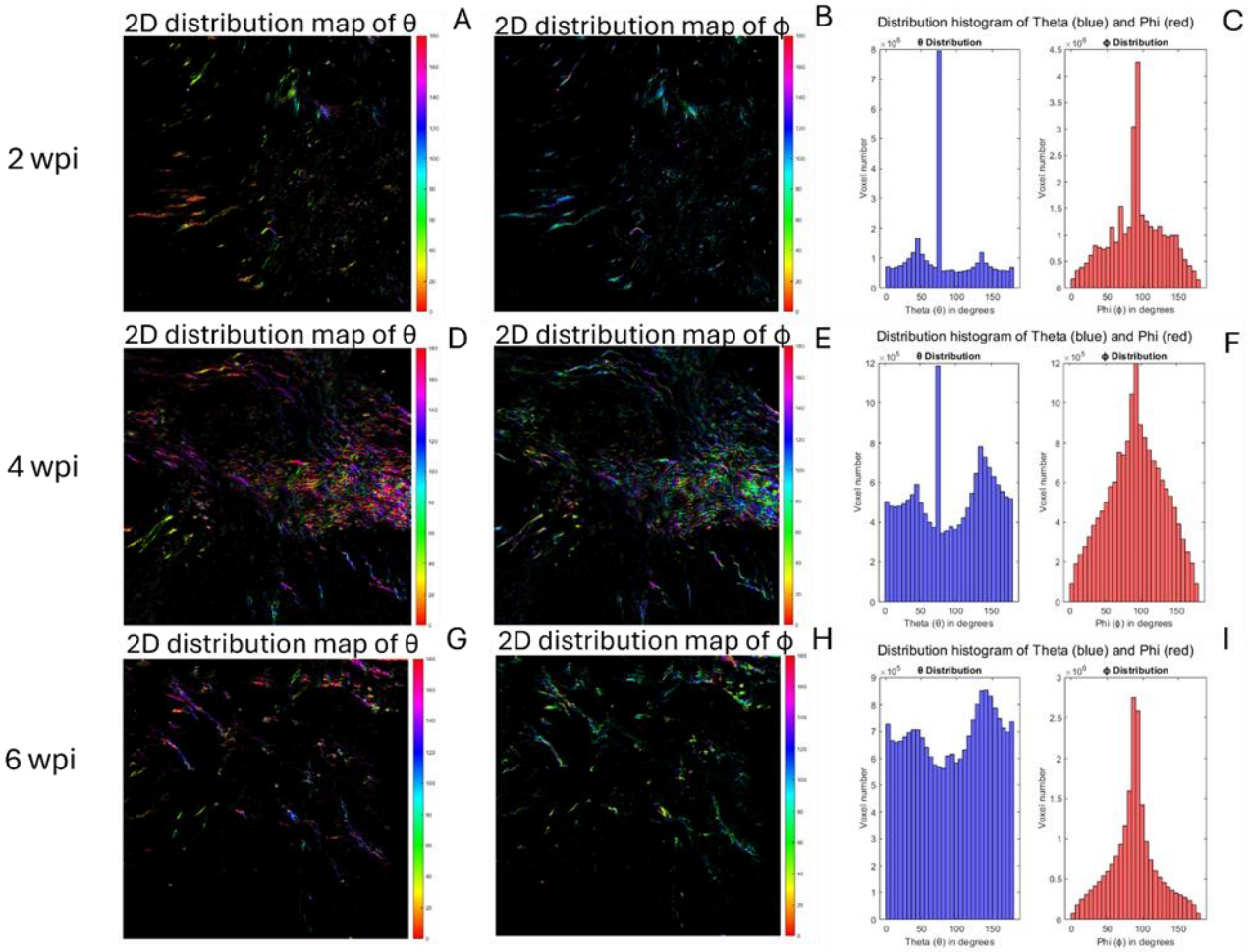

Figure 36: 3D collagen orientation in the lesion core over time. Each row corresponds to a post-injury timepoint (top to bottom: 2, 4 and 6 wpi) and their respective orientation histogram. All images are extracted from the lesion site; for visualization we show a single slice through the 3D volume. Left: 2D distribution map of θ (azimuth, in-plane) degrees. Middle: 2D distribution map of φ(out-of-plane) in degrees. Right: number of voxel orientation histograms of the two angles computed over the entire segmented lesion volume for the corresponding timepoint. Colo bars span 0-180° and the same LUT is used across panels. Narrow, single-peaked histograms indicate locally aligned bundles, whereas broader or multimodal distributions reflect increased 3D dispersion.

Figure 36 presents the 2D distribution maps of the angles θ and φ at different time points. From these maps, it appears that collagen in the lesion core undergoes temporal changes in its organization. Since only one animal is shown here, these observations remain descriptive. The

φ maps and histograms on figure 36 consistently exhibit a distribution centered around 90°, indicating that here most fibers remain confined to the sectioning plane, with only a minority oriented out of plane. In contrast, the θ distributions appear rather uniform overall, with no clear preferential orientation. An apparent feature around 70° is observed at 2 and 4 wpi, but this may reflect an artifact rather than a sub-population and is not further interpreted given the sample size here.

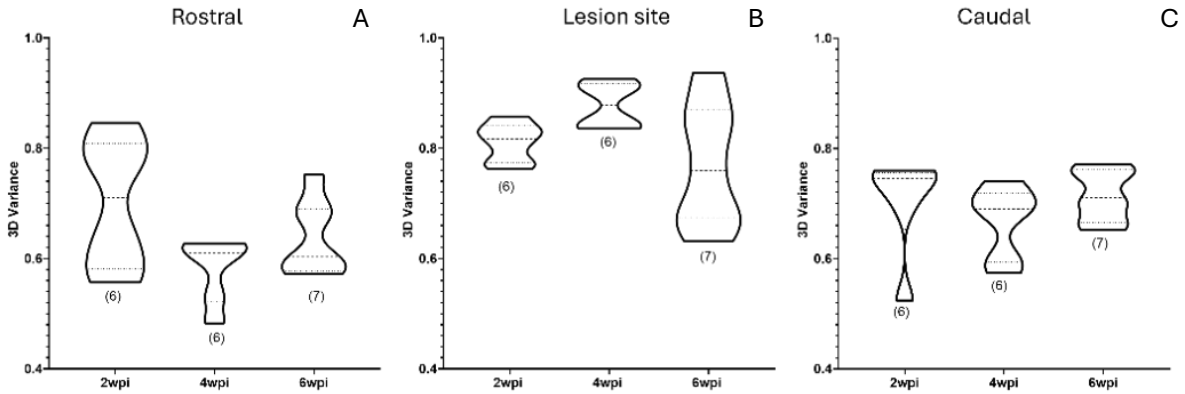

Figure 37: Variance of collagen fiber orientation in 3D SHG datasets across post-injury timepoints, at 2, 4 and 6 wpi on a 50 µm thick longitudinal section for each region (660 x 660 nm). Data are displayed as violin plots, showing the distribution of variance values for each timepoint. The dashed horizontal line represents the median of each group, while the width of each plot reflects the density of values.

In the context of SCI, 3D directional variance (3D-DV) is particularly relevant because fibroblast infiltration and vascular remodeling are all uneven processes that generate microscale structural heterogeneity. Peaks in variance typically correspond to active remodeling phases, when different cell types deposit collagen in overlapping but non-aligned configurations (Soderblom et al., 2013; Cox & Erler., 2011); subsequent decreases indicate local stabilization, when fibers coalesce into bundles or achieve more consistent alignment. Our analysis of 3D-DV across rostral, lesion and caudal zones is presented in figure 37.

At 2 wpi, the rostral zone (Figure 37.A) displayed relatively high 3D-DV values, with a mean value at 0.71 (note that values between 0.3 and 0.6 are typically associated with preferential alignment; Liu et al., 2017), this indicates that the rostral end was still outside the range of strong orientation. Instead, the network remained relatively disorganized, and the broad dispersion of values pointed to a heterogeneous state across subregion, with some areas exhibiting more pronounced disorder than others. By 4 wpi, the 3D-DV decreased, with the median shifting down to approximately 0.61. This placed the rostral collagen network closer to

the range associated with preferential alignment, implying that fibers started to adopt more preferential orientations. At the same time, the disappearance of higher-variance subpopulations suggested that the ECM had become less heterogeneous, with fewer domains deviating toward extreme disorganization. This transition likely corresponds to a phase of bundle consolidation, as fibers are progressively compacted or guided by mechanical forces exerted at the lesion border (Cox & Erler, 2011). At 6 wpi, the median 3D-DV value remained comparable to 4 wpi (0.60), but the distribution broadened again with the reappearance of high 3D-DV value subpopulations. This suggests that while the rostral border preserved a moderate global level or order, localized regions of disorganization re-emerged. Such late-stage heterogeneity could result from ongoing remodeling, where some areas undergo stabilization into straighter bundles while others remain influenced by persistent cellular activity.

At 2 wpi, the lesion site (Figure 37.B) presented a 3D-DV distribution that was more restricted than in the rostral region, but with overall higher values. The median was close to 0.8, a level that clearly indicates the absence of any preferential orientation. Two subpopulations could be distinguished, though they remained very close to each other, suggesting that despite the restricted spread, the collagen network inside the lesion core was already dominated by disorganization. This suggests a phase in which collagen deposition occurs but without structural guidance, leading to a relatively uniform but highly chaotic state. By 4 wpi, the 3D-DV distribution shifted toward even higher values (0.87). Two distinct subpopulations could still be identified, but both were centered in the disorganized range, one at 0.85 and the other one at 0.95, which corresponds to near-complete structural randomness. This indicates that while collagen deposition intensified, it did so in a way that amplified the overall chaos, with little evidence of local alignment. This pattern is consistent with a lesion environment heavily populated by fibroblasts and meningeal cells laying down dense ECM without spatial order reinforcing the impression of a structurally random scar core at this stage (Soderblom et al., 2013). In contrast, at 6 wpi, the median 3D-DV decreased slightly to around 0.76, suggesting that the collagen network started a reorganization process. Although this value remains in the disordered range, it signals the initiation of structural maturation, with fibers starting to align locally and reduce the overall heterogeneity of the lesion site. The persistence of high values, however, indicated that the process is far from complete. The lesion scar at 6 wpi, thus embodies a transitional state: no longer in the disorganized deposition phase, but not yet consolidated into a preferentially aligned architecture.

At 2 wpi, the caudal region (Figure 37.C) exhibited a broad 3D-DV distribution, with most fibers concentrated around a median value of 0.74. This value reflects a disorganized network without preferential orientation. Interestingly, a secondary subpopulation appeared around 0.5, which falls within the range associated with the onset of preferential alignment. This suggests that while the bulk of the caudal ECM was still chaotic, localized domains started to display partial organization, possibly reflecting compaction of collagen fibers in isolated patches. By 4 wpi, the median 3D-DV shifted downward to 0.69, indicating a modest reduction in global disorganization. Two subpopulations were distinguishable, one centered at 0.7 and another slightly lower at 0.6. Both values remain within the range of weak orientation, but their presence suggests that the caudal ECM was diversifying, with some regions entering a more structured state while others remained poorly organized. At 6 wpi, the 3D-DV profile stabilized with the median remaining close to 0.7 but the distribution becoming narrower and more compact. A subpopulation was still evident at 0.65, showing that while most of the caudal zone remained globally disorganized, there was now a greater homogeneity across the tissue. In other words, the collagen network became more uniform in its level of disorder. Note that no significant differences were observed for any of these 3D results. The summary results between 2D and 3D analysis are presented in table 2.

	3D Variance			2D entropy		
	Rostrale	Lesion site	Caudal	Rostrale	Lesion site	Caudal
2wpi	0,71 ± 0,11	0,81 ± 0,04	0,74 ± 0,09	0,94 ± 0,02	0,95 ± 0,01	0,92 ± 0,03
4wpi	0,61 ± 0,06	0,87 ± 0,04	0,69 ± 0,06	0,97 ± 0,01	0,97 ± 0,02	0,97 ± 0,05
6wpi	0,60 ± 0,07	0,76 ± 0,11	0,71 ± 0,04	0,92 ± 0,01	0,95 ± 0,04	0,96 ± 0,03

Table 2: Comparison of 3D variance and 2D entropy of collagen fiber for each region at 2, 4 and 6 wpi. Values are expressed as mean ± SD

III.2.4 Discussion on the evolution of the scar in 2D and 3D Analysis

The 2D analysis of collagen remodeling provided a first layer of quantitative insight into the temporal and spatial dynamics of the fibrotic scar, yet by design it compresses a 3D fibrous architecture into a single plane. Metrics such as tortuosity, total fiber length, variance and entropy revealed consistent trajectories: an initial phase of fibers growth and diversification culminating around 4 wpi, followed by a partial consolidation at 6 wpi. These descriptors

captured the balance between fibers apparition and their further organization highlighting regional asymmetries between rostral and caudal areas and demonstrated that the lesion core remains the most structurally heterogenous zone. However, collagen is not a planar material; it is an inherently 3D fibrillar network, in which alignment, bundling and orientation can extend along depth as much as along the imaging plane. Restricting the analysis to 2D inevitably obscures these out-of-plane contributions and may underestimate or misclassify certain aspects of fiber organization. This limitation has been emphasized in other fibrotic contexts, where SHG or multiphoton microscopy analysis restricted to planar sections failed to detect vertical fasciculation or laminar stratification that became evident in volumetric reconstructions (Liu et al., 2017). For this reason, transitioning from 2D to 3D descriptors is not simply a matter of completeness; it is essential for an accurate understanding of how the scar organizes in space. The bridge between the 2D and 3D analyses lies in the variance-entropy pair. In 2D, variance is defined locally while entropy is computed globally over the entire field of view, and it quantifies the overall diversity of orientations and intensities in the image. The combination of these two descriptors already hinted at the complexity of the scar: high variance indicated microscale domains of heterogeneous organization, whereas high entropy confirmed the lack of a single dominant orientation across the image. In 3D, these notions coalesce into the global directional variance. Instead of summarizing variability within a plane, the 3D-DV integrates voxel orientations throughout the entire volume, accounting for both in-plane and out-of-plane contributions. In this sense, 3D variance can be viewed as the volumetric analogue of 2D entropy but enriched with directional information that reflects tilt and azimuthal angles in space (Liu et al., 2017). It is precisely this added dimension that allows us to determine whether the fibrous collagen scar acquires depth-dependent orientation patterns that are invisible to planar projections. Then angular histograms of θ and φ further extend this logic. In 2D analysis, one can infer whether fibers are more or less aligned within the imaging plane, but it is impossible to know whether they rise or fall across depth. By contrast, 3D histograms directly visualize how fiber orientations distribute across the entire solid angle of the volume. Narrow peaks suggest bundles adopting a preferred orientation; broad, multimodal distributions indicate isotropy or multiple competing alignments. In our dataset, these histograms confirmed that most fibers remained close to the imaging plane (φ=90°). Another critical reason for moving to 3D descriptors is that fibrotic scars in the CNS are not homogeneous sheets but volumetric structures. Histological studies and 3D reconstructions from cleared tissue consistently

demonstrate that the fibrotic scar forms a dense border surrounding the lesion, extending along the rostrocaudal axis and encasing the core in a capsule-like manner (Wanner et al., 2013; Bradbury & Burnside, 2019; Dorrier et al., 2021). This capsule is not isotropic: fibroblasts infiltrating from the meninges or vasculature encounter distinct mechanical environments, leading to local guidance cues that can orient collagen along stress lines. Recent single-cell analyses have further shown that fibroblast subtypes contribute differently to the 3D arrangement of the scar, with some subsets generating highly aligned bundles while others produce more disordered matrices (Xue et al., 2024). Such cellular heterogeneity is unlikely to manifest identically across depth, reinforcing the importance of volumetric readouts. By integrating both 2D and 3D descriptors, we are able to cross-validate our interpretations and refine our biological conclusions. The 2D results indicated that by 6 weeks, collagen had partially consolidated into bundles but without a dominant global orientation. In contrast, the 3D-DV analysis revealed a different trend as variance decreased from 2 to 4 wpi in the rostral and caudal region, suggesting partial homogenization, but increased again at 6 wpi, consistent with the emergence of local heterogeneities. Only the lesion site, in 2D and 3D, show a decreasing in variance, indicating a reorganization of the collagen network at the core of the scar at 6 wpi. This consistency across 2D and 3D strengthens the conclusion that the fibrotic scar reaches a state of partial order but remains structurally heterogeneous. Moreover, the ability to directly assess φ demonstrated that despite this partial reorganization, most fibers remain largely confined to the imaging plane, with limited vertical alignment. This is biologically significant, because the persistence of in-plane orientation without depth organization implies that the scar stabilizes mechanically along the borders but does not generate vertical tracts. The transition to 3D analysis is also essential for situating our work within translational and biomaterial contexts. Many scaffold-based interventions for SCI now focus on imposing anisotropy and alignment in 3D, mimicking the longitudinal tracts of the spinal cord (Sousa et al., 2023). Our SHG based descriptors clearly show that endogenous scar collagen fails to develop a degree of anisotropy and alignment. This structural deficit highlights an architectural feature of the fibrotic scar that may be the cause of blocking axonal regrowth, while providing a quantitative reference against which biomaterial interventions can be evaluated. In this respect, the 3D variance and orientation histograms go beyond descriptive imaging; they provide a direct link between the biology of scar maturation and the design of interventional strategies. As recently emphasized by Fang et al. (2025), a central obstacle in

developing collagen-based biomaterials for CNS repair is precisely that native scar collagen remains disorganized and inhibitory. Our results not only capture this disorganization but also reveal its partial and incomplete resolution over time, reinforcing the need for engineered scaffolds that can impose more favorable architecture.

The temporal trajectory of collagen remodeling after SCI in our dataset is best understood as a biphasic process, yet one in which 2D and 3D descriptors do not always evolve in parallel. At 2 wpi, the descriptors from 2D and 3D analysis converge. Biologically, this state corresponds to primary collagen formation: fibers are already present within the lesion, but they extend in a random, non-preferential manner, no matter the region. By 4 wpi, the scar enters a phase of maximal heterogeneity, but here the divergence between the two models becomes apparent. In the 2D analysis, all metrics point to a surge of complexity while the 3D-DV reveals a more nuanced picture with the median 3D-DV decreasing to median values of 0.6-0.7. This would normally suggest a trend toward partial alignment and reduced heterogeneity. However, the distributions broaden, and subpopulations remain evident: while some domains indeed move toward lower variance and partial order, others retain higher variance levels. In other words, the scar does not consolidate uniformly. The lesion core is the exception. Here, both 2D and 3D analyses agree: variance rises, confirming that the lesion core is the most disorganized region at 4 wpi. The biological interpretation of this apparent contradiction between 2D and 3D at 4 wpi lies in the sensitivity to projection versus volume. Similar discrepancies between planar and volumetric descriptors have been reported in other fibrotic tissues, where bundles span depth but appear irregular in single planes (Bredfeldt et al., 2014; Liu et al., 2017). By 6 wpi, both 2D and 3D align in reflecting partial consolidation of collagen. In 2D, the decrease in variance and entropy relative to 4wpi mirrors histological data showing that CNS fibrotic scars transition from early disarray to more structured bundles in the chronic phase (Wanner et al., 2013; Tran et al., 2021; Soderblom et al., 2013). On the 3D side, variance across regions declines, particularly in the rostral compartment where median values approach 0.6. This result defines a clear initial phase of primary collagen deposition, followed by expansion marked by structural chaos and finally late compaction into more organized but still heterogeneous bundles (Göritz et al., 2011; Dorrier et al., 2021). The divergence observed at 4 wpi between 2D and 3D perspectives is particularly revealing. While 2D metrics suggest maximal disorganization, 3D data reveal that rostral and caudal regions already exhibit emerging subpopulations with lower variance, signaling partial volumetric orientation. This pattern reflects the phenomenon

seen in other fibrotic systems where planar sections amplify chaos by collapsing depth-dependent alignment (Liu et al., 2017; Dorrier et al., 2021). It underscores the essential role of 3D descriptors, which unveil organizational nuances invisible in 2D alone.

III.3 In-vitro collagen constructs

III.3.1 Collagen growth method

In a bottom-up approach collagen fiber structures have been elaborated to monitor their assembly. AFM imaging was employed to evaluate the morphology of the fibrillary networks for each protocol of growth. We've used both telocollagen (Tcol) and atelocollagen (Acol) in order to assess possible structural differences arising from the presence or absence of telopeptides.

III.3.1.1 Cold Start method

AFM images obtained for collagen fiber obtained by the Cold start method are presented in Figure 38. These results revealed that Tcol assembled into a dense, highly entangled fibrillary network, with bundles appearing irregular and heterogeneous in diameter (Figure 38.A and B). In contrast, Acol formed looser and more dispersed fibrils with a tendency to generate individual elongated filaments rather than dense aggregates (Figure 38.C and D). Using AFM line profiles (Figure 38 E. and F) on these measurements, we determined an average width of 103±24 nm for Tcol fibrils and 74±27 nm for Acol fibrils.

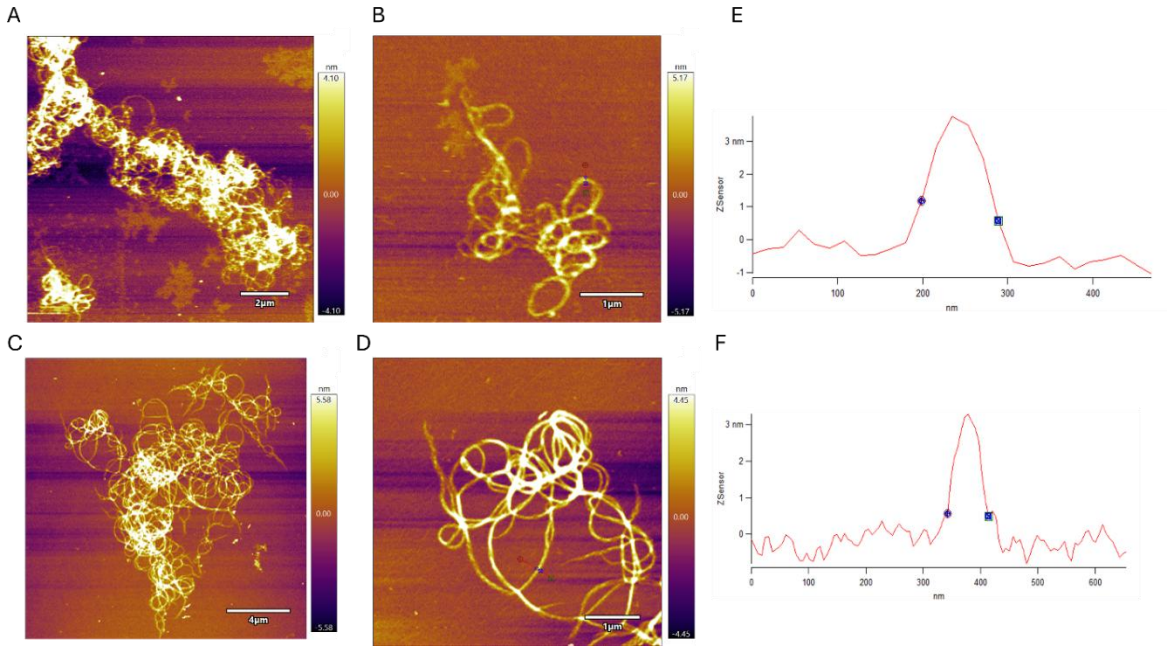

Figure 38: AFM images of in-vitro type I collagen fibrils obtained with Cold Start method. A,B Telocollagen, C,D Atelocollagen AFM height images. E and F representative cross-sectional line profiles taken across single fibrils in the corresponding images.

III.3.1.2 pH Controlled collagen growth

In the pH-controlled protocol, fibrillogenesis was initiated by progressively adjusting the solution pH to neutrality (pH=7). This approach yielded networks that were morphologically distinct from those obtained via the cold start method. Tcol (Figure 39.A and B) exhibited long, continuous fibrils forming bundles with fewer discontinuities than observed under the cold start condition. Line profiles (Figure 39.C) confirmed relatively uniform diameters along the fibrils. In contrast, Acol (Figure 39.D and E) formed fibrils that appeared fragmented, showing D-band, with alternating thick and thin regions along their length. The line profiles (Figure 39.F) highlight these periodic modulations, in agreement with previous reports of incomplete or irregular fibril assembly in the absence of telopeptides. Under these conditions, the apparent widths are 445±30 nm for Tcol and 460±85 nm for Acol.

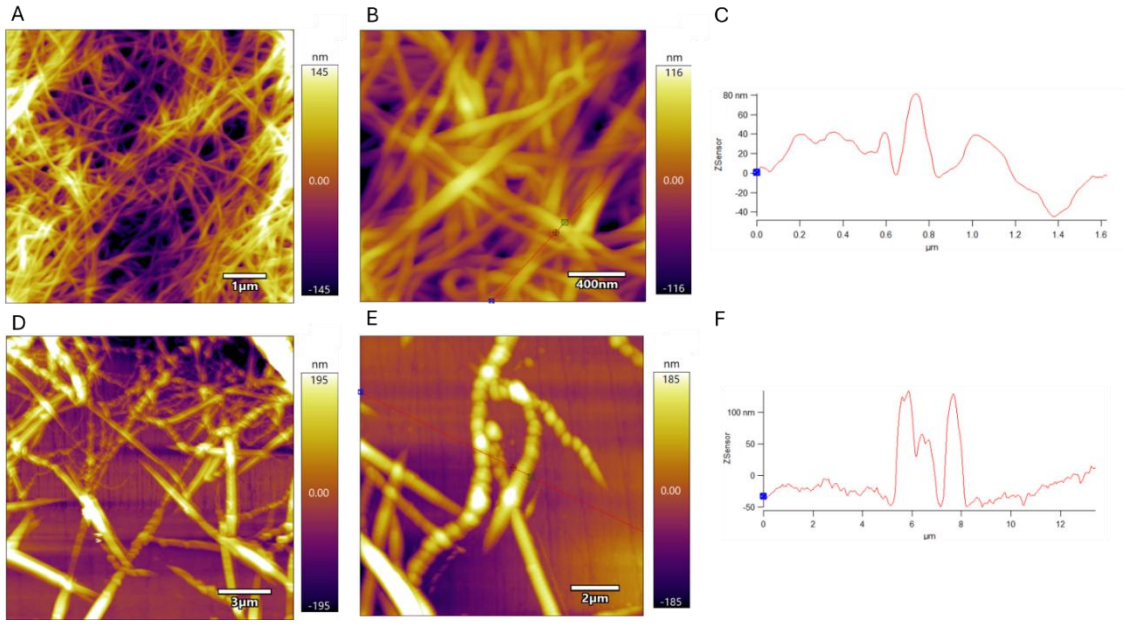

Figure 39: AFM imaging of in-vitro type I collagen fibrils prepared by pH control. Height images A, B Telocollagen and D, E Atelocollagen. C and F representative cross-section profiles used to estimate the apparent lateral size of individual fibrils.

III.3.1.3 Ionic forces to form bundles of collagen fibers

A third strategy was tested by partially replacing the solvent with a neutralizing solution (N-solution). AFM images (Figure 40) showed that increasing N-solution content led to the formation of thick, rope-like fibrils bundles with diameters reaching several hundreds of nanometers. The measured average lateral width across profiles was approximately 242±43nm for the smallest fibers and exceeded a micron for the largest ones.

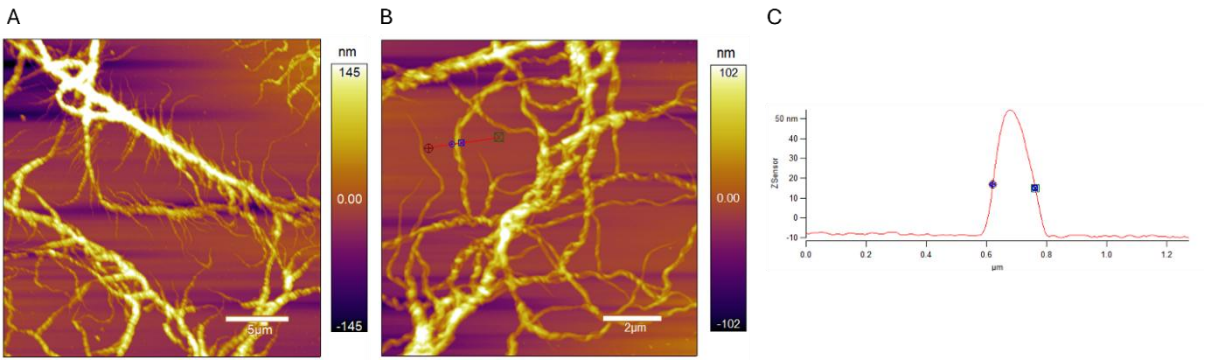

Figure 40: AFM characterization of modified type I collagen matrices (Oh et al., 2020). A and B AFM height images of fibrillar network. C corresponding cross-section used to estimate the apparent lateral fibril width.

III.3.2 Second harmonic scattering (SHS) experiments

III.3.2.1 Hyperpolarizability

The first hyperpolarizability of Tcol and Acol solution was determined from SHS measurements as a function of the incident laser power as presented in Chapter 2.3.2.2 with Figure 23. The SHS intensity measured for the atelocollagen solution was almost 2x higher than for telocollagen with $(286\pm16)\text{x}10^{-30}$ esu and $(176\pm14)\text{x}10^{-30}$ esu respectively. These results are in good agreement with the literature, which reinforces the robustness of our measurements (Deniset-Besseau et al., 2009; Shcheslavskiy et al., 2005). Interestingly, the lower hyperpolarizability obtained for Tcol is somewhat counterintuitive. Telopeptides have often been described as structural elements that facilitate fibrillogenesis, thereby promoting the alignment of collagen triple helices into ordered arrays (Maher et al., 2022). A more ordered supramolecular assembly would normally be expected to enhance the coherent summation of molecular hyperpolarizabilities, and thus yield a higher macroscopic β. Our observation of the opposite trend suggests that the nonlinear optical response of collagen cannot be explained only in terms of fibril formation and macroscopic order. Instead, the presence of telopeptides may disrupt the constructive interference of the elementary harmonophores within the triple helix, leading to a possible breakdown of the non-centrosymmetry of the structure. Similar decrease in β has previously been reported for highly concentrated collagen solutions, where the formation of large supramolecular aggregates was proposed to reduce non-centrosymmetry and attenuate the SHS response (Shcheslavskiy et al., 2005).

To further investigate whether the decrease in β arises from structural reorganization at the molecular scale or from supramolecular aggregation, we performed pH-dependent SHS measurements. Our hypothesis was that acidic conditions stabilize collagen in a monomeric or oligomeric state, while increasing the pH progressively promotes self-assembly into fibrils. We therefore recorded SHS intensities for collagen solutions as the pH varied from 2 to 7. However, beyond pH=3, we observed the spontaneous formation of a white gel within the quartz cell, associated with significant light scattering and attenuation of the SHS signal. Because this multiple scattering artifact prevented reliable quantification, the analysis of β was restricted to the pH 2-3 interval.

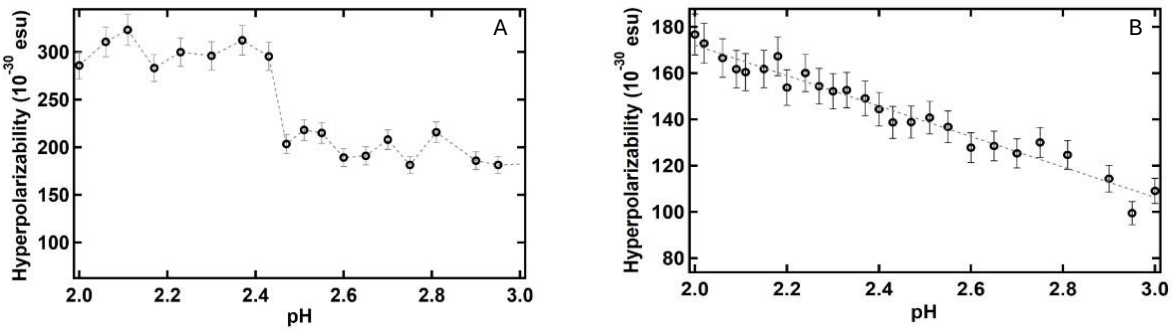

Figure 41: Hyperpolarizability as a function of pH for A) Atelocollagen and B) Telocollagen, error bares are standard deviation, curves are drawn to guide the eyes.

Figure 41 shows the evolution of hyperpolarizability as a function of pH for both collagen types. Across the entire investigated range, Acol displayed higher β values than Tcol. Specifically, Acol values ranged between ≈ 300 x 10^{-30} and 190 x 10^{-30} esu, whereas telocollagen decreased more gradually from ≈ 180 x 10^{-30} to 110 x 10^{-30} esu. These results suggest that the absence of telopeptides in Acol favors a more constructive alignment of the rigid triple-helical domains, resulting in stronger coherent amplification of the SHS response. In addition, the compact supramolecular arrangement of Acol helices may allow more efficient coupling of local dipoles, thus enhancing the effective β compared to Tcol, where telopeptides are likely to introduce structural looseness or heterogeneity.

In figure 41.A, for Acol a marked decrease in hyperpolarizability was detected around pH=2.4, after which β values stabilized at a lower value. This abrupt drop suggests the onset of early aggregation or fibrillogenesis, as also confirmed by the visual observation of loosely formed gel-like structures in the cell at this pH. In contrast, the Tcol hyperpolarizability (Figure 41.B) did not display a sharp transition but rather a steady linear decrease in β across the 2-3 pH range. This behavior is indicative of a gradual progression towards more centrosymmetric supramolecular assemblies, consistent with the notion that telopeptides modulate fibrillogenesis kinetics and prevent sudden, large-scale structural transition. These results highlight the high sensitivity of SHS to subtle molecular and supramolecular changes in collagen solutions, even under strongly acidic conditions. They also emphasize the distinct nonlinear optical responses of atelocollagen and telocollagen. The absence of telopeptides appears to promote a more coherent and constructive hyperpolarizability at low pH but simultaneously predisposes atelocollagen to undergo sudden fibrillogenesis around pH=2.4. By contrast, Tcol displays a

weaker but more gradual evolution of β, reflecting slower and more progressive assembly dynamics.

III.3.2.2 Depolarization ratio

To obtain additional insight into the molecular symmetry of collagen solutions, we've performed polarization-resolved SHS (P-SHS) experiments. In this configuration, the SHS intensity was recorded as a function of the incident polarization angle γ, while analyzing the emitted signal in two orthogonal detection channels. P-SHS experiments were carried out to determine the depolarization ratio enabling the study of molecular symmetry (Deniset-Besseau et al., 2009).

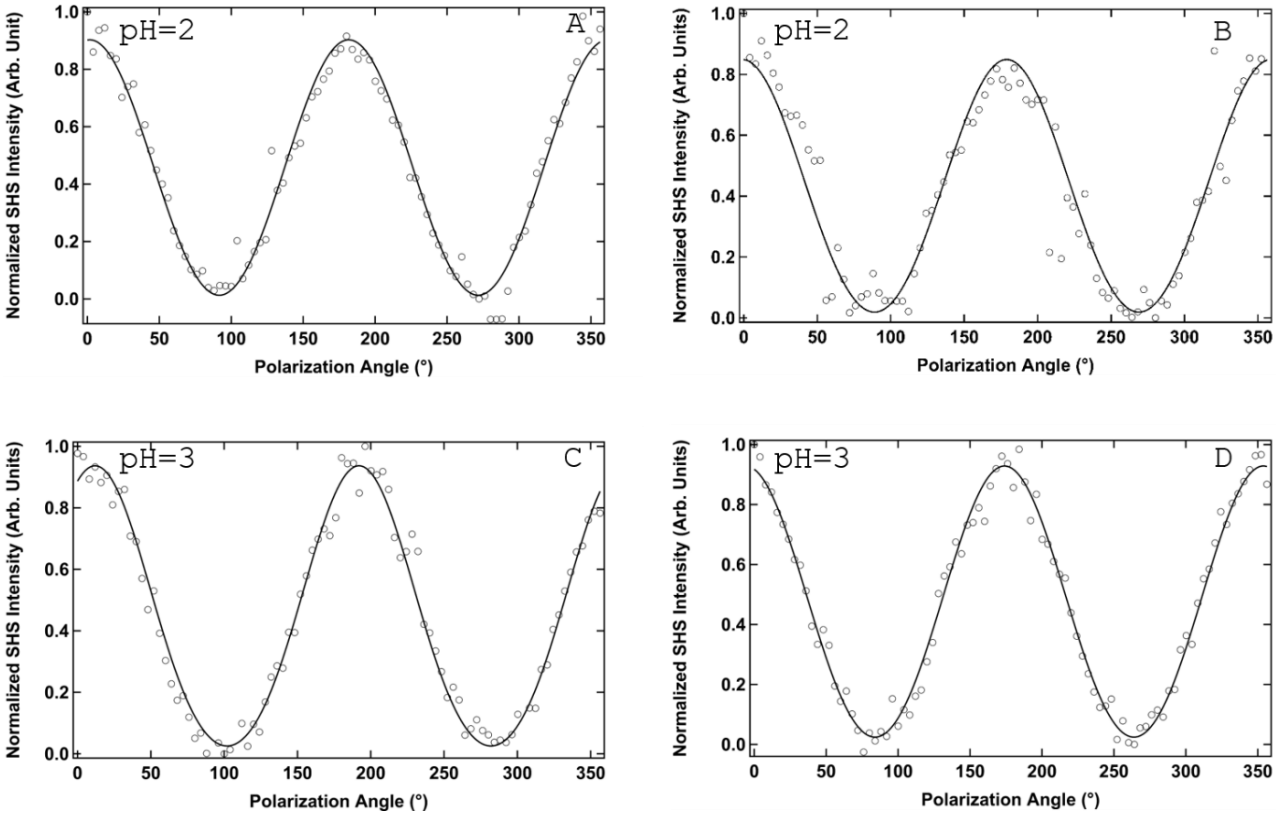

Figure 42: Polarization Curves for Atelocollagen A) at pH 2 C) at pH 3 and Telocollagen B) at pH 2 D) at pH 3. The polarization angle of the incident beam was tuned, while the output SHS signal is selected here in vertical (V) polarization

Figure 42 presents the polarization-resolved SHS intensity profiles obtained for both Acol and Tcol at pH=2 and pH=3, corresponding to the lowest and highest pH values where P-SHS experiments were performed. The vertical (V) detection curves clearly exhibit the expected two-lobed angular dependence, characteristic of second harmonic scattering from collagen, and

this feature was consistently observed for both collagen types regardless of the pH condition (Deniset-Besseau et al., 2009). These experimental profiles were fitted with equation 38 presented in Chapter II (3.2.3), providing the parameters a^V and c^V required for depolarization ratio (DR) determination.

From these fits, the DR values were calculated as 0.12 at pH=2 and 0.48 at pH=3 for Acol, while Tcol showed a constant DR of 0.28 at both pH values. These values fall within the dipolar regime, indicating that for both collagen types the dominant nonlinear response retains a largely dipolar symmetry (Zyss & Brasselet., 2002; Zyss, 1994). The fact that Tcol exhibits an essentially invariant DR across the tested pH further suggests that its supramolecular organization remains relatively stable in acidic conditions, whereas Acol undergoes a detectable shift in molecular symmetry as the pH increases.

To gain a more precise view of this evolution, we extended the analysis by computing DR values across the range of pH 2-3. These measurements were performed by recording SHS polarization profiles for incident polarization angles γ from 0° to 180°, with the analyzer fixed in vertical channel (Γ=90°). This systematic approach enabled us to map how the symmetry of the nonlinear optical response evolves during the early stages of collagen assembly and to directly compare the behaviors of telocollagen and atelocollagen under identical conditions.

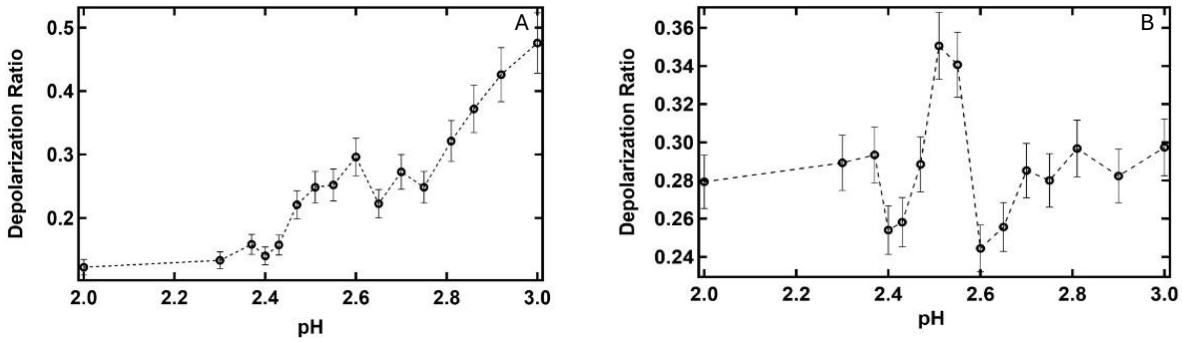

Figure 43: Depolarization ratio evolution as a function of pH for A) Atelocollagen and B) Telocollagen, curves are drawn to guide the eyes.

Figure 43.A illustrates the variation of DR as a function of pH for Acol. A gradual increase of DR from pH=2 to pH=3 from 0.12 to 0.48 is observed, pointing to a clear evolution in molecular symmetry. Notably, the rise in DR coincides with the pH around 2.4 at which the hyperpolarizability began to drop significantly (Figure 41), suggesting that both parameters

capture complementary aspects of the same structural transition. In contrast, figure 43.B highlights a different trend for Tcol. Here, DR remained relatively stable around 0.28 until approximately pH 2.4-2.6, at which point a marked increase was detected before going back to 0.28 around pH=2.7. This indicates that Tcol preserves its initial symmetry over a wider pH interval compared to Acol, only undergoing detectable reorganization within a narrower pH interval.

These results emphasize the sensitivity of DR as a probe for changes in molecular symmetry. They also reveal that the two collagen types respond differently to pH. Atelocollagen's progressive increase in DR indicates the development of a more complex symmetry structure, whereas the relatively constant DR of telocollagen over most of the tested range reflects greater stability in its supramolecular organization (Brasselet et al., 2011). Full DR values with error bars as a function of pH is presented in Table 1, enabling quantitative comparison and following conventions commonly adopted in SHS studies. Our assumption was that Tcol, owing to is intact telopeptides and higher tendency to self-associate, would undergo fibrillogenesis earlier than Acol. Surprisingly, however, both forms of collagen displayed gelation at around 2.5, with only Acol showing a pronounced shift in symmetry parameters by pH=3. Furthermore, contrary to expectations, no appreciable rise in SHS intensity was observed. In the case of Tcol, the apparent loss of signal can be attributed to the onset of gel formation, where the gel matrix scatters and attenuates the signal.

pH	DR Acol (± SD)	DR Tcol (± SD)
2	0.122 ± 0.012	0.279 ± 0.030
2.3	0.133 ± 0.015	0.289 ± 0.032
2.37	0.159 ± 0.018	0.293 ± 0.033
2.4	0.140 ± 0.021	0.254 ± 0.026
2.43	0.157 ± 0.022	0.258 ± 0.026
2.47	0.221 ± 0.024	0.288 ± 0.029
2.51	0.249 ± 0.028	0.351 ± 0.038
2.55	0.252 ± 0.027	0.341 ± 0.036
2.6	0.296 ± 0.035	0.244 ± 0.025
2.65	0.223 ± 0.028	0.256 ± 0.027
2.7	0.273 ± 0.031	0.285 ± 0.029
2.75	0.249 ± 0.025	0.280 ± 0.030
2.81	0.321 ± 0.031	0.297 ± 0.031
2.86	0.372 ± 0.042	N/A
2.92	0.426 ± 0.043	0.282 ± 0.032

3	0.476 ± 0.048	0.297 ± 0.028

Table 3: Depolarization ratio (DR) values measured for Acol and Tcol at different pH levels, with standard deviations (SD) represented as error bars.

In addition to the SHS measurements, we used AFM to visualize the supramolecular organization of both atelocollagen and telocollagen under different values of pH. For optimal imaging resolution, the samples deposited on mica were dried prior to analysis and the resulting images revealed pronounced differences between the two collagen forms. At pH=2, AFM images of Acol (Figure 44.A and 44.B) showed a relatively sparse network, with only limited fiber formation apparent. In contrast, Tcol displayed a markedly different behavior under the same conditions (Figure 45.A and 45.B), where fibers adopted a more parallel orientation with a higher degree of supramolecular organization. When recorded at varying magnifications, the distinction between the two collagen types became ever clearer. High-resolution AFM images of Acol (Figure 44.A) revealed individual, isolated fibrils lacking both preferential orientation and higher-order assembly. Conversely, Tcol images (Figure 45.A) displayed an extensive network of fibers aligned in parallel, covering nearly the entire substrate. AFM images at different scale for pH=2 are presented for Acol and Tcol in Appendix I and Appendix II respectively. Raising the pH to 3 further accentuated these differences. Acol fibers adopted a wavy, unstructured morphology, with fibrils remaining randomly oriented and poorly interconnected (Figure 44.C). In contrast, Tcol formed a dense, interconnected fibrillar network that resembled a mesh-like scaffold (Figure 45.C), consistent with more advanced stages of fiber growth and maturation. Again, magnification-dependent imaging underscored this divergence: Acol showed loosely associated fiber bundles with no directional preferences (Appendix III.A) and, at a higher resolution, small, isolated fibrils lacking interconnection (Appendix III.C). Tcol, on the other hand, exhibited an organized fibrillar framework at larger scale (Appendix IV.A), while higher magnification images (Appendix IV.C) confirmed the presence of a homogeneously interconnected collagen mesh.

These morphological distinctions align closely with previous investigations into collagen fibrillogenesis and network architecture. Previous work employing shear rheology and computational simulations has shown that fibrillar connectivity and network plasticity are directly governed by the density of intermolecular cross-links and the hierarchical organization

of the fibers (Gisbert et al., 2021). Similarly, studies assessing the influence of polymerization parameters on collagen hydrogel formation have demonstrated that pH and molecular composition critically determine fibrillar assembly and alignment (Antoine et al., 2014). Since the organization of collagen fibers strongly impacts their mechanical resilience and overall structural performance, alignment is now recognized as a central determinant of functional behavior (Antoine et al., 2014). Furthermore, the earliest phases of collagen self-assembly are highly sensitive to environmental factors such as pH and ionic strength, which provides a plausible explanation for the distincts morphologies recorded between atelocollagen and telocollagen in our study (Alizadeh et al., 2022). In particular, the emergence of homogeneous, interconnected mesh-like in telocollagen samples supports the conclusion that telopeptides are essential for stabilizing intermolecular associations and enhancing supramolecular cohesion (Shayegan et al., 2016).

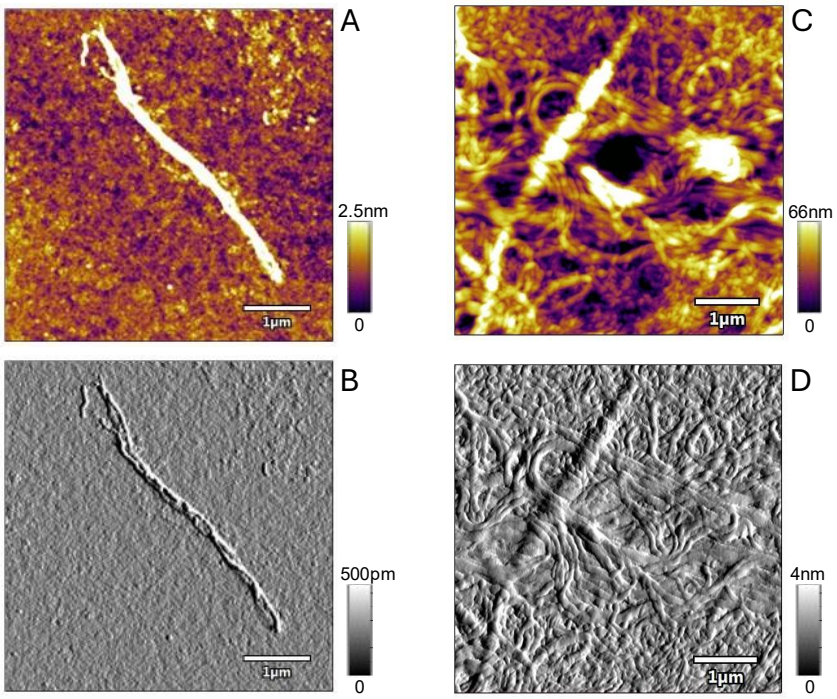

Figure 44: AFM topographic images (A, C) and amplitude images (B, D) of the atelocollagen sample at pH=2 (A, B) and pH=3 (C, D) . A and B display small fibrils without any network formation. C and D show loosely twisted fibrils forming smaller mesh works than telocollagen fibrils.

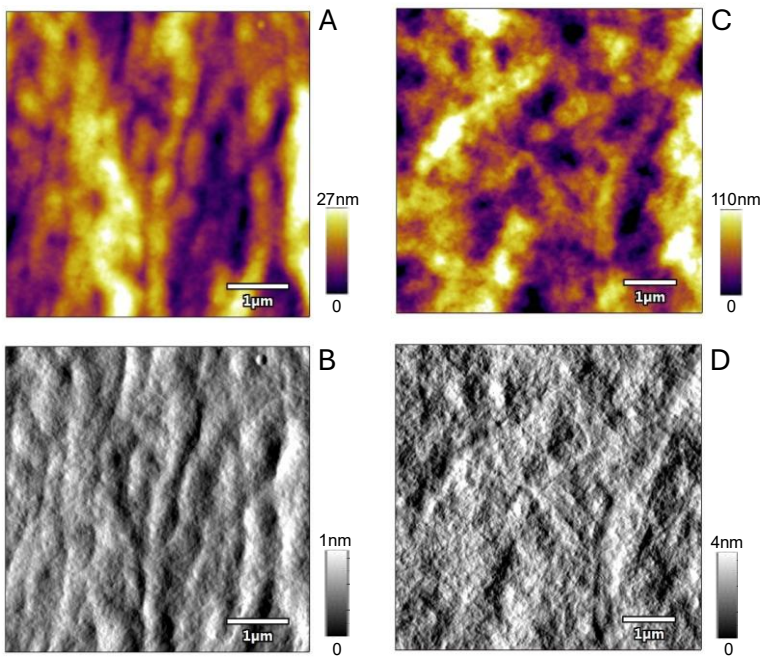

Figure 45: AFM topographic images (A, C) and amplitude images (B, D) of the telocollagen sample at pH =2 (A, B) and pH=3 (C, D). A and B display a network of parallel fibrils. C and D show a mesh-like structure

III.3.3 Vibrational Sum Frequency Generation (VSFG) experiments

To get deeper insight on collagen assembly, in complement of the SHS analysis, VSFG experiments were conducted in the spectral window between 1150 and 1700 cm^{-1}, which encompasses the amide I, II and III vibrational bands and vibrational modes of amino-acid side chains. These modes arise from the characteristic molecular vibration of the peptide backbone, primarily C=O stretching (amide I), CH_3 bending and CH_2 scissoring (sidechain) and the C-N/C-C stretching and N-H bending (amide III) and are used to probe the secondary structure of proteins, including the triple-helical organization of collagen. The amide I band is the most widely used vibrational marker to monitor protein conformation, though its interpretation in aqueous environments is often complicated as it is overlapping with the strong water bending mode near 1640-1645 cm^{-1} (Barth, 2007). The amide II band is less sensitive to secondary structure and is strongly perturbed by overlapping with side-chain absorptions, such as those from tyrosine, glutamine or asparagine residues (Krimm and Bandekar, 1986). The amide III band has the advantage of being unaffected by water absorption and is highly sensitive to protein conformation (Bandekar, 1992). In addition, several vibrational contributions from amino-acid side chains provide complementary structural information. In type I collagen, the amide III region is particularly distinctive, displaying three main components at approximately 1280, 1240 and 1202 cm^{-1}, with the central feature being the most intense (Frushour and

Koening, 1975; Payne and Veis, 1988). These spectral features are strongly influenced by the unique Gly-X-Y repeat (commonly Gly-Pro-Hyp) of the collagen triple helix, and they serve as highly sensitive markers for monitoring structural integrity or supramolecular assembly (Gelse et al., 2003). In our work, we restrict the analysis to the 1150-1700 cm^{-1} region to simultaneously probe amide I and III vibrations and side-chain mode, thereby gaining a more complete picture of the secondary structure of the collagen assemblies.

III.3.3.1 VSFG spectra of the PPG peptide, Tcol and Acol

In a first step, we compare the VSFG spectra obtained for the peptide model $(PPG)_{10}$, Tcol and Acol at pH=3. These spectra are presented in the figure 46 and reveal clear differences in both peak position and their relative intensity between the different samples and conditions at three polarizations (ppp, ssp, psp).

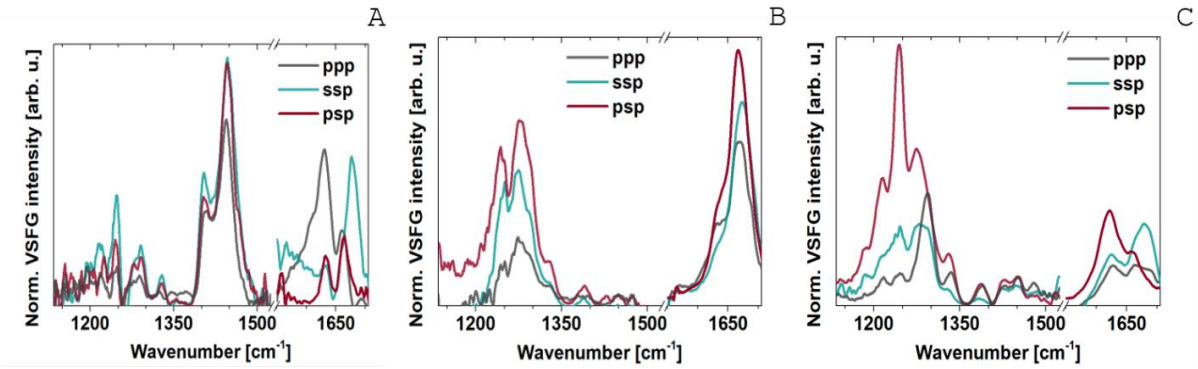

Figure 46: Normalized VSFG spectra recorded in the 1150-1700cm^{-1} spectral range under ppp (black), ssp (cyan) and psp (red) polarization combinations. A) PPP_{10} peptide B) Tcol at pH=3. D) Acol at pH=3.

In the amide III region (1190-1335 cm^{-1}), which is one of the most structurally sensitive parts of the vibrational spectrum of proteins and peptides. which mainly arises from a combination of C-N stretching and N-H bending but also incorporates some substantial contributions from side-chain motions and intermolecular interactions (Bandekar, 1992). This spectral region has long been recognized as a conformational marker, as its frequencies and intensities are highly dependent on secondary structural motifs (Bandekar, 1992). For PPG_{10} peptide (Figure 46.A), the VSFG spectra exhibit a weak signal in the amide III region. However, two distinct proline-associated vibrations, typically at 1270 and 1300 cm^{-1} can be observed that are assigned to coupled C-N/C-C stretching and N-H bending of the backbone (Bandekar, 1992). These features are consistent with the repetitive proline-proline-glycine sequence and reflect the ordered local geometry of the triple helix. The spectral simplicity of the peptide highlights

localized vibrational modes with limited intermolecular coupling, a phenomenon also described in small peptide systems (Schweitzer-Stenner et al., 2002). In Tcol, (Figure 46.B), the amide III region exhibits a more complex profile with intense peaks: a strong feature near 1242 cm^{-1}, followed by intense contributions at 1273 and 1293 cm^{-1}, and a weaker but discernible band at 1328 cm^{-1}. These peaks correspond respectively to backbone N-H bending coupled with C-N stretching, CH_2 wagging modes involving proline residues, and twisting vibrations of proline side chains together with ordered lateral chain contributions (Barth, 2007). In Acol (Figure 46.C), the profile differs from both the peptides and Tcol spectra. A distinct peak at 1217 cm^{-1}, visible also in peptide' spectra, which can be attributed to coupled C-C stretching and N-H bending vibrations associated with intact triple-helical motifs. This suggests that despite the absence of telopeptides, Acol retains a helical backbone signature. A weaker contribution is present at 1242 cm^{-1}, suggesting that the vibrational mode linked to C-N stretching and N-H bending remains less pronounced in atelocollagen than in telocollagen. In contrast, a very intense band is observed at 1293 cm^{-1}, assigned to proline twisting and CH_2 side-chain motions. The strong intensity of this feature highlights the central role of proline residues in the spectral landscape when telopeptides are absent. Finally, a less intense but still discernible band appears at 1328 cm^{-1}, reflecting localized CH_2 wagging/twisting contributions associated with partially ordered side chains. Figure 47.B is an omit, contoured map providing a three-dimensional "envelope" of density around the atoms, allowing one to visualize where the structural elements are located in space and to assess whether the fitted model is consistent with the measured electron density.

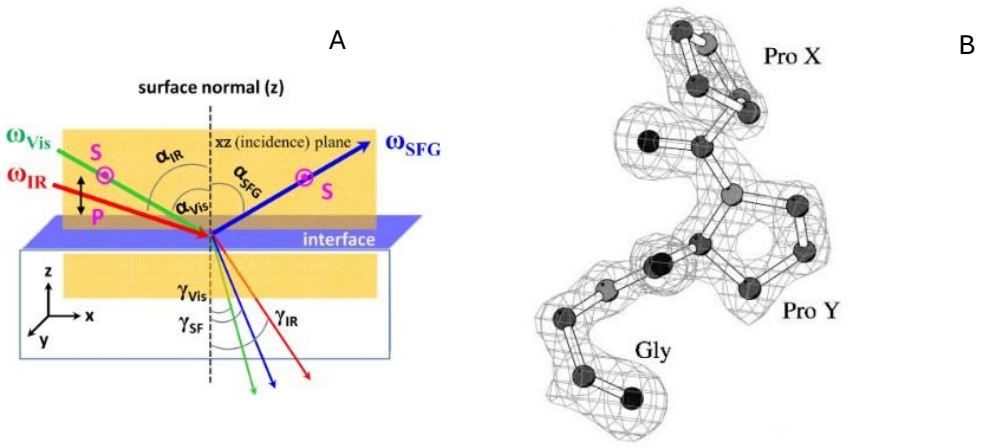

Figure 47: A) Schematic representation of VSFG experimental geometry in reflection mode. The incident visible (ω_{vis}) in green and infrared (ω_{IR}) in red overlap at the interface and generate the SFG (ω_{SFG}) in blue. Angles of incidence are defined relative

to the surface normal (z-axis). S- and P- polarizations are indicated, with S polarized light perpendicular and P polarized light parallel to the plane of incidence. B) Omit map (Fo-Fc) of a representative triplet contoured at 3.5 (From Berisio et al., 2002)

In both Acol and Tcol, the amide III signal shows a clear polarization dependence: it is strongest in psp, weaker in ssp, and minimal in ppp.

In the sidechain region (1380-1450 cm^{-1}), the PPG_{10} peptide displays an intense spectral profile with two strong bands: the CH_3 bending vibration near ~1388 cm^{-1} and the CH_2 scissoring vibration around ~1448 cm^{-1}, both commonly assigned to proline side-chain modes (Bandekar, 1992; Bella, 2016). In Tcol, this region forms a weaker envelope, though both bands remain detectable. Acol shows a same pattern than Tcol: the ~1388 cm^{-1} CH_3 band and the ~1448 cm^{-1} CH_2 scissoring band are weaker but still detectable. This suggests that even without telopeptides, methylene groups can adopt relatively ordered configurations, and that fibrillar cohesion can also emerge from backbone-side-chain interactions intrinsic to the triple helix (Kadler et al., 1996). Overall, this region is much less intense in Tcol and Acol than in the peptide.

The amide I band, typically ranging from 1600 to 1700 cm^{-1}, is a crucial spectral marker used for assessing protein secondary structure, as it predominantly arises from C=O stretching vibrations coupled with N-H bending modes (Krimm & Bandekar, 1986; Barth, 2007; Lorenz-Fonfría, 2020). Its high sensitivity to alterations in molecular geometry and hydrogen-bonding patterns enables it to serve as a reliable probe of protein conformational states (Baronio et al., 2020; Roeters et al., 2013). The amide I band has been extensively characterized in collagen studies due to its importance in reflecting structural integrity and dynamics (de Campos Vidal & Mello, 2011; Okuyama, 2008; Johansson & Castner, 2010).

In the vibrational spectra of the PPG_{10}, the amide I band is dominated by two peaks: for the ppp polarization one centered 1632 cm^{-1} and an equivalent contribution in the ssp spectra around 1670 cm^{-1}. This spectral orientation provides a structural fingerprint of the collagen-like triple helix. The relatively high intensity observed in ppp polarization reflects the strong out-of-plane contribution, indicating that a significant fraction of the carbonyl transition dipoles are oriented radially, with components along the fibril axis, consistent with the organized geometry of the triple helix. However, as emphasized by Lazarev et al. (1985), the amide I band in collagen is inherently complex, with multiple overlapping components influenced by sequence and environment, which complicates a straightforward structural interpretation. Taken together, the

amide I profile of the PPG_{10} peptide shows two well-defined components near 1630 and 1670 cm^{-1}, a spectroscopic signature consistent with an intact triple-helical state (Krimm & Bandekar, 1986; Lorenz-Fonfría, 2020). For Tcol, notable spectral changes compared to the peptides are observed in the amide I region. The dominant feature is now an intense band centered at 1660-1670 cm^{-1}, which is most pronounced in the psp polarization. The 1630 cm^{-1} component no longer appears as a distinct maximum but rather as a shoulder. The persistence of a shoulder at 1630 cm^{-1}, particularly in the psp spectra, reflects residual triple-helical domains with intact hydrogen-bonded C=O stretches (Barth, 2007; Okuyama, 2008). The distinct spectral patterns for the PPG_{10} peptide and Tcol underscore the impact of supramolecular packing in native collagen, where backbone modes lose centrosymmetry and reorganize anisotropically during fibrillar assembly (Johansson & Koelsch, 2014; Johansson & Castner, 2010). Acol exhibits spectral differences compared to the Tcol or peptide spectra. The amide I region here is characterized by a dual peak pattern around 1630 and 1660 cm^{-1}. The 1630 cm^{-1} component appears as a distinct peak, with maximal intensity at psp polarization. This dual-peak pattern, with the same vibrations appearing for the peptide and Tcol, but at much lower intensities reflect an altered structure that could be linked to the absence of telopeptides, which normally stabilize interhelical coupling and enforce axial alignment (Holmes et al., 2017; Maher et al., 2022). Removal of telopeptides weakens cooperative vibrational coupling and

reduces fibrillar order, yielding a spectral signature in the amide I region characterized by two distinct peaks, contrasting with Tcol.

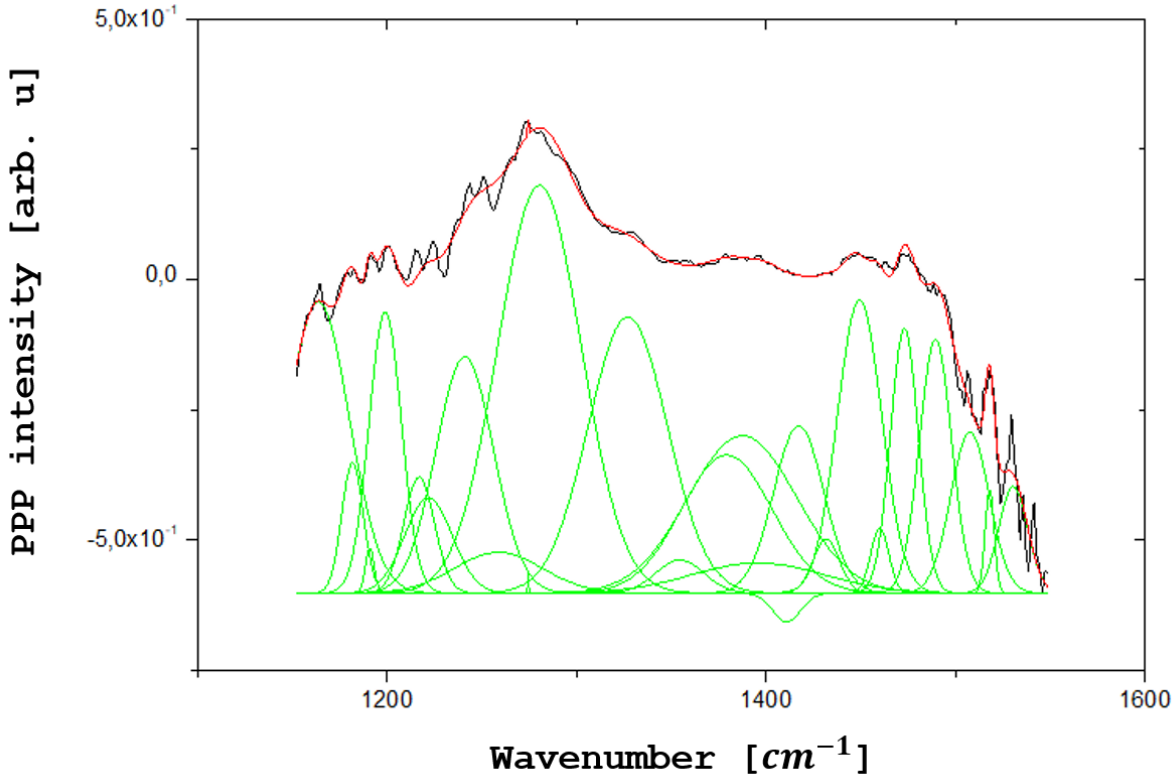

Figure 48: Example of Gaussian fitting procedure applied to the ppp-polarized VSFG spectrum of collagen. The experimental spectrum (black line) is reproduced by the global fit (red line), obtained as the sum of individual Gaussian components (green curves). This deconvolution allows accurate determination of peak positions and relative intensities, which were subsequently used to select representative vibrational modes.

To quantitatively extract orientational information, the spectral complexity observed across the amide I, II and III regions must be reduced to a set of representative vibrational modes. Because the full VSFG spectra contains multiple overlapping contributions, we first determined the peak position by performing Gaussian fits of the experimental spectra. An example of such a fit is shown in figure 48, while the complete sets of fits are provided in the Appendix V.

From these fits, we retained only a subset of well-defined and reproducible peaks that can be reliably tracked across samples and for the three polarizations. For Tcol and Acol, 10 characteristic peaks were selected based on their spectral clarity, reproducibility and biological relevance in ligh of previous IR and Raman studies of collagen (Krimm & Bandekar, 1986; Frank et al., 2007; Okuyama et al., 2008). For the PPG_{10} peptide, 8 peaks were selected with their exact position that could differ slightly due to distinct backbone environments and reduced

supramolecular constraints. These representative bands, presented in table 4, provide a consistent framework for quantitative comparison and for determining tilt angle (θ), defined here as the inclination of the vibrational dipole moment with respect to the surface normal (here also the fibril axis).

Peak position (cm^{-1})	Binding type	Peptide	Tcol	Acol
1217	C-C stretch + N-H bend (Amide III), intact triple helix	+		+
1242	Amide III, N-H bending + C-N stretch, helix structure	+	++	+
1273	CH_2 wagging/ Amide III, proline	+	++	
1293	Amide III or CH_2 twisting of proline		++	++
1328	CH_2 wagging twisting - ordered side chains		+	+
1388	CH_3 bending (methyl group of proline)	++	+	+
1448	CH_2 scissoring, lateral side chain marker	++	+	+
1632	C=O stretch, triple helix, Amide I	++	++	++
1669	Disordered chain (Amide I)	++	++	++
1674	Weakly coupled C=O	++	++	++

Table 4: Selected vibrational peaks of the measured VSFG spectra (1135-1700 cm^{-1}) and used for orientational analysis. The table lists the peak position, the corresponding vibrational assignment, and the relative intensity observed for the PPG_{10} peptide, Tcol and Acol samples. Symbols indicate the relative presence of each band: "+" denotes the presence of the peak, "++" highlights a comparatively stronger or dominant feature. Peaks were chosen based on their reproducibility across polarizations and their established structural relevance to the collagen backbone and side-chain organization

III.3.3.2 Determination of tilt angle θ

Having identified a consistent set of representative vibrational bands (Table 4) through Gaussian fitting of the experimental spectra, we then used these peaks to quantitatively extract orientational information. In particular, the intensity measured in VSFG for a given polarization configuration can be directly related to the effective second-order susceptibility. In VSFG, the measured effective susceptibility $\chi_{eff}^{(2)}$corresponds to a Fresnel-weighted combination of the macroscopic susceptibilities $\chi_{ijk}^{(2)}$. As explained in Chapter II.3.3.3, in our case the only independent components considered are $\beta_{zzz}$and β_{zxx}. After orientational averaging, however,

these two microscopic elements give rise to four independent macroscopic susceptibilities ($\chi_{zzz}, \chi_{zxx}, \chi_{xxz}, \chi_{xzx}$), which contribute differently depending on the chosen polarization geometry. Thus, the analysis requires fitting four effective β parameters, which represent the combinations of β that reproduce the macroscopic χ elements and are presented in table 5. The fitting procedure was carried out in two steps. First, the ppp spectra was used to determine the optimal set of parameters $\{\beta_{zzz}, \beta_{zxx}, \theta\}$. The tilt angle θ of the helix with respect to the surface normal was treated as a free parameter, while the β values were allowed to vary slightly around literature-derived ratios (Deniset-Besseau et al., 2009; Loison & Simon, 2010). Once a consistent fit was obtained in ppp, these values were fixed and directly applied to the ssp and psp spectra.

Tensor elements	PPG_{10} peptide	Telocollagen	Atelocollagen
β_{zzz}	$1.9 \times 10^{-30}\ esu$	$15.9 \times 10^{-30}\ esu$	$72.5 \times 10^{-30}\ esu$
β_{zxx}	$0.84 \times 10^{-30}\ esu$	$4.4 \times 10^{-30}\ esu$	$21.3 \times 10^{-30}\ esu$
β_{yxz}	$3.21 \times 10^{-30}\ esu$	$12.4 \times 10^{-30}\ esu$	$34.2 \times 10^{-30}\ esu$
β_{zyx}	$0.84 \times 10^{-30}\ esu$	$31.6 \times 10^{-30}\ esu$	$583 \times 10^{-30}\ esu$

Table 5: Extracted hyperpolarizability tensor elements for PPG_{10}, Tcol and Acol obtained from PPP VSFG spectra fitting.

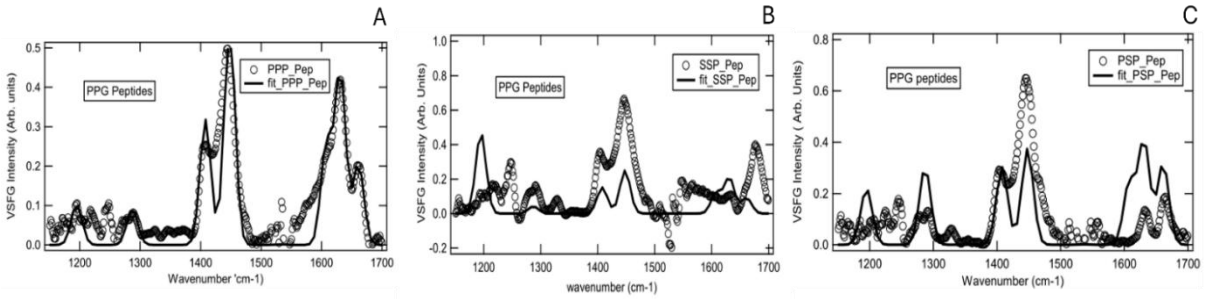

Figure 49: Experimental VSFG spectra (circles) of the PPG peptide model compared with theoretical fits (solid lines) obtained from the polarization-resolved analysis. A) PPP polarization, used as the primary fitting reference to determine the set of β and ϑ parameters. B) SSP polarization, where the same parameters reproduce the spectral lineshape but show deviations in intensity. C) PSP polarization, which includes both achiral and chiral contributions.

In the case of PPG_{10} peptide, the fits of the VSFG spectra are presented in Figure 49. In ppp polarization (Figure 49.A), the fit closely reproduces the experimental spectrum, confirming that the chosen set of β and θ parameters provide a reliable description of the vibrational response. For ssp (Figure 49.B), using the same β and θ values, the fit reproduces the overall lineshape but shows systematic deviations in intensity. In the amide II-III region, the calculated intensity is higher than for the experimental values, while in the amide I region the fit is of largely lower intensity than the signal. These differences indicate that transverse vibrational

contributions are less accurately captured by optimized parameters in ppp. The psp spectrum (Figure 49.C) requires particular attention as it includes both achiral and chiral tensor components.

The equations 50 show that psp polarization probes a linear combination of achiral and chiral contributions, making it particularly sensitive to the chiral vibrational response of the peptide helix. In practice, the fit follows the peak but with some differences in intensity, which is higher near 1200 and 1280 cm^{-1}, while the fit matches well around 1400-1410 cm^{-1}. At 1450 cm^{-1}, the simulated band is weaker than in the experiment. In the amide III region, the vibrational peaks are clearly reproduced by the fit but with higher intensity than measured, reflecting the limitations of applying ppp-optimized parameters to this polarization geometry. Despite these differences in intensity, the peak's fitting in the psp analysis confirms that the model adequately accounts for the combined achiral and chiral contributions of the peptide. Since the model reproduces the spectral shape reasonably well (despite minor deviations), we used the parameters optimized for the ppp polarization to extract the tilt angle θ for each vibrational band. The obtained angles are listed in table 6.

Peak Position	Binding type	Angle θ (degrees)
1195	Amide III N-H bend, C-N stretch, sensitive to the triple helix	-130.1
1287	CH_2 twisting	102.5
1408	CH_3 bending (methyl group)	22.2
1448	CH_2 scissoring, side chain marker	52.4
1534	O-C=N	2.9
1608	Amide I, usually present in well ordered peptide	19.4
1631	C=O stretch (triple helix)	-27.9
1661	C=O stretch	-71

Table 6: Representative vibrational bands used for orientational analysis of the PPG_{10} peptide, with the corresponding tilt angles θ (in degrees) extracted from the fits. Assignments follow established IR and Raman studies of collagen and proline-rich peptides

The sign of θ is often determined by the phase convention used in fitting the $\chi^{(2)}$elements, in many studies of interfacial molecular orientation, θ is defined relative to the surface normal (i.e. molecule normal (Zhuang et al., 1999). In our measurement, what carries structural information is mainly the magnitude and the tilt angle θ across vibrational modes.

Within the amide I region, the bands at 1608 and 1631 cm^{-1} exhibit tilt angles of ~19° and 28° with respect to the surface normal, corresponding to ~70° and 60° relative to the fibril axis. This geometry suggests that the C=O groups are predominantly oriented radially outward rather than

axially. Such an orientation is consistent with the canonical structure of the collagen triple helix, in which many carbonyl groups are exposed to the solvent and participate in inter-chain hydrogen bonding (Berisio et al., 2002; Bella, 2016; Shoulders & Raines, 2009). The higher-frequency component at 1661 cm^{-1} exhibits a near-axial orientation ($\theta \approx 71°$) relative to the fibril axis. This orientation suggests that a subset of carbonyl groups contribute with limited tilt, in contrast to the more radially oriented populations at 1608 and 1631 cm^{-1}. Similar heterogeneity in the amide I band of collagen, involving both achiral and chiral contributions from C=O groups, has been reported in SFG-VS studies (Reiser et al., 2012). In the 1400-1550 cm^{-1} region, the CH_3 bending vibration at 1408 cm^{-1} exhibits a nearly radial orientation ($\theta \approx 22°$), consistent with the placement of proline pyrrolidine rings on the outer surface of the triple helix (Berisio et al., 2002). The CH_2 scissoring at 1448 cm^{-1} shows an intermediate tilt ($\theta \approx 52°$), in line with its assignment to proline methylene vibrations that are sensitive to local conformational constraints (Bandekar, 1992; Shoulders & Raines, 2009). At 1534 cm^{-1}, the extracted tilt is very small, indicating that the transition dipole is nearly perpendicular to the fibril axis. In the amide III region, the 1195 cm^{-1} band is tilted obliquely (~40° off the fibril axis). This vibration arises from a combination of C-N stretching and N-H bending, which is known to be highly sensitive to peptide conformation (Bandekar, 1992; Schweitzer-Stenner et al., 2002). The vibrational band observed at 1287 cm^{-1} reflects coupling between proline side-chain geometry and the helical backbone. Its near-axial orientation is consistent with the steric constraints imposed by the pyrrolidine ring, which are known to strongly influence both the vibrational characteristics and the stability of the collagen triple helix (Bandekar, 1992; Schweitzer-Stenner et al., 2002).

The same methodology is then applied to Tcol and Acol samples, the results are presented in figure 50.

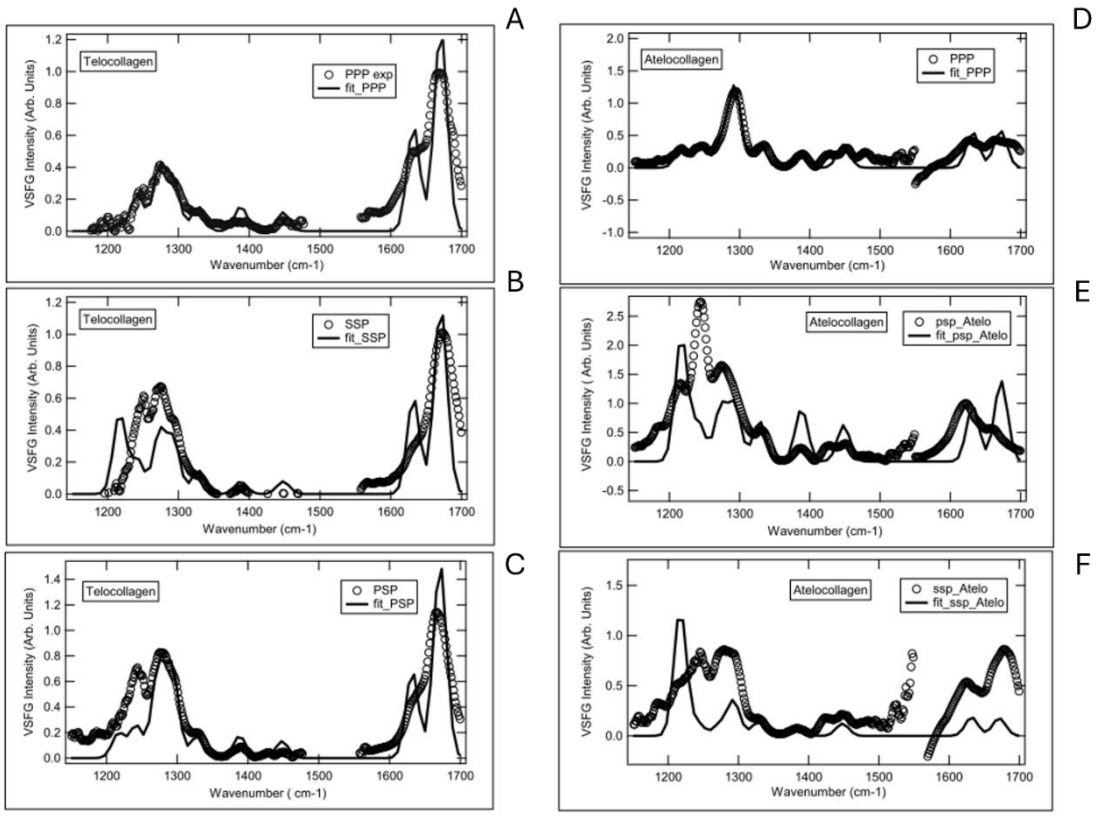

Figure 50: Polarization-resolved VSFG spectra of telocollagen (left) and atelocollagen (right) at pH=3 with corresponding fits. Open circles represent experimental spectra, and solid lines are the fitted curves. A), B) and C) are the spectra for ppp, ssp and psp polarizations respectively for the Tcol. D), E) and F) are the spectra for ppp, ssp and psp polarization respectively for Acol. Fits were optimized for the ppp spectra and then applied without modification to the ssp and psp spectra.

For Tcol, the ppp spectrum (Figure 50.A) is well reproduced by the fit, including the amide I region (1630-1670 cm^{-1}). For the ssp and psp spectra (Figure 50.B and 50.C), the fits also follow the overall lineshape, though some differences appear, notably in the amide III regions, where the calculated intensities exceed the experimental signal. The good agreement in the amide I region across polarizations indicates that the orientational parameters extracted from ppp spectra remain valid, consistent with a more ordered environment in telocollagen. For Acol, the situation differs. While the ppp fit reproduces the spectrum (Figure 50.D), deviations are more pronounced for the other polarizations. In the psp and ssp spectra (Figure 50.E and 50.F), the fits fail to capture relative intensities. This difference may result from our assumption that all fibers on the substrate share the same orientation. In practice, as shown by the AFM images (Figure 51.A1), fibers within the plan can adopt different orientations. Since psp and ssp polarization are probing other direction than ppp, this hypothesis may induce artefact like here.

Peak position (cm^{-1})	Binding type	Telocollagen Angle θ (degrees)	Atelocollagen Angle θ (degrees)
1217	C-C stretch + N-H bend (Amide III), intact triple helix	171.7	176.5
1242	Amide III, N-H bending + C-N stretch, helix structure	7.1	1.4
1273	CH_2 wagging/ Amide III, proline	-95.4	91.6
1293	Amide III or CH_2 twisting of proline	94.5	91.6
1328	CH_2 wagging twisting - ordered side chains	5.8	1.5
1388	CH_3 bending (methyl group of proline)	5.8	89.3
1448	CH_2 scissoring, lateral side chain marker	174.9	1.4
1632	C=O stretch, triple helix, Amide I	11.9	1.7
1669	Disordered chain (Amide I)	13.9	1.3
1674	Weakly coupled C=O	-84.2	-89.2

Table 7: Representative vibrational bands used for orientational analysis in telocollagen and atelocollagen at pH=3, with corresponding tilt angles θ (in degrees) extracted from the fits. Assignments follow established IR and Raman studies of collagen and proline-rich peptides

The extracted θ values, table 7, reveal pronounced differences between Tcol and Acol, underscoring the structural role of telopeptides during fibrillogenesis.

In the amide I region, the 1674 cm^{-1} band, assigned to weakly coupled C=O groups, exhibits tilt angles close to the fibril axis in both Tcol and Acol, indicating a similar near-axial orientation regardless of the presence of telopeptides. The bands at 1632 cm^{-1} (C=O stretch) and 1669 cm^{-1} (disordered chain component) both display small tilt angles in Tcol, while in Acol these values approach 0°, consistent with a collapse toward near-normal orientation of backbone carbonyls upon telopeptide removal. In the amide II/side-chain region, the band at 1448 cm^{-1} is oriented nearly perpendicular to the fibril axis in both Tcol and Acol, whereas the CH_3 bending mode at 1388 cm^{-1} shifts from a near-normal orientation in Tcol to nearly axial in Acol. Since proline methyl groups are located on the periphery of the triple helix and are sensitive to packing (Bandekar, 1992; Shoulders & Raines, 2009), this difference may reflect a change in the supramolecular environment of peripheral side chains when telopeptides are absent. In the amide III region (1200-1350 cm^{-1}), Tcol and Acol exhibit very similar

orientational patterns. The proline-related amide III components near 1273/1293 cm^{-1} remain close to the fibril axis in both samples, while the bands at 1217 and 1242 cm^{-1} are predominantly oriented perpendicular to the fibril axis. These results suggest that removal of the telopeptides has only a limited effect on the local amide III orientation.

Compared to the PPG_{10} peptides, which exhibit consistent tilt anisotropy across amide I, II, and III modes characteristic of an intact triple helix (Persikov et al., 2005), Tcol retains residual anisotropy in the backbone modes (e.g., small tilt at 1632 and 1669 cm^{-1}), while Acol shows tilt angles close to 0° in the same bands. This suggests a reduction of supramolecular alignment despite preservation of the local triple-helical motif.

Overall, the tilt angles measured for Acol and Tcol are highly similar across backbone-related vibrations (amide I and III bands), indicating that removal of telopeptides does not substantially perturb the local orientation of the triple-helical core. The main differences appear in the side-chain vibrational modes (CH_2 and CH_3), where Acol shows altered orientations compared to Tcol. This points to a specific role of telopeptides in regulating supramolecular packing, likely by constraining lateral interactions and stabilizing inter-fibrillar cross-links. In their absence, side chains may adopt slightly different spatial arrangements, reflecting a loss of packing constraints rather than a disruption of the helical backbone.

III.3.3.3 AFM images of collagen constructs

To have a visual picture on the samples studies by VSFG, AFM was employed to characterize the morphology of Acol and Tcol samples deposited on CaF2 substrates. Figure 51 and 52 gather the 3D topographic reconstruction and the corresponding height/amplitude images recorded at three different scan sizes (15 µm, 3µm and 600nm), providing multiscale insight into fibrillar organization. At large scales (15µm, Figure 52.A.1, B.1; 51.A., B.1), marked differences in morphology between the two systems can be observed. Acol displays loosely twisted fibrils forming a non-cross-linked fibrillar network. This behavior is consistent with previous AFM observations on mica, where the presence of telopeptides was found to promote fibril-fibril cross-linking and stabilize mesh-like assemblies (de Lizaraga et al., 2025). Cross-sectional profiles along the fast scan direction (profile 1 and 2 in Figure 51.C) further highlight these differences: atelocollagen exhibits narrow, well-defined height features corresponding to isolated fibrils, while telocollagen presents broader modulations indicative of bundles and cross-linked fibrils.

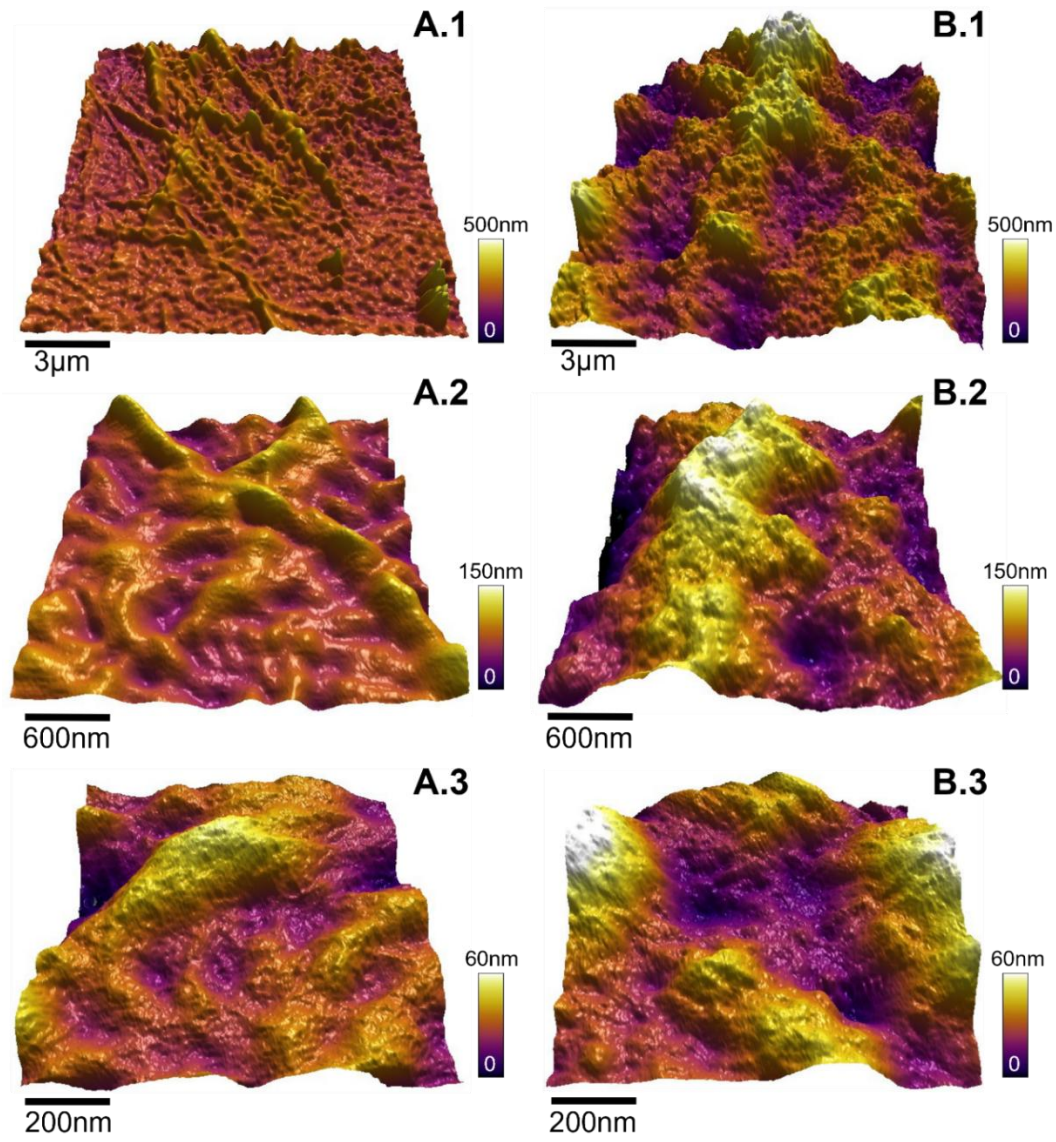

C.1

Acol roughness (nm)

A.1	A.2	A.3
25.9	13.0	8.5

C.2

Tcol roughness (nm)

B.1	B.2	B.3
84.6	32.8	11.5

Figure 51: A) 3D reconstructions of topographic AFM height images of atelocollagen and B) telocollagen on CaF2 at pH=3, at three different scan sizes. Dark brown in the linear color bar represents deeper regions, while white depicts the higher portions of the samples. Atelocollagen shows loosely twisted fibrils forming smaller mesh works than telocollagen fibrils, which present a mesh-like structure. C) Tables displaying the corresponding RMS values. Telocollagen presents higher roughness values than atelocollagen at each different scan size.

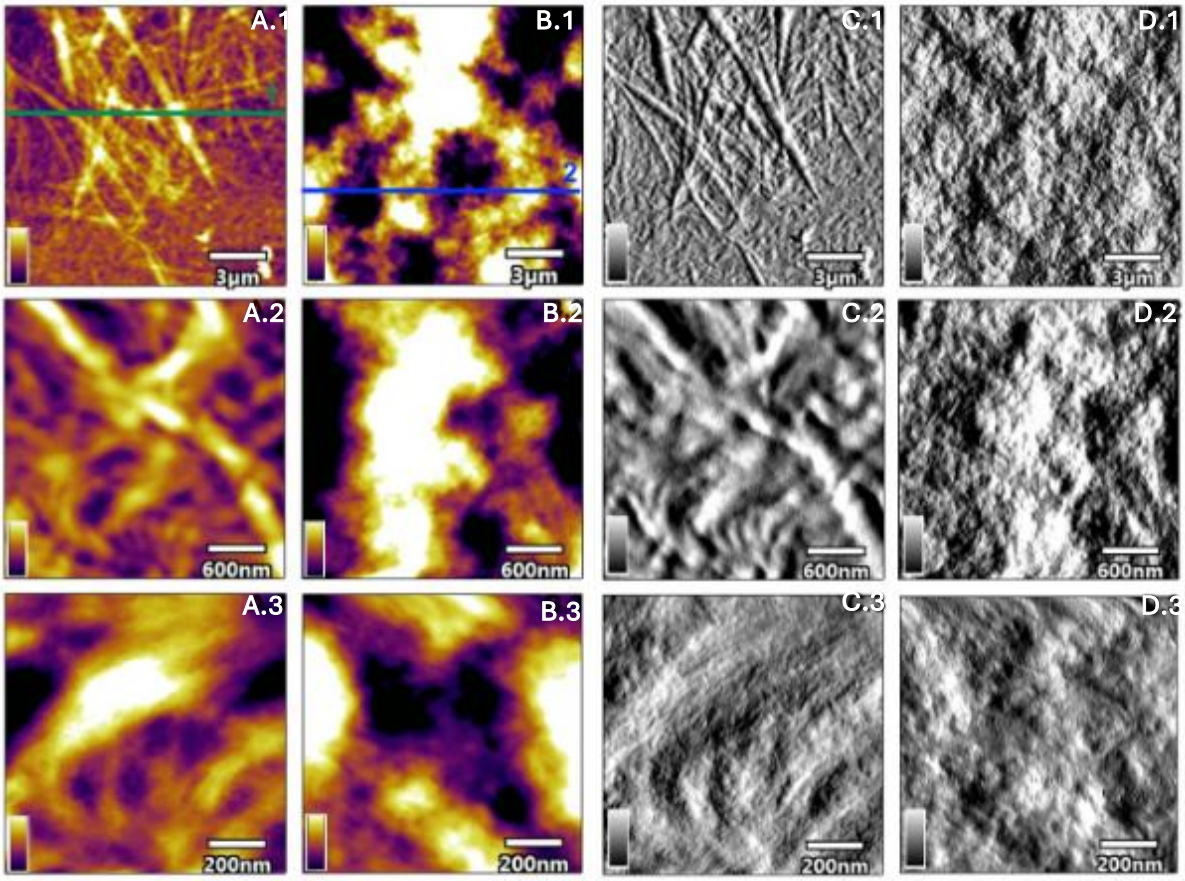

Figure 52: A) AFM height images of atelocollagen and B) telocollagen on CaF2 at pH=3, and at three different scan sizes. Linear brown color bar goes from 0 to 150nm for A.1 and B.1, from 0 to 60nm for A.2 and B.2 and from 0 to 30nm. (C, D) Corresponding amplitude images. Linear grey color bar goes from 0 to 5nm for C.1 and D.1, from 0 to 1nm for C.2 and D.2 and from 0 to 500pm for C.3 and D.3. Both height and amplitude images highlight the fact that Acol fibers adopt a wavy and non-cross-linked arranged structure while Tcol sample present a cross-linked, mesh-like fibrillar assembly.

At intermediate and small scales (600nm and 200nm, Figure 52.A.2-A.3, B.2-B.3), Tcol consistently presents higher surface roughness (RMS values, Tables C.1 and C.2) compared to Acol, in agreement with the formation of a robust, interconnected mesh-work. By contrast, atelocollagen retains a smoother and more heterogeneous topography, reflecting reduced supramolecular constraints. AFM phase images (Fig. 54.A and B) provide complementary information on the viscoelastic properties of the collagen constructs. Phase contrast is significantly enhanced in telocollagen, with bright yellow regions corresponding to stiff cross-linked domains, whereas atelocollagen shows darker regions consistent with softer, less ordered structures. These observations support the interpretation that the removal of telopeptides impairs cross-linking, yielding mechanically weaker fibrillar assembly.

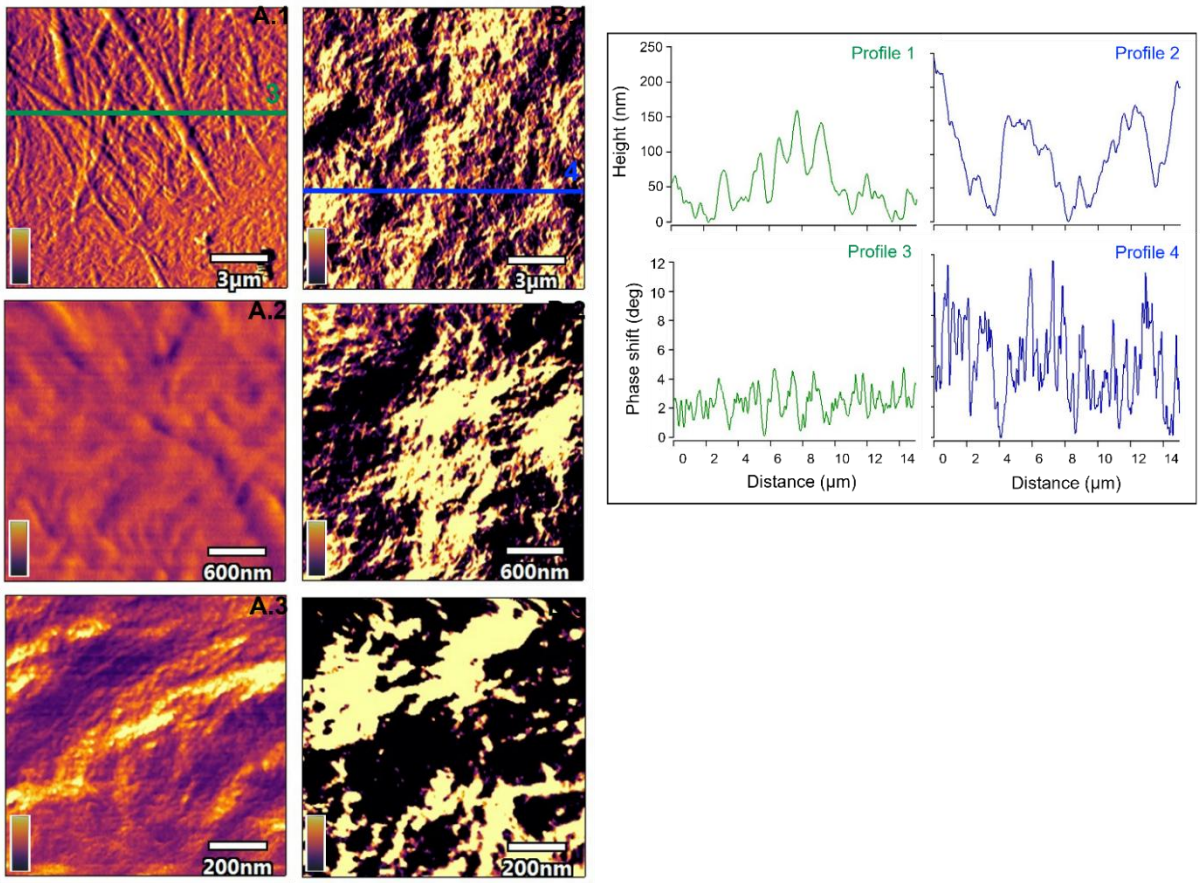

Figure 53: A) AFM phase images of atelocollagen at pH=3 and B) telocollagen on CaF2 at pH=3, and at three different scan sizes. Linear inferno color code bar goes from 0 to 5° for A.1 and B.1, from 0 to 3° for A.2 and B.2 and from 0 to 2° for A.3 and B.3. Black in the color bar represents phase shift values near 0, violet and orange represents phase shift values near the scale medium value, while yellow depicts the higher phase shift values. Yellow regions of the phase images correspond to the stiffer sample areas while black correspond to the softer domains. (C) Height profiles extracted from Fig. 52 A.1 and B.1 panels and phase shifts extracted from Fig 53 A.1 and B.1 panels. Height profiles are in accordance with the measured RMS values, while phase shifts quantified the difference between the viscoelastic behavior of Acol (4° maximum phase shift, 2° average shift) and Tcol samples (12° maximum phase shift, 5° average shift).

The orientational information extracted from VSFG, expressed through the tilt angles θ across vibrational modes, finds direct support in the AFM morphological analysis. In telocollagen, the large positive and negative θ values observed in the amide III region reflect orientational anisotropy, consistent with the cross-linked fibrillar meshwork visualized by AFM. However, these amide III (and also amide I) markers show little difference between Tcol and Acol, indicating that local triple-helical orientation is not the main driver of supramolecular divergence. By contrast, side-chain-related modes in the amide II region exhibit clear differences. In telocollagen, both CH_2 scissoring and CH_3 bending are tilted toward the surface normal (radial orientation), a geometry favorable for lateral contacts and mesh-like packing. In atelocollagen, CH_2 scissoring remains near the axis ($\theta \approx 0°$), while CH_3 bending at 1388 cm^{-1}

is reoriented along the fibril axis. This axial alignment likely reduces lateral interaction sites, weakening supramolecular cohesion.

Taken together, these spectroscopic observations align with AFM images: telocollagen assembles into a denser, cross-linked meshwork, whereas atelocollagen forms more loosely organized fibrils with predominantly axial side-chain orientation and only localized anisotropy. These results suggest that telopeptides specifically contribute to stabilizing supramolecular packing through their effect on side-chain orientation, while their removal reduces orientational coherence and favors a more isotropic network.

IV. General conclusion and perspectives

The work presented in this manuscript relied on nonlinear optical imaging and spectroscopic techniques to explore collagen assembly and structure at different scales. Two distinct but interconnected approaches have been followed. First, as a continuation of C. Manescos' doctoral work, second harmonic generation (SHG) imaging was employed to investigate the morphology and organization of collagen fibers on larger scale and in 3D within spinal cord lesions, where their remodeling plays a crucial role in scar formation and regenerative failure. In a second step, a bottom-up approach was implemented to generate collagen fibers at various degrees of organization and investigate their assembly and structure combining second harmonic scattering (SHS), vibrational sum frequency generation (VSFG) and atomic force microscopy (AFM). This multimodal approach enabled the study of collagen from simplified peptide models to fibrillar assemblies, allowing to get insight into their molecular orientation or supramolecular assembly and symmetry.

The doctoral thesis of C. Manesco, has highlighted collagen as a potential biological marker of fibrosis, emphasizing the importance of understanding its structure and dynamics in the context of SCI. Thus, collagen as the dominant structural component, largely determines the morphology and mechanical properties of the scar and its accumulation and reorganization therefore emerge as central hallmarks of the scarring process. By capturing the spatial orientation and orientation of fibrillar networks, SHG provides critical information on the remodeling of the ECM during scar formation.

SHG imaging was employed as a label-free modality to visualize collagen fiber *ex vivo*. The specificity of SHG for non-centrosymmetric structures made it ideally suited for detecting fibrillar collagen, allowing us to monitor its reorganization within the lesion. In parallel, the two-photon excited fluorescence (2PEF) monitored via multiphoton microscopy provided complementary information on the cellular environment. The simultaneous acquisition of both channels allows us to visualize the structure of the tissue and the presence of fibrosis. Advanced image processing and reconstruction techniques were developed to extract quantitative metrics from SHG images. The 2D analysis method, previously developed by C. Manesco, allowed us to quantify fiber orientation in the plane section. Building on this approach, we then

implemented a 3D method described by Liu et al. (2017). This extension enabled to determine the volumetric directional variance and to extract the angular distribution of collagen fibers.

At tissue level, SHG imaging monitored the presence and progressive remodeling of collagen within SCI. The quantitative analysis performed in both 2D and 3D demonstrates a progressive increase in collagen content and organization. This evolution was particularly evident between 2 and 4 wpi at the lesion site, with an increase of total length of the collagen fibers and their heterogeneous organization. By 6 wpi, the metrics suggested a plateau in collagen deposition, consistent with the transition toward a reorganization phase, where structural remodeling persists with possibly, a concomitant apparition of new collagen fibrils, but at a slower rate. In the adjacent region of the lesion site (i.e. rostral and caudal) the 2D and 3D analysis diverged, indicating that collagen remodeling outside the lesion site is more heterogeneous than suggested by planar projections. 2D metrics report fiber alignment and density in a planar projection whereas 3D variance reveals depth-dependent collagen microdomains and structural order or disorder that remain hidden in the 2D analysis. These results emphasize that combining 2D and 3D descriptors provides a more complete picture of scar maturation.

In parallel, *in vitro* bottom-up approaches were presented to investigate collagen organization under controlled conditions. SHS was described as a powerful tool for quantifying fibrillar symmetry and detecting changes induced by environmental factors such as pH or the presence of telopeptides. VSFG spectroscopy was introduced as a complementary probe of molecular orientation, capable of resolving the anisotropy of specific vibrational modes within the amide bands. Together SHS and VSFG provide a direct link between supramolecular symmetry and molecular orientation, two fundamental aspects of collagen organization.

Unlike SHG imaging, which provides spatially resolved maps, SHS yields information on the global supramolecular organization and symmetry of collagen fibrils in bulk. In this work, SHS was used to monitor the role of pH and telopeptides in collagen self-assembly. At fibrillar scale, SHS experiments were performed on *in vitro* collagen models to probe the effect of pH and telopeptides on supramolecular symmetry. Surprisingly, Tcol displayed a reduced but more stable SHS intensity, contrary to the expectation that stronger cross-linking would yield a higher nonlinear response. This unexpected behavior suggests that telopeptide-mediated stabilization constrains fibrillar organization in a way that reduces scattering efficiency while maintaining structural stability. In contrast, Acol showed a less stable signal, reflecting a more disordered

structure due to the absence of telopeptides. Polarization-resolved SHS further revealed distinct behavior in the supramolecular symmetry of the two types of collagens. Tcol maintained a predominantly dipolar organization, consistent with the presence of telopeptide that favor axial alignment and cooperative packing. Acol tended to evolve toward an octupolar-like symmetry, reflecting the loss of cooperative alignment in the absence of telopeptides. This divergence highlights the crucial role of telopeptides in preserving dipolar symmetry during fibrillogenesis.

To go beyond supramolecular symmetry and probe collagen at the molecular scale, we employed VSFG, which selectively probes vibrational modes that are both IR- and Raman-active. We focused on the amide I (1600-1700 cm^{-1}), II (1500-1600 cm^{-1}) extended to include with side-chain modes (1360-1450 cm^{-1}) and III (1200-1350 cm^{-1}) regions, which are particularly informative for the collagen and PPG_{10} peptides. A fitting procedure was developed to connect the measured effective susceptibilities to the underlying macroscopic tensor components. This enabled us to determine the orientation (tilt angle θ) of specific molecular bonds relative to the surface normal. In this way, we could directly compare Tcol and Acol assemblies, complemented by AFM imaging, which revealed consistent differences in fibril packing and cross-linking between the two types of collagens.

Using this approach, PPG_{10} peptide provided a reference for the triple helix. In the amide I region, the PPG_{10} peptide displayed pronounced anisotropy, with vibrational dipoles oriented both along the fibril axis and in radial directions, reflecting the structural order of the isolated triple helix. In fibrillar collagen, the orientations shifted toward more radial alignment: Tcol retained a small deviation from purely radial geometry, whereas Acol exhibited almost fully radial dipoles. In the amide II region, dominated by side-chain contributions, the PPG_{10} peptide exhibited intermediate tilt angles for both CH_3 and CH_2 modes, reflecting a balance between radial and axial orientations. In fibrillar collagen, the orientations became more constrained: in Tcol, CH_3 and CH_2 dipoles were both radial, indicating a reorganization of side-chain geometry upon fibrillogenesis. In Acol, CH_3 dipoles were almost fully axial whereas CH_2 dipoles were nearly radial, pointing to a breakdown of the balanced orientation seen in PPG_{10} and the more ordered redistribution observed in Tcol. These contrasting behaviors underline the role of telopeptides in maintaining coherent side-chain orientations within the fibrillar network. In the amide III region, the VSFG response of Tcol and Acol was very similar, indicating that the removal of telopeptides has little influence on the orientational organization of the backbone in

this spectral window. This contrasts with the more pronounced differences observed in the amide I and II regions.

Altogether, these results show that while the triple-helical motif is preserved in both collagens, telopeptides are essential to maintain residual orientational order and coherent side-chain organization within the fibrillar state. AFM measurements provided complementary validation of these spectroscopic findings. Height and phase images revealed that Tcol assembles into a cross-linked fibrillar meshwork with higher roughness, consistent with cooperative stabilization, whereas Acol forms loosely arranged, non-cross-linked fibrils with reduced stiffness. The strong correspondence between orientational order revealed by VSFG and morphological features observed by AFM reinforces the conclusion that telopeptides play a central role in collagen assembly. Together with SHS, which probes supramolecular symmetry, VSFG provides direct molecular-scale insight into orientation, offering a comprehensive picture of how telopeptides regulate both structure and stability in collagen fibrils.

In the context of SCI, one of the key perspectives is to continue to explore the time dependent organization of collagen fibers after spinal cord injury. We've observed a dynamic shift in fibers' organization between 4 and 6 wpi, confirming that collagen can serve as a biomarker of the fibrotic scar. The next step is to extend these observations to a later, 12 wpi timepoint. By examining whether reorganization continues or stabilizes over a longer period, we can better understand chronic versus acute scarring phases. Additionally, one of our perspectives is to use BCARS (Broadband Coherent Anti-Stokes Raman Spectroscopy) to obtain richer chemical maps on the injured spinal cord tissue alongside structural data. BCARS is a label-free vibrational imaging technique that extends conventional Raman microscopy by exploiting coherent excitation schemes to overcome the intrinsically weak scattering cross-section of spontaneous Raman (Camp Jr et al., 2014; Camp & Cicerone 2015). It relies on the simultaneous interaction of a narrowband pump and a broadband Stokes beam, generating an anti-Stokes signal across the full fingerprint region in a single acquisition (Hartshorn et al., 2013). Compared to spontaneous Raman, BCARS offers 10-to-100-time faster acquisition, higher signal-to-noise ratios and access to multiple vibrational transitions simultaneously, enabling sensitive and specific detection of proteins, lipids and nucleic acids (Kong et al., 2015; Krafft & Popp, 2019). The ability of BCARS to simultaneously probe ECM components and cellular populations makes it particularly relevant for our study. To relate chemistry to lesion

topology, this imaging method will be performed pairwise on ipsilateral vs. contralateral and along the rostro-caudal axis. Hyperspectral datasets will be acquired for the same post-injury timepoints to track the acute-to-chronic transition. This will enable to detect spatial gradients of extracellular matrix and lipids emanating from the lesion core and assess whether chemical remodeling remains confined or propagates rostro-caudally. Preliminary BCARS images (Figure 54) show the pertinence of the method to respond to these questions and work is ongoing to will refine analysis pipelines to assess not only the lesion core but also perilesional regions of the spinal cord.

On the *in vitro*, bottom-up approach side, we plan to extend the VSFG measurements across a broad range of pH conditions (pH=3 has been done), from 2 to 7 to better replicate physiological environments. Combined with AFM, this will provide clearer insight into how collagen assembly and fibers' growth evolves at different pH values. By systematically comparing atelocollagen and telocollagen at these conditions, we can better understand the role of pH and telopeptides in collagen assembly. Finally, a key future direction is the development of a "scar-in-a-jar" model (Stebler et al., 2021). By using fibroblasts to recreate fibrotic tissue in vitro, we can apply our VSFG and SHS techniques to monitor formation fibrosis over time. This bottom-up approach will allow us to manipulate variables like pH, temperature and ionic strength to see their influence on the fibrillogenesis, ultimately bridging the gap between simple peptide models and complex fibrotic tissue.

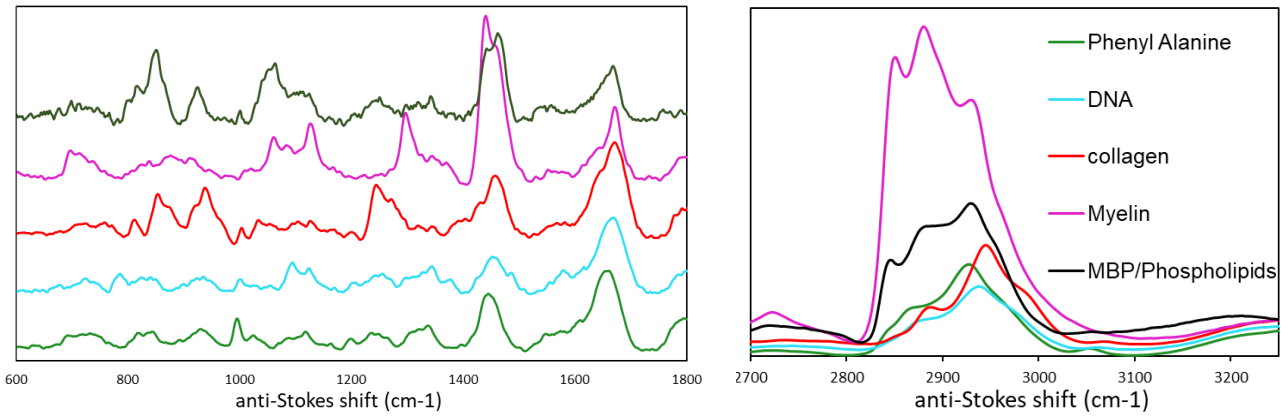

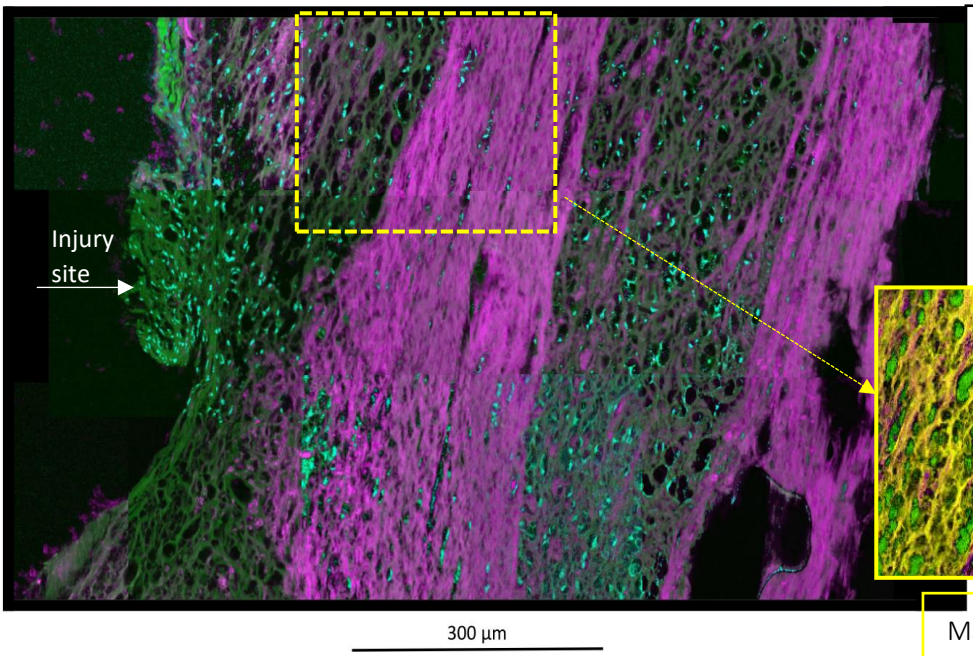

Magenta : Myelin (Lipids 2850 cm^{-1})

Cyan : Cell nucleus (DNA/RNA 786 cm^{-1})

Green : Protein fibrous network (Phenylalanine 1004 cm^{-1})

Magenta : Cholesterol (700 cm^{-1})

Yellow : Collagen (954 cm^{-1})

Green : Myelin binding protein MBP (1044, 1061 cm^{-1})

Figure 54: Broadband coherent anti-Stokes Raman scattering (BCARS) spectra and chemical imaging of mouse spinal cord tissue at 6 weeks post-injury. Spectra were acquired from 50 µm-thick cryosections of Aldh1L1-eGFP transgenic mice to highlight phenylalanine, DNA (cell nuclei), collagen, myelin, and MBP/phospholipids. Representative spectra in the fingerprint region (600-1800 cm^{-1}, top left) and CH-stretch region (2800-3200 cm^{-1}, top right) illustrate the characteristic vibrational signatures of these biomolecular components. False-color BCARS maps (bottom) show the spatial distribution of myelin (magenta), DNA/cells (cyan), and protein fibrous network (green) across the injured spinal cord. The injury site is indicated on the left. The yellow box highlights a zoomed-in view of the transition between white matter and gray matter at the lesion boundary with cholesterol (magenta), collagen (yellow) and myelin binding protein MBP (green)highlighted.

V. References

Adur, J., 2012. Quantitative changes in human epithelial cancers and osteogenesis imperfecta disease detected using nonlinear multicontrast microscopy. J. Biomed. Opt 17, 081407. https://doi.org/10.1117/1.JBO.17.8.081407

Ahuja, C.S., Nori, S., Tetreault, L., Wilson, J., Kwon, B., Harrop, J., Choi, D., Fehlings, M.G., 2017. Traumatic Spinal Cord Injury—Repair and Regeneration. NEUROSURGERY 80, S9–S22. https://doi.org/10.1093/neuros/nyw080

Alizadeh, A., Dyck, S.M., Karimi-Abdolrezaee, S., 2019. Traumatic Spinal Cord Injury: An Overview of Pathophysiology, Models and Acute Injury Mechanisms. Front. Neurol. 10, 282. https://doi.org/10.3389/fneur.2019.00282

Alizadeh, M., Krouglov, S., Barzda, V., 2022. Digital polarimetric second harmonic generation microscopy of partially oriented fiber structures. https://doi.org/10.1101/2022.08.23.504933

Antoine, E.E., Vlachos, P.P., Rylander, M.N., 2014. Review of Collagen I Hydrogels for Bioengineered Tissue Microenvironments: Characterization of Mechanics, Structure, and Transport. Tissue Engineering Part B: Reviews 20, 683–696. https://doi.org/10.1089/ten.teb.2014.0086

Armstrong, J.A., Bloembergen, N., Ducuing, J., Pershan, P.S., 1962. Interactions between Light Waves in a Nonlinear Dielectric. Phys. Rev. 127, 1918–1939. https://doi.org/10.1103/PhysRev.127.1918

Arseni, L., Lombardi, A., Orioli, D., 2018. From Structure to Phenotype: Impact of Collagen Alterations on Human Health. IJMS 19, 1407. https://doi.org/10.3390/ijms19051407

Asselberghs, I., Hennrich, G., Clays, K., 2006. Proton-Triggered Octopolar NLO Chromophores. J. Phys. Chem. A 110, 6271–6275. https://doi.org/10.1021/jp061452m

Ayazi, M., Zivkovic, S., Hammel, G., Stefanovic, B., Ren, Y., 2022. Fibrotic Scar in CNS Injuries: From the Cellular Origins of Fibroblasts to the Molecular Processes of Fibrotic Scar Formation. Cells 11, 2371. https://doi.org/10.3390/cells11152371

Bandekar, J., 1992. Amide modes and protein conformation. Biochimica et Biophysica Acta (BBA) - Protein Structure and Molecular Enzymology 1120, 123–143. https://doi.org/10.1016/0167-4838(92)90261-B

Baronio, C.M., Barth, A., 2020. The Amide I Spectrum of Proteins—Optimization of Transition Dipole Coupling Parameters Using Density Functional Theory Calculations. J. Phys. Chem. B acs.jpcb.9b11793. https://doi.org/10.1021/acs.jpcb.9b11793

Barth, A., 2007. Infrared spectroscopy of proteins. Biochimica et Biophysica Acta (BBA) - Bioenergetics 1767, 1073–1101. https://doi.org/10.1016/j.bbabio.2007.06.004

Barth, A., Zscherp, C., 2002. What vibrations tell about proteins. Quart. Rev. Biophys. 35, 369–430. https://doi.org/10.1017/S0033583502003815

Beck, K., Brodsky, B., n.d., 1998. Supercoiled Protein Motifs: The Collagen Triple-Helix and the a-Helical Coiled Coil. Struct Biol.;122(1-2):17-29. doi: 10.1006/jsbi.1998.3965. PMID: 9724603.

Belkin, M.A., Kulakov, T.A., Ernst, K.-H., Yan, L., Shen, Y.R., 2000. Sum-Frequency Vibrational Spectroscopy on Chiral Liquids: A Novel Technique to Probe Molecular Chirality. Phys. Rev. Lett. 85, 4474–4477. https://doi.org/10.1103/PhysRevLett.85.4474

Bella, J., 2016. Collagen structure: new tricks from a very old dog. Biochemical Journal 473, 1001–1025. https://doi.org/10.1042/BJ20151169

Bellver-Landete, V., Bretheau, F., Mailhot, B., Vallières, N., Lessard, M., Janelle, M.-E., Vernoux, N., Tremblay, M.-È., Fuehrmann, T., Shoichet, M.S., Lacroix, S., 2019. Microglia are an essential component of the neuroprotective scar that forms after spinal cord injury. Nat Commun 10, 518. https://doi.org/10.1038/s41467-019-08446-0

Berisio, R., Vitagliano, L., Mazzarella, L., Zagari, A., 2002. Crystal structure of the collagen triple helix model $[(Pro\text{-}Pro\text{-}Gly)_{10}]_3$. Protein Science 11, 262–270. https://doi.org/10.1110/ps.32602

Bersohn, R., Pao, Y.-H., Frisch, H.L., 1966. Double-Quantum Light Scattering by Molecules. The Journal of Chemical Physics 45, 3184–3198. https://doi.org/10.1063/1.1728092

Bighinati, A., Khalajzeyqami, Z., Baldassarro, V.A., Lorenzini, L., Cescatti, M., Moretti, M., Giardino, L., Calzà, L., 2021. Time-Course Changes of Extracellular Matrix Encoding Genes Expression Level in the Spinal Cord Following Contusion Injury—A Data-Driven Approach. IJMS 22, 1744. https://doi.org/10.3390/ijms22041744

Binnig, G., Quate, C.F., Gerber, Ch., 1986. Atomic Force Microscope. Phys. Rev. Lett. 56, 930–933. https://doi.org/10.1103/PhysRevLett.56.930

Bloembergen, N., Pershan, P.S., 1962. Light Waves at the Boundary of Nonlinear Media. Phys. Rev. 128, 606–622. https://doi.org/10.1103/PhysRev.128.606

Bradbury, E.J., Burnside, E.R., 2019. Moving beyond the glial scar for spinal cord repair. Nat Commun 10, 3879. https://doi.org/10.1038/s41467-019-11707-7

Brasselet, S., 2011. Polarization-resolved nonlinear microscopy: application to structural molecular and biological imaging. Adv. Opt. Photon. 3, 205. https://doi.org/10.1364/AOP.3.000205

Bredfeldt, J.S., Liu, Y., Pehlke, C.A., Conklin, M.W., Szulczewski, J.M., Inman, D.R., Keely, P.J., Nowak, R.D., Mackie, T.R., Eliceiri, K.W., 2014. Computational segmentation of collagen fibers from second-harmonic generation images of breast cancer. J. Biomed. Opt 19, 016007. https://doi.org/10.1117/1.JBO.19.1.016007

Brown, E., McKee, T., diTomaso, E., Pluen, A., Seed, B., Boucher, Y., Jain, R.K., 2003. Dynamic imaging of collagen and its modulation in tumors in vivo using second-harmonic generation. Nat Med 9, 796–800. https://doi.org/10.1038/nm879

Brown, J., Timpl, R.; The Collagen Superfamily. *Int Arch Allergy Immunol* 1 April 1995; 107 (4): 484–490. https://doi.org/10.1159/000237090

Camp Jr, C.H., Cicerone, M.T., 2015. Chemically sensitive bioimaging with coherent Raman scattering. Nature Photon 9, 295–305. https://doi.org/10.1038/nphoton.2015.60

Camp Jr, C.H., Lee, Y.J., Heddleston, J.M., Hartshorn, C.M., Walker, A.R.H., Rich, J.N., Lathia, J.D., Cicerone, M.T., 2014. High-speed coherent Raman fingerprint imaging of biological tissues. Nature Photon 8, 627–634. https://doi.org/10.1038/nphoton.2014.145

Campagnola, P., 2011. Second Harmonic Generation Imaging Microscopy: Applications to Diseases Diagnostics. Anal. Chem. 83, 3224–3231. https://doi.org/10.1021/ac1032325

Campagnola, P.J., Loew, L.M., 2003. Second-harmonic imaging microscopy for visualizing biomolecular arrays in cells, tissues and organisms. Nat Biotechnol 21, 1356–1360. https://doi.org/10.1038/nbt894

Campagnola, P.J., Millard, A.C., Terasaki, M., Hoppe, P.E., Malone, C.J., Mohler, W.A., 2002. Three-Dimensional High-Resolution Second-Harmonic Generation Imaging of Endogenous Structural Proteins in Biological Tissues. Biophysical Journal 82, 493–508. https://doi.org/10.1016/S0006-3495(02)75414-3

Chen, X., Nadiarynkh, O., Plotnikov, S., Campagnola, P.J., 2012. Second harmonic generation microscopy for quantitative analysis of collagen fibrillar structure. Nat Protoc 7, 654–669. https://doi.org/10.1038/nprot.2012.009

Chen, Z., 2010. Investigating buried polymer interfaces using sum frequency generation vibrational spectroscopy. Progress in Polymer Science 35, 1376–1402. https://doi.org/10.1016/j.progpolymsci.2010.07.003

Cheng, L., Cai, B., Lu, D., Zeng, H., 2023. The role of mitochondrial energy metabolism in neuroprotection and axonal regeneration after spinal cord injury. Mitochondrion 69, 57–63. https://doi.org/10.1016/j.mito.2023.01.009

Cheriyan, T., Ryan, D.J., Weinreb, J.H., Cheriyan, J., Paul, J.C., Lafage, V., Kirsch, T., Errico, T.J., 2014. Spinal cord injury models: a review. Spinal Cord 52, 588–595. https://doi.org/10.1038/sc.2014.91

Cox, T.R., Erler, J.T., 2011. Remodeling and homeostasis of the extracellular matrix: implications for fibrotic diseases and cancer. Disease Models & Mechanisms 4, 165–178. https://doi.org/10.1242/dmm.004077

Cowan, P.M., Mcgavin, S., North A.C., 1955 The polypeptide chain configuration of collagen. Nature. Dec 3;176(4492):1062-4. doi: 10.1038/1761062a0. PMID: 13272747.

Cripps, R.A., Lee, B.B., Wing, P., Weerts, E., Mackay, J., Brown, D., 2011. A global map for traumatic spinal cord injury epidemiology: towards a living data repository for injury prevention. Spinal Cord 49, 493–501. https://doi.org/10.1038/sc.2010.146

De Campos Vidal, B., Mello, M.L.S., 2011. Collagen type I amide I band infrared spectroscopy. Micron 42, 283–289. https://doi.org/10.1016/j.micron.2010.09.010

De Lizaraga, J., Martin, M., Salmon, E., Cloitre, T., Gergely, C., Jonin, C., 2025. Probing the Role of Telopeptides in Collagen Fibrillogenesis by Second Harmonic Scattering. J. Phys. Chem. B 129, 9020–9029. https://doi.org/10.1021/acs.jpcb.5c02016

Deniset-Besseau, A., Duboisset, J., Benichou, E., Hache, F., Brevet, P.-F., Schanne-Klein, M.-C., 2009. Measurement of the Second-Order Hyperpolarizability of the Collagen Triple Helix and Determination of Its Physical Origin. J. Phys. Chem. B 113, 13437–13445. https://doi.org/10.1021/jp9046837

Diab, M., Wu, J.-J., Eyre, D.R., 1996. Collagen type IX from human cartilage: a structural profile of intermolecular cross-linking sites. Biochemical Journal 314, 327–332. https://doi.org/10.1042/bj3140327

Dias, D.O., Göritz, C., 2018. Fibrotic scarring following lesions to the central nervous system. Matrix Biology 68–69, 561–570. https://doi.org/10.1016/j.matbio.2018.02.009

Dias, D.O., Kalkitsas, J., Kelahmetoglu, Y., Estrada, C.P., Tatarishvili, J., Holl, D., Jansson, L., Banitalebi, S., Amiry-Moghaddam, M., Ernst, A., Huttner, H.B., Kokaia, Z., Lindvall, O., Brundin, L., Frisén, J., Göritz, C., 2021. Pericyte-derived fibrotic scarring is conserved across diverse central nervous system lesions. Nat Commun 12, 5501. https://doi.org/10.1038/s41467-021-25585-5

Dias, D.O., Kim, H., Holl, D., Werne Solnestam, B., Lundeberg, J., Carlén, M., Göritz, C., Frisén, J., 2018. Reducing Pericyte-Derived Scarring Promotes Recovery after Spinal Cord Injury. Cell 173, 153-165.e22. https://doi.org/10.1016/j.cell.2018.02.004

Dorrier, C.E., Aran, D., Haenelt, E.A., Sheehy, R.N., Hoi, K.K., Pintarić, L., Chen, Y., Lizama, C.O., Cautivo, K.M., Weiner, G.A., Popko, B., Fancy, S.P.J., Arnold, T.D., Daneman, R., 2021. CNS fibroblasts form a fibrotic scar in response to immune cell infiltration. Nat Neurosci 24, 234–244. https://doi.org/10.1038/s41593-020-00770-9

Drzewiecki, K.E., Grisham, D.R., Parmar, A.S., Nanda, V., Shreiber, D.I., 2016. Circular Dichroism Spectroscopy of Collagen Fibrillogenesis: A New Use for an Old Technique. Biophysical Journal 111, 2377–2386. https://doi.org/10.1016/j.bpj.2016.10.023

Duboisset, J., n.d., 2009. Génération de seconde harmonique de biomolécules : des acides aminés aux protéines

Duboisset, J., Deniset-Besseau, A., Benichou, E., Russier-Antoine, I., Lascoux, N., Jonin, C., Hache, F., Schanne-Klein, M.-C., Brevet, P.-F., 2013. A Bottom-Up Approach to Build the

Hyperpolarizability of Peptides and Proteins from their Amino Acids. J. Phys. Chem. B 117, 9877–9881. https://doi.org/10.1021/jp312574q

Duncan, G.J., Manesh, S.B., Hilton, B.J., Assinck, P., Liu, J., Moulson, A., Plemel, J.R., Tetzlaff, W., 2018. Locomotor recovery following contusive spinal cord injury does not require oligodendrocyte remyelination. Nat Commun 9, 3066. https://doi.org/10.1038/s41467-018-05473-1

Egeblad, M., Nakasone, E.S., Werb, Z., 2010. Tumors as Organs: Complex Tissues that Interface with the Entire Organism. Developmental Cell 18, 884–901. https://doi.org/10.1016/j.devcel.2010.05.012

Ellingson, A., Pancheri, N., Schiele, N., 2022. Regulators of collagen crosslinking in developing and adult tendons. eCM 43, 130–152. https://doi.org/10.22203/eCM.v043a11

Eyre, D.R., Wu, J.-J., 2005. Collagen Cross-Links, in: Brinckmann, J., Notbohm, H., Müller, P.K. (Eds.), Collagen, Topics in Current Chemistry. Springer Berlin Heidelberg, Berlin, Heidelberg, pp. 207–229. https://doi.org/10.1007/b103828

Fang, F., Wang, X., Tao, Y., Su, Y., Dan, W., Du, Z., Liu, X., Shen, Y., 2025. Collagen-based biomaterials in neural injury repair: current advances and future perspectives. Collagen & Leather 7, 27. https://doi.org/10.1186/s42825-025-00209-6

Fawcett, J.W., Asher, Richard.A., 1999. The glial scar and central nervous system repair. Brain Research Bulletin 49, 377–391. https://doi.org/10.1016/S0361-9230(99)00072-6

Fichard, A., Kleman, J.-P., Ruggiero, F., 1994. Another Look at Collagen V and Xl Molecules.

Filipp, M., Travis, B., Henry, S., Idzikowski, E., Magnuson, S., Loh, M., Hellenbrand, D., Hanna, A., 2019. Differences in neuroplasticity after spinal cord injury in varying animal models and humans. Neural Regen Res 14, 7. https://doi.org/10.4103/1673-5374.243694

Flack, J., Sharma, K., Xie, J., 2022. Delving into the recent advancements of spinal cord injury treatment: a review of recent progress. Neural Regen Res 17, 283. https://doi.org/10.4103/1673-5374.317961

Foroutan, P., Quarrington, R.D., Jones, C.F., 2024. Mechanisms and risk factors associated with spinal cord injury, facet fracture, and level of dislocation, in occupants with cervical spine dislocations sustained in motor vehicle crashes. Traffic Injury Prevention 25, 1129–1136. https://doi.org/10.1080/15389588.2024.2378133

Franken, P.A., Hill, A.E., Peters, C.W., Weinreich, G., 1961. Generation of Optical Harmonics. Phys. Rev. Lett. 7, 118–119. https://doi.org/10.1103/PhysRevLett.7.118

Freund, I., Deutsch, M., Sprecher, A., 1986. Connective tissue polarity. Optical second-harmonic microscopy, crossed-beam summation, and small-angle scattering in rat-tail tendon. Biophysical Journal 50, 693–712. https://doi.org/10.1016/S0006-3495(86)83510-X

Frushour, B.G., Koenig, J.L., 1975. Raman scattering of collagen, gelatin, and elastin. Biopolymers 14, 379–391. https://doi.org/10.1002/bip.1975.360140211

Gale, M., Pollanen, M.S., Markiewicz, P., Goh, M.C., 1995. Sequential assembly of collagen revealed by atomic force microscopy. Biophysical Journal 68, 2124–2128. https://doi.org/10.1016/S0006-3495(95)80393-0

Galli, R., Sitoci-Ficici, K.H., Uckermann, O., Later, R., Marečková, M., Koch, M., Leipnitz, E., Schackert, G., Koch, E., Gelinsky, M., Steiner, G., Kirsch, M., 2018. Label-free multiphoton microscopy reveals relevant tissue changes induced by alginate hydrogel implantation in rat spinal cord injury. Sci Rep 8, 10841. https://doi.org/10.1038/s41598-018-29140-z

García, R., Pérez, R., 2002. Dynamic atomic force microscopy methods. Surface Science Reports 47, 197–301. https://doi.org/10.1016/S0167-5729(02)00077-8

Gashtrodkhani, A., Ghorbani, S., School of Medicine, Shahroud University of Medical Sciences, Shahroud, Iran., Andalib, S., Research Unit of Neurology, Department of Clinical Research, Faculty of Health Sciences, University of Southern Denmark, Odense, Denmark. AND Department of Neurology, Odense University Hospital, Odense, Denmark. AND Neuroscience Research Center, Trauma Institute, Guilan University of Medical Sciences, Rasht, Iran., 2025. Spinal Cord Injury and Neuroplasticity. IRJNS 10, 0–0. https://doi.org/10.32598/irjns.10.28

Gelse, K., 2003. Collagens—structure, function, and biosynthesis. Advanced Drug Delivery Reviews 55, 1531–1546. https://doi.org/10.1016/j.addr.2003.08.002

Gisbert, V.G., Benaglia, S., Uhlig, M.R., Proksch, R., Garcia, R., 2021. High-Speed Nanomechanical Mapping of the Early Stages of Collagen Growth by Bimodal Force Microscopy. ACS Nano 15, 1850–1857. https://doi.org/10.1021/acsnano.0c10159

Gliksten, L., Yip, P.K., 2023. Current Spinal Cord Injury Animal Models are Too Simplistic for Clinical Translation. Journal of Experimental Neurology 4, 6–10. https://doi.org/10.33696/Neurol.4.068

Gogoi, A., Konwer, S., Zhuo, G.-Y., 2021. Polarimetric Measurements of Surface Chirality Based on Linear and Nonlinear Light Scattering. Front. Chem. 8, 611833. https://doi.org/10.3389/fchem.2020.611833

Göritz, C., Dias, D.O., Tomilin, N., Barbacid, M., Shupliakov, O., Frisén, J., 2011. A Pericyte Origin of Spinal Cord Scar Tissue. Science 333, 238–242. https://doi.org/10.1126/science.1203165

Gutsmann, T., Fantner, G.E., Venturoni, M., Ekani-Nkodo, A., Thompson, J.B., Kindt, J.H., Morse, D.E., Fygenson, D.K., Hansma, P.K., 2003. Evidence that Collagen Fibrils in Tendons Are Inhomogeneously Structured in a Tubelike Manner. Biophysical Journal 84, 2593–2598. https://doi.org/10.1016/S0006-3495(03)75064-4

Guyot-Sionnest, P., Hunt, J.H., Shen, Y.R., 1987. Sum-frequency vibrational spectroscopy of a Langmuir film: Study of molecular orientation of a two-dimensional system. Phys. Rev. Lett. 59, 1597–1600. https://doi.org/10.1103/PhysRevLett.59.1597

Han, Y., Hsu, J., Ge, N.-H., Potma, E.O., 2015. Polarization-Sensitive Sum-Frequency Generation Microscopy of Collagen Fibers. J. Phys. Chem. B 119, 3356–3365. https://doi.org/10.1021/jp511058b

Harris, J.R., Soliakov, A., Lewis, R.J., 2013. In vitro fibrillogenesis of collagen type I in varying ionic and pH conditions. Micron 49, 60–68. https://doi.org/10.1016/j.micron.2013.03.004

Hartshorn, C.M., Lee, Y.J., Camp, C.H., Liu, Z., Heddleston, J., Canfield, N., Rhodes, T.A., Hight Walker, A.R., Marsac, P.J., Cicerone, M.T., 2013. Multicomponent Chemical Imaging of Pharmaceutical Solid Dosage Forms with Broadband CARS Microscopy. Anal. Chem. 85, 8102–8111. https://doi.org/10.1021/ac400671p

Heiner, Z., Der, A., Petrov, V., Mero, M., 2024. Nonlinear vibrational spectrometer for bioapplications featuring narrowband 1-µm pulses and a recycled OPA pump beam. Opt. Express 32, 45029. https://doi.org/10.1364/OE.539940

Heiner, Z., Petrov, V., Mero, M., 2017. Compact, high-repetition-rate source for broadband sum-frequency generation spectroscopy. APL Photonics 2, 066102. https://doi.org/10.1063/1.4983691

Heiner, Z., Wang, L., Petrov, V., Mero, M., 2019. Broadband vibrational sum-frequency generation spectrometer at 100 kHz in the 950-1750 cm^{-1} spectral range utilizing a $LiGaS_2$ optical parametric amplifier. Opt. Express 27, 15289. https://doi.org/10.1364/OE.27.015289

Hirose, C., Akamatsu, N., Domen, K., 1992. Formulas for the analysis of surface sum-frequency generation spectrum by CH stretching modes of methyl and methylene groups. The Journal of Chemical Physics 96, 997–1004. https://doi.org/10.1063/1.462120

Holmes, R., Kirk, S., Tronci, G., Yang, X., Wood, D., 2017. Influence of telopeptides on the structural and physical properties of polymeric and monomeric acid-soluble type I collagen. Materials Science and Engineering: C 77, 823–827. https://doi.org/10.1016/j.msec.2017.03.267

Hörl, D., Rojas Rusak, F., Preusser, F., Tillberg, P., Randel, N., Chhetri, R.K., Cardona, A., Keller, P.J., Harz, H., Leonhardt, H., Treier, M., Preibisch, S., 2019. BigStitcher: reconstructing high-resolution image datasets of cleared and expanded samples. Nat Methods 16, 870–874. https://doi.org/10.1038/s41592-019-0501-0

Hu, X., Xu, W., Ren, Y., Wang, Z., He, X., Huang, R., Ma, B., Zhao, J., Zhu, R., Cheng, L., 2023. Spinal cord injury: molecular mechanisms and therapeutic interventions. Sig Transduct Target Ther 8, 245. https://doi.org/10.1038/s41392-023-01477-6

Jessen, N.A., Munk, A.S.F., Lundgaard, I., Nedergaard, M., 2015. The Glymphatic System: A Beginner's Guide. Neurochem Res 40, 2583–2599. https://doi.org/10.1007/s11064-015-1581-6

Jin, Z., Tian, L., Zhang, Y., Zhang, X., Kang, J., Dong, H., Huang, N., Pan, L., Ning, B., 2022. Apigenin inhibits fibrous scar formation after acute spinal cord injury through TGFβ/SMADs signaling pathway. CNS Neurosci Ther 28, 1883–1894. https://doi.org/10.1111/cns.13929

Johansson, P.K., Castner, D.G., 2019. Vibrational Sum-Frequency Scattering as a Sensitive Approach to Detect Structural Changes in Collagen Fibers Treated with Surfactants. Langmuir 35, 7848–7857. https://doi.org/10.1021/acs.langmuir.9b00412

Johansson, P.K., Koelsch, P., 2014b. Vibrational Sum-Frequency Scattering for Detailed Studies of Collagen Fibers in Aqueous Environments. J. Am. Chem. Soc. 136, 13598–13601. https://doi.org/10.1021/ja508190d

Johnson, C.M., Sugiharto, A.B., Roke, S., 2007. Surface and bulk structure of poly-(lactic acid) films studied by vibrational sum frequency generation spectroscopy. Chemical Physics Letters 449, 191–195. https://doi.org/10.1016/j.cplett.2007.10.061

Jonkman, J.E.N., Swoger, J., Kress, H., Rohrbach, A., Stelzer, E.H.K., 2003. [18] Resolution in optical microscopy, in: Methods in Enzymology. Elsevier, pp. 416–446. https://doi.org/10.1016/S0076-6879(03)60122-9

Kadler, Karl.E., Baldock, C., Bella, J., Boot-Handfort, R.P., 2007. Collagens at a glance, in: Unconventional Collagens. Oxford University PressOxford, pp. 68–72. https://doi.org/10.1093/oso/9780198505457.003.0007

Kalluri, R., 2003. Basement membranes: structure, assembly and role in tumour angiogenesis. Nat Rev Cancer 3, 422–433. https://doi.org/10.1038/nrc1094

Karsdal, M.A., Nielsen, S.H., Leeming, D.J., Langholm, L.L., Nielsen, M.J., Manon-Jensen, T., Siebuhr, A., Gudmann, N.S., Rønnow, S., Sand, J.M., Daniels, S.J., Mortensen, J.H., Schuppan, D., 2016. The good and the bad collagens of fibrosis – Their role in signaling and organ function. Advanced Drug Delivery Reviews 121, 43–56. https://doi.org/10.1016/j.addr.2017.07.014

Kong, K., Kendall, C., Stone, N., Notingher, I., 2015. Raman spectroscopy for medical diagnostics — From in-vitro biofluid assays to in-vivo cancer detection. Advanced Drug Delivery Reviews 89, 121–134. https://doi.org/10.1016/j.addr.2015.03.009

Krafft, C., Popp, J., 2019. Medical needs for translational biophotonics with the focus on Raman-based methods. Transl Biophotonics 1, e201900018. https://doi.org/10.1002/tbio.201900018

Krimm, S., Bandekar, J., 1986. Vibrational Spectroscopy and Conformation of Peptides, Polypeptides, and Proteins, in: Advances in Protein Chemistry. Elsevier, pp. 181–364. https://doi.org/10.1016/S0065-3233(08)60528-8

Kumar, V., Coluccelli, N., Polli, D., 2018. Coherent Optical Spectroscopy/Microscopy and Applications, in: Molecular and Laser Spectroscopy. Elsevier, pp. 87–115. https://doi.org/10.1016/B978-0-12-849883-5.00005-X

Lambert, A.G., Davies, P.B., Neivandt, D.J., 2005. Implementing the Theory of Sum Frequency Generation Vibrational Spectroscopy: A Tutorial Review. Applied Spectroscopy Reviews 40, 103–145. https://doi.org/10.1081/ASR-200038326

Lazarev, Yu.A., Grishkovsky, B.A., Khromova, T.B., 1985. Amide I band of IR spectrum and structure of collagen and related polypeptides. Biopolymers 24, 1449–1478. https://doi.org/10.1002/bip.360240804

Li, Z., Yu, S., Hu, X., Li, Y., You, X., Tian, D., Cheng, L., Zheng, M., Jing, J., 2021. Fibrotic Scar After Spinal Cord Injury: Crosstalk With Other Cells, Cellular Origin, Function, and Mechanism. Front. Cell. Neurosci. 15, 720938. https://doi.org/10.3389/fncel.2021.720938

Li, Z., Yu, S., Liu, Y., Hu, X., Li, Y., Xiao, Z., Chen, Y., Tian, D., Xu, X., Cheng, L., Zheng, M., Jing, J., 2022. SU16f inhibits fibrotic scar formation and facilitates axon regeneration and locomotor function recovery after spinal cord injury by blocking the PDGFRβ pathway. J Neuroinflammation 19, 95. https://doi.org/10.1186/s12974-022-02449-3

Lin, S., Patrawalla, N.Y., Zhai, Y., Dong, P., Kishore, V., Gu, L., 2024. Computational and Experimental Characterization of Aligned Collagen across Varied Crosslinking Degrees. Micromachines 15, 851. https://doi.org/10.3390/mi15070851

Liu, Z., Pouli, D., Sood, D., Sundarakrishnan, A., Hui Mingalone, C.K., Arendt, L.M., Alonzo, C., Quinn, K.P., Kuperwasser, C., Zeng, L., Schnelldorfer, T., Kaplan, D.L., Georgakoudi, I., 2017. Automated quantification of three-dimensional organization of fiber-like structures in biological tissues. Biomaterials 116, 34–47. https://doi.org/10.1016/j.biomaterials.2016.11.041

Liu, Z., Quinn, K.P., Speroni, L., Arendt, L., Kuperwasser, C., Sonnenschein, C., Soto, A.M., Georgakoudi, I., 2015. Rapid three-dimensional quantification of voxel-wise collagen fiber orientation. Biomed. Opt. Express 6, 2294. https://doi.org/10.1364/BOE.6.002294

Lorenz-Fonfria, V.A., 2020. Infrared Difference Spectroscopy of Proteins: From Bands to Bonds. Chem. Rev. 120, 3466–3576. https://doi.org/10.1021/acs.chemrev.9b00449

Loison, C., Simon, D., 2010. Additive Model for the Second Harmonic Generation Hyperpolarizability Applied to a Collagen-Mimicking Peptide $(Pro\text{-}Pro\text{-}Gly)_{10}$. J. Phys. Chem. A 114, 7769–7779. https://doi.org/10.1021/jp100997q

Magonov, S.N., Elings, V., Whangbo, M.-H., 1997. Phase imaging and stiffness in tapping-mode atomic force microscopy. Surface Science Letters 375, L385–L91.

Maher, M.K., White, J.F., Glattauer, V., Yue, Z., Hughes, T.C., Ramshaw, J.A.M., Wallace, G.G., 2022. Variation in Hydrogel Formation and Network Structure for Telo-, Atelo- and Methacrylated Collagens. Polymers 14, 1775. https://doi.org/10.3390/polym14091775

Maiman, T.H., 1960. Stimulated Optical Radiation in Ruby. Nature 187, 493–494. https://doi.org/10.1038/187493a0

Manesco, C., n.d. Etude photonique et nano-mécanique pour le suivi sans marquage de la cicatrice fibrotique dans les lésions de la moelle épinière chez la souris.

Manesco, C., Cloitre, T., Martin, M., Gerber, Y.N., Perrin, F.E., Saavedra-Villanueva, O., Gergely, C., 2025. Undergrowth Collagen Fibers Analysis by Fingerprint Enhancement Method. Biology of the Cell 117, e70001. https://doi.org/10.1111/boc.70001

Manesco, C., Saavedra-Villanueva, O., Martin, M., De Lizaraga, J., Varga, B., Cloitre, T., Gerber, Y.N., Perrin, F.E., Gergely, C., 2023. Organization of collagen fibers and tissue hardening: Markers of fibrotic scarring after spinal cord injury in mice revealed by multiphoton-atomic force microscopy imaging. Nanomedicine: Nanotechnology, Biology and Medicine 53, 102699. https://doi.org/10.1016/j.nano.2023.102699

Marinelli, S., Vacca, V., De Angelis, F., Pieroni, L., Orsini, T., Parisi, C., Soligo, M., Protto, V., Manni, L., Guerrieri, R., Pavone, F., 2019. Innovative mouse model mimicking human-like features of spinal cord injury: efficacy of Docosahexaenoic acid on acute and chronic phases. Sci Rep 9, 8883. https://doi.org/10.1038/s41598-019-45037-x

Merritt, C.H., Taylor, M.A., Yelton, C.J., Ray, S.K., 2019. Economic impact of traumatic spinal cord injuries in the United States. NN 2019. https://doi.org/10.20517/2347-8659.2019.15

Miller, K.S., Connizzo, B.K., Feeney, E., Tucker, J.J., Soslowsky, L.J., 2012. Examining Differences in Local Collagen Fiber Crimp Frequency Throughout Mechanical Testing in a Developmental Mouse Supraspinatus Tendon Model. Journal of Biomechanical Engineering 134, 041004. https://doi.org/10.1115/1.4006538

Mistry, R., Veres, M., Issa, F., 2022. A Systematic Review Comparing Animal and Human Scarring Models. Front. Surg. 9, 711094. https://doi.org/10.3389/fsurg.2022.711094

Morita, A., Hynes, J.T., 2002. A Theoretical Analysis of the Sum Frequency Generation Spectrum of the Water Surface. II. Time-Dependent Approach. J. Phys. Chem. B 106, 673–685. https://doi.org/10.1021/jp0133438

Moretti, L., Stalfort, J., Barker, T.H., Abebayehu, D., 2022. The interplay of fibroblasts, the extracellular matrix, and inflammation in scar formation. Journal of Biological Chemistry 298, 101530. https://doi.org/10.1016/j.jbc.2021.101530

Myllyharju, J., 2004. Collagens, modifying enzymes and their mutations in humans, flies and worms. Trends in Genetics 20, 33–43. https://doi.org/10.1016/j.tig.2003.11.004

Nadiarnykh, O., Plotnikov, S., Mohler, W.A., Kalajzic, I., Redford-Badwal, D., Campagnola, P.J., 2007. Second harmonic generation imaging microscopy studies of osteogenesis imperfecta. J. Biomed. Opt. 12, 051805. https://doi.org/10.1117/1.2799538

Nguyen, K.T., Le Clair, S.V., Ye, S., Chen, Z., 2009. Orientation Determination of Protein Helical Secondary Structures Using Linear and Nonlinear Vibrational Spectroscopy. J. Phys. Chem. B 113, 12169–12180. https://doi.org/10.1021/jp904153z

Nishihara, T., Doty, P., 1958. The sonic fragmentation of collagen macromolecules. Proc. Natl. Acad. Sci. U.S.A. 44, 411–417. https://doi.org/10.1073/pnas.44.5.411

Norenberg, M.D., Smith, J., Marcillo, A., 2004. The Pathology of Human Spinal Cord Injury: Defining the Problems. Journal of Neurotrauma 21, 429–440. https://doi.org/10.1089/089771504323004575

Noristani, H.N., Sabourin, J.C., Boukhaddaoui, H., Chan-Seng, E., Gerber, Y.N., Perrin, F.E., 2016. Spinal cord injury induces astroglial conversion towards neuronal lineage. Mol Neurodegeneration 11, 68. https://doi.org/10.1186/s13024-016-0133-0

Oh, S., Nguyen, Q.D., Chung, K.-H., Lee, H., 2020. Bundling of Collagen Fibrils Using Sodium Sulfate for Biomimetic Cell Culturing. ACS Omega 5, 3444–3452. https://doi.org/10.1021/acsomega.9b03704

Oheim, M., Beaurepaire, E., Chaigneau, E., Mertz, J., Charpak, S., 2001. Two-photon microscopy in brain tissue: parameters influencing the imaging depth. Journal of Neuroscience Methods 111, 29–37. https://doi.org/10.1016/S0165-0270(01)00438-1

Okuyama, K., 2008. Revisiting the Molecular Structure of Collagen. Connective Tissue Research 49, 299–310. https://doi.org/10.1080/03008200802325110

Okuyama, Kenji, Okuyama, Kaoru, Arnott, S., Takayanagi, M., Kakudo, M., 1981. Crystal and molecular structure of a collagen-like polypeptide (Pro-Pro-Gly)10. Journal of Molecular Biology 152, 427–443. https://doi.org/10.1016/0022-2836(81)90252-7

Oudar, J.L., Chemla, D.S., 1977. Hyperpolarizabilities of the nitroanilines and their relations to the excited state dipole moment. The Journal of Chemical Physics 66, 2664–2668. https://doi.org/10.1063/1.434213

Pakshir, P., Hinz, B., 2018. The big five in fibrosis: Macrophages, myofibroblasts, matrix, mechanics, and miscommunication. Matrix Biology 68–69, 81–93. https://doi.org/10.1016/j.matbio.2018.01.019

Patel, N., Kirmi, O., 2009. Anatomy and Imaging of the Normal Meninges. Seminars in Ultrasound, CT and MRI 30, 559–564. https://doi.org/10.1053/j.sult.2009.08.006

Payne, K.J., Veis, A., 1988. Fourier transform ir spectroscopy of collagen and gelatin solutions: Deconvolution of the amide I band for conformational studies. Biopolymers 27, 1749–1760. https://doi.org/10.1002/bip.360271105

Pena, A.-M., 2006. Ge´n´eration de seconde harmonique par le collag`ene et application `a l'´etude de fibroses par microscopie multiphoton.

Pena, A.-M., Boulesteix, T., Dartigalongue, T., Schanne-Klein, M.-C., 2005. Chiroptical Effects in the Second Harmonic Signal of Collagens I and IV. J. Am. Chem. Soc. 127, 10314–10322. https://doi.org/10.1021/ja0520969

Perez, J.-C., Gerber, Y.N., Perrin, F.E., 2021. Dynamic Diversity of Glial Response Among Species in Spinal Cord Injury. Front. Aging Neurosci. 13, 769548. https://doi.org/10.3389/fnagi.2021.769548

Perrin, F.E., Gerber, Y.N (Ed.), 2025. Spine Surgery: General Considerations and Fundamental Concepts Vol. 1, SFCR Experts Series. Springer Nature Switzerland, Cham. https://doi.org/10.1007/978-3-031-85446-0

Persikov, A.V., Ramshaw, J.A.M., Brodsky, B., 2000. Collagen model peptides: Sequence dependence of triple-helix stability. Biopolymers 55, 436–450. https://doi.org/10.1002/1097-0282(2000)55:6<436::AID-BIP1019>3.0.CO;2-D

Plumb, D.A., Dhir, V., Mironov, A., Ferrara, L., Poulsom, R., Kadler, K.E., Thornton, D.J., Briggs, M.D., Boot-Handford, R.P., 2007. Collagen XXVII Is Developmentally Regulated and Forms Thin Fibrillar Structures Distinct from Those of Classical Vertebrate Fibrillar Collagens. Journal of Biological Chemistry 282, 12791–12795. https://doi.org/10.1074/jbc.C700021200

Poulen, G., Perrin, F.E., 2024. Advances in spinal cord injury: insights from non-human primates. Neural Regeneration Research 19, 2354–2364. https://doi.org/10.4103/NRR.NRR-D-23-01505

Prockop, J.D., Kivirikko, K.I., n.d. Collagens: Molecular Biology, Diseases, and Potentials for Therapy.

Provenzano, P.P., Inman, D.R., Eliceiri, K.W., Knittel, J.G., Yan, L., Rueden, C.T., White, J.G., Keely, P.J., 2008. Collagen density promotes mammary tumor initiation and progression. BMC Med 6, 11. https://doi.org/10.1186/1741-7015-6-11

Putman, C.A.J., Van Der Werf, K.O., De Grooth, B.G., Van Hulst, N.F., Greve, J., 1994. Tapping mode atomic force microscopy in liquid. Applied Physics Letters 64, 2454–2456. https://doi.org/10.1063/1.111597

Ramachandran, G.N., Kartha, G., 1955. Structure of Collagen. Nature 176, 593–595. https://doi.org/10.1038/176593a0

Reiser, K.M., McCourt, A.B., Yankelevich, D.R., Knoesen, A., 2012. Structural Origins of Chiral Second-Order Optical Nonlinearity in Collagen: Amide I Band. Biophysical Journal 103, 2177–2186. https://doi.org/10.1016/j.bpj.2012.10.017

Revillod, G., Duboisset, J., Russier-Antoine, I., Benichou, E., Jonin, C., Brevet, P.-F., 2021. Second Harmonic Scattering of Molecular Aggregates. Symmetry 13, 206. https://doi.org/10.3390/sym13020206

Rezakhaniha, R., Agianniotis, A., Schrauwen, J.T.C., Griffa, A., Sage, D., Bouten, C.V.C., Van De Vosse, F.N., Unser, M., Stergiopulos, N., 2012. Experimental investigation of collagen waviness and orientation in the arterial adventitia using confocal laser scanning microscopy. Biomech Model Mechanobiol 11, 461–473. https://doi.org/10.1007/s10237-011-0325-z

Ricard-Blum, S., 2011. The Collagen Family. Cold Spring Harbor Perspectives in Biology 3, a004978–a004978. https://doi.org/10.1101/cshperspect.a004978

Rich, A., Crick, F.H.C., 1961. The molecular structure of collagen. Journal of Molecular Biology 3, 483-IN4. https://doi.org/10.1016/S0022-2836(61)80016-8

Richmond, G.L., 2002. Molecular Bonding and Interactions at Aqueous Surfaces as Probed by Vibrational Sum Frequency Spectroscopy. Chem. Rev. 102, 2693–2724. https://doi.org/10.1021/cr0006876

Rivard, M., Popov, K., Couture, C., Laliberté, M., Bertrand-Grenier, A., Martin, F., Pépin, H., Pfeffer, C.P., Brown, C., Ramunno, L., Légaré, F., 2014. Imaging the noncentrosymmetric structural organization of tendon with Interferometric Second Harmonic Generation microscopy. Journal of Biophotonics 7, 638–646. https://doi.org/10.1002/jbio.201300036

Rocha-Mendoza, I., Yankelevich, D.R., Wang, M., Reiser, K.M., Frank, C.W., Knoesen, A., 2007. Sum Frequency Vibrational Spectroscopy: The Molecular Origins of the Optical Second-Order Nonlinearity of Collagen. Biophysical Journal 93, 4433–4444. https://doi.org/10.1529/biophysj.107.111047

Schweitzer-Stenner, R., Eker, F., Huang, Q., Griebenow, K., Mroz, P.A., Kozlowski, P.M., 2002. Structure Analysis of Dipeptides in Water by Exploring and Utilizing the Structural Sensitivity of Amide III by Polarized Visible Raman, FTIR−Spectroscopy and DFT Based Normal Coordinate Analysis. J. Phys. Chem. B 106, 4294–4304. https://doi.org/10.1021/jp0137118

Shayegan, M., Altindal, T., Kiefl, E., Forde, N.R., 2016. Intact Telopeptides Enhance Interactions between Collagens. Biophysical Journal 111, 2404–2416. https://doi.org/10.1016/j.bpj.2016.10.039

Shcheslavskiy, V.I., Petrov, G.I., Yakovlev, V.V., 2005. Nonlinear optical properties of collagen in solution. Chemical Physics Letters 402, 170–174. https://doi.org/10.1016/j.cplett.2004.12.023

Shen, R., 1984. Principles Of Nonlinear Optics - Y. R. Shen.

Shen, Y.R., 1989. Surface properties probed by second-harmonic and sum-frequency generation. Nature Vol. 337, 519–525.

Shen, Y.R., Ostroverkhov, V., 2006. Sum-Frequency Vibrational Spectroscopy on Water Interfaces: Polar Orientation of Water Molecules at Interfaces. Chem. Rev. 106, 1140–1154. https://doi.org/10.1021/cr040377d

Shin, J., Hur, J., Lee, J.E., Kang, Y.J., Kim, S.J., Kim, S., Choi, H.-Y., 2023. The Efficacy of Atelocollagen to Inhibit Fibrotic Proliferation in Tenon Tissue: In vitro Study. Ophthalmic Res 66, 86–98. https://doi.org/10.1159/000525762

Shoulders, M.D., Raines, R.T., 2009. Collagen Structure and Stability. Annu. Rev. Biochem. 78, 929–958. https://doi.org/10.1146/annurev.biochem.77.032207.120833

Silver, J., Miller, J.H., 2004. Regeneration beyond the glial scar. Nat Rev Neurosci 5, 146–156. https://doi.org/10.1038/nrn1326

Slyker, L., Diamantides, N., Kim, J., Bonassar, L.J., 2022. Mechanical performance of collagen gels is dependent on purity, α1/α2 ratio, and telopeptides. J Biomedical Materials Res 110, 11–20. https://doi.org/10.1002/jbm.a.37261

Soderblom, C., Luo, X., Blumenthal, E., Bray, E., Lyapichev, K., Ramos, J., Krishnan, V., Lai-Hsu, C., Park, K.K., Tsoulfas, P., Lee, J.K., 2013. Perivascular Fibroblasts Form the Fibrotic Scar after Contusive Spinal Cord Injury. J. Neurosci. 33, 13882–13887. https://doi.org/10.1523/JNEUROSCI.2524-13.2013

Sousa, J.P.M., Stratakis, E., Mano, J., Marques, P.A.A.P., 2023. Anisotropic 3D scaffolds for spinal cord guided repair: Current concepts. Biomaterials Advances 148, 213353. https://doi.org/10.1016/j.bioadv.2023.213353

Sterner, R.C., Sterner, R.M., 2023. Immune response following traumatic spinal cord injury: Pathophysiology and therapies. Front. Immunol. 13, 1084101. https://doi.org/10.3389/fimmu.2022.1084101

Stoller, P., Reiser, K.M., Celliers, P.M., Rubenchik, A.M., 2002. Polarization-Modulated Second Harmonic Generation in Collagen. Biophysical Journal 82, 3330–3342. https://doi.org/10.1016/S0006-3495(02)75673-7

Strupler, M., Hernest, M., Fligny, C., Martin, J.-L., Tharaux, P.-L., Schanne-Klein, M.-C., 2008. Second harmonic microscopy to quantify renal interstitial fibrosis and arterial remodeling. J. Biomed. Opt. 13, 054041. https://doi.org/10.1117/1.2981830

Strupler, M., Pena, A.-M., Hernest, M., Tharaux, P.-L., Martin, J.-L., Beaurepaire, E., Schanne-Klein, M.-C., 2007. Second harmonic imaging and scoring of collagen in fibrotic tissues. Opt. Express 15, 4054. https://doi.org/10.1364/OE.15.004054

Sun, S., Bisson, P.J., Bonn, M., Shultz, M.J., Backus, E.H.G., 2019. Phase-Sensitive Sum-Frequency Generation Measurements Using a Femtosecond Nonlinear Interferometer. J. Phys. Chem. C 123, 7266–7270. https://doi.org/10.1021/acs.jpcc.9b00861

Suzuki, H., Sakai, T., 2021. Current Concepts of Stem Cell Therapy for Chronic Spinal Cord Injury. IJMS 22, 7435. https://doi.org/10.3390/ijms22147435

Swartz, E.E., Floyd, R.T., Cendoma, M., n.d. Cervical Spine Functional Anatomy and the Biomechanics of Injury Due to Compressive Loading.

Taufalele, P.V., VanderBurgh, J.A., Muñoz, A., Zanotelli, M.R., Reinhart-King, C.A., 2019. Fiber alignment drives changes in architectural and mechanical features in collagen matrices. PLoS ONE 14, e0216537. https://doi.org/10.1371/journal.pone.0216537

Teulon, C., Tidu, A., Portier, F., Mosser, G., Schanne-Klein, M.-C., 2016. Probing the 3D structure of cornea-like collagen liquid crystals with polarization-resolved SHG microscopy. Opt. Express 24, 16084. https://doi.org/10.1364/OE.24.016084

Tihăuan, B.-M., Pircalabioru, G.G., Axinie (Bucos), M., Marinaș, I.C., Nicoară, A.-C., Măruțescu, L., Oprea, O., Matei, E., Maier, S.S., 2022. Crosslinked Collagenic Scaffold Behavior Evaluation by Physico-Chemical, Mechanical and Biological Assessments in an In Vitro Microenvironment. Polymers 14, 2430. https://doi.org/10.3390/polym14122430

Tran, A.P., Warren, P.M., Silver, J., 2018. The Biology of Regeneration Failure and Success After Spinal Cord Injury. Physiological Reviews 98, 881–917. https://doi.org/10.1152/physrev.00017.2017

Tuer, A.E., Krouglov, S., Prent, N., Cisek, R., Sandkuijl, D., Yasufuku, K., Wilson, B.C., Barzda, V., 2011. Nonlinear Optical Properties of Type I Collagen Fibers Studied by Polarization Dependent Second Harmonic Generation Microscopy. J. Phys. Chem. B 115, 12759–12769. https://doi.org/10.1021/jp206308k

Ünal, M., Sezgin, A.B., 2021. Dura Mater: Anatomy and Clinical Implication. JBBS 11, 239–247. https://doi.org/10.4236/jbbs.2021.1110019

Vanacore, R.M., Friedman, D.B., Ham, A.-J.L., Sundaramoorthy, M., Hudson, B.G., 2005. Identification of S-Hydroxylysyl-methionine as the Covalent Cross-link of the Noncollagenous (NC1) Hexamer of the α1α1α2 Collagen IV Network. Journal of Biological Chemistry 280, 29300–29310. https://doi.org/10.1074/jbc.M502752200

Velling, T., Risteli, J., Wennerberg, K., Mosher, D.F., Johansson, S., 2002. Polymerization of Type I and III Collagens Is Dependent On Fibronectin and Enhanced By Integrins α11β1and α2β1. Journal of Biological Chemistry 277, 37377–37381. https://doi.org/10.1074/jbc.M206286200

Verstappen, K., Aquarius, R., Klymov, A., Wever, K.E., Damveld, L., Leeuwenburgh, S.C.G., Bartels, R.H.M.A., Hooijmans, C.R., Walboomers, X.F., 2022. Systematic Evaluation of Spinal

Cord Injury Animal Models in the Field of Biomaterials. Tissue Engineering Part B: Reviews 28, 1169–1179. https://doi.org/10.1089/ten.teb.2021.0194

Wang, H.-F., Gan †, W., Lu †, R., Rao †, Y., Wu †, B.-H., 2005. Quantitative spectral and orientational analysis in surface sum frequency generation vibrational spectroscopy (SFG-VS). International Reviews in Physical Chemistry 24, 191–256. https://doi.org/10.1080/01442350500225894

Wanner, I.B., Anderson, M.A., Song, B., Levine, J., Fernandez, A., Gray-Thompson, Z., Ao, Y., Sofroniew, M.V., 2013. Glial Scar Borders Are Formed by Newly Proliferated, Elongated Astrocytes That Interact to Corral Inflammatory and Fibrotic Cells via STAT3-Dependent Mechanisms after Spinal Cord Injury. Journal of Neuroscience 33, 12870–12886. https://doi.org/10.1523/JNEUROSCI.2121-13.2013

Wenstrup, R.J., Florer, J.B., Brunskill, E.W., Bell, S.M., Chervoneva, I., Birk, D.E., 2004. Type V Collagen Controls the Initiation of Collagen Fibril Assembly. Journal of Biological Chemistry 279, 53331–53337. https://doi.org/10.1074/jbc.M409622200

Williams, R.M., Zipfel, W.R., Webb, W.W., 2005. Interpreting Second-Harmonic Generation Images of Collagen I Fibrils. Biophysical Journal 88, 1377–1386. https://doi.org/10.1529/biophysj.104.047308

Wu, J., Lu, B., Yang, R., Chen, Y., Chen, X., Li, Y., 2021. EphB2 knockdown decreases the formation of astroglial-fibrotic scars to promote nerve regeneration after spinal cord injury in rats. CNS Neurosci Ther 27, 714–724. https://doi.org/10.1111/cns.13641

Wu, W., He, S., Wu, J., Chen, C., Li, X., Liu, K., Qu, J.Y., 2022. Publisher Correction: Long-term in vivo imaging of mouse spinal cord through an optically cleared intervertebral window. Nat Commun 13, 3930. https://doi.org/10.1038/s41467-022-31648-y

Xiao, X., Deng, Q., Zeng, X., Lai, B.-Q., Ma, Y.-H., Li, G., Zeng, Y.-S., Ding, Y., 2022. Transcription Profiling of a Revealed the Potential Molecular Mechanism of Governor Vessel Electroacupuncture for Spinal Cord Injury in Rats. Neurospine 19, 757–769. https://doi.org/10.14245/ns.2244452.226

Xing, Y., Xiao, Y., Zhao, M., Zhou, J., Zhao, K., Xiao, C., 2025. The role of oxidative stress in spinal cord ischemia reperfusion injury: mechanisms and therapeutic implications. Front. Cell. Neurosci. 19, 1590493. https://doi.org/10.3389/fncel.2025.1590493

Xue, X., Wu, X., Fan, Y., Han, S., Zhang, H., Sun, Y., Yin, Y., Yin, M., Chen, B., Sun, Z., Zhao, S., Zhang, Q., Liu, W., Zhang, J., Li, J., Shi, Y., Xiao, Z., Dai, J., Zhao, Y., 2024. Heterogeneous fibroblasts contribute to fibrotic scar formation after spinal cord injury in mice and monkeys. Nat Commun 15, 6321. https://doi.org/10.1038/s41467-024-50564-x

Yan, E.C.Y., Fu, L., Wang, Z., Liu, W., 2014. Biological Macromolecules at Interfaces Probed by Chiral Vibrational Sum Frequency Generation Spectroscopy. Chem. Rev. 114, 8471–8498. https://doi.org/10.1021/cr4006044

Yao, F., Luo, Y., Liu, Y.-C., Chen, Y.-H., Li, Y.-T., Hu, X.-Y., You, X.-Y., Yu, S.-S., Li, Z.-Y., Chen, L., Tian, D.-S., Zheng, M.-G., Cheng, L., Jing, J.-H., 2022. Imatinib inhibits pericyte-fibroblast transition and inflammation and promotes axon regeneration by blocking the PDGF-BB/PDGFRβ pathway in spinal cord injury. Inflamm Regener 42, 44. https://doi.org/10.1186/s41232-022-00223-9

Zhu, X.D., Suhr, H., Shen, Y.R., 1987. Surface vibrational spectroscopy by infrared-visible sum frequency generation. Phys. Rev. B 35, 3047–3050. https://doi.org/10.1103/PhysRevB.35.3047

Zhuang, X., Miranda, P.B., Kim, D., Shen, Y.R., 1999. Mapping molecular orientation and conformation at interfaces by surface nonlinear optics. Phys. Rev. B 59, 12632–12640. https://doi.org/10.1103/PhysRevB.59.12632

Zipfel, W.R., Williams, R.M., Christie, R., Nikitin, A.Y., Hyman, B.T., Webb, W.W., 2003. Live tissue intrinsic emission microscopy using multiphoton-excited native fluorescence and second harmonic generation. Proc. Natl. Acad. Sci. U.S.A. 100, 7075–7080. https://doi.org/10.1073/pnas.0832308100

Zyss, J., 1993. Molecular engineering implications of rotational invariance in quadratic nonlinear optics: From dipolar to octupolar molecules and materials. The Journal of Chemical Physics 98, 6583–6599. https://doi.org/10.1063/1.464802

Zyss, J., Brasselet, S., 2002. From Dipolar Molecular Engineering to Multipolar Photonic Engineering in Nonlinear Optics, in: Kajzar, F., Reinisch, R. (Eds.), Beam Shaping and Control with Nonlinear Optics, NATO Science Series: B: Kluwer Academic Publishers, Boston, pp. 77–100. https://doi.org/10.1007/0-306-47079-9_3

VI. Appendix

Appendix I

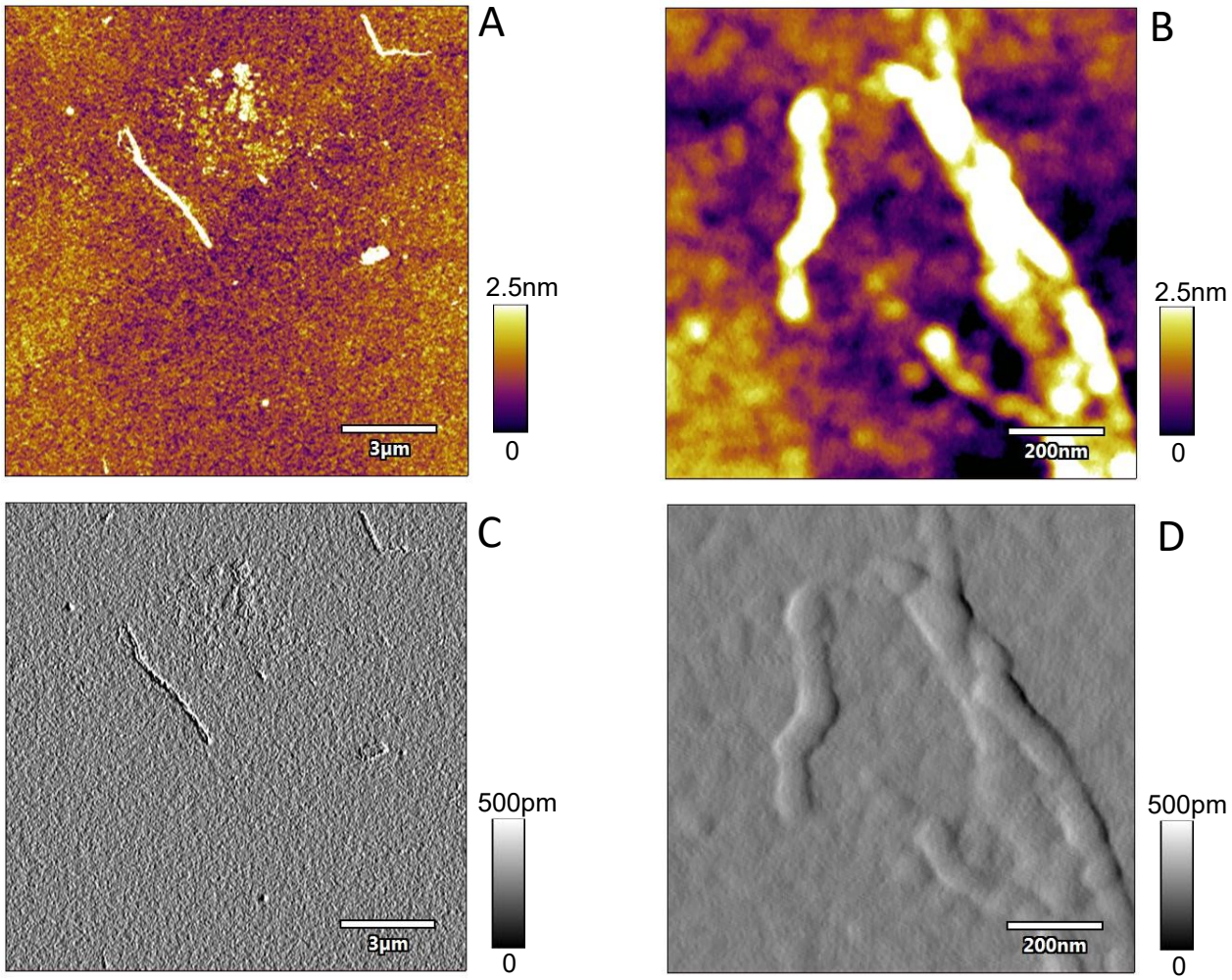

Figure 55: AFM topographic images (A, B) and amplitude images (C, D) at different scales of the atelocollagen sample at pH=2. A and B show individual, isolated fibers with no preferential orientation or apparent organization. C and D display amplitude images, corresponding to respectively A and B, highlighting edges and fine structural features..

Appendix II

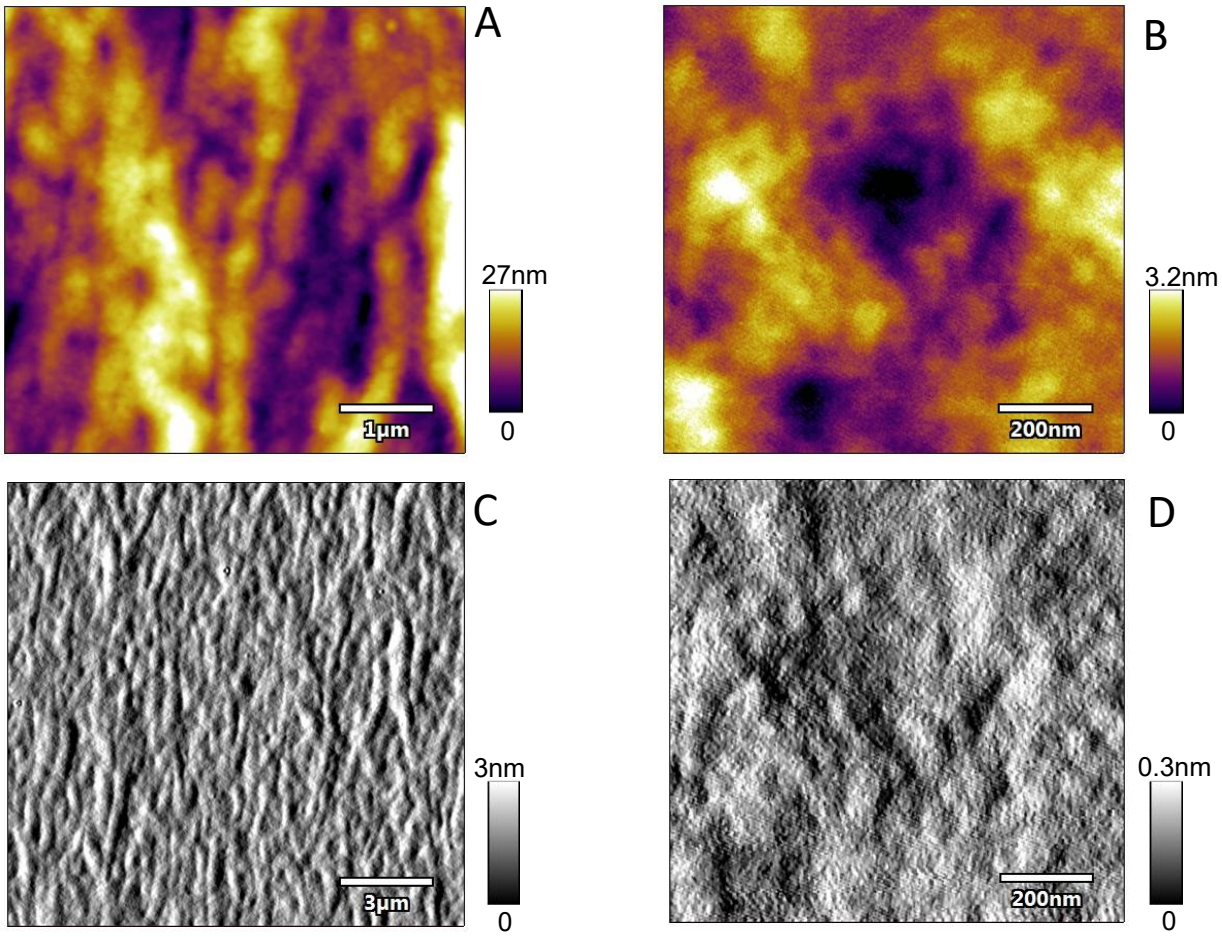

Figure 56: AFM topographic images (A, B) and amplitude images (C, D) at different scales of the telocollagen sample at pH=2. A and B reveal a structured organization of Tcol, characterized by parallel fibers covering all the area. C and D display amplitude images, corresponding to respectively A and B, highlighting edges and fine structural features.

Appendix III

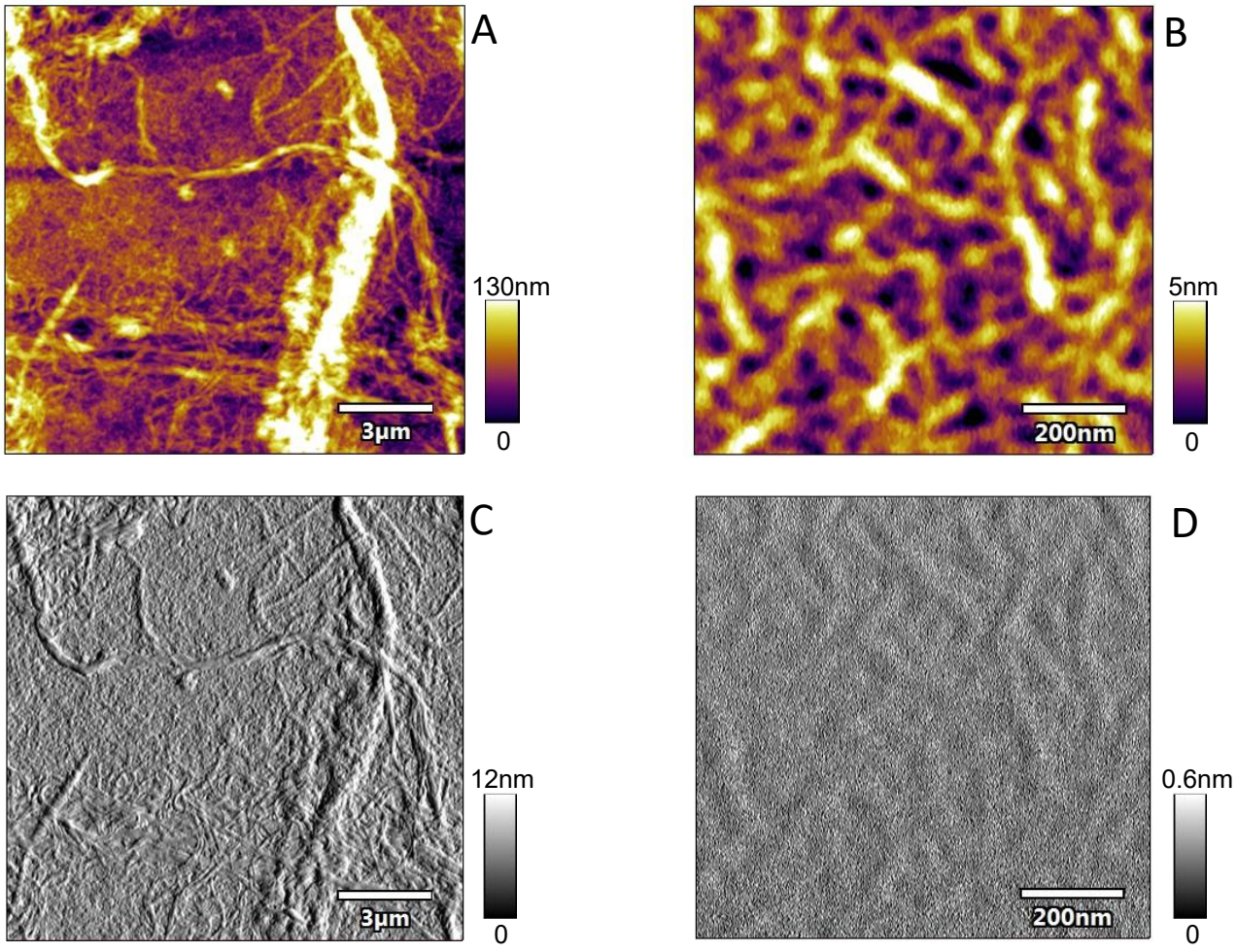

Figure 57: AFM topographic images (A, B) and amplitude images (C, D) at different scales of the atelocollagen sample at pH=3. A and C display bundles of fiber, with no preferential orientation. and B and D at a lower scale shows smaller fibers with no interconnection. C and D display amplitude images, corresponding to respectively A and B, highlighting edges and fine structural features.

Appendix IV

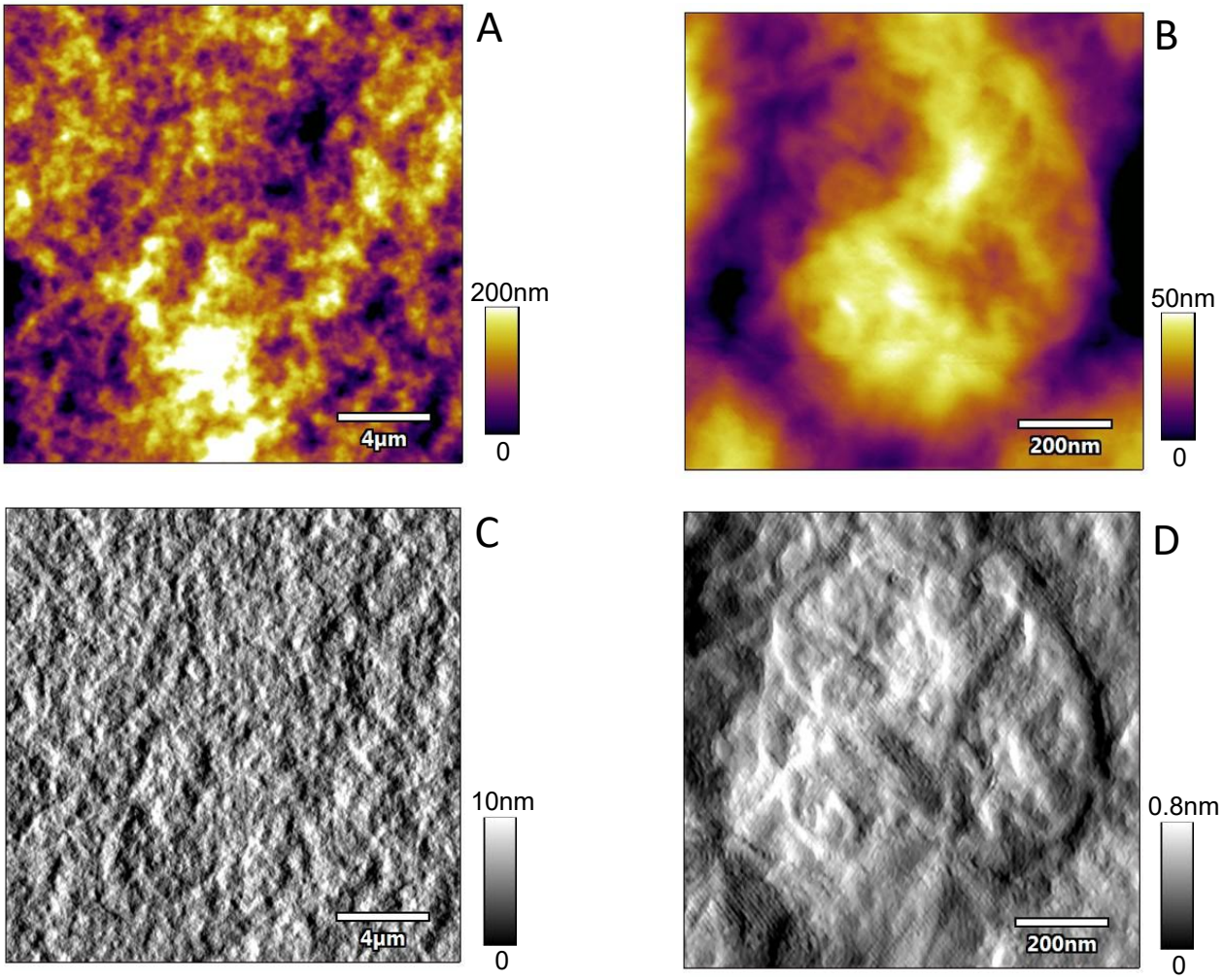

Figure 58: AFM topographic images (A, B) and amplitude images (C, D) at different scales of the telocollagen sample at pH=3. A and C exhibit an homogeneous network of fibers, which is confirmed by images at lower scale (B and D) where we can see interconnected fibers. C and D display amplitude images, corresponding to respectively A and B, highlighting edges and fine structural features.

Appendix V

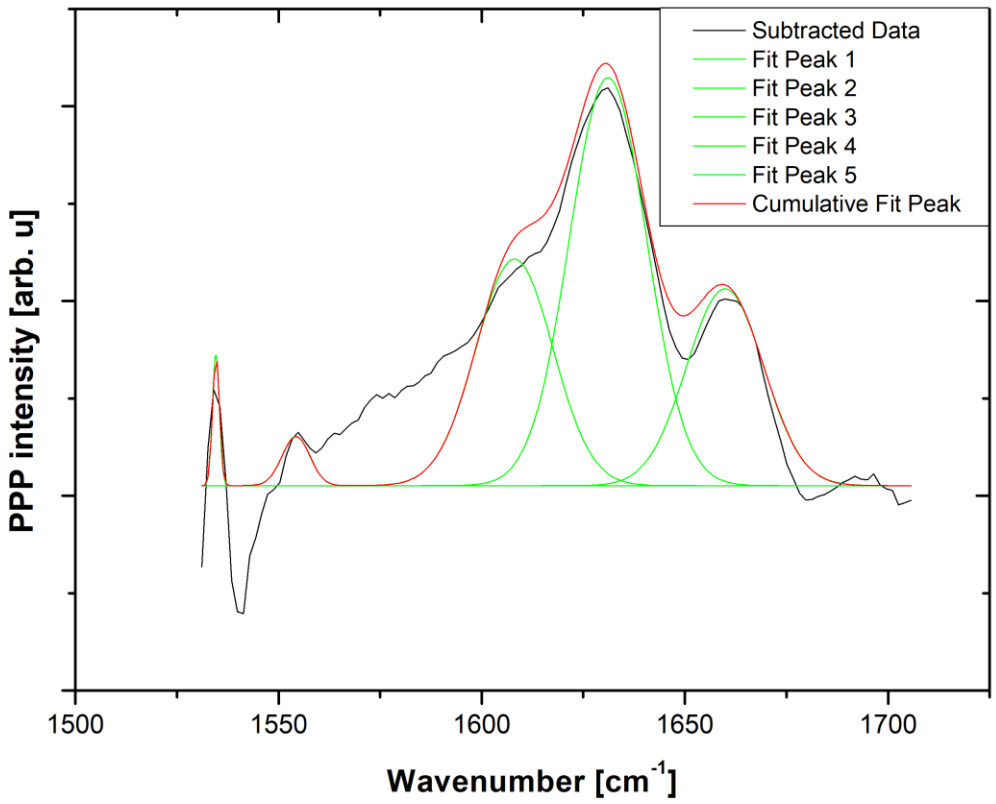

Figure 59: Gaussian fitting procedure applied to the ppp-polarized VSFG spectrum of PPG_{10} amide I band. The experimental spectrum (black line) is reproduced by the global fit (red line), obtained as the sum of individual Gaussian components (green curves).

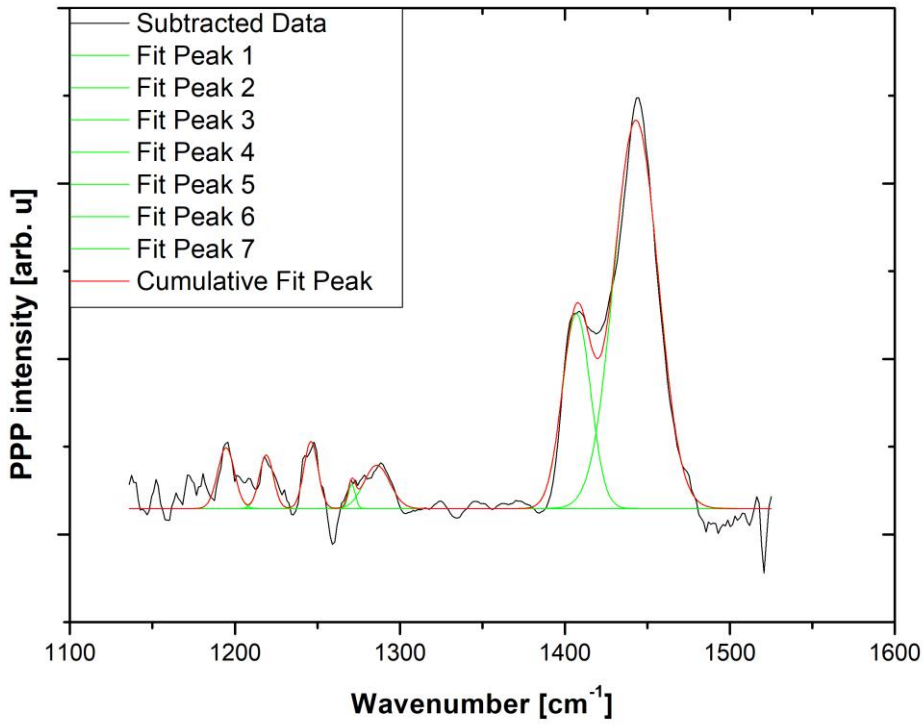

Figure 60: Gaussian fitting procedure applied to the ppp-polarized VSFG spectrum of PPG_{10} amide II and III bands. The experimental spectrum (black line) is reproduced by the global fit (red line), obtained as the sum of individual Gaussian components (green curves).

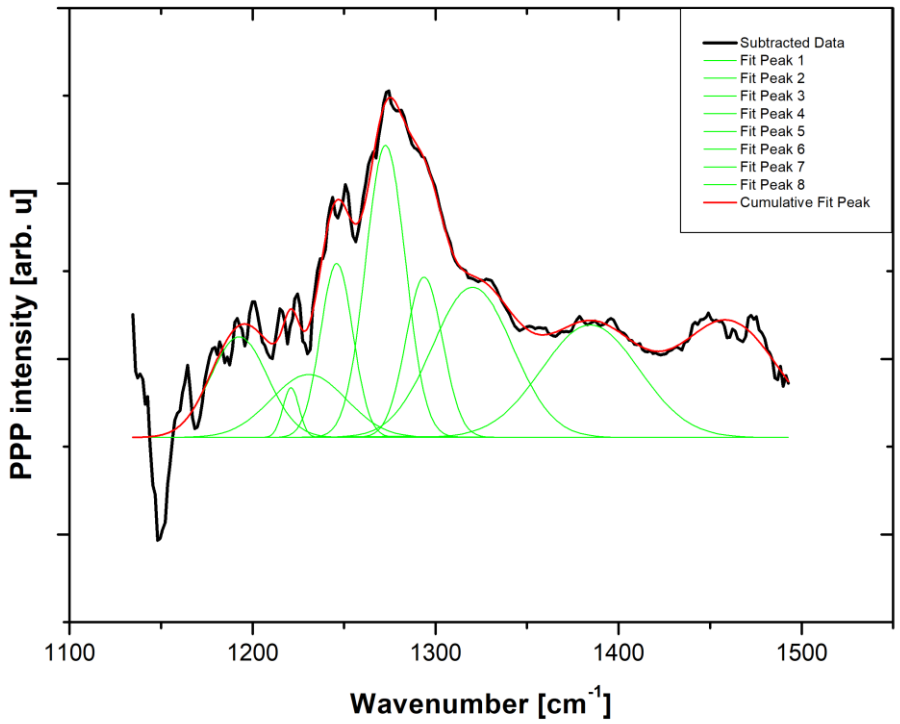

Figure 61: Gaussian fitting procedure applied to the ppp-polarized VSFG spectrum of Tcol amide II and III bands. The experimental spectrum (black line) is reproduced by the global fit (red line), obtained as the sum of individual Gaussian components (green curves).

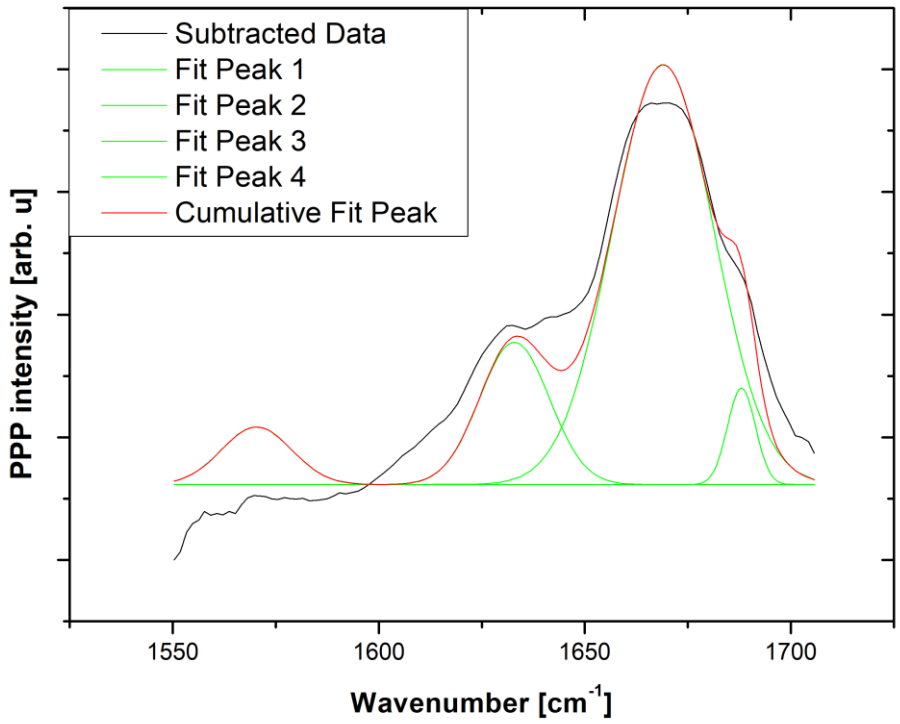

Figure 62: Gaussian fitting procedure applied to the ppp-polarized VSFG spectrum of Acol amide II band. The experimental spectrum (black line) is reproduced by the global fit (red line), obtained as the sum of individual Gaussian components (green curves).

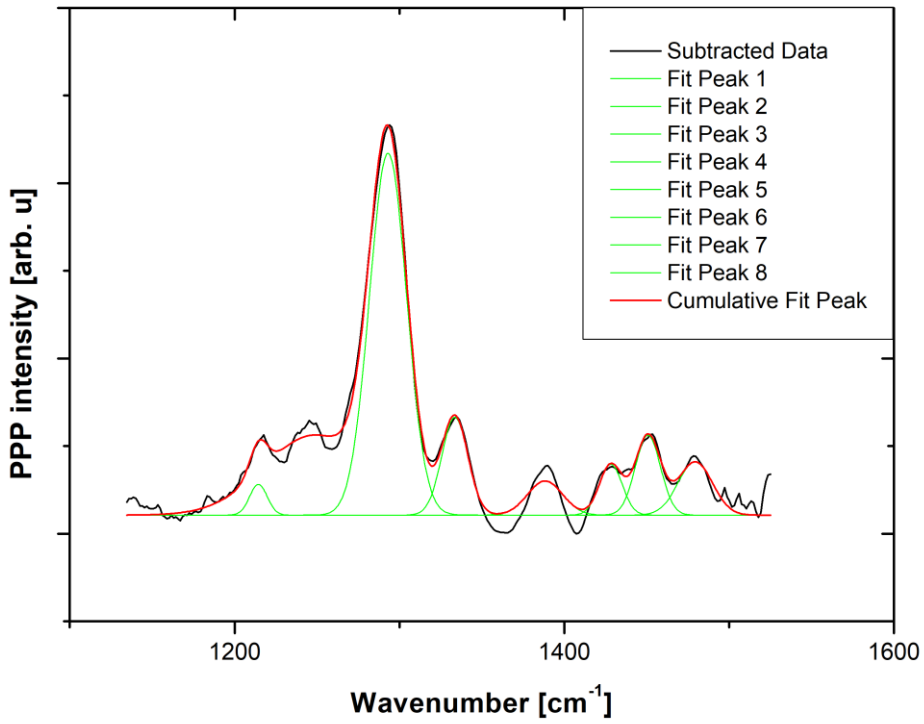

Figure 63: Gaussian fitting procedure applied to the ppp-polarized VSFG spectrum of Acol amide II and III bands. The experimental spectrum (black line) is reproduced by the global fit (red line), obtained as the sum of individual Gaussian components (green curves).

Étude multimodale en optique non linéaire de l'assemblage du collagène aux cicatrices fibrotiques de la moelle épinière dans un modèle murin

Le collagène est la protéine la plus abondante du corps humain et joue un rôle central dans la fibrose. Néanmoins de nombreux aspects de sa fibrillogenèse et de son organisation supramoléculaire restent mal compris. Dans cette thèse, la formation du collagène a été étudiée à différentes échelles, de l'organisation tissulaire jusqu'à l'assemblage moléculaire. Au niveau tissulaire, nous avons analysé l'organisation du collagène dans la cicatrice fibreuse, suite à la lésion de moelle épinière dans un modèle murin, à l'aide d'imagerie SHG, combinée à une analyse 2D (« fingerprint ») et une analyse 3D de variance. Les deux approches convergent sur la dynamique observée au cœur de la lésion mais divergent dans les régions adjacentes, rostral ou caudal de la moelle. Cette divergence indique que les métriques planaires et les descripteurs volumiques capturent des facettes distinctes du remodelage cicatriciel. Pour explorer les mécanismes moléculaires et supramoléculaires de la fibrillogenèse du collagène, nous avons adopté une approche « bottom-up » *in vitro*. Une stratégie multimodale combinant la SHS, la VSFG et l'AFM a permis d'identifier des signatures structurales du collagène à différents stades de la fibrillogenèse et a mis en évidence le rôle crucial des telopeptides dans la modulation de l'ordre polaire et de l'organisation supramoléculaire.

Mots-clés : Collagène, génération de seconde harmonique (SHG), diffusion de seconde harmonique (SHS), somme de fréquences vibrationnelle (VSFG), microscopie à force atomique (AFM), fibrose, fibrillogenèse

Multimodal non-linear optical approach to assess fibrillogenesis in collagen constructs and spinal cord injury in mice model

Collagen, the most abundant protein in the body, plays a central role in fibrosis, yet many aspects of its fibrillogenesis and supramolecular organization remain poorly understood. In this thesis, collagen formation was investigated across multiple scales, from tissue remodeling to molecular assembly. At the tissue level, we analyzed collagen organization in the fibrotic scar in a spinal cord injury mice model, using SHG imaging combined with a custom made 2D fingerprint and a 3D variance analysis. Both approaches converged on the dynamics at the lesion core but differ for the adjacent rostral and caudal regions. This discrepancy indicates that planar metrics and volumetric descriptors capture distinct facets of scar remodeling. To probe molecular and supramolecular mechanisms of collagen fibrillogenesis, we adopted a bottom-up *in vitro* approach. A multimodal strategy combining SHS, VSFG and AFM was developed, which identified structural signatures of collagen at different stages of fibrillogenesis and revealed the crucial role of telopeptides in modulating polar order and supramolecular assembly.

Keywords : collagen, second harmonic generation (SHG), second harmonic scattering (SHS), vibrational sum frequency generation (VSFG), atomic force microscopy (AFM), fibrosis, fibrillogenesis.